

**Formulation and Characterization of Polymer Nanoparticles for
Ultrasound-Induced Drug Release**

**Formulierung und Charakterisierung von Polymer-Nanopartikeln
für ultraschallinduzierte Wirkstofffreisetzung**

Der naturwissenschaftlichen Fakultät
der Friedrich-Alexander-Universität Erlangen-Nürnberg

zur

Erlangung des Doktorgrades Dr. rer. nat.

vorgelegt von

Ula Savšek

aus Ljubljana

Als Dissertation genehmigt von der Naturwissen-
schaftlichen Fakultät der Friedrich-Alexander-Universität
Erlangen-Nürnberg

Tag der mündlichen Prüfung: 04.06.2024

Gutachter/in: Prof. Dr. Dagmar Fischer
Prof. Dr. Stefan J. Rupitsch

Für meine Eltern

Za moje starše

Acknowledgements

First, I would like to express my deepest gratitude to my supervisor Prof. Dr. Dagmar Fischer, who guided me throughout the last years and gave me the opportunity to not only grow scientifically, but also on a personal level. Thank you very much for all your advice along the way as well as the support and motivation in less successful times. Besides your contributions to the thesis, you created a great atmosphere within our group, and I always enjoyed my everyday work life.

Many thanks also to Prof. Dr. Geoffrey Lee not only for seeing the potential in me and giving me the opportunity to join the group and work on the project, but for being an excellent supervisor during the first two years.

Furthermore, I want to thank Prof. Dr. Stefan J. Rupitsch and Prof. Dr. Helmut Ermer for their enthusiastic supervision as part of the collaboration with University of Freiburg and Univeristätsklinik Erlangen. I highly appreciated the valuable input and support during our scientific discussions. Special thanks also go to Benedikt George for providing technical assistance in Erlangen, as well as during my visits in Freiburg. I would have been lost without you. I also thank Anže Zidar, Prof. Dr. Matjaž Jeras and Prof. Dr. Julijana Kristl from University in Ljubljana for the corporation and the Deutschen Forschungsgesellschaft (DFG) for their trust, which made the collaborative projects (ER 94/33, LE 626/16-1, RU 1656/2-1) financially possible.

Thank you so much to all the colleagues, who contributed to the great working atmosphere during my PhD. I especially will not forget our parties, afternoon activities and weekend trips and most importantly coffee breaks and I will always be grateful for the friendships that were built during this time in my life. Without your support this thesis would have not been possible. My special thanks go to my lab mates, Lukas, Jan and Christian. I really enjoyed the time with you guys in the lab. Additionally, I especially want to thank Anna-Lena and Caro for always being there, if needed not only for scientific advice. Many thanks also got to Pia for her contributions and support especially at the beginning of the project.

Finally, I want to express my tremendous gratitude to my parents Tomaž and Ines and to my brother Gal. Thank you a lot for everything you made possible for me, your support and love. I am very lucky to always know you by my side. I want to give a big thanks to Fabian, for being a rock-solid support throughout my PhD journey. His patience during my thesis struggles and

the constant encouragement made all the difference. I am very happy to have you by my side on this remarkable journey.

List of Abbreviations

ALF	artificial lysosomal fluid
ANOVA	analysis of variance
ApoC	apolipoprotein C
ApoE	apolipoprotein E
ApoH	apolipoprotein H
AUC	area under the curve
BCA	bicinchoninic acid
BSA	bovine serum albumin
B-mode	brightness mode
C6	coumarin 6
CNTs	carbon nanotubes
DIN	German National Organization of Standardization (germ. <i>Deutsches Institut für Normung</i>)
DLS	dynamic light scattering
DSC	differential scanning calorimetry
EMA	European Medicines Agency
EN	European Standards (germ. <i>Europäische Norm</i>)
EPR	enhanced permeability and retention
FBS	fetal bovine serum
FDA	US Food and Drug Administration
FFT	fast Fourier transform
FUS	focused ultrasound
HS	human serum
HSA	human serum albumin
ICH	International Council for Harmonization of Technical Requirements for Pharmaceuticals for Human Use
IgG	immunoglobulin G
irAEs	immune-related adverse events
ISO	International Organization for Standardization
LDH	lactate dehydrogenase
LLF	Luer lock female
LNCaP	lymph node carcinoma of the prostate

MI	mechanical index
MPS	mononuclear phagocyte system
MSNs	mesoporous silica nanoparticles
MTS	3-[4,5-dimethylthiazol-2-yl]-5-[3-carboxymethoxyphenyl]-2-[4-sulfophenyl]-2H-tetrazolium, Inner Salt
MTT	3-[4,5-dimethylthiazol-2-yl]-2,5-diphenyltetrazolium bromide
MWCO	molecular weight cut-off
NC	nanocapsules
NS	nanospheres
O/W	oil-in-water
O-phase	organic phase
PBMC	human peripheral blood mononuclear cells
PBS	phosphate buffered saline pH 7.4
PCL	poly(ϵ -caprolactone)
PDI	polydispersity index
PEG	poly(ethylene glycol)
pI	isoelectric point
PLA	poly(lactic acid)
PLGA	poly(lactic- <i>co</i> -glycolic acid)
PSD	power spectral density
PVA	poly(vinyl alcohol)
RAS	rat sarcoma virus
RES	reticuloendothelial system
RF	radio frequency
RhB	rhodamine B
RPMI	Roswell Park Memorial Institute 1640 cell culture medium
SD	standard deviation
SDS	sodium dodecyl sulfate
SDS-PAGE	sodium dodecyl sulfate polyacrylic gel electrophoresis
SEM	scanning electron microscopy
TEM	transmission electron microscopy
T _g	glass transition temperature
T _m	melting temperature
TRIS	tris(hydroxymethyl)aminomethane

VSD	voltage spectral density
W/O	water-in-oil
W/O/W	water-in-oil-in-water
W-phase	aqueous phase
XRD	X-ray diffractometry

1 Table of Contents

Acknowledgements.....	v
List of Abbreviations.....	vii
1 Table of Contents	x
2 Theoretical Background	1
2.1 Cancer as its Basics	1
2.1.1 The Genetic Basis of Cancer	2
2.1.2 The Current Methods of Cancer Treatment.....	3
2.1.2.1 Chemotherapy.....	4
2.1.2.2 Immunotherapy.....	5
2.1.2.3 Radiotherapy.....	5
2.1.2.4 Surgery	5
2.2 Role of Nanoparticles in Cancer Treatment.....	6
2.2.1 Nanoparticles for Drug Delivery and Therapeutics.....	7
2.2.2 Examples of Nanoparticles in Cancer Research.....	8
2.2.2.1 Inorganic Nanoparticles.....	8
2.2.2.2 Liposomes.....	9
2.2.2.3 Polymeric Micelles	10
2.2.2.4 Dendrimers	11
2.2.2.5 Polymer Nanoparticles	11
2.2.3 Preparation Procedures of Polymeric Nanoparticles	12
2.2.3.1 Nanoprecipitation	12
2.2.3.2 The Emulsion Methods.....	13
2.2.3.3 Salting-Out Method	14
2.2.3.4 Supercritical Fluid Technology	15
2.2.3.5 Electrospraying.....	15
2.2.3.6 Microfluidics	15
2.3 Targeted Delivery of Tumors Using Nanoparticles	16
2.3.1 Active Targeting.....	16

2.3.2	Passive Targeting.....	17
2.4	Ultrasound Enhanced Drug Delivery	18
2.4.1	The Physics of Ultrasound.....	19
2.4.2	Acoustic Cavitation	22
2.4.3	Ultrasound-Triggered Mechanism of Drug Delivery	24
3	General Introduction	26
4	Materials and Methods	28
4.1	Formulation and Physicochemical Characterization of Nanoparticles	28
4.1.1	Nanoparticle Preparation	28
4.1.1.1	Nanospheres	28
4.1.1.2	Nanocapsules.....	29
4.1.1.3	PEGylated Nanocapsules.....	30
4.1.2	Freeze-Drying of Nanoparticles	30
4.1.3	Physicochemical Characterization.....	31
4.1.3.1	Laser Light Scattering	31
4.1.3.2	Quantification of Production Yield	31
4.1.3.3	Quantification of Dye Load and Encapsulation Efficiency	31
4.1.3.4	Quantification of the Residual PVA Content	32
4.1.3.5	Differential Scanning Calorimetry (DSC).....	33
4.1.3.6	X-Ray Diffractometry (XRD)	33
4.1.3.7	Transmission Electron Microscopy (TEM).....	33
4.1.3.8	Scanning Electron Microscopy (SEM).....	34
4.1.3.9	Karl-Fischer Titration.....	34
4.2	Ultrasound Measurements Set-Ups	34
4.2.1	Set-Up 1: Detection of Cavitation Behavior of NS and NC in a Cuvette.....	34
4.2.2	Set-Up 2: Determination of the Presence of NC with Imaging Method.....	36
4.2.3	Set-Up 3: Detection of Cavitation Behavior of NC in Through-Flow System.....	36
4.3	Stability Studies.....	37
4.3.1	Storage Stability Study of Nanocapsules.....	37

4.3.2	Colloidal Stability of Nanocapsules in Different Test Media.....	37
4.4	Characterization of the Protein Corona.....	38
4.4.1	Serum Protein Adsorption on Nanocapsules.....	38
4.4.2	Nanocapsule Protein Corona Characterization.....	39
4.4.2.1	Bicinchoninic Acid Assay (BCA Assay).....	39
4.4.2.2	Sodium Dodecyl Sulfate Polyacrylic Gel Electrophoresis (SDS-PAGE).....	39
4.5	Statistical Analysis.....	40
4.6	Biological Studies.....	40
4.6.1	In Vitro Cell Cultures.....	40
4.6.2	3-[4,5-dimethylthiazol-2-yl]-5-[3-carboxymethoxyphenyl]-2-[4-sulfophenyl]-2H-tetrazolium, Inner Salt (MTS) Assay.....	41
4.6.3	Lactate Dehydrogenase (LDH) Assay.....	42
5	Results and Discussion.....	43
5.1	Evidence of Inertial Cavitation of Polymer Nanoparticles.....	43
5.2	Effect of Process and Formulation Parameters on Polymer Nanoparticles for Ultrasound Model Drug Delivery.....	48
5.2.1	Impact of Polymer Concentrations on the Cavitation Activity of Nanospheres.....	48
5.2.2	Effect of Dye-to-Polymer Ratio on the Ultrasound Sensitivity of Nanospheres.....	51
5.2.3	Influence of the Purification by Tangential Flow Filtration on Ultrasound Cavitation...	53
5.2.4	Investigating Ultrasound Sensitivity Affected by Dye Hydrophilicity in Nanospheres..	55
5.2.5	Effect of Polymer Type on Dye Encapsulation and Cavitation Activity of Nanospheres	58
5.2.6	Impact of Different Types of PLGA Nanocarriers on Acoustic Cavitation.....	61
5.3	Optimization of the Formulation of Nanocapsules for Ultrasound Model Drug Delivery.....	65
5.3.1	Effect of Stabilizer Concentration on Physicochemical Properties and Inertial Cavitation of Nanocapsules.....	65
5.3.2	Influence of Homogenization and Polymer Type on Nanocapsule Cavitation.....	70
5.3.3	Impact of PEGylation on Ultrasound Cavitation of Nanocapsules.....	78
5.4	Stability of Nanocapsules.....	83
5.4.1	Storage Stability of Lyophilized Nanocapsule Formulations.....	83

5.4.2	Determination of the Physicochemical Properties and Ultrasound Activity of Nanocapsules after Incubation in Different Biologically Relevant Media.....	90
5.5	Investigation of Parameters Influencing Acoustic Measurements.....	93
5.5.1	Cavitation Activity of Nanocapsules at Different Frequencies.....	93
5.5.2	Impact of Water Tank Temperature on Ultrasound Cavitation of Nanocapsules.....	95
5.5.3	Impact of the Presence of Ethanol on Acoustic Cavitation of Nanocapsules.....	96
5.5.4	The Use of Tissue Mimicking Phantoms.....	97
5.6	Analysis of Protein Corona Composition on Nanocapsules.....	100
5.6.1	Effect of the Inertial Cavitation of Nanocapsules on the Serum Protein Adsorption....	101
5.6.2	Influence of Serum Incubation Temperature on Cavitation Activity.....	102
5.6.3	Determination of Physicochemical Properties and Ultrasound Activity of Nanocapsules after Incubation in Different Culture Media.....	105
5.6.4	Effect of Polymer Molar Mass and PEGylation on the Protein Corona and Depending on the Serum Type.....	109
5.6.5	Influence of pH and Ionic Strength on Protein Corona and Inertial Cavitation.....	112
5.7	Biological Studies of NC Suitable for Ultrasound Model Drug Delivery.....	117
5.7.1	Influence of PLGA NC with and without PEG on Metabolic Cell Activity.....	118
5.7.2	Determination of Membrane Damage in LNCaP Cells Detected by LDH Assay.....	121
6	Conclusion.....	122
7	Zusammenfassung.....	126
8	References.....	130
9	Appendix.....	154
9.1	Publications and Conference Contributions.....	154
9.1.1	Publications.....	154
9.1.2	Conference Contributions.....	154
9.2	Erklärung der Eigenleistung.....	156

2 Theoretical Background

Cancer is one of the leading causes of death in the world. It affects people of all ages, gender, races, different social, ethical and economic backgrounds. Cancer is caused by mutations to the DNA within cells arising from external forces, such as ultraviolet radiation, chemicals, smoking, and viral carcinogens or from spontaneous genetic mutation [1]. Currently many cancer treatments are available to cure, shrink or stop the progression of a tumor. Taking prostate cancer as an example, the treatment would be based on the extent of the cancer. The guidelines purpose an initial therapy with radiation or hormone drugs at low-risk group. By high-risk group invasive treatment options using surgery are being used to remove as much of the cancer as possible followed with chemotherapy and radiation therapy [2]. Using cytotoxic agents side effects often occur due to the nonspecific distribution of the drug in the body [3]. Unfavorable side effects occur when drugs are not preferentially taken up by tumor tissue, but instead accumulate in healthy tissue [4].

Thanks to remarkable efforts made in cancer diagnosis, treatment and prevention over the past 25 years, survival rates improved for many types of cancer. Ongoing research areas are mainly focused on the development of nanosized delivery platforms [5], new therapeutic targets such as vascularization of a tumor, known as angiogenesis [6], and specific targeted delivery of therapeutics [7].

Current research in the field of medical nanotechnology has demonstrated its advantages for cancer treatment and diagnostics. This technology seems promising, as it aims to develop nanocarriers to deliver chemotherapeutics selectively to the tumor cells with controlled and sustained release of drugs while obtaining minimum toxicity to healthy cells.

2.1 Cancer as its Basics

Cancer poses a huge treat to public health systems, where incidence rates have increased in both developed and underdeveloped countries [1]. The research from 2020 revealed 4 million new cases of cancer and over 1.9 million cancer-related deaths in Europe. The most common causes of death were cancer of the lung, colorectal, female breast and pancreatic cancer with 380,000, 250,000, 140,000 and 130,000 deaths, respectively [8]. They represent almost half of the overall burden of cancer in Europe (Figure 1).

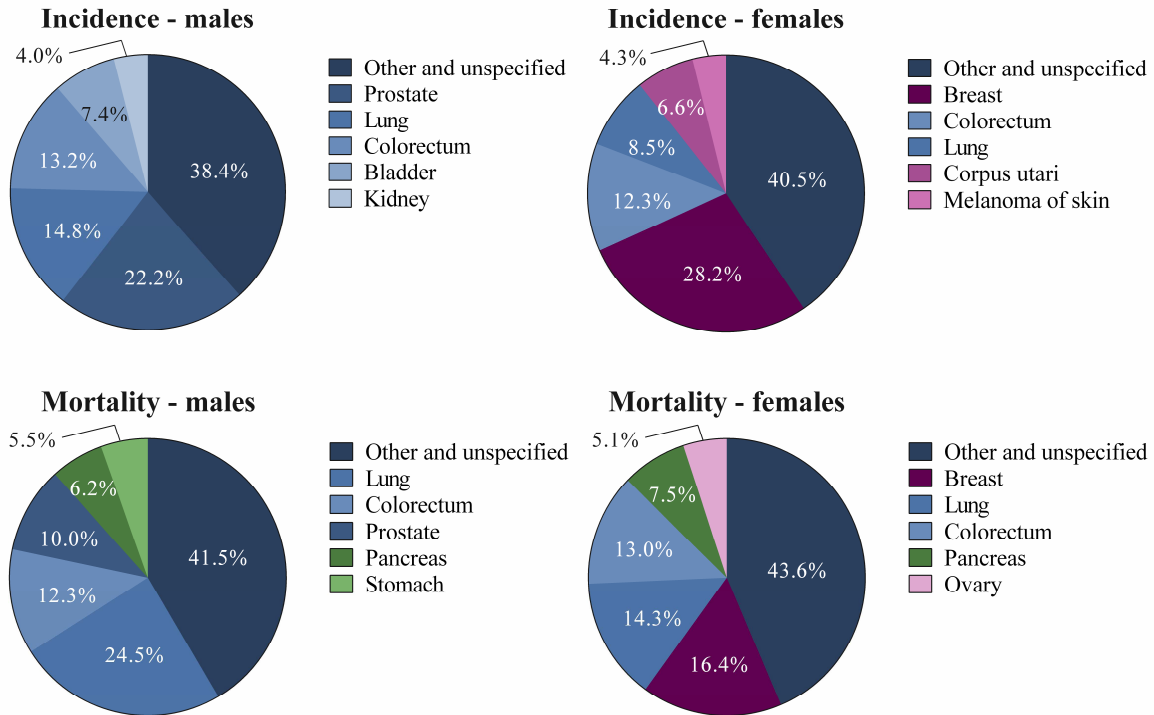


Figure 1 Distribution of cases and deaths for the five most common cancers in Europe in 2020 for males and females [8].

One of the greatest risk factor for developing cancer is aging, as elderly people are more likely to develop cancer compared with younger people [9]. Approximately 60% of cancer diagnoses and 70% of all cancer deaths occur by patients of 65 years or older [10]. It has been proposed that this disproportional increase with age is associated with the accumulation of mutations over the years [11]. As the population continues to age, a 47% increase in cancer incidence from 2020 to 2040 is projected to occur worldwide, assuming that national rates estimated in 2020 remain constant [12].

2.1.1 The Genetic Basis of Cancer

Cancer is a genetic disorder and it is termed as the malignant, autonomous growth of cells that have acquired mutations and epigenetic changes which leads to escape of normal growth control mechanism and uncontrolled cell division in the body [1, 13]. This is a complicated, multistep process, which demands accumulation of many genetic changes. These genetic alterations include truncation of proteins, altered amino acids or altered reading frame [13].

Cancer originates from mutations in genes that control proliferation, generally resulting from inactivation of tumor suppressor genes and/or conversion of proto-oncogenes to oncogenes. The normal proliferation and progression of a cell cycle which includes activation of a control system, reparation of the DNA damage, normal cell division, and induction of apoptosis

(programmed cell death), is controlled through different regulatory proteins. Sometimes, these regulatory proteins are not able to repair the damage in a normal cell [1, 14, 15]. At this point, a tumor suppression gene, known as p53, is activated to block the cell cycle and induce apoptosis. This gene has been identified as “the guardian of the genome” and has the ability to bind to ubiquitin which leads to proteasomal degradation, recognition of damaged DNA by the protein kinases ataxia telangiectasia mutated as well as ataxia telangiectasia and Rad3-related followed by phosphorylation of p53. With the activation of p53 through these kinases, cell cycle arrest is imposed [1]. However, this repair mechanism is mutated in more than 50% of all cancers resulting in inactivation of the p53 protein. This makes it unable to give a signal and activate the apoptotic machinery of the cell, resulting in uncontrolled proliferation of the cells and formation of cancer tissue [1, 13, 14]. Another example is the rat sarcoma virus (RAS) gene in the signal transduction cascade, the most frequently mutated oncogene in human cancer. The mutant form of the gene binds guanosine-5'-triphosphate permanently which leads to turning down a number of important functions for controlled cellular proliferation. Permanently activated RAS gene stimulates cells without any external trigger in an uncontrolled way [1].

However, it is unlikely that all occurring mutations involve tumor suppressor genes or oncogenes. It appears that several other cancer-associated genetic changes allow the tumor to survive, grow and disseminate. They could be listed in six categories or “hallmarks of cancer” [13, 15, 16] that describe the biological capabilities of healthy cells to evolve progressively to neoplastic state. These are:

1. loss of contact inhibition that prevent suppression of tumor cell proliferation,
2. excessive response to growth promoting signals or insensitivity to growth inhibitory signals,
3. resistance to apoptosis or evasion of growth suppression,
4. immortality through increased telomerase activity,
5. evasion of immune defense, and
6. induced angiogenesis.

2.1.2 The Current Methods of Cancer Treatment

Cancer therapy may be planned by considering different factors including the type and stage of cancer, age, gender and health status of the patient to provide sufficient eradication of the tumor or to inhibit and delay its growth. Chemotherapy, surgery, radiotherapy and immunotherapy are the most common types of cancer treatment [17], which often offer low rates of antitumor efficacy associated and serious side effect. Therefore, development of new better-tolerated

therapeutic applications with less side effect are an urgent need. The purpose of this section is to provide a brief overview of the traditional cancer therapies and their downsides.

2.1.2.1 Chemotherapy

Chemotherapy is commonly a first choice for cancer treatment. Many different kinds of chemotherapy are used to treat cancer, alone or in the combination with other treatments, including hormone therapy and molecular target therapy. Based on their different chemical composition and mechanism of action, cytotoxic drugs can be divided into several categories, known as alkylating agents, antimetabolites, topoisomerase inhibitors, mitotic inhibitors and corticosteroids. Chemotherapy could be indicated as neoadjuvant therapy before surgery to decrease tumor size, as well as adjuvant therapy after surgery to prevent tumor recurrence or in combination with radiation therapy during surgery [18].

Cytotoxic drugs used in chemotherapy target cells at different phases of the cell cycle. The nonspecific agents kill cells during any phase of the cell cycle while specific agents affect cancer cells only during a certain phase [19]. The major concern for chemotherapy is toxicity. These compounds do not distinguished between healthy cells such as bone marrow, intestinal epithelium and skin cells, and present a narrow therapeutic index with a small difference between the dose required for an antitumor effect and that responsible for unacceptable toxicity [20, 21]. Side effects are usually nausea, vomiting, mucosal injury, obstipation, diarrhea, myelosuppression and alopecia [22, 23]. Due to these undesirable effects, patient resistance to the therapy often increases, which leads to decreased survival, higher treatment failure rates and health care costs [15, 19, 20, 24].

Some cytotoxic drugs may affect cells of vital organs and cause permanent damage to the kidneys, lungs, nervous system and heart. Repeated administrations of anthracyclines could cause cardiotoxicity due to oxidative stress and apoptosis. A high dose of alkylating drugs, ifosfamide and cyclophosphamide, may lead in life-threatening heart failure and arrhythmias [23]. Meanwhile, cancer treatment often leaves damaged cognitive functions resulting in dysfunction of episodic memory, slow information processing, deficit in attention and etiological functions that could first appear after some months or years. It was shown that doxorubicin and cyclophosphamide have a negative impact on many domains of cognitive function in approximately 40% of women undergoing chemotherapy for breast cancer, probably because of the reduced production of new progenitor cells in the hippocampus [25, 26]. Another example is the nephrotoxicity by treatment with commonly used cytotoxic agent such as cisplatin. The kidney cell injury and death appeared via signaling pathway of protein kinase C δ ,

which appears to be the same pathway responsible for chemotherapeutic effects of cisplatin in tumors [27].

2.1.2.2 Immunotherapy

In year 2011, US Food and Drug Administration (FDA) approved ipilimumab as a first drug for immunotherapy for treating metastatic melanoma. The most common immunotherapy currently involves immune checkpoint inhibitors and others (T-cell transfer therapy, monoclonal antibodies, treatment vaccines [28]), which are using the immune system to fight against cancer. Most of these are monoclonal antibodies targeting immune checkpoints including CTLA4, PD-1 and PD-L1 [29]. Although, they have improved overall survival of patients with rapidly fatal cancer [29, 30], the treatment often resulted in life-threatening and long-term consequences, such as unknown side effects, management of chronic conditions as well as financial issues [31]. Immune-related adverse events (irAEs) are very common, can occur many weeks or months after treatment and can risk any organ [32]. The oncologic treatment of these patients can be challenging because they require treatment over a longer period compared to other cancer therapies.

2.1.2.3 Radiotherapy

Radiation therapy is one of the most cost-effective method for cancer treatment that contributes to cure in about 40% of cases alone as a curative therapy in a variety of tumor types or more commonly with concomitant surgery and/or chemotherapy [24]. The aim is to deliver a lethal dose of high-energy radiation from X-rays, gamma rays or electrons to tumor tissue to induce DNA damage, kill cancer cells and shrink tumor size. In contrast to chemotherapy drugs, the radiotherapy is normally delivered from outside the body and localized to the tumor area [33]. It is also relative safe and painless for the patient. However, it is difficult to avoid the damage of the healthy tissue, which results in severe side effect in 5-10% of treated patients [34]. Most common radiotherapy effects are hair loss, delayed wound healing, induration of the skin, myocarditis, pneumonitis and vascular stenosis [18]. In attempt to avoid this, the dose of the radiotherapy often is reduced that could result in failure of the cancer treatment and poor prognosis. Thus, a major consideration in the use of radiotherapy is how to maximize effectiveness of the therapy within the capacity of acceptable dose that adjacent healthy tissues can tolerate radiation injury [35].

2.1.2.4 Surgery

Surgery is the most effective treatment for early stage of solid tumor (ovarian, breast, intestinal and lung tumor), as it attempts to remove 100% of the malignant cells. However, it means

removing tissue from the body and is a crucial intervention for providing a chance of cure for patients [24]. A surgery of breast cancer has been shown to cause persistent breast pain in 25% of women and a strong correlation between depression and chronic pain [36]. Despite modern surgical techniques and instrumentation, residual tumor cells may remain in the surgical margins after the procedure or be inadvertent seeded during the surgery, which promotes the risk for tumor relapse and metastasis [37, 38]. Additional chemotherapy and radiotherapy are commonly used as postoperative cancer treatment to reduce the possibility of recurrence of the tumor [37], which could prolong the cure period.

2.2 Role of Nanoparticles in Cancer Treatment

The term “nanotechnology” was presented in 1959 by the Nobel laureate Richard P. Feynman in his lecture “*There’s Plenty of Room at the Bottom*” [39], which acted as a springboard for all further revolutionary developments in the field of nanotechnology. Nanotechnology includes various types of materials and particles labelled as “nano” due to their size at nanoscale level (10^{-9} m). The nanotechnology guidance published by FDA in 2014 provided a framework for the regulations of nanotechnology products and can be used as a screening tool to all FDA-regulated products [40]. It describes two points that should be considered, when the product involves application of nanotechnology [40]:

1. *whether a material or end product is engineered to have at least one external dimension, or an internal or surface structure, in the nanoscale range (approximately 1 nm to 100 nm);*
2. *whether a material or end product is engineered to exhibit properties or phenomena, including physical or chemical properties or biological effects, that are attributable to its dimension(s), even if these dimensions fall outside the nanoscale range, up to one micrometer (1,000 nm).*

Meanwhile, in 2011 European Commission defines the term “nanomaterial”, with the review “Recommendation on the definition of nanomaterial 2011/696/EU” and adopted it in 2022 with a new version 2022/C 229/01. According to it [41]:

a “nanomaterial” means a natural, incidental or manufactured material consisting of solid particles that are present, either on their own or as identifiable consistent particles in aggregates or agglomerates, and where 50 % or more of these particles in the number-based size distribution fulfil at least one of the following conditions:

1. *one or more external dimensions of the particle are in the size range 1 nm to 100 nm;*

2. *the particle has an elongate shape, such as a rod, fiber or tube, where two external dimensions are smaller than 1 nm and the other dimension is larger than 100 nm;*
3. *the particle has a plate-like shape, where one external dimension is smaller than 1 nm and the other dimensions are larger than 100 nm.*

So far, no unified definition of nanomaterial has been accepted worldwide, which is leading to varying use of the term "nanoparticle" in the scientific literature. Especially in the pharmaceutical field, where nanoparticles are usually used for drug delivery and therapeutic applications, the size is often described between 1 nm and 1000 nm [42].

2.2.1 Nanoparticles for Drug Delivery and Therapeutics

Application of nanoparticles in medicine is promising alternative for drug delivery and solution for many limitations and problems of conventional drug delivery systems. The main challenges of drugs are limited targeting, low therapeutic indices, poor water solubility, and the induction of their resistances [43]. In contrast to conventional pathway of drug delivery, nanoparticles aim to improve the target accumulation and efficient release of the drug at the desired site, increase therapeutic efficiency and reduce the intensity and incidence of severe side effects by concentrating in cancer tissue rather than in healthy tissues [44]. Nanoparticles are attractive as cancer therapeutics due to their variety in size, composition, surface properties, and stability. The properties of each nanoparticle system can be developed in a manner to enhance the drug delivery. For instance, nanoparticles with hydrophilic surfaces are utilized for to extend circulation time, whereas positively charged nanoparticles are used to enhance endocytosis [45, 46]. The most common types of nanoscaled delivery systems for targeted drug delivery in cancer research include polymeric nanospheres (NS) and nanocapsules (NC), liposomes, micelles, dendrimers, protein and inorganic nanoparticles. The first approach to load nanoparticles with pharmaceutical active ingredients was described in 1960s, when doxorubicin was encapsulated in liposomes for cancer treatment [47]. In the last 30 years, the European Medicines Agency (EMA) and FDA have approved several nanoparticle formulations for cancer therapy. Among the nanoscaled delivery systems, the lipid based nanoparticles presents 56% of the total approved nanopharmaceuticals for cancer treatment. The rest are mainly included as protein-drug conjugates (38%) and metallic based nanoformulations (6%). They are summarized in Table 1.

Table 1 Nanoscaled delivery systems for cancer therapy on the market (adapted from [48]).

Nanoparticle system	Product name®	Active component	Indication	Approval (Year)
Lipid based nanoparticles	Doxil	Doxorubicin	Kaposi's ca., ovarian ca., multiple myeloma	FDA (1995)
	Caelyx	Doxorubicin	Metastatic breast ca., ovarian ca., Kaposi's ca., multiple myeloma	EMA (1996)
	DaunoXome	Daunorubicin	Kaposi's ca.	FDA (1996)
	Myocet	Doxorubicin	Metastatic breast ca.	EMA (2000)
	Mepact	Mifamurtide	Osteosarcoma	EMA (2009)
	Ameluz	5-Aminolevulinic acid	Superficial and/or nodular basal cell carcinoma	EMA (2011)
	Marqibo	Vincristine	Acute lymphoid leukemia	FDA (2012)
	Onivyde	Irinotecan	Pancreatic ca., colorectal ca.	FDA (2015)
	Vyxeos	Daunorubicin Cytarabine	Acute myeloid leukemia	EMA (2018)
Protein-drug conjugates	Oncaspar	Pegaspargase	Acute lymphoblastic leukemia	FDA (1994)
	Ontak	Denileukin Diftox	Cutaneous T-cells lymphoma	FDA (1999)
	Eligard	Leuprorelin acetate	Prostate ca.	FDA (2002)
	Abraxane	Paclitaxel	Breast ca., non-small lung ca., pancreatic ca.	FDA (2005)
	Kadcyla	DM1 (or Emtansine)	HER2+ breast ca.	EMA (2013) FDA (2013)
	Pazenir	Paclitaxel	Metastatic breast ca., metastatic adenocarcinoma of the pancreas, non-small cell lung ca.	EMA (2019)
Metallic nanoparticles for magnetic hyperthermia	NanoTherm	Iron oxide	Glioblastoma ca., prostate ca., pancreatic ca.	EMA (2013)

Abbreviation: ca.: cancer

2.2.2 Examples of Nanoparticles in Cancer Research

2.2.2.1 Inorganic Nanoparticles

Most commonly used inorganic nanoparticles in the diagnosis and treatment of cancer include mesoporous silica nanoparticles (MSNs), iron oxide nanoparticles, carbon nanotubes (CNTs), gold nanoparticles and porous silicon. Inorganic nanoparticles have attracted great interest in medicine due to their diverse functionality, wide range of sizes and shapes and unique physical and chemical properties. They have a good physical stability, an increased surface area, which increase loading capacity and a good biocompatibility and versatility when it comes to surface

functionalization [49]. However, some inorganic nanoparticles, such as CNTs, are not biodegradable and could have a cytotoxic effect [50].

MSNs are the most widely used inorganic nanoparticles for controlled drug delivery. These are silica nanoparticles with meso-nanoscale pores in a honeycomb-like arrangement with pores sizing from 2 nm to 50 nm and a multifunctional tunable morphology that provides a high surface area and pore volume [51, 52]. Besides, MSNs induce a low immunogenicity and a good biocompatibility. They are excellent options for the delivery of several anticancer drugs and other theranostic agents, including diagnostic molecules and enzymes to the targeting site [53]. Another commonly used inorganic nanoparticles are CNTs, rolled up cylinders of graphene sheets. They served as carriers for small drugs, proteins, plasmid DNA and RNA to target cells through endocytosis with an ability for high drug loading due to a high specific surface area. CNTs possess good optical properties and thus can be utilized for photothermal cancer eradication [54]. The inert and nontoxic nature of gold nanoparticles makes them a suitable nanocarrier system applicable in biomedical field [55]. The drug could be attached on the external surface of the gold nanoparticles or encapsulated in the hollow interiors of gold nanoshells and nanocages [56]. Additionally, gold nanocarriers have strong photothermal properties that could be used for direct cancer treatment even without cytotoxic drug. Moreover, they could be used for cancer diagnostics due to their fluorescence and multiphoton luminescence properties and strong optical absorption [53, 57]. To date, NanoTherm[®] is the only metallic-based nanoformulation for cancer therapy that is approved by FDA and EMA. Magnetic fluid hyperthermia, as cancer therapy, is using a colloidal dispersion of iron oxide nanoparticles coated with amino silane. After direct introduction of the iron oxide nanoparticles into the tumor, an alternating magnetic field is applied to destroy the cancer cells by heating [48, 58].

2.2.2.2 *Liposomes*

Liposomes are spherical vesicles composed of synthetic or natural phospholipids and cholesterol, with specific net properties expressed in physicochemical features including permeability, and charge density [59]. Amphiphilic phospholipid molecules close the lipid bilayer and encapsulate the aqueous interior due to interactions between their hydrophilic head groups with aqueous phase, while protecting their hydrophobic groups from the aqueous environment [60]. These self-associated liposomes are classified as unilamellar and multilamellar and could encapsulate water-soluble drugs in the aqueous core, lipidic drugs in the lipid bilayer and amphiphilic drugs partitioned at the bilayer surface [61]. Liposomes offer

several advantages over many other nanocarriers including biocompatibility, capacity for self-assembly and ability to carry large drug payloads of hydrophilic and hydrophobic drugs. Moreover, liposomes could be designed for passive or active targeting on cancer cells due to modifications of the outer surface of liposome by adding additional molecules such as antibodies, peptides, proteins and carbohydrates, which control biological characteristics of liposomes [62]. Despite these advantages, they have demonstrated several disadvantages that became obvious during clinical application. A potential disadvantage is that the mononuclear phagocyte system (MPS) could recognize them as foreign objects followed by their removal by opsonisation, and the reticuloendothelial system (RES) [63, 64]. To overcome this limitation, progress took place in the 1990s with the development of sterically stable liposomes functionalized with poly(ethylene glycol) (PEG) molecules. Increase in steric stabilization reduced the MPS clearance that resulted in prolonged circulation and localization in tumor [63-66]. The first FDA and EMA-approved anti-tumor liposomal PEGylated formulations were Doxil[®] in the USA and Caelyx[®] in Europe with the active pharmaceutical ingredient doxorubicin (Table 1) [59, 60, 67].

2.2.2.3 Polymeric Micelles

Polymeric micelles are formed of amphiphilic block copolymers with self-assembly properties to create a structure with a hydrophobic inner core and a hydrophilic outer shell which varies in composition [68, 69]. Copolymers consist from highly water soluble and flexible polymers, such as PEG and poloxamers constructing the hydrophilic shell of the polymeric micelles, and hydrophobic polymers, such as poly(lactic-*co*-glycolic acid) (PLGA), poly(lactic acid) (PLA) and poly (ϵ -caprolactone) (PCL) comprising the hydrophobic core [70]. The advantage of such a structure over other delivery systems is the ability to load a hydrophobic drug into the core, hydrophilic drug into the shell and amphiphilic drug in-between. The outer shell can be modified to achieve the desired properties for sufficient transport to the tumor site [69, 71, 72]. Additional reasons for the use of micelles in the drug delivery is the small diameter below 100 nm that can reduce the uptake by the RES and the hydrophilic surface increasing the circulation time [45]. However, some challenges appeared in formulation of polymeric micelles including low drug delivery or instability when diluted in the bloodstream [70]. Until today, only one polymeric micellar formulation, named as Genexol-PM[®] has been approved in South Korea. It uses a block copolymer of PEG and PLA (mPEG-PLA) to encapsulate paclitaxel. The formulation allows higher dose of administration with less hypersensitivity than Taxol[®], where paclitaxel is solubilized in ethanol and Cremophor[®], used for the treatment of breast cancer, pancreatic cancer and non-small cell lung cancer [73].

2.2.2.4 Dendrimers

A well-defined structure of dendrimers is characterized by repeated branching of a polymer around a central core to form a three-dimensional geometrical structure. Dendrimers are formed from monomers using polymerization that defines the length of branching units and are sterically limited [59, 74, 75]. Dendrimers offer multiple advantages. They are stable structures with surface groups that could be functionalized for targeted drug delivery by conjugation of ligand [76-78]. Due to the high branching, drug molecules could be easily incorporated in the multifunctional sphere or coupled to functional groups [75]. Dendrimers have been widely explored for the delivery of poorly soluble anticancer agents [79]. However, a main disadvantage of dendrimers is their rapid systemic clearance and insufficient tumor accumulation. The rapid elimination from the bloodstream and their small size (1-15 nm [80]) prevent them to take significant advantage of the enhanced permeability and retention (EPR) effect resulting in inefficient delivery and accumulation within tumor [81]. There is no formulation using dendrimers for cancer treatment on the market yet, but there are several studies, which are using easy functionalization of dendrimers to target tumors. One of these examples is the recent study of Nigam *et al.* [82], who combined magnetic chemotherapy and hyperthermia for cervical cancer treatment. They covered iron oxide nanoparticles with dendrimers and loaded them with doxorubicin [82]. Another example is the conjugation of folic acid to dendrimers for the successful delivery of siRNA to lung cancer cells [83].

2.2.2.5 Polymer Nanoparticles

Polymer nanoparticles are commonly defined as solid, colloidal systems, where polymers have been used as the construction material [84]. Generally, there are two main types of polymer nanoparticles, NS and NC (Figure 2). NS consist of a spherical polymeric matrix in which the drug is uniformly dispersed throughout the particle, while NC are vesicular systems with a single polymer shell and an aqueous or oily core in which the drug is confined [75, 85, 86]. In the preparation process of polymer nanoparticles for drug delivery, the choice of the polymer material is very important and it depends on the type of application, duration of drug release and nature of the active ingredient. Polymers for drug delivery systems can be classified as hydrophilic or hydrophobic, charged or noncharged and natural or synthetic [85, 87]. Among natural polymers, are generally used polysaccharides (chitosan, dextran) as well as proteins (albumin, gelatin, collagen), while synthetic polymers include polyethers, polyesters and vinyl polymer polystyrene [88]. Polymeric nanoparticles are generally easy to synthesize, have high stability, and are biocompatible and biodegradable [89]. They offer the advantage of easy surface modification [90], allowing them to deliver drugs, proteins and genetic material to

targeted tissues. However, limitations of polymeric nanoparticles include an increased risk of particle aggregation and toxicity [91]. Only a few polymeric nanomedicines have gained FDA approval and are used in the clinic. However, many clinical trials are currently testing polymeric nanocarriers [92].

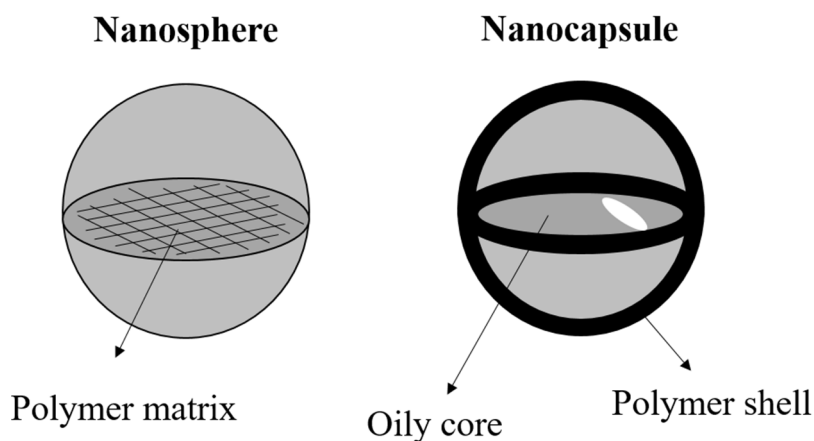


Figure 2 Structure of polymer NS and NC.

2.2.3 Preparation Procedures of Polymeric Nanoparticles

2.2.3.1 Nanoprecipitation

Nanoprecipitation is a method for the preparation of polymeric nanoparticles, which was developed by Fessi *et al.* [93]. It is also known as solvent displacement method or interfacial disposition (Figure 3) where drug is entrapped in the polymer matrix of NS or dispersed in the oily core of NC. The interfacial disposition of polymers takes place after displacement of a semi-polar solvent in the lipophilic phase, miscible with water. Due to rapid diffusion of the solvent into a non-solvent phase, the interfacial tension between these two solutions decreases, resulting in a higher surface area and formation of well-defined droplets of nanoparticles [93, 94]. The NS are prepared by a precipitation, which includes Maragoni effect [95], while NC formation is governed by the ouzo effect [96]. The nanoprecipitation process requires (i) a suitable organic solvent which is partly miscible in water and could be removed by moderate stirring, evaporation under reduced pressure or by tangential ultrafiltration, (ii) polymer dissolved in the organic phase (O-phase), and (iii) an aqueous phase (W-phase) with a water-in-oil (W/O) stabilizer in which the polymer is not soluble. To prepare NC *via* nanoprecipitation the composition of the O-phase additionally contains an oil. The nanoprecipitation method is mostly applicable for the encapsulation of lipophilic drugs, which are usually added to the organic solvent [84, 97]. However, Barichello *et al.* have shown that this method could be possibly used in formulations for proteins and peptides [98] but with very

low encapsulation efficiency. Among natural polymers, allyl starch [99] and dextran ester [100] are used. More commonly used polymers are biodegradable such as synthetic PLA [101], PLGA [102] and PCL [103, 104]. This one-step nanoparticle preparation technique is fast, simple, reproducible and widely used for the preparation of NC and NS. However, the high encapsulation efficiency could be achieved for hydrophobic drugs, while hydrophilic drugs suffer from drug leakage to the external medium, resulting in low drug content in the nanoparticles.

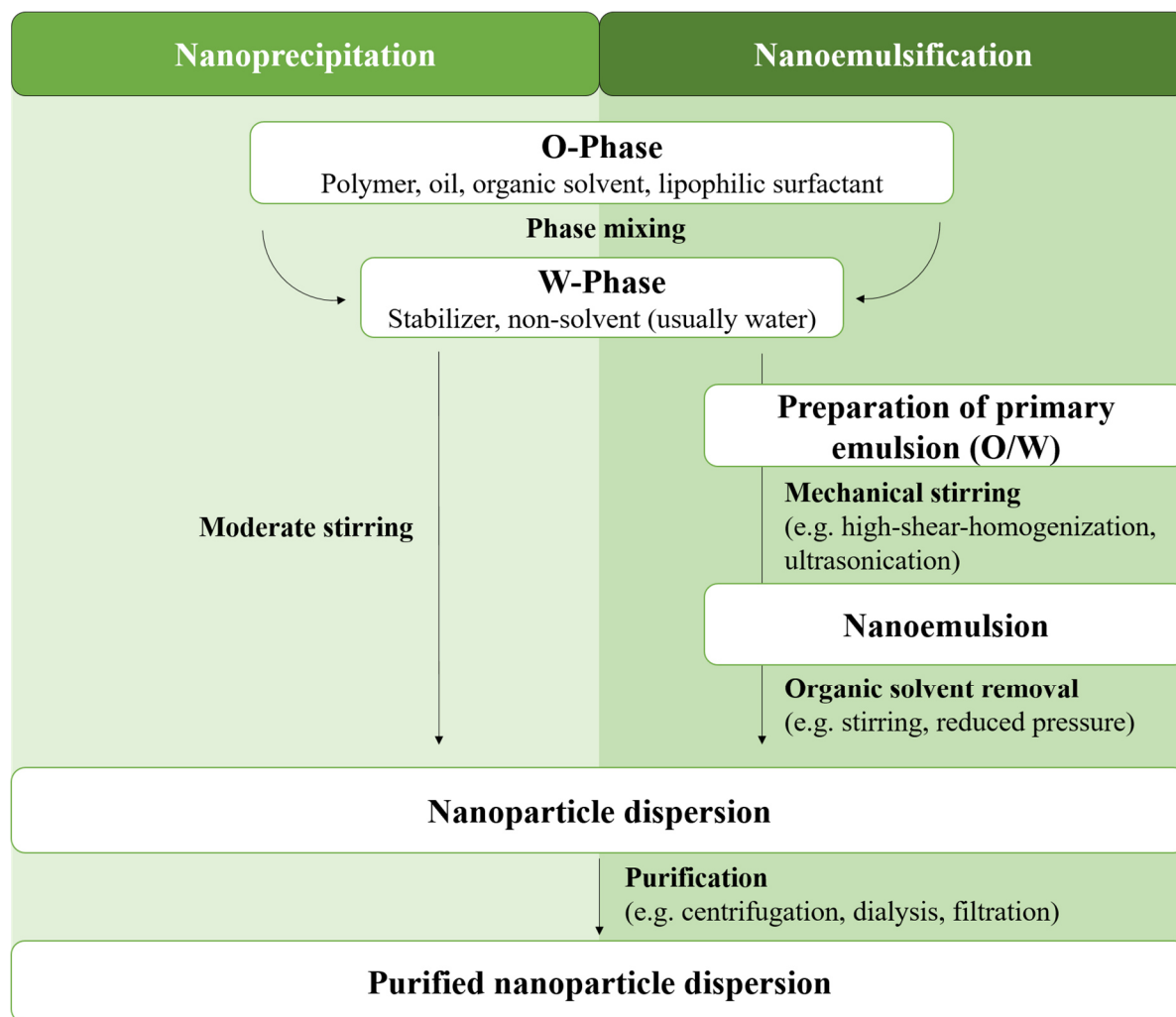


Figure 3 A schematic overview of the nanoprecipitation and nanoemulsification method used for the formulation of NS and NC. Adapted from [105].

2.2.3.2 The Emulsion Methods

Emulsion-based methods are among the most widely used techniques for preparing polymer nanoparticle preparation as they offer several advantages. These techniques are known for their rapid and simple operation, ability to encapsulate drugs with different physicochemical properties, and cost-effectiveness in terms of equipment required. Though it includes more steps than nanoprecipitation technique (Figure 3) and it uses high volumes of water. They could be

divided into emulsification-diffusion, emulsification-evaporation, emulsification-coacervation and double emulsification [106]. The emulsification-diffusion method is one of the most commonly used method for polymeric nanoparticle preparation. This technique was utilized by Leroux *et al.* [107] for NS preparation and then by Quintanar-Guerrero *et al.* [108] to prepare NC. Depending on the aqueous solubility of the drug, oil-in-water (O/W) single emulsions, or water-in-oil-in-water (W/O/W) double emulsion systems can be used. For the encapsulation of hydrophobic compounds, PLGA and the drug are dissolved together in the O-phase and then emulsified with an aqueous solution containing a surfactant, such as poloxamer 188, polysorbate 80, or poly(vinyl alcohol) (PVA). For single-emulsion production, both phases are mixed by high-speed homogenization or ultrasonication to form a stable O/W emulsion [109, 110]. Encapsulation of a hydrophilic drug involves an initial formation of a W/O emulsion, in which the drug is in the W-phase and the polymer is in the O-phase. Subsequently, the primary W/O emulsion is emulsified in the second aqueous solution containing the surfactant to form W/O/W system [110]. The next steps include the removal of the organic solvent through diffusion or evaporation and purification with ultracentrifugation to collect nanoparticles and remove residual excipients [94].

2.2.3.3 Salting-Out Method

The salting-out method, disclosed by Bindschaedler *et al.* [111], is a modified version of solvent diffusion or emulsification method that involves a salting-out process while avoiding the use of surfactants or chlorinated solvents in the emulsification step. The polymer is dissolved into the organic solvent, which is usually water-miscible and added to a saturated aqueous solution containing a salting-out agent. Electrolytes such as calcium chloride, magnesium chloride and magnesium acetate or non-electrolytes such as sucrose, are commonly used as suitable salting-out agents. Due to their presence, the W-phase does not mix with the O-phase which leads in the formation of the emulsion. This emulsion is diluted with a large volume of water or an aqueous solution to enhance the reverse salting-out effect resulting in the diffusion of the organic solvent into the W-phase, precipitation of the polymer and thus inducing the formation of nanoparticles [112-115]. The salting-out agent and the organic solvent could be eliminated by centrifugation or cross-flow filtration. High efficiency, easy scale up, speed and simplicity of operation are advantages of salting-out method. However, it is limited to hydrophobic drugs and selected salting-out agents that do not precipitate. Another disadvantage is the extensive washing, which represents a time-consuming and difficult procedure [115, 116].

2.2.3.4 *Supercritical Fluid Technology*

The supercritical fluid technology offers a simple, high quality and solvent free process with suitable technological properties [117]. The technique is based on the use of a supercritical fluid such as carbon dioxide and water [118], which can either be in liquid or gas form. It is employed above its thermodynamic critical point of temperature and pressure. After dissolution of drug and polymer in an environment friendly solvent, the mixture is solubilized in the supercritical fluid, followed by the rapid expansion of the solution across a capillary nozzle into ambient air. Due to rapid pressure reduction during the expansion, it comes to supersaturation and formation of homogeneous nuclei, resulting in dispersed nanoparticles [119, 120]. Even though this technique utilizes no organic solvent, it has some limitations, for example high equipment and energy costs, difficulty to dissolve strong polar substances in supercritical carbon dioxide and broad nanoparticle size distribution [84, 119].

2.2.3.5 *Electrospraying*

The electrospraying is a simple, one-step approach to prepare polymeric nanoparticles with the use of high voltage. A hydrophilic or hydrophobic drug is mixed to the polymer solution, which is applied into a syringe and infused at a constant rate using a syringe pump. The high voltage forces the solution to appear from the syringe in form of droplets, followed by solvent evaporation and formation of nanoparticles [121]. Not only synthetic polymers, such as PLA, PLGA and PCL, but also natural polymers, such as alginate and chitosan, can be used [122]. This technology is also convenient for proteins or carbohydrates without losing their bioactivity [123]. Other advantages include rapid preparation, low cost, easy control of the process, high reproducibility and high encapsulation efficiency [124]. However, the shear stress involved in the nozzle may induce degradation of e.g. the proteins and enzymes [125].

2.2.3.6 *Microfluidics*

Nanoparticle preparation in microfluidic systems is performed in a microreactor of an inner dimension smaller than 1 mm. It includes a microfluidic chip that uses micron-scale channels to handle fluids and are often made of polymers such as polydimethylsiloxane or glass [126]. The microfluidic platform comprises two types of systems: single-phase continuous flow system with continuous laminar flow of multiple fluids and multiphase flow system divided into segmented flow and drop microreactors [127]. This systems demonstrate several advantages over conventional batch synthesis including high reproducibility and controllability, low reagent consumption and high-throughput preparation of nanoparticles [128]. Droplet microfluidics also enable currently inaccessible high-throughput screening application.

Nevertheless, there are some challenges, such as the possibility of channel clogging, expensive substrates such as glass and silica, the complex device design, and the complicated scale-up process [129].

2.3 Targeted Delivery of Tumors Using Nanoparticles

Nanoparticle drug delivery can be either an active or a passive process. Passive delivery refers on the tumor biology presented near the cancer cells, whereas active targeting needs an external active biomolecule linked to the nanoparticle system.

2.3.1 Active Targeting

Nanoparticles that are engineered for active targeting to the tumor cells use peripherally conjugated or functionalized biomolecules, such as peptides, proteins, nucleic acids, monoclonal antibodies, sugars or small molecules to improve specific nanoparticle accumulation at the tumor site. Ideally, active biomolecules selectively bind with high affinity for target molecules, such as proteins, sugars or lipids, overexpressed or selectively expressed on the surface of cancer cells as opposed to healthy cells [15, 130-133].

The main intensions of active targeting involve [130]:

- 1.) identification of cancer cells due to selective binding of active biomolecules with specific ligands on the cell surface,
- 2.) avoidance of non-specific interaction of active biomolecules with non-cancer cells,
- 3.) high local concentration of the nanoparticles on the outer surface of the target cells to achieve the functional dose before drug rush dilute through normal circulation and renal clearance,
- 4.) enhancement of the cellular uptake of the drug and
- 5.) effective transport of the nanoparticles due to long circulation times through the EPR effect.

The design of ligand-functionalized nanoparticle drug carriers has to be in sufficient quality to allow multipoint binding at the tumor site. The efficiency of an active targeting system is evaluated by the targeting specificity of the target molecule and the delivering capacity of the ligand-functionalized nanoparticle [133]. The targeting specificity is defined by the bioavailability and the interaction between ligand-functionalized nanoparticle and target cell. However, the development of the nanoparticle system could be challenging due to biology of the systems in a human body, such as RES, immune system and weak perfusion of tumors [15,

130]. Therefore, nanoparticles developed for active targeting need to remain in the blood circulation, be able to escape immune system and increase diffusion rates.

Active targeting could be additionally divided into different levels, including tissue, intrinsic, systematic specific and gender specific [15]. The purpose of systematic cancer targeting is to act fast in uncontrolled cell replication, metastasis and angiogenesis [130]. Some cancers, including lung, breast, prostate, ovarian and head cancer, express on the surface of their cells high levels of folate receptors which makes them suitable targets for nanoparticles with folic acid ligand [134]. Due to rapid and uncontrolled cancer cell proliferation, the demand for iron in tumor cells is greater. This enhances the expression of iron-binding glycoprotein transferrin on the surface of cancer cells, which can be exploited as a target molecule [130, 134]. Despite the advantages of active targeting of nanoparticles, only 0.7% of the administered nanoparticle dose was found to be delivered to a solid tumor [135].

2.3.2 Passive Targeting

Nanoparticle systems exploit the nature of tumor dysregulated growth and its progression for passive targeting. The growth of tumor cells is much faster in comparison with normal cells and can lead to overgrowth of the cells and proliferation of small masses. The growth of tumor cells continues until the tumor reaches the diffusion limit size of about 2 mm³. This limiting environment affects nutrition, amino acids and glucose intake and oxygen delivery. Normal cells are not able to survive, while tumor cells could overcome these limitations by inducing and maintaining the tumor blood supply in an event called angiogenesis [46, 136]. In comparison with normal blood vessels, the biology of angiogenesis shows the lack of pericytes, several abnormalities in the basement membrane, and high level of proliferating endothelial cells [136]. Normal physiological vessels are constructed from tight endothelial junctions up to 10 nm in size. The size of the pores between the leaky endothelial cells of the tumor ranges from 100 nm to 1200 nm depending on the tumor type [137, 138] which allows enhanced permeability of nanoparticles to pass through the vessel wall and reach tumor cells [75]. In addition, the lymphatic drainage system also undergoes abnormality resulting in higher tumor interstitial pressure in the tumor inner core than in the surrounding tissue. This prevents normal diffusion of molecules and cause their concentration in the center of the tumor [75, 136]. Moreover, the nanoparticles that gain interstitial access to the tumor may stay longer in the tumor interstitium. The effect of the combination of poor lymphatic drainage and leaky vasculature is termed as the EPR effect and allows nanoparticles to enter and accumulate in

tumor tissue (Figure 4). The EPR concept is regarded as a “gold standard” in the formulation of new agents for cancer treatment [139].

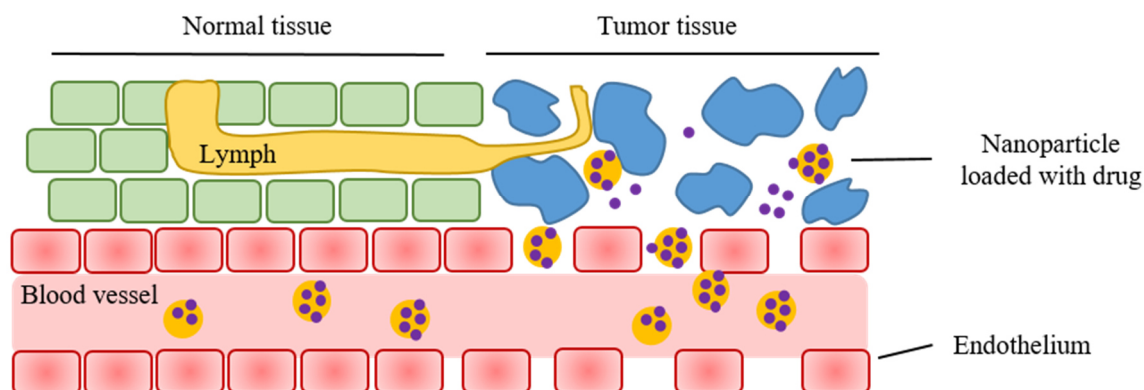


Figure 4 EPR effect for nanoparticle targeting.

However, with the use of passive targeting to reach the tumor, some limitation may appear: the different extent of tumor vascularization and angiogenesis [140], the high interstitial fluid pressure that prevents the efficient uptake and homogenous distribution of the therapeutic agents in the tumor [141]. However, the passive form of tumor targeting is one of the most used methods to reach a tumor. Upon successful localization of the nanoparticles inside the tumor, the drug needs to be released from its carrier to generate a therapeutic effect. As the correlation between accumulation and therapeutic effect is often difficult to control, different mechanisms have been investigated for triggered release. Application of internal stimuli such as temperature and pH or external stimuli like magnetic fields and lasers allowing a time- and special-controlled targeting of cells [142-146]. Another externally triggered method is ultrasound, which is used in cancer diagnostics and treatment [147, 148].

2.4 Ultrasound Enhanced Drug Delivery

For the past decades ultrasound has been mostly used in diagnostic imaging in the medical field [149]. In recent years, however, ultrasound has been also used for the treatment of several diseases and represents an effective and promising stimulus for achieving a controlled drug release to a region of interest without disrupting surrounding tissue. The use of ultrasound in the combination with drug-loaded nanocarriers increases the attention in the medicine for cancer treatment [150-153] mostly due to its non-invasive, non-ionizing and painless transmission of energy into the body, ability to focus the beam with the precision on the diseased tissue and relatively low-costs. However, homogeneous exposure of large zones and targeting moving organs are still a challenge [153].

2.4.1 The Physics of Ultrasound

Ultrasound is a sound wave propagating through homogeneous isotropic medium as a longitudinal wave with a frequency higher than the human audible range [154, 155]. Audible sounds include the range between 20 Hz and 20 kHz, while ultrasound propagates at frequencies higher than 20 kHz (Figure 5).

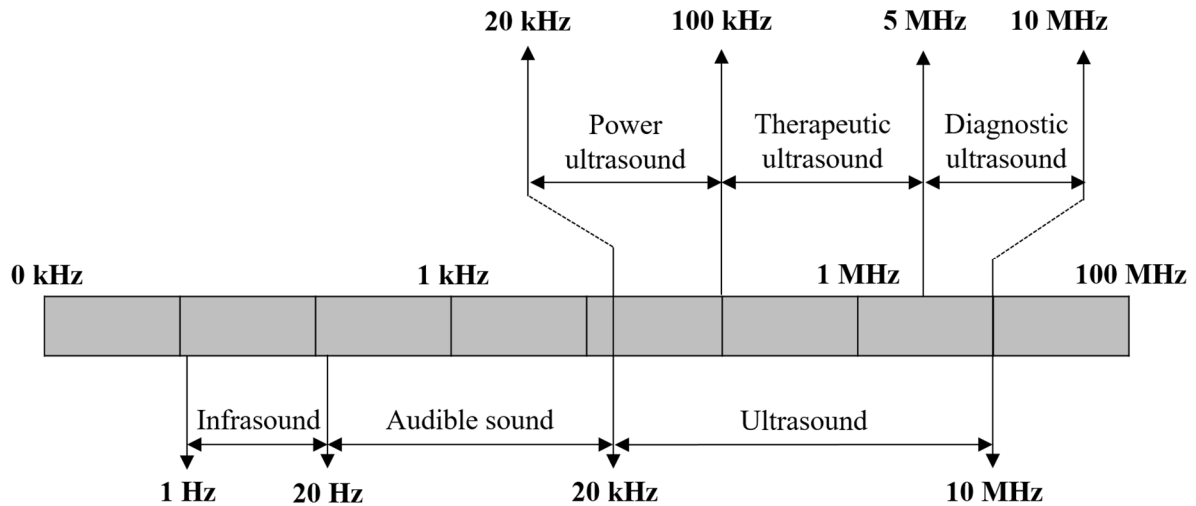


Figure 5 Frequency range of sound waves including infrasound, audible sound and ultrasound [156, 157].

Oscillating piezoelectric ceramics are often used to generate or detect ultrasound waves [155]. When voltage is applied on the crystals, a pressure field is produced on the atoms, which induces compressions (at high pressure) or expansions (at low pressure) of the material and generates periodic ultrasound waves emanating from the probe [158]. In Figure 6A some variables of the sound waves are shown. The amplitude of the sound wave is the maximum change in pressure caused by the wave at a specific location. The period in ultrasound is the time to complete one cycle from one peak to the start of the next one, and is expressed in microseconds. The same dimension of one complete cycle could be expressed in meters as wavelength. The frequency of a sound wave is the number of cycles per second and is measured in megahertz due to the high frequency of ultrasound.

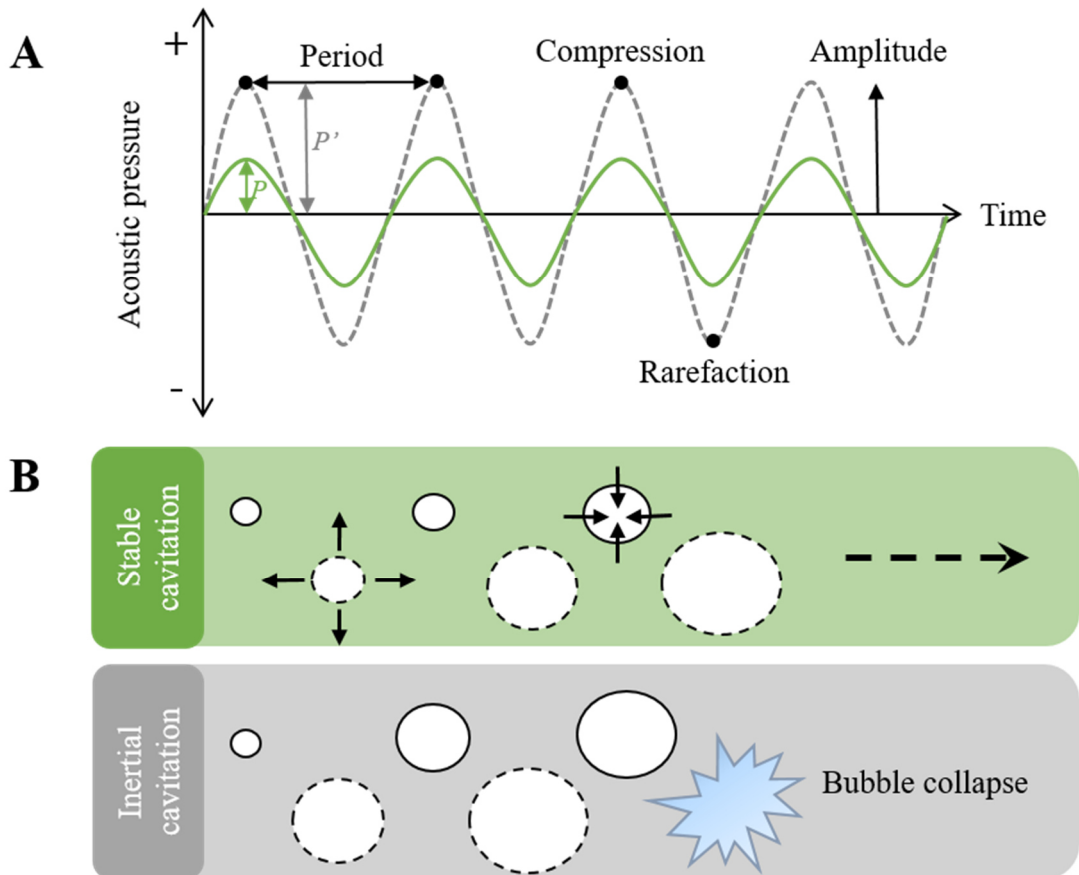


Figure 6 Cavitation induced by ultrasound. (A) A plot of a sound wave producing alternating compression and rarefaction at low P and high pressure P' . (B) Schematic depiction of inertial and stable cavitation of a bubble.

Ultrasound waves travel through a medium with an acoustic speed depending on the material characteristics (Table 2). More rigid and less compressible materials such as bone or metal feature a higher sound velocity whereas water and soft tissues as well as air show the lowest values. When ultrasound waves pass through tissue, they are either absorbed or they reach the target tissue and the waves are reflected back to the transducer. Adsorption is the process in which sound energy is converted into other energy forms such as heat, chemical energy, or light and is determined by an attenuation coefficient. Various attenuation coefficients for air, water and different tissues are presented in Table 2. The attenuation is generally much higher for hard than soft tissue [155]. The reflection rate is determined by acoustic impedances of two different tissues on each side of the boundary (Table 2). The more significant the difference in acoustic impedance is, the greater is the percentage of energy that will be reflected at the interface of the materials [154]. Acoustic impedance Z is dependent on tissue density ρ and acoustic speed in the tissue c , as

$$Z = \rho \cdot c .$$

Table 2 Speed of transmission of ultrasound, attenuation coefficient and acoustic impedances of air, water and various tissues [155, 159-165].

Material	Density [kg/m³] at 37 °C	Acoustic speed [m/s]	Attenuation coefficient at 1 MHz [dB/cm]	Acoustic impedance [Pa/m³]
Air	1.3	331	12.0	0.0004
Water	998	1480	0.002	1.48
Blood	1050	1584	0.20	1.66
Muscle	1070	1580	1.09	1.69
Skull bone	1700	3360	13.02	5.7

For medical application, the ultrasound can be modulated by varying several parameters such as frequency and intensity. Medical ultrasound can be divided into three fields depending on the frequency (Figure 5): low frequency (20-100 kHz) as power ultrasound used for focused ultrasound surgery [156], medium frequency (0.1-5 MHz) for therapeutic application [153, 166] and high frequency (5-10 MHz) for diagnostic purposes [167]. The frequency specifies the spatial resolution and the depth of the penetration into the body. The higher the frequency, the better is the resolution. This is important when using imaging ultrasound. In this case, higher frequencies will be chosen to get a higher image resolution. The penetration depth is inversely proportional to the frequency [155]. At about 1 MHz the ultrasound wave penetrates for about 10 cm, which is the most of the body, whereas at frequencies higher than 10 MHz, the penetration is only 1 cm [153].

The second parameter is ultrasound intensity, which plays a role for the amount of energy delivered to the desired location. When an ultrasound wave travels from the transducer through the tissue, it induces pressure changes of the surrounding medium, which is directly related to the amount of energy received by the target tissue. The acoustic pressure P applied on the tissue appears as periodic compression and rarefaction event (Figure 6A). The pressure, which is expressed in Pa, can be measured by using a hydrophone [153]. The ultrasound intensity I refers to the amount of energy delivered by the ultrasound wave over a specific area, measured in W/cm² [168]. It is related to the acoustic pressure P , the density of the medium ρ and the acoustic speed in the medium c , which reads as

$$I = \frac{P^2}{\rho c}$$

2.4.2 Acoustic Cavitation

Acoustic cavitation is defined as the formation of one or more cavities in response to an acoustic field. The critical aspect of cavitation is the cavitation threshold, which includes the minimum acoustic pressure required to initiate cavitation [169]. Acoustic cavitation includes the nucleation or formation of bubble and bubble growth, oscillation and collapse in a liquid medium induced by the ultrasound wave [156]. It is classified in two different types, called stable and inertial cavitation, which are graphically presented in Figure 6. Stable or non-inertial cavitation includes oscillating bubbles that grow until they reach their resonance size and keep oscillating around their equilibrium diameter. The cavitation is permanent and bubbles continue to oscillate for many cycles if the excitation peak rarefaction pressure stays below a certain threshold [170]. Inertial or transient cavitation occurs at a higher peak negative pressure, which leads to an asymmetrical oscillation of bubbles and their expansion to multiple of their original size. This further leads to violent implosion and bubble collapse, which can cause various bioeffects including the generation of shock waves [171], microjets [172], high temperatures [173] and erosion of materials [174].

The formation of bubble, so called nucleation can typically occur in two forms: homogenous or heterogeneous. In the case of homogenous nucleation, the nucleation takes place in the pure liquid without any impurities or gas [169, 175]. The nucleation process requires sufficient acoustic pressures to overcome the neutral cohesion with highest tensile strength and transition from water to steam to produce bubble nuclei. Moreover, the peak negative pressure, also time of acoustic excitation and the waveform are important for the prediction of cavitation inception and activity [176]. Apfel and Holland assumed that an optimally sized bubble at a given frequency exceeded the threshold for inertial cavitation. For an inertial cavitation at higher frequencies, smaller bubbles are required for cavitation to occur at the lowest possible peak negative pressure [176].

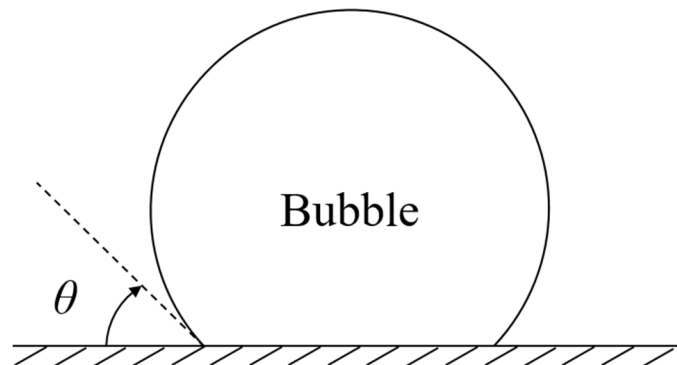


Figure 7 A bubble formed at a flat solid wall with contact angle θ [177].

However, in real systems, almost all nucleations occur on the surface of impurities in liquids and are called heterogeneous nucleations. Any interface with another material has potential importance for nucleation [169, 178]. In this work, polymer nanoparticles are used as cavitation inducers. In Figure 7, contact angle at the intersection between liquid, vapor bubble, and solid surface is denoted by θ . It follows that the energy barrier is at the maximum when the contact angle is zero and homogeneous nucleation occurs. However, the surface is not always flat, so the effect of other surface geometrics such as nanoparticle with rough surface must be taken into account. There are different models to quantify wettability on the surface that consider the role of surface roughness. One of them is a *Cassie-Baxter* model, where drops of liquid are presumed to have contact with the top of the nanoparticle without penetrating the pores. Air pockets are supposed to be trapped under the liquid, which gives a composite surface [179]. This may be due to Laplace pressure resulting in air entrapment on the nanoparticle surface. Figure 8A illustrates the representation of the *Cassie-Baxter* model, where H indicates the depth of the pores, the contact angle is denoted by θ , and the enclosed volume of air is indicated by V . The pressures of air and liquid are denoted by p_A and p_L respectively. When there is a sudden decrease in hydrostatic pressure, the trapped gas may expand (Figure 8B) or merge with other trapped gas pockets, resulting in the formation of a larger bubble [180]. During ultrasound treatment with each rarefaction water invades the bubble forming gas, causing the bubble size to increase therefore reducing the surface tension. After several amplitudes, the bubble eventually undergoes cavitation, which leads to a collapse of a bubble at the interface to the solids resulting in microjets which can also cause erosion and abrasion [169].

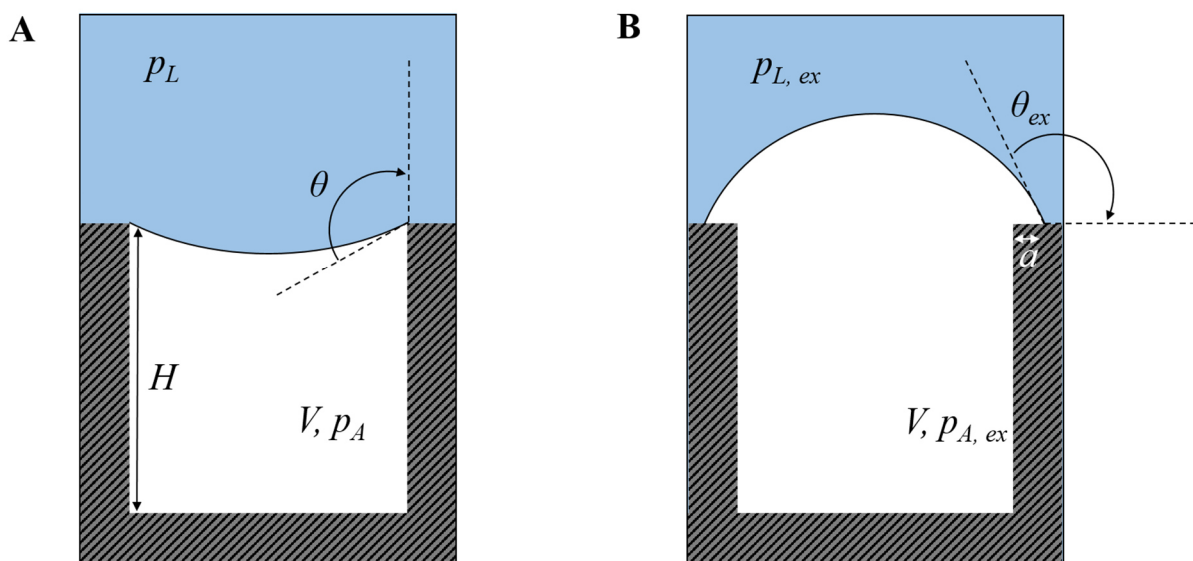


Figure 8 Illustration of a structured hydrophobic pore underwater with a side view of the (A) *Cassie-Baxter* model and (B) with bubble expansion. Adapted from [180].

Before using ultrasound for therapeutic purposes, the frequency and peak negative pressure must be adjusted to not put tissue under mechanical stress, which would result in tissue destruction. The limit values are described by using the mechanical index (MI) to describe the mechanical bioeffects. The MI is a measure of the acoustic pressure related to the ultrasound frequency and is defined as

$$MI = \frac{p}{\sqrt{f}},$$

where p denotes the peak rarefaction pressure in MPa, and f represents the frequency of the ultrasound wave in MHz [181]. The FDA approves a MI value of 1.9 as a maximum in clinical use [182]. This study focused on intermediate (MI = 0.2-0.5) and high (MI = 0.5-1.9) acoustic powers, where bubbles undergo non-linear oscillation resulting in bubble destruction [181, 183].

2.4.3 Ultrasound-Triggered Mechanism of Drug Delivery

Ultrasound drug delivery relies on mechanical effects and is induced inside the blood vessels by bubble cavitation. This causes pressure forces, shear-related acoustic streaming, or even high-velocity microjets once the bubbles collapse [184]. These effects may be beneficial in releasing drugs from micro- and nanocarriers and delivering agents across the biological barriers. One of the first ultrasound-triggered drug carriers were microbubbles. They are normally used as ultrasound contrast agents and are 1-10 μm vesicular particles with a shell made of lipids, proteins or polymers and filled with gas [151]. On the market, they are available as SonazoidTM, Definity[®], SonoVue[®] and OptisonTM [185]. Additionally, their shell can be loaded with active ingredients or functionalized with targeting ligands for targeted control or even nanoparticles [186, 187]. The destruction of the oscillating microbubbles could increase the permeability of the nearby endothelial cells and improve drug delivery to the target site [188]. The advances of the microbubbles are their well-accepted acoustic enhancing ability and safety profile. However, they are relatively large and intravenous administration is confined to blood vessels. They could not enter the tumor tissue without sonoporation. To overcome this barrier, nanodroplets and nanobubbles with sizes smaller than 1 μm were developed. Nanobubbles are similar to microbubbles only with a size between 50 and 300 nm, which allows them to enter the tumor tissue [189, 190]. Nanodroplets are nanosized particles with shell made of polymers or lipids and filled with perfluorocarbon or perfluorohexane liquid. After their accumulation in the tumor, the ultrasound is applied, which causes the vaporization of the liquid to gas and the formation of microbubbles in the tumor, which is called acoustic droplet vaporization [191]. In the last years, some attempts to prepare polymer nanoparticles without

external gas or vaporized liquid were encountered in the literature. Kwan *et al.* prepared nanocups made of polystyrene for distribution of therapeutic agents in the tumor. After the formation of nanocups, the nanoparticle dispersion was dried. Upon rehydration, the nanocups trapped air within the cup-cavity. The nanocup with nanobubble was activated upon exposure to ultrasound, which caused bubble collapse and drug release [192].

3 General Introduction

Cancer is a multifaceted disease characterized by the uncontrolled proliferation and metastasis of abnormal cells, leading to significant morbidity and mortality worldwide [12]. Besides surgery and radiation therapy, in particular cytotoxic agents belong to the gold standard for cancer treatment [17]. However, they often cause severe side effects due to their cytotoxic nature and unspecific distribution of the drug in the body. One concept to diminish the side effect profile of a cytotoxic drug therapy is to improve or control the distribution of the drug in a way that the drug is especially accumulated at the tumor tissue, causing less damage to healthy cells. This concept is also known as drug targeting/targeted drug delivery and could be achieved with nanotechnology-based drug delivery [193]. Nanoparticles provide advantages in passively or actively targeting drugs and bring opportunities for controlled release of drugs, allowing sufficient time for the drug to enhance a therapeutic effect. The aim of this work was to develop nanoparticles for the encapsulation of a cytotoxic model drug for targeted drug delivery. Several different types of nanocarriers with different compositions, sizes, architectures and surface properties have already been developed for delivering their payload to tumor cells [53]. These include liposomes [60], dendrimers [194], micelles [69], polymeric nanoparticles [195], inorganic nanoparticles made of metal oxide and hybrid nanocarriers [196]. The nanoparticles used in this work were based on polymers. Biodegradable and biocompatible PLA and PLGA polymers were processed with emulsion and nanoprecipitation methods to prepare NS and NC with the aim to encapsulate small drug molecules.

Due to the uniqueness of solid tumors (leaky vasculature and defective lymphatic drainage) and the small size of the nanoparticles, the nanoparticles could be used for passive targeting to tumor cells. Tumor accumulation is achieved based on a phenomenon known as the EPR effect, where the prolonged circulation time of nanoparticles enables them to reach the cancer cells and enter the extracellular matrix of the tumor [197], where anti-tumor agents are inactivated until they are released inside the cell. In this regard, different stimuli such as pH [146] and the presence of enzymes [198], or external stimuli such as magnetic field [142], light [144], heat [145], and ultrasound [143, 147] could be employed to release drugs from polymer nanoparticles in a controlled manner. The focus of this work was to use an externally applied low-intensity, focus ultrasound (FUS) to trigger a controlled local release of the therapeutic agents from polymer nanoparticles. It is a non-invasive method without ionizing radiation, easy to handle, and with the possibility to control the depth of the tissue penetration by adjusting frequency, cycles and exposure time [150]. The local release of a drug in the body can be achieved through a focused

ultrasonic wave field by using the inertial cavitation effect of nanoparticles [199]. Nanoparticles that are able to release the drug by this mechanism are also referred to as sonosensitive nanoparticles. The cavitation activity of sonosensitive nanoparticles can be attributed to the presence of nanoscale gas bubbles trapped on the rough surfaces introduced by the freeze-drying process. The inertial cavitation involves rapid expansion and violent collapse of a bubble in a liquid during the compression phase of the wave [200, 201], which causes nanoparticle damage and drug release.

The combination of polymer nanoparticles and ultrasound therapy offers a promising approach for cancer treatment. In this study, several model drug NS and NC were developed to respond in an ultrasound field. A systematic comparison of the particles based on different physicochemical parameters revealed differences and similarities between the production methods and evaluated their impact on ultrasound enhanced drug release. The properties of the nanoparticles were monitored under different storage conditions throughout the entire testing period. Additionally, the formation and composition of the protein corona in serum was investigated as a function of the particle properties to evaluate the impact on colloidal stability and cavitation activity. Another important criterion for the development of an innovative drug delivery system is biocompatibility. The peripheral blood mononuclear cells (PBMC) and prostate cells were used to investigate the toxic potential of variously modified nanoparticles.

Overall, this thesis describes the development of polymer sonosensitive nanoparticles that can be used for treatment of cancer.

4 Materials and Methods

4.1 Formulation and Physicochemical Characterization of Nanoparticles

4.1.1 Nanoparticle Preparation

4.1.1.1 Nanospheres

Drug-containing NS were prepared by nanoprecipitation technique (Figure 9) according to Fessi *et al.* [93] using a double-syringe connecting technique.

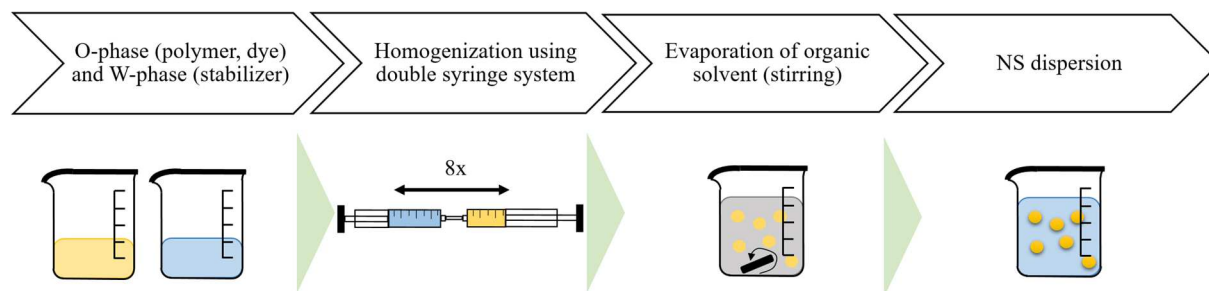


Figure 9 Graphic illustration of NS preparation process using nanoprecipitation method with two glass syringes connected *via* Luer lock connection.

Different types of commercial polymers were used: poly-(L-lactic acid) (PLA, Resomer[®] L206 S) and poly(D,L-lactic-co-glycolic acid) (PLGA, Resomer[®] RG 752 H, M_n 4,000-15,000 g/mol) obtained from Evonik, Darmstadt, Germany and Boehringer Ingelheim, Ingelheim, Germany, respectively. 3%, 6% or 12% (m/V) polymer solution dissolved in 0.5 mL dichloromethane (Carl Roth GmbH + Co. KG, Karlsruhe, Germany) was added to the solution of rhodamine B (RhB, Fluka Chemie GmbH, Buchs, Switzerland) or coumarin 6 (C6, Sigma-Aldrich Chemie GmbH, Steinheim, Germany) dissolved in 12 mL acetone (Carl Roth) in 1:100, 1:250, 1:500 or 1:1000 dye-to-polymer ratio (O-phase). The W-phase contained 25 mL of 0.27% (m/V) Poloxamer 188 (Lutrol[®] F68, BASF AG, Mannheim, Germany) dissolved in ultrapure water and filtered through a cellulose acetate filter (0.2 μ m, Sartorius AG, Göttingen, Germany). The O-phase and W-phase, each were filled in two 50 mL glass syringes with metal Luer lock tip (Fortuna[®] Optima[®], Poulten & Graf GmbH, Wertheim, Germany) connected with Luer lock female (LLF, Carl Roth) system. Glass syringes were connected to 5 cm long connecting tube (polyvinyl chloride, 3.2 \times 2.6 mm, Sartorius) with two LLF connectors. Both solutions were gently mixed eight times pushing the syringes back and forth. The organic solvent of the resulting mixture was evaporated in a beaker at room temperature overnight while being stirred at 120 rpm. The resulting dispersion was purified by tangential-flow filtration using a peristaltic pump (Masterflex[®] L/S[®], Easy-Load[®], Cole-Parmer[®], Vernon Hills, USA) and stabilized cellulose membrane (Vivaflow 50 R, molecular weight cut-off (MWCO) 100,000, Sartorius) or centrifugation (30 min, 17,070 \times g, Allegra 64R, Beckman Coulter Biomedical GmbH,

München, Germany) for formulations containing RhB or C6, respectively. Blank polymeric NS were formulated by the same procedure without RhB or C6.

4.1.1.2 Nanocapsules

The NC were prepared by an emulsification-diffusion evaporation technique [202, 203] graphically presented in Figure 10.

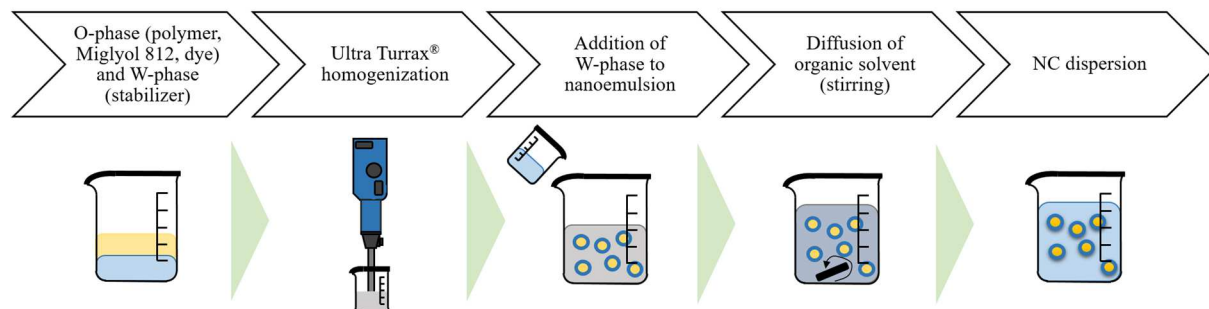


Figure 10 Graphical representation of the emulsion-diffusion method for preparation of NC using Ultra Turrax® homogenization.

The O-phase consisted of 6 mL ethyl acetate (ROTIPURAN®, Carl Roth), 5% (w/w) Miglyol 812 (Caesar & Loretz GmbH, Hilden, Germany) and 2% (w/w) PLGA. Different types of commercial PLGA polymers were used: Resomer® RG 752 H (M_n 4,000-15,000 g/mol) obtained from Boehringer Ingelheim, Resomer® RG 502 (M_n 7,000-17,000 g/mol), RG 503 (M_n 24,000-38,000 g/mol), RG 504 (M_n 38,000-54,000 g/mol), RG 505 (M_n 54,000-69,000 g/mol), all ester terminated, and RG 502H (M_n 7,000-17,000 g/mol), acid terminated, were purchased from Sigma-Aldrich. As fluorescence dye C6 was used in a ratio dye to polymer of 1:250. The W-phase was prepared by dissolution of 2.5% (m/V) PVA (Mowiol® 4-88, M_n 31,000 g/mol, 86.7-88.7 mol% hydrolysis, 630 polymerization, Sigma-Aldrich) as stabilizer in ultrapure water. The O-phase was added dropwise to 24 mL aqueous solution under stirring (400 rpm) to form an O/W emulsion and additionally homogenized using an Ultra-Turrax® T25 (IKA-Werke, Staufen, Germany) at 11,000, 12,600, 15,000 or 20,000 rpm for 8 min. In the second step, 120 mL water were added to the emulsion, and the organic solvent was evaporated at room temperature overnight under stirring at 120 rpm. The NC dispersion was purified three times by centrifugation (30 min, $17,070 \times g$, Allegra 64R) and following redispersion into 15 % (m/V) aqueous solution of trehalose (Sigma-Aldrich) used as cryoprotectant for the following freeze-drying process presented in section 4.1.2.

4.1.1.3 PEGylated Nanocapsules

The preparation of PEGylated NC was performed by the standard protocol for NC described above. Various blends of 2% (w/w) poly(ethylene glycol) methyl ether-*block*-poly(lactide-co-glycolic acid) (PEG_{2k}-PLGA_{11.5k}, PEG average M_n 2,000 g/mol, PLGA average M_n 11,500 g/mol and PEG_{5k}-PLGA_{7k}, PEG average M_n 5,000 g/mol, PLGA average M_n 7,000 g/mol, all purchased from Sigma-Aldrich) and non-PEGylated PLGA (Resomer[®] RG 502) were dissolved in ethyl acetate, leading to final PEGylation degrees between 0% and 38% (w/w) was presented in Table 3. After purification with centrifugation, samples were resuspended into 15% (m/V) aqueous trehalose solution and freeze-dried as described in section 4.1.2.

Table 3 Different PEGylated NC formulations prepared of Resomer[®] RG 502 and PEG_{2k}-PLGA_{11.5k} or PEG_{5k}-PLGA_{7k} and their PEG content as percentage.

PEG _{2k} -PLGA _{11.5k}	PEG [%]	PEG _{5k} -PLGA _{7k}	PEG [%]
0% (100% RG 502)	0		
10%	1.5	10%	3.9
25%	3.7	25%	9.6
50%	7.4	50%	19.2
75%	11.5	75%	28.8
90%	13.3	90%	34.7
100% (0% RG 502)	14.8	100% (0% RG 502)	38.5

4.1.2 Freeze-Drying of Nanoparticles

NS and NC formulations were freeze-dried in 10R vials (SCHOTT AG, Mainz, Germany) as 3 mL aliquots in a VirTis Genesis 25EL Pilot Lyophilizer (SP Scientific, Gardiner, New York, USA) with a shelf area of 0.57 m². All sample-filled vials were surrounded by vials filled with 15% (m/V) aqueous trehalose solution. Product temperature was measured using copper/constant thermocouples (Omega, Norwalk, USA) placed in the bottom center of the vial. The applied cycle conditions for freeze-drying are shown in Table 4. Samples were precooled for 60 min at 10 °C and then frozen at -1 °C/min to -40 °C and held constant for 2 h to ensure that all the samples reached shelf temperature. For the primary drying the vacuum was applied to 75 mTorr and temperature was increased to -20°C for 48 h. The endpoint of primary drying was controlled by comparative pressure measurement between Pirani gauge and capacity manometer. Secondary drying was performed for 18 h at 20 °C and 75 mTorr. Samples were stoppered under vacuum atmosphere and sealed with crimp caps. All processes were monitored with the software Encore Control System (Version 4.9).

Table 4 Overview of process parameters for different freeze-drying cycles including cooling, freezing, primary drying and secondary drying.

Step	Ramp [°C/min]	Temperature [°C]	Pressure [mTorr]	Holding time [h]
Cooling	-	10	-	1
Freezing	1	-40	-	2
Primary drying	0.44	-20	75	48
Secondary drying	0.33	20	75	18

4.1.3 Physicochemical Characterization

4.1.3.1 Laser Light Scattering

Hydrodynamic diameter, polydispersity index (PDI) and zeta potential were measured in ultrapure water using the Zetasizer Ultra (Malvern Instruments, Herrenberg, Germany). Hydrodynamic diameter and PDI were measured in polystyrene cuvettes (Sarstedt AG & Co. KG, Nuembrecht, Germany) at 633 nm, 25 °C and a scattering angle of 173° *via* dynamic light scattering (DLS) technique. For measurements of zeta potential a folded DTS 1070 capillary cell (Malvern Instruments) was used and the electrophoretic mobility was determined at 25 °C. For calculations the refractive index of 1.33 and 1.65 as well as viscosity of 0.88 mPa·s and 1.46 mPa s for ultrapure water and 15% (m/V) aqueous trehalose solution, respectively, were applied at 25 °C. As particle size standard polystyrene particles (200 nm) from Sigma-Aldrich were used. Evaluation of Z-Average (intensity weighed mean hydrodynamic size) and PDI was performed with the ZS XPLORER Software (Malvern Panalytical Ltd., 1.2.0.91), graphic representation was created with GraphPad Prism 6, Boston, USA. All measurements were performed at least with three measurements *per* sample to calculate the mean values \pm standard deviation (SD).

4.1.3.2 Quantification of Production Yield

To quantify the nanoparticle amount after centrifugation, pellets were dispersed in 2 mL ultrapure water and 50 μ L dispersion was weighed into an aluminum pan and dried to constant weight at 80 °C for 2 h in a drying oven (Mettler GmbH + Co.KG, Schwabach, Germany). For cooling, the pan was placed in a desiccator before it was weighed again. The particle amount in the dispersion was calculated as the difference between empty pan and pan with the sample after drying. The values were calculated as mean \pm SD from three independent samples.

4.1.3.3 Quantification of Dye Load and Encapsulation Efficiency

The amount of embedded dye was quantified by measuring the fluorescence in the LS-55 spectrometer (Perkin Elmer Instruments, Rodgau-Juegesheim, Germany) at λ_{exc} 553 nm/ λ_{em} 574 nm for RhB and λ_{exc} 458 nm/ λ_{em} 509 nm for C6. Therefore, 50 μ L of NS

or NC dispersion was extracted with acetone at a ratio of 1:20 for 2 h under shaking at 70 rpm (Mini-100 Orbital Genie™, Scientific Industries, New York, USA) at room temperature. Prior to fluorescence analysis, the samples were diluted at a ratio of 1:20 with a mixture of methanol (Fischer Scientific, Loughborough, UK) and ultrapure water (75%:25% (V/V)). Quantification was carried out using a calibration curve from 0.01-0.05 µg/mL (linearity of response: $r^2 = 0.996$) for RhB and 0.001-0.14 µg/mL ($r^2 = 0.999$) for C6. Dye load (%) of the nanoparticles was calculated as the ratio of encapsulated dye *per* weight of nanoparticles:

$$\text{Dye load [\%]} = \frac{\text{Weight of dye in nanoparticles [mg]}}{\text{Weight of nanoparticles [mg]}} \times 100 .$$

Entrapment efficiency (%) was expressed as the ratio of the determined dye load in the nanoparticles related to the theoretical drug load:

$$\text{Entrapment efficiency [\%]} = \frac{\text{Weight of dye in nanoparticles [mg]}}{\text{Weight of initial dye [mg]}} \times 100 .$$

Data were collected and analyzed by the FL WinLab Software (Perkin Elmer Instruments). The values were calculated as mean \pm SD from three independent samples.

4.1.3.4 Quantification of the Residual PVA Content

The determination of the residual PVA content in the NC after purification was carried out based on a method according to Sahoo *et al.* and Grune *et al.* [204, 205]. For this purpose, 1 µg/mL C6-loaded NC stock solution was prepared in 0.5 M NaOH (Fischer Scientific) and treated in an ultrasonic bath for 15 min at 60 °C to fully dissolve the particles. Subsequently, 400 µL of the NC solution were neutralized with 180 µL 1 N hydrochloric acid (Carl Roth) and adjusted to 1000 µL with ultrapure water. Afterwards, samples were stained by the addition of 600 µL of a 0.65 M boric acid (Carl Roth), 100 µL iodine/potassium iodide solution (0.05 M/0.15 M, Fluka Chemie, and Carl Roth, respectively) and 300 µL ultrapure water followed by centrifugation at $30.000 \times g$ for 15 min (Avanti Zentrifuge, Beckman Coulter Biomedical). The supernatant was collected and the PVA concentration was quantified using colorimetric reaction by absorption measurements at 650 nm wavelength (GENESYS™ 10S UV/VIS-Spektralphotometer, Thermo Scientific™, Karlsruhe, Germany). As standard solutions, serial dilutions of PVA in a concentration range of 0-60 µg were prepared in the same way as the NC samples and used for a calibration curve. The percentage amount (w/w) of the PVA was determined for the each formulation and represented as mean \pm SD by triplicates.

4.1.3.5 Differential Scanning Calorimetry (DSC)

The thermal behavior of different polymers and the freeze-dried samples were studied using the DSC 822e (Mettler Toledo, Giessen, Germany) under nitrogen (Linde, Germany) atmosphere. To prevent oxidation within the system, all experiments were performed under nitrogen flow rate of 30 mL/min, supplemented by a secondary stream of nitrogen at 100 mL/min to prevent condensation due to cooling. Powder samples (10-20 mg) were sealed in aluminum pans (Mettler Toledo). Polymer granules, freeze-dried nanoparticles and physical mixtures were heated from 5 °C to 220 °C applying a heating rate of 10 °C/min. After cooling down (10 °C/min) the same heating step was performed again. The inflection point of the glass transition temperature (T_g) and melting temperature (T_m) were evaluated using the Mettler STARe Software (Mettler Toledo).

4.1.3.6 X-Ray Diffractometry (XRD)

Powder XRD measurements were used as a measure of crystallinity of the lyophilized samples. Measurements were made with the X'pert MPD diffractometer (Panalytical, Amsterdam, The Netherlands) with Cu K α radiation ($\lambda=0.15418$ nm, 40 kV, 40 mA). Powder samples were transferred on a stainless-steel sample holder (slot width: 2.0 mm) and the surface was smoothed with a microscope slide. Diffraction patterns were collected with a scan range of 0.5-40° at a step size of 0.02 °/s. All measurements were carried out under inert nitrogen gas atmosphere and at room temperature. The samples were measured once and the data was collected by software X'Pert Data Collector (Panalytical) and evaluated by X'Pert Graphics (Panalytical).

4.1.3.7 Transmission Electron Microscopy (TEM)

The morphology of NS and NC was evaluated by TEM. Freshly prepared aqueous NS or NC dispersion (2 μ l) was pipetted on a carbon coated copper grid (mesh 300, Plano GmbH, Wetzlar, Germany). After 3 min the excess water was drawn through the grid using a filter paper. Then the particles were stained with 2% (w/w) phosphotungstic acid (5 μ l) (Sigma-Aldrich) for 2 min, before again drawn with filter paper. Finally, the samples were washed twice with 6 μ l of water and dried in a glove box with a relative humidity of less than 1% before further investigation. TEM analyzes were carried out with a CM300 UltraTWIN instrumentation (Philips, Eindhoven, The Netherlands) operated at an acceleration of 300 kV with a LaB6 cathode and a variable spot size. Images were obtained with a CCD camera and edited with the open-source software ImageJ (Fiji, [206]).

4.1.3.8 Scanning Electron Microscopy (SEM)

For SEM, nanodispersions on TEM copper grids were sputtered with a thin film of gold-palladium at 5 kV and 5 mA (Hummer JR Techniques, Munich, Germany) for 30 s under argon atmosphere to prevent charging effects. SEM was performed on a Carl Zeiss Gemini Ultra55 (Carl Zeiss AG, Oberkochen, Germany). Samples were visualized with an InLens detector using an accelerating voltage of 2.4 kV, a working distance of 4 mm and a 40,000x magnification.

4.1.3.9 Karl-Fischer Titration

The residual moisture content of the lyophilized products was determined using the coulometric Karl Fischer titrator Metronom 823 KF Coulometer (Mettler Toledo) with HydranalTM Coulomat AG reagent (Honeywell, Seelze, Germany) and the 832 KF Thermoprep oven (Metrohm, Filderstadt, Germany). About 50-100 mg sample were weighed directly into 6 mL crimp glass vials (Metrohm, Filderstadt, Germany) under nitrogen atmosphere (relative humidity $\leq 0.1\%$) and sealed with aluminum caps with rubber hole (Carl Roth). Vials were placed in the 832 KF Thermoprep oven and pierced with a double hollow steel needle. The inlet needle introduces nitrogen (0.7 L/min) into the vial with heated sample, and the outlet needle transports the nitrogen containing released moisture in a coulometric titration cell, where the Karl Fischer water determination takes place. Prior to the measurements, a system control test was performed by measuring an ultrapure water standard (HydranalTM Water Standard KF, water content $\sim 5.55\%$, Honeywell) at 230 °C. The samples were analyzed at an oven temperature of 120 °C. Residual moisture was calculated as percentage of powder mass initially used for the measurement (w/w).

4.2 Ultrasound Measurements Set-Ups

4.2.1 Set-Up 1: Detection of Cavitation Behavior of NS and NC in a Cuvette

To evaluate the cavitation activity of nanoparticles, freeze-dried NS and NC were reconstituted with 3 mL ultrapure water, slightly waved, let sit for 20 min to allow full reconstitution and placed in a polystyrene cuvette (Sarstedt). Nanodispersions were exposed to a sequence of 0.6 ms long 650 kHz, 750 kHz, 850 kHz or 950 kHz bursts and a peak rarefaction pressure of 1.02 MPa for 200 cycles about 560 s in the FUS (Figure 11). Samples were collected after ultrasound treatment followed by centrifugation ($17,070 \times g$, Avanti Zentrifuge, Beckman Coulter Biomedical) for 15 min. Supernatants were collected for dye quantification by fluorescence spectroscopy as described above.

By using a proportional–integral–derivative controller (CN7800, Omega), four heating rods (Schego 548, Schego, Offenbach, Germany), a platinum resistance temperature sensor (RS Pro Pt100, RS components, Corby, UK), and a circulation pump (EHEIM GmbH) with a capacity of 170 L/h a homogeneous temperature distribution (25–40°C) was generated in the water tank. An arbitrary waveform generator (33120A, Agilent, USA) was used to create the transmit signal which was amplified by a 1000 W radio frequency (RF) power amplifier (1140LA, ENI, USA) and transferred to an ultrasound transmitter (H-231, Sonic Concepts, USA) *via* an 50 Ω RF impedance matching network. Each of these transmitted burst sequences generate a cavitation noise signal, which was measured *via* a hydrophone receiver (V315, Olympus, Hamburg, Germany). The polystyrene cuvette filled with the sample was positioned at the center of an acrylic glass water tank in the focus region of the transmitter (H-231, Sonic Concepts, Bothell, USA) and the hydrophone at an angle of 90° (perpendicular to each other). Software MATLAB R2019a (Mathworks Inc., Natick, USA) was used to control the devices and to analyze the cavitation noise signals. By applying fast Fourier transform (FFT), summing up the squared direct frequency components over a certain bandwidth and normalizing it to mentioned bandwidth afterwards, the power spectral density (PSD) was calculated. The measure used for verifying the cavitation activity was voltage spectral density (VSD) determined by

$$VSD = \sqrt{\frac{\sum_{n=i_S}^{i_E} u(n)^2}{B}},$$

whereas $u(n)$ describes the discrete frequency magnitudes of FFT of the digitized measurement signal and B the investigated bandwidth, ranging from frequency index i_S to i_E . In general, a higher value of VSD corresponds to a higher cavitation activity in the bandwidth of interest. The results were both given as the trend of the VSD over time and as the area under the curve (AUC), which was calculated to generate a suitable comparison parameter.

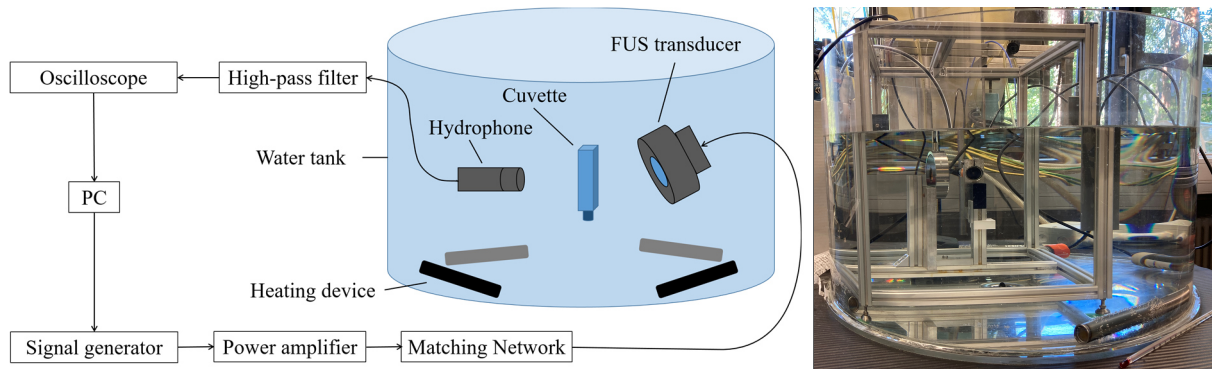


Figure 11 Experimental set-up 1 (left) and a photo (right) for measuring cavitation activity of NS and NC.

4.2.2 Set-Up 2: Determination of the Presence of NC with Imaging Method

Figure 12 depicts the experiment set-up for an active imaging method in a polystyrene cuvette. The experimental conditions stayed the same. The water temperature was left constant at 30 °C and the reconstitution of NC took place in 3 mL ultrapure water for 20 min. The ultrasonic transducer emitted signals through the cuvette and cavitation of NC was imaged with a SonixTOUCH ultrasound imaging system (Ultrasonix, Bellingham, USA). A linear array transducer (L9-4/38, Ultrasonix) with a center frequency of 5 MHz was employed. Ultrasound images were acquired in pulse-echo imaging mode with 0.325 MI at a transmit frequency of 9 MHz. The frame rate for all experiments was 1 frame per second (fps). Images were evaluated with MATLAB R2019a software and are presented in section 5.1.

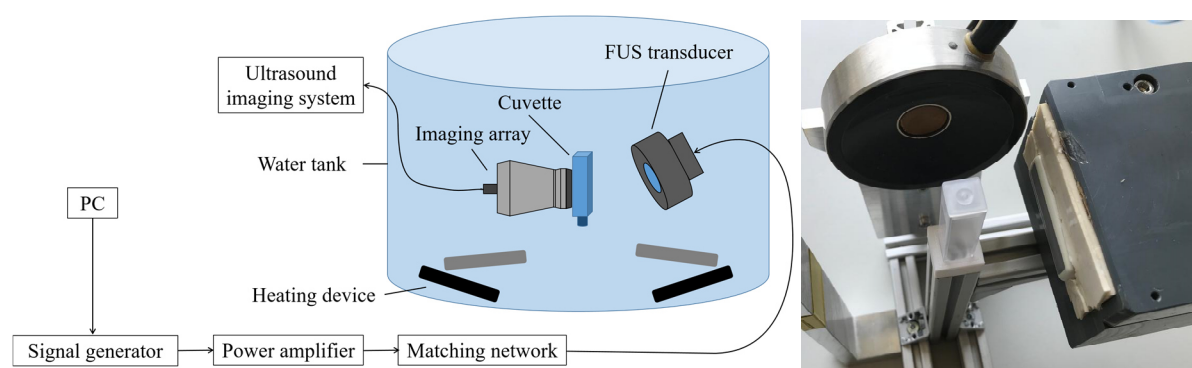


Figure 12 Experimental set-up 2 (left) and a photo (right) for imaging ultrasound measurement of NC.

4.2.3 Set-Up 3: Detection of Cavitation Behavior of NC in Through-Flow System

NC cavitation measurement was carried out in a flow-through system with a use of phantom (Figure 13). A tissue mimicking phantom was made of 10% (m/V) aqueous PVA (Elvanol[®] 71-30, DuPont, Wilmington, USA) solution which was poured into mold (100 mm × 63 mm × 63 mm) with a 3 mm wide canal in the middle. The mold was then heated to 78 °C in a water bath (Haake W45, Thermo Scientific) for 60 min. Afterwards it was kept at the room temperature for 60 min to cool down and to remove the air bubbles from the solution. The mold was processed through two freeze-thaw cycle. In each free-thaw cycle, the sample was frozen at -18 °C for 6 h and 15 min and then thawed at room temperature for 6 h and 15 min. During thawing, the ultrapure water was poured over the mold. After completing two freeze-thawing cycles, the mold was removed and phantom was stored in ultrapure water in the fridge at 4 °C to prevent dehydration.

For the ultrasound measurement, the phantom was placed in the center of the water tank at 30 °C. The peristaltic pump (15KS, Boxer GmbH, Ottobeuren, Germany) constantly pumped the aqueous NC dispersion through the canal at a velocity of 10 cm/s. The phantom was

arranged in the focal zone of the FUS transducer. The transmitted signals were received by the perpendicularly situated hydrophone, filtered through a passive high-pass filter and measured with a digital oscilloscope. The excitation signal consisted of a sinusoidal burst with the frequency of 750 kHz and a duration length of 0.6 ms. In total, cavitation was triggered with 80 bursts. The results were collected and analyzed with software MATLAB R2019a and presented in section 5.5.4. Samples were collected after ultrasound treatment followed by centrifugation ($17,070 \times g$, Avanti Zentrifuge, Beckman Coulter Biomedical) for 15 min. Supernatants were collected for dye quantification by fluorescence spectroscopy as described above.

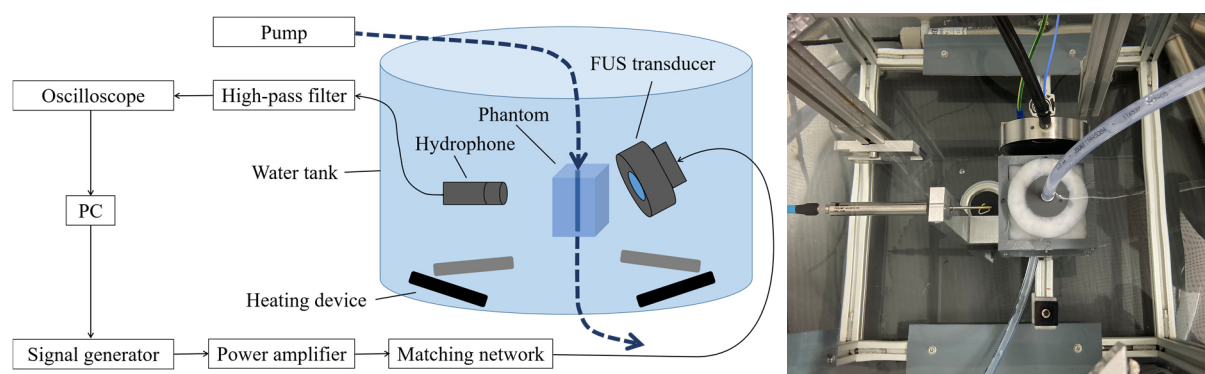


Figure 13 Experimental set-up 3 (left) and a photo (right) for cavitation detection of NC in through-flow phantom system.

4.3 Stability Studies

4.3.1 Storage Stability Study of Nanocapsules

For stability testing, selected freeze-dried C6-loaded and blank NC were sealed in 10R vials with aluminum peel-off seals (Wheaton[®], DWK Life Science GmbH, Mainz, Germany) and stored at three different temperatures for 6 months. They were stored at 2-8 °C, at room temperature (25 °C) and in a climate cabinet with 40 °C. The temperature was controlled with glass thermometer. Accelerated temperature storage conditions followed the International Council for Harmonization of Technical Requirements for Pharmaceuticals for Human Use (ICH) Q1A guideline published by the EMA, which recommended a test frequency after 0 months, 3 months and 6 months [207]. Physicochemical changes of the NC and the ultrasound activity were investigated at four time points (0 weeks, 6 weeks, 12 weeks and 6 months) using the methods described above.

4.3.2 Colloidal Stability of Nanocapsules in Different Test Media

Freeze-dried NC were redispersed at a concentration of 0.5 mg/mL in six different media: ultrapure water, 5% (m/V) glucose (Carl Roth), 0.9 % (m/V) NaCl (Carl Roth), phosphate buffered saline pH 7.4 (PBS), Roswell Park Memorial Institute 1640 cell culture medium

supplemented with GlutaMAX[®] (RPMI, Gibco[®], Life Technologies Europe B.V., Bleiswijk, the Netherlands) and artificial lysosomal fluid (ALF, pH 4.5). The compositions of PBS and ALF are presented in Table 5. The osmolarity of the media was measured by a freezing point osmometer (K-7400, KNAUER, Germany), calibrated with 400 mOsmol/kg NaCl aqueous solution (KNAUER) and ultrapure water (0 mOsmol/kg). This method is based on the freezing-point depression caused by a solute dissolved in water. After the solution is supercooled without freezing, the freezing is initiated by vibrating and the freezing-point is measured. The pH was determined using the Mettler Toledo MP220 pH meter. NC dispersions were incubated in different media for 5 min at room temperature. Additionally, NC dispersions were incubated in 10 % fetal bovine serum (FBS, Gibco[®]) for 1 h at 37 °C. Characterization of NC in the different dispersion media with or without 10 % FBS were performed as described in section 4.1.3.1. For zeta potential measurements samples incubated in FBS were additionally purified by three cycles of centrifugation (20 min, 22,000 × g, 4 °C, Allegra 64R, Beckman Coulter Biomedical) and redispersed in ultrapure water.

Table 5 Composition of the characterization media for the dispersion of NC, used for biological simulation media.

Medium	Abbreviation	pH	Composition (pro 1 L H ₂ O)
phosphate buffered saline	PBS	7.4	1.78 g Na ₂ HPO ₄ x 2 H ₂ O; 0.24 g KH ₂ PO ₄ ; 8.0 g NaCl; 0.20 g KCl (all purchased from Carl Roth)
artificial lysosomal fluid (according to Marques <i>et al.</i> and Rabel <i>et al.</i> [208, 209])	ALF	4.5	0.128 g CaCl ₂ x 2 H ₂ O (Carl Roth); 20.8 g citric acid (Carl Roth); 0.059 g glycerol (Carl Roth); 0.05 g MgCl ₂ (Carl Roth); 0.077 g sodium citrate x 2 H ₂ O (Carl Roth); 3.21 g NaCl (Carl Roth); 0.179 g Na ₂ HPO ₄ x 7 H ₂ O (Carl Roth); 0.085 g sodium lactate (Sigma-Aldrich); 6.0 g NaOH (Fischer Scientific); 0.086 g sodium pyruvate (Sigma-Aldrich); 0.039 g NaSO ₄ (Carl Roth); 0.09 g sodium tartrat x 2 H ₂ O (Honeywell); 2.703 mL formaldehyde 37% (Merck KGaA, Darmstadt, Germany)

4.4 Characterization of the Protein Corona

4.4.1 Serum Protein Adsorption on Nanocapsules

The evaluation of the adsorption of biomolecules on the NC surface was performed after incubation in serum. 50 µL of the NC dispersion in different media (section 4.3.2) was added to 200 µL undiluted FBS or human serum (HS, Sigma-Aldrich) and incubated for 1 h at 37 °C to induce the formation of a biomolecule corona. After the incubation period, samples were purified by threefold centrifugation (20 min, 22,000 × g, 4 °C, Allegra 64R, Beckman Coulter Biomedical) and using ultrapure water. After the last centrifugation step, pellets were dispersed in 50 µL 1% (m/V) sodium dodecyl sulfate (SDS, Carl Roth) and stored at 4 °C for further experiments. In order to assess the influence of the incubation temperature of NC with serum proteins, NC were incubated in aqueous 10% (m/V) bovine serum albumin (BSA, Bio&Sell

GmbH, Feucht, Germany) or human serum albumin (HSA, Albumin Fraction V, Carl Roth) with a concentration of 40 mg/mL. Incubation of NC in BSA or HSA was performed at 25 °C and 37 °C for 60 min.

4.4.2 Nanocapsule Protein Corona Characterization

4.4.2.1 Bicinchoninic Acid Assay (BCA Assay)

A PierceTM BCA assay kit (Thermo Scientific) was used for detection of the total amount of bound proteins and a photometric method according to the supplier's protocol was performed. Briefly, after incubation of the NC with the serum and redispersion of the pellet in 1% SDS (section 4.4.1), samples were heated to 96 °C for 7 min to detach bound proteins. 10 µL of each sample were pipetted in a 96-well microplate and mixed with 200 µL of the freshly prepared BCA solution. Following 1 h incubation at 37 °C, the samples were measured at a wavelength of 562 nm using the SPARK[®] plate reader (Tecan Deutschland GmbH, Crailsheim, Germany). Quantification was performed using a BSA based calibration curve. Serial dilutions were prepared with 1% (m/V) SDS in a concentration range of 0-300 µg/mL. The amount of bound protein (µg)/ particle (mg) was calculated based on the calibration curve and represented as mean ± SD. Each sample was tested as triplicate.

4.4.2.2 Sodium Dodecyl Sulfate Polyacrylic Gel Electrophoresis (SDS-PAGE)

After protein corona formation (section 4.4.1), the redispersed pellets in 1% SDS were heated to 96 °C for 7 min for denaturation. Volumes of 15 µL of each NC sample as well as 5% FBS or 5% HS without NC were mixed with sample buffer [5% β-mercaptoethanol, 62.5 mmol tris(hydroxymethyl)aminomethane (TRIS)-HCl, 25% (V/V) glycerol, 1% (m/V) SDS, 0.01% (V/V) bromophenol blue, all purchased by Carl Roth] in a ratio of 1:1 and heated up to 96 °C for 7 min. Samples as well as the serum positive controls and the protein standard (Der bunte Tobias, GRP, Haag a.d. Amper, Germany) were loaded onto 4-12% Q-PAGETM TGN Precast gels (Carl Roth). Separation was run at a constant voltage at 200 V for 40 min in an electrophoresis chamber (Hoefer SE260, SERVA Electrophoresis GmbH, Heidelberg, Germany) with TRIS-glycine running buffer [25 mM TRIS base (Carl Roth), 192 mM glycine (Sigma-Aldrich), 0.1% (m/V) SDS]. The resulting gel was fixed [79% water, 1% orthophosphoric (Carl Roth), 20% methanol] and stained with colloidal Coomassie Brilliant Blue prepared with 120 mL methanol, 40 mL water and 40 mL ROTI[®] Blue 5x concentrate (Carl Roth). After overnight staining, the gel was washed with methanol:water (1:3, V/V) for 90 min. Finally, DOC-PRINT CX3 (Vilber, Collégien, France) was used as gel documentation system with the software BioVision (Vilber) for final evaluation.

4.5 Statistical Analysis

Statistical analysis was performed using GraphPad Prism 6. The student's t-test and analysis of variance (ANOVA) were used. The level of significance (α) was 0.05 for all tests with p -value ≤ 0.05 indicating statistical significance.

4.6 Biological Studies

The experiments were performed at the Chair of Pharmaceutical Technology, University of Ljubljana, Slovenia.

4.6.1 *In Vitro* Cell Cultures

A cryovial containing frozen lymph node carcinoma of the prostate (LNCaP) cell line (CRL-1740TM, ATCC, Virginia, USA) was thawed and washed with RPMI 1640 medium (Sigma-Aldrich) by centrifugation at 1500 rpm for 6 minutes (Centric 322 PLC, Tehtnica, Železniki, Slovenia). After discarding the supernatant, the remaining cells were resuspended in cell culture medium using 1 mL RPMI 1640 containing 10% FBS and counted in a Neubauer improved chamber (Brand GmbH + Co. KG, Wertheim, Germany) using 0.4% trypan blue solution (Sigma). The LNCaP cells were diluted with cell culture medium to obtain a suspension containing 2.5×10^4 cells *per* mL.

PBMC mostly including lymphocytes (T, B and NK cells) and monocytes were isolated from whole buffy coats obtained from the Blood transfusion center of Slovenia, by flotation, using Lympholyte[®]-H solution (Cedarlane, Burlington, Canada), after which they were counted, frozen and stored in liquid nitrogen until being used. A cryovial with frozen PBMC was thawed and washed with RPMI 1640 medium by centrifugation at 1700 rpm for 8 min (Centric 322 PLC). The supernatant was discarded, and the cells were resuspended in 1 mL of the serum-free BioTargetTM medium (Biological Industries, Haemek, Israel), which was supplemented with 1% Antibiotic Antimycotic Solution (Sigma-Aldrich) and 1% GlutaMAXTM solution (Gibco[®]) to obtain the final cell culture medium. Subsequently, PBMCs were counted in a Neubauer chamber using 0.4% trypan blue solution and the cell dispersion was diluted with cell culture medium to a concentration of 1×10^6 cells *per* mL. Subsequently, 80 μ L of LNCaP dispersion (2.0×10^3 cells) or 80 μ L PBMC dispersion (1.0×10^5 cells) were distributed *per* well of a 96 flat bottom well microtiter plate (TPP, Trasadingen, Switzerland) and incubated at 37 °C, 5% CO₂ and 95% relative humidity in a CO₂ incubator (Haereus, Hanau, Germany) for 24 h before 20 μ L of each NC suspensions were added.

Stock solutions of NC were prepared in sterile ultrapure water at a concentration of 3 mg/mL for all tested formulations: blank PLGA (Resomer[®] RG 502) NC, C6-loaded PLGA (Resomer[®] RG 502) NC, blank PEG_{2k}-PLGA_{11.5k} NC, and C6-loaded PEG_{2k}-PLGA_{11.5k} NC. Their further dilutions were prepared by diluting 50 µL of each stock suspension with 450 µL of the appropriate cell culture medium for LNCaP cells or PBMC to obtain final concentrations of 300 µg/mL and 30 µg/mL. The final NC concentration in the microtiter plate resulted in the following concentrations: 600 µg/mL, 60 µg/mL and 6 µg/mL. Water controls were prepared with the same dilutions as NC (D1, D2 and D3).

4.6.2 3-[4,5-dimethylthiazol-2-yl]-5-[3-carboxymethoxyphenyl]-2-[4-sulfophenyl]-2H-tetrazolium, Inner Salt (MTS) Assay

The *in vitro* effect of NC was colorimetrically evaluated by measuring their impact on the LNCaP and PBMC proliferation activity. After pre-incubation of LNCaP cells and PBMC for 24 h, cells were treated with NC for 72 h. The CellTiter 96[®] Aqueous One Solution Cell Proliferation Assay (Promega, Madison, Wisconsin, USA) containing MTS was performed according to a modified method of Buttke *et al.* [210] in triplicates according to manufacturer's guidelines. Briefly, 20 µL MTS reagent were directly added to 100 µL of the cell culture in the wells and incubated for 4 h at 37 °C, 5% CO₂ and 95% relative humidity in a CO₂ incubator, followed by addition of 25 µL 20% SDS (Merck) solution *per well* and incubation for 45 min at room temperature, protected from light. Absorbance was recorded at 490 nm by using a microplate reader (BioTek Synergy H4, Winooski, Vermont, USA). The negative control consisted of LNCaP cells or PBMC without any NC added and the positive control was obtained after adding 50 µL 9% Triton X-100 (Sigma-Aldrich) solution to untreated cells. The samples used for determining the background absorbance were prepared by mixing 80 µL of cell culture medium with 20 µL of each tested NC dilution. The calculation of the percentage cell viability was performed relative to the negative control after subtraction of the background values using the following equation:

$$\text{Cell Viability [\%]} = \frac{\text{Mean OD}_{\text{Treated cells}} - \text{Mean OD}_{\text{Background}}}{\text{Mean OD}_{\text{Negative control}} - \text{Mean OD}_{\text{Background}}} \times 100 .$$

According to German national organization of standardization (Deutsches Institut für Normung, DIN), European Standards (Europäische Norm, EN) and International Organization for Standardization (ISO) 10993-5 [211], a cell viability <70% was classified as cytotoxic. The determination of cell viability was performed for each particle formulation as a triplicate measurement and presented as mean ± SD.

4.6.3 Lactate Dehydrogenase (LDH) Assay

The LNCaP cells were plated in 96-well microtiter plate at a concentration of 2.0×10^3 cells/well, pre-incubated for 24 h in the cell culture medium and then treated for 6 h with NC suspensions. The LDH concentration was determined using a commercial LDH cytotoxicity assay kit (Promega) according to the manufacturer's instructions. Briefly, 50 μ L of each cell culture were transferred into separate wells of a new 96 well plate and 50 μ L of the CytoTox 96[®] Reagent (Promega) were added into each well. Following 30 min incubation at room temperature, 50 μ L aliquots of 1 M acetic acid (Merck) were added to each well and absorbance was measured at 490 nm using the microplate reader. Cells only treated with cell culture medium were used as negative control. The positive control was obtained after adding 50 μ L 9% Triton X-100 solution to untreated LNCaP cells to obtain the maximum LDH release. The samples used for determining the background absorbance were prepared by mixing 80 μ L cell culture medium with 20 μ L of each tested NC dilution. All experiments were performed in triplicate. The results, corrected for NC's absorbance and spontaneous LDH release (negative control) relative to 100% LDH release (positive control) were presented as % cytotoxicity, using the following equation:

$$\text{Cytotoxicity [\%]} = \frac{\text{Mean OD}_{\text{Treated}} - \text{Mean OD}_{\text{Background}}}{\text{Mean OD}_{\text{Negative control}} - \text{Mean OD}_{\text{Background}}} \times 100 .$$

The determination of cytotoxicity was performed for each particle formulation as a triplicate measurement and presented as mean \pm SD.

5 Results and Discussion

5.1 Evidence of Inertial Cavitation of Polymer Nanoparticles

An ultrasound-sensitive nanoparticle drug delivery system requires nanoparticles capable of encapsulating drugs as well as acoustic activation that is necessary for drug release. To achieve a satisfactory response to ultrasound stimulation, an ultrasound-sensitive vehicle is needed. Ultrasound-triggered drug release from liposomes [212], lipid nanobubbles [153] or even polymer nanoaggregates [213] and polymer nanocups [192] has been already investigated. In the present study, two different types of unloaded polymer-based nanoparticles were set up to develop a new approach for ultrasound treatment. NS were made of PLA polymer (Resomer[®] L206 S) and poloxamer 188 as stabilizer by nanoprecipitation technique. NC were prepared by emulsion-diffusion technique using the shell polymer PLGA (Resomer[®] RG 502), Miglyol[®] 812 as inner oil and the steric stabilizer PVA. Average hydrodynamic diameters measured by laser light scattering were found to be around 130 nm (NS) and 230 nm (NC), and zeta potential was for both formulations around -20 mV (data not shown). After washing, samples were redispersed in 15% (m/V) aqueous trehalose solution and freeze-died.

TEM (Figure 14 A and B) and SEM (Figure 14 C and D) investigations revealed the presence of spherical particles with typical sizes found for DLS investigations comparable between both types of nanostructures. Compared to NS, NC had a 100 nm larger mean size. In NC images two different structures were detected (Figure 14 B and D): intact NC with oily core still present and destroyed capsules with residues of the polymer shell. In comparison to NC, NS did not showed any ring-shaped morphology in electron microscopic images (Figure 14 A and B) referring to a matrix nanostructure. Varela-Fernández *et al.*, who compared PLGA NS and PLGA NC, already detected a similar difference between NS and NC. The NC had a larger particle size and showed a typical ring-shaped morphology [214]. Alam *et al.* showed that NC buckle and collapse, when they release their cargo. To understand the pathways for buckling, they investigated the dynamics of NC collapse *via* analysis of *in situ* TEM image sequences. When the cargo began leaking from the capsule, appeared the indentation of the capsule, which resulted in a NC transforming to a bowl-shaped morphology with a single indentation [215]. Similar bowl-shape morphologies were also seen in Figure 14 B and D.

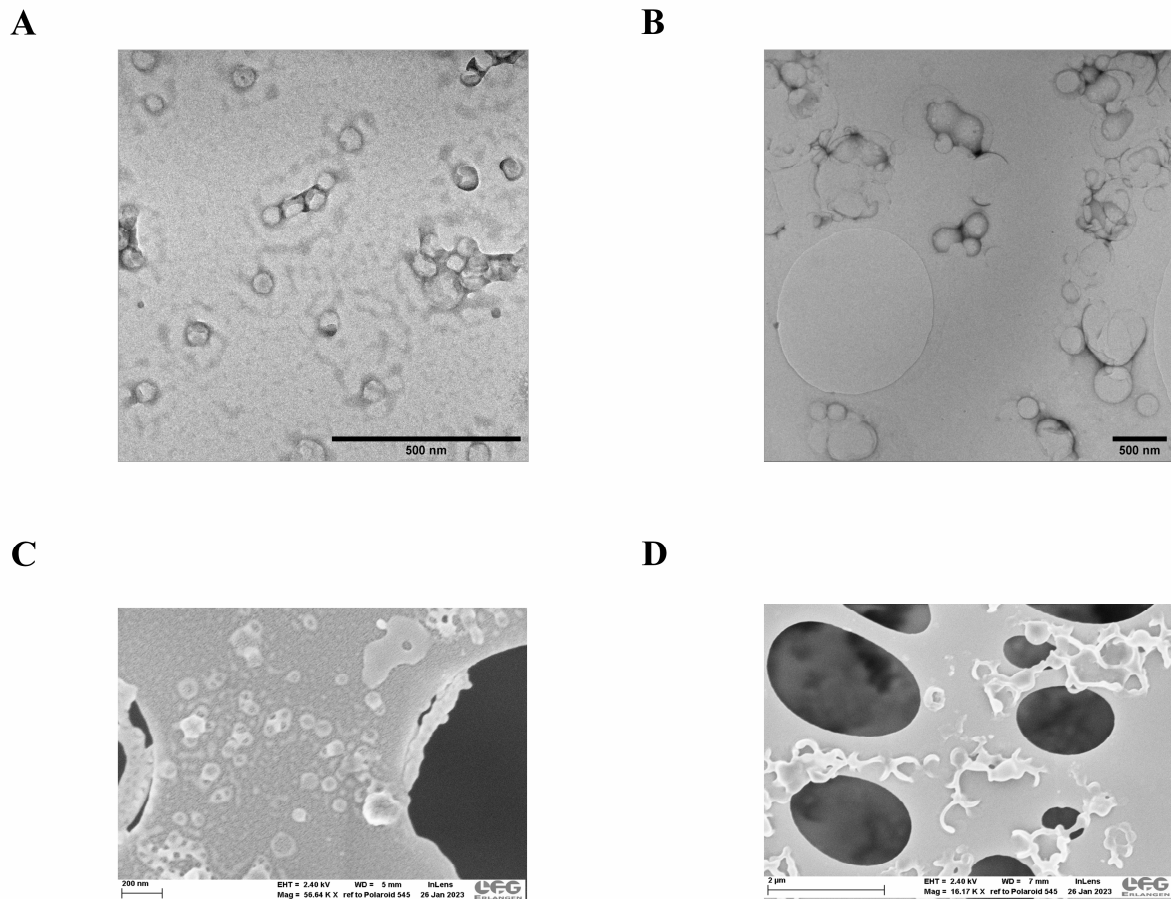


Figure 14 Representative TEM images (A, B) and SEM images (C, D) of PLA NS (A, C) and PLGA NC (B, D). Ultrasound measurements of rehydrated nanoparticles were performed with passive measurement technique, where the detection of acoustic emission is generated from bubble cavitation at the acoustic parameters of 0.6 ms long 750 kHz bursts and a peak rarefaction pressure of 1.02 MPa. The VSD was used to evaluate the inertial cavitation [216].

For cavitation measurements, talcum at a concentration of 1.25% (m/V) in water was used as ultrasound standard. The specific rough hydrophobic surface of talcum is known to lower the threshold of cavitation. Talcum provides heterogeneous air bubble formation on the surface and therefore, leads to constant cavitation. Bhatnagar *et al.* [217] and Hiltl *et al.* [218] already used talcum as cavitation nuclei to achieve inertial cavitation, when ultrasound was applied. In order to ensure that the captured noise signal is induced by talcum, measurements were additionally carried out with ultrapure water as negative control. As shown in Figure 15, talcum led to high inertial cavitation activity ($0.5 \times 10^{-6} \text{ V}/\sqrt{\text{Hz}}$), while pure water did not ($<0.1 \times 10^{-6} \text{ V}/\sqrt{\text{Hz}}$). During the process of inertial cavitation, air bubbles can expand beyond a critical size at higher ultrasound pressures, leading to an unstable growth and a violent collapse, which emit a broadband noise signal [219, 220]. The shock waves emitted by the fragmented bubbles

result in generating the broadband noise whose threshold can be used as an indicator for the presence of inertial cavitation activity [221, 222].

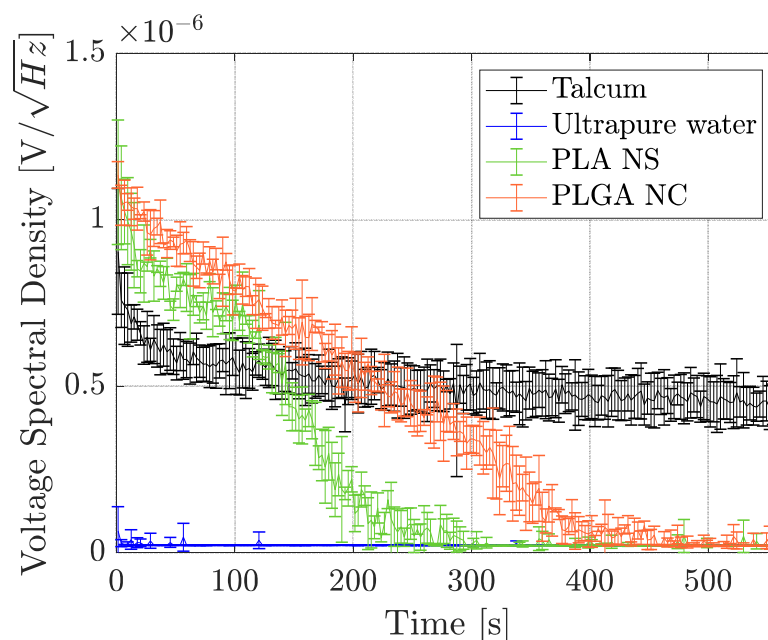


Figure 15 Passive acoustic response of talcum, ultrapure water, PLA NS and PLGA NC on insonation. The results are given as plots of VSD *versus* time for mean of three replicate individual samples. Measurements were performed in set-up 1 at 750 kHz and 1.02 MPa.

Additionally, rehydrated freeze-dried PLA NS and PLGA NC were tested for their cavitation activity, which is shown in Figure 15. Both types of nanoparticles showed an initially high acoustic activity ($1.0 \times 10^{-6} \text{ V}/\sqrt{\text{Hz}}$), compared to talcum. Hiltl *et al.* has concluded that non-lyophilized nanoparticles are not ultrasound active and that freeze-drying and rehydration are two important steps for the high broadband response of nanoparticles [200]. After rehydration of NC, interface between water and hydrophobic surface of NC likely exist in a *Cassie-Baxter* state [223]. Water is unable to wet all the pores thus air could be entrapped on the surface. The pressure difference across the water-air interfaces is balanced by the Laplace pressure, which results in a poor wetting effect [180]. For this reason, the air nanobubbles remain stable on the hydrophobic surface of nanoparticles and continuously grow under ultrasound insonation. The growth of air nanobubbles to larger bubbles during ultrasound exposure was demonstrated by Yildirim *et al.* on MSNs [224] and could be promoted by a coalescence of neighboring nanobubbles. This could occur when two pores including air bubbles are close enough to each other to flatten together and form larger bubbles [225]. When sufficient negative acoustic pressure is achieved during the insonation, air bubbles collapse and induce jet streams, shock waves and disruption of neighboring nanoparticles. However, PLA NS and PLGA NC continually declined in broadband noise over time, when finally no cavitation activity was

detected anymore. PLA NS lost their cavitation activity after 200 s and PLGA NC after 400 s. A similar trend in VSD values for rehydrated and filtered PLA NS has been already shown in the literature [200], where an initial rapid increase in the VSD was followed by a continual decline in broadband noise already after 25 s.

Besides a passive measurement method, where receiving transducer detects the acoustic emission signals from collapsing bubble, an active cavitation detection was used. The active measurement method has been classified as a technique that detects the backscattered signals directly from the existing bubble in the target zone [226]. In this study, a conventional ultrasound imaging array was used in an active measurement set-up (Figure 12) to determine whether or not the inertial cavitation of the PLGA (Resomer[®] RG 502) NC has been locally exceeded in a cuvette. PLGA NC were examined with or without FUS excitation signal. Single high frequency pulses were sent to the cuvette filled with rehydrated PLGA NC and its echo was detected to perform a B-mode (brightness mode) imaging. These ultrasound scans represented the target area of the cuvette containing PLGA NC, which is highlighted with a blue dashed line in Figure 16. When the FUS excitation signal was sent to the cuvette, this caused the inertial cavitation of NC, which could be seen as orange dots inside the cuvette in Figure 16. However, when no FUS excitation signal was sent to the cuvette, no inertial cavitation occurred and color inside the cuvette stayed black. These findings suggested that freeze-dried, rehydrated PLGA NC were capable of seeding inertial cavitation, which was confirmed by passive and active ultrasound measurements.

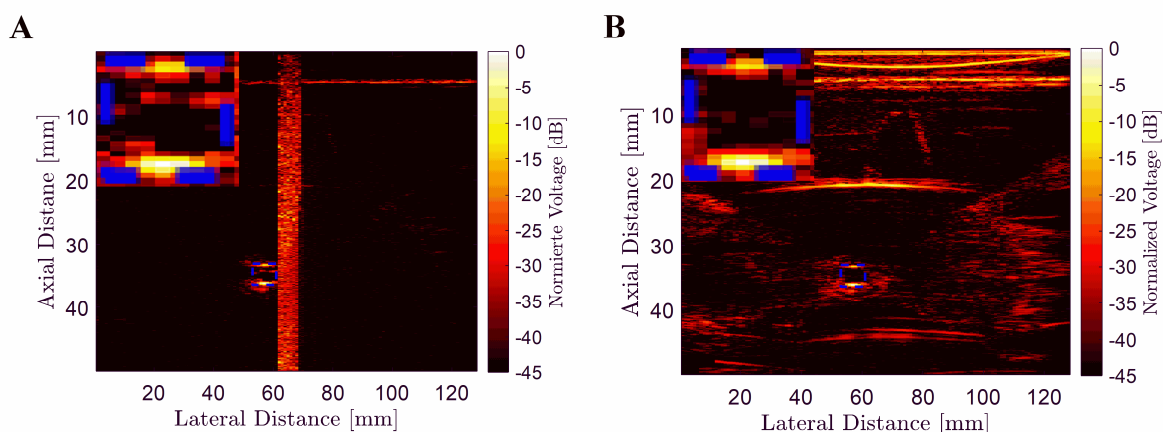


Figure 16 Active imaging measurements of PLGA NC (A) with and (B) without excitation signal. Blue dashed line represents the rim of cuvette and is enlarged in the left upper corner of the pictures. Measurements were performed in set-up 2.

Since cavitation activity could be dependent on the amount of air bubbles [221] trapped on the surface of nanoparticles and consequently, on the amount of nanoparticles, the PLGA

(Resomer[®] RG 502) NC concentration-dependency between 0 $\mu\text{g/mL}$ and 412.5 $\mu\text{g/mL}$ was investigated by the passive measurement technique. Kinetic VSD profiles of the PLGA NC showed a marked concentration-dependent response as shown in Figure 17A. Even at the lowest particle concentration (0.04 $\mu\text{g/mL}$), PLGA NC produced an ultrasound signal that was ~ 4 -fold more intense than the signal of ultrapure water. At particle concentrations lower than 40 $\mu\text{g/mL}$, the ultrasound signal increased almost linearly. On the other hand, at higher concentrations the increase of the mean values of the AUC of VSD, which was calculated *via* the sum of VSD *versus* time, was less pronounced (Figure 17B). The increase of PLGA NC concentration has led to the increase of the number of air bubbles that collapsed and emitted ultrasound signal. A similar effect was reported by Montoya Mira *et al.*, who used MSNs in concentrations between 0 $\mu\text{g/mL}$ and 200 $\mu\text{g/mL}$ to demonstrate the concentration-dependency on the ultrasound intensity [227]. In another study, Tamarov *et al.* investigated the concentration dependent echogenicity of mesoporous Janus nanoparticles using a conventional diagnostic scanner. The increase of nanoparticle concentration from 50 $\mu\text{g/mL}$ to 500 $\mu\text{g/mL}$ resulted in a higher number of cavitating bubbles and a subsequent increase of the contrast in B-mode images in the volume irradiated by ultrasound [228].

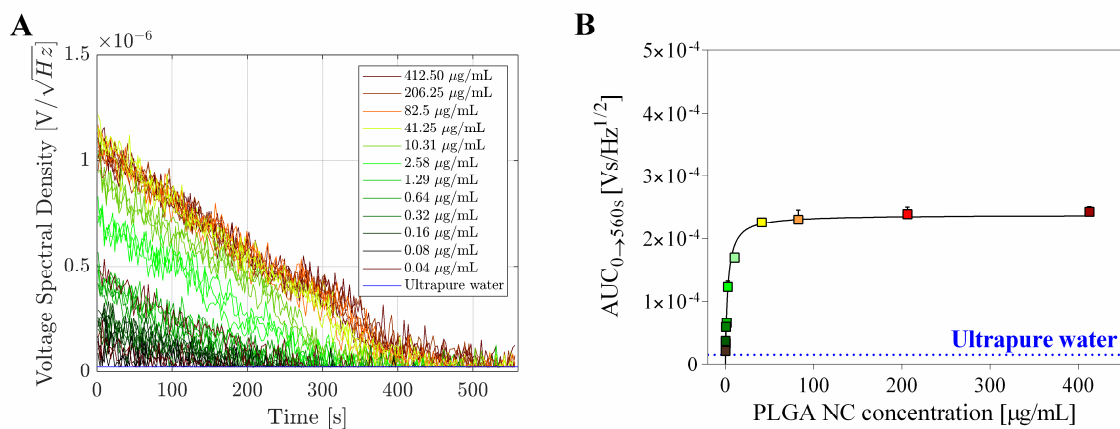


Figure 17 Effect of PLGA NC concentration on the ultrasound intensity at 750 kHz, 1.02 MPa (set-up 1) for 560 s. (A) Ultrasound response of different concentrations of PLGA NC given as plot of VSD, *versus* time for three replicate individual sample. (B) AUC of VSD for different PLGA NC concentration. Bottom blue line represents the AUC of ultrapure water (n=3).

Taking these data together, both, PLA NS and PLGA NC have strong cavitation potential, which was proven by the passive and active measurement method. The cavitation activity of PLGA NC is dependent on particle concentration. For the further experiments, a nanoparticle concentration of at least 100 $\mu\text{g/mL}$ was used to preserve the maximum cavitation activity.

5.2 Effect of Process and Formulation Parameters on Polymer Nanoparticles for Ultrasound Model Drug Delivery

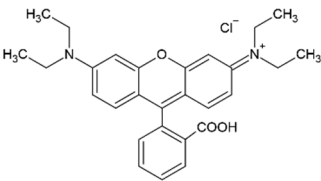
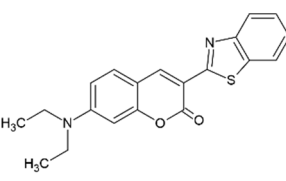
Experimental parameters such as polymer type and concentration, purification, dye concentration and nanostructure type were investigated for particle size, PDI, zeta potential, dye encapsulation, and ultrasound activity. All experiments were conducted by varying one parameter and keeping all the other process parameters constant.

5.2.1 Impact of Polymer Concentrations on the Cavitation Activity of Nanospheres

In the present study, NS were prepared to encapsulate the water soluble dye RhB. The properties of RhB are presented in

Table 6. Three different NS were synthesized with nanoprecipitation method using the steric stabilizer poloxamer 188 and different PLA concentrations (3%, 6% and 12% (m/V)). NS were purified with tangential flow filtration in order to evaluate the impact of the polymer concentration on ultrasound activity and particle stability upon ultrasound treatment. Dye-to-polymer ratio was kept constant at 1:500, as well as the volume of the O-phase (12.5 mL).

Table 6 Properties of RhB and C6 [229, 230].

	Rhodamine B (RhB)	Coumarin 6 (C6)
Structural formula		
Molecular weight [g/mol]	479.01	350.4
Solubility in water [mg/mL]	56.5	<1.0
Solubility in acetone [mg/mL]	1.5	1.0
Absorption spectrum in methanol [nm]	553	459
Emission spectrum in methanol [nm]	574	509

Particle size and PDI measurements were conducted before and after freeze-drying as well as after ultrasound treatment (Figure 18A). Together with zeta potential measurements, they provided insight into colloidal particle stability. After removal of unloaded RhB by tangential flow filtration and freeze-drying, samples were rehydrated and ultrasound response was measured. Before freeze-drying, NS exhibited mean particle sizes of 127 nm, 162 nm and 221 nm for 3%, 6% and 12% PLA formulations, respectively (Figure 18A). The mean PDI was

below 0.2 for all formulations before freeze-drying representing monomodal size distribution. The concentration of the polymer was found to have a pronounced effect on the hydrodynamic diameter. The high PLA concentrations (6% and 12%) formed NS that were about 70-170 nm larger compared to those made of 3% PLA. This is in accordance with Sharma *et al.* and Zweers *et al.* who explained the effect with the increasing viscosity of the O-phase at higher polymer concentration and therefore, decreased efficiency of droplet breakdown resulting in the formation of larger emulsion droplets [231, 232].

The zeta potential was measured by electrophoretic mobility and is commonly used to characterize the surface charge property of the nanoparticles. It represents an electronic repulsion between particles and is often used as a parameter for suspension stability in colloidal dispersions [233]. The NS surface charge did not change with higher polymer concentrations with values between -18 mV and -20 mV i.e. only dependent on the type of polymer (Figure 18B). After freeze-drying, the particle sizes of all formulations were increased by 20-50%, as well as the PDI, indicating a tendency of the NS to aggregate. This could be due to the mechanical stress during freeze-drying, as reported by Trenkenshuhe *et al.* Freezing is the first step in freeze-drying, where crystal formation, interfacial effects, and phase separation could occur. In the drying phase, nanoparticles could lose the hydration shell as well as steric and depletion stabilization [234].

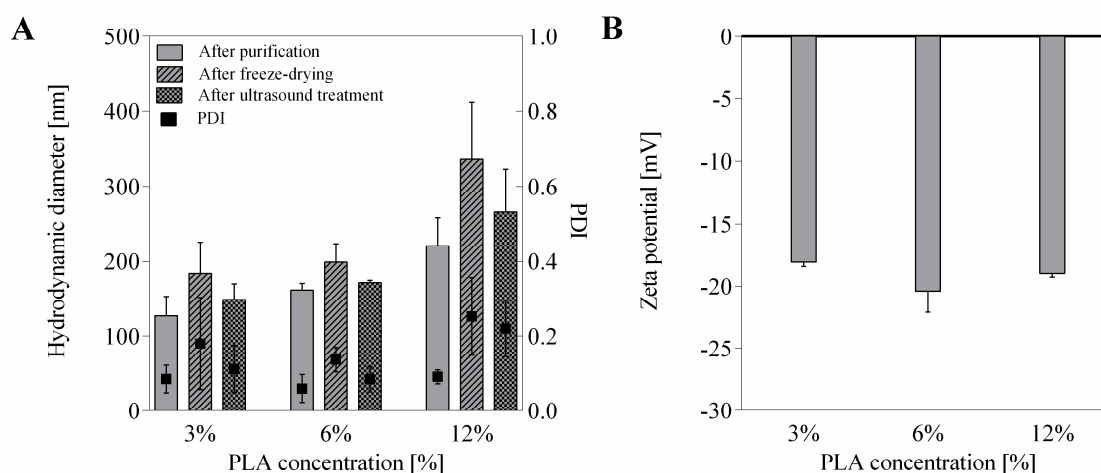


Figure 18 Bar charts comparing particle size (A), PDI (A) and zeta potential (B) of RhB NS prepared with different PLA concentrations, analyzed by DLS techniques in water before (A, B) and after (A) freeze-drying as well as after ultrasound treatment (A). Results are reported as mean \pm SD from three independent batches.

In Figure 19A, VSD of NS ultrasound response is plotted over time of 560 s. All curves started at a VSD level of 1.0×10^{-6} V/ $\sqrt{\text{Hz}}$, but differed in the half-life, which resulted in different AUC of VSD (Figure 19B). AUC values of 6% PLA NS (3.38×10^{-4} V/ $\text{Hz}^{1/2}$) and

12% PLA NS ($3.71 \times 10^{-4} \text{ V/Hz}^{1/2}$) were significantly ($p \leq 0.001$) higher than AUC value of 3% PLA NS ($1.46 \times 10^{-4} \text{ V/Hz}^{1/2}$). The acoustic activity of 3% PLA NS decreased over a period of 300 s until it reached the minimal inertial cavitation. NS prepared with 6% and 12% PLA demonstrated a higher acoustic activity over the whole period of treatment and still showed cavitation responses of $0.3 \times 10^{-6} \text{ V}/\sqrt{\text{Hz}}$ and $0.5 \times 10^{-6} \text{ V}/\sqrt{\text{Hz}}$, respectively, at the end of treatment. Comparable cavitation profiles were presented by Kwan *et al.* The results of three differently sized polystyrene nanocups demonstrated sustainable and gradually decaying inertial cavitation activity throughout the 10 min exposure. Large particles (790 nm) demonstrated stronger cavitation activity as medium (450 nm) and small (170 nm) particles. The authors assumed that the probability of inertial cavitation is directly proportional to the likelihood of a suitably sized cavity being present in the ultrasound field [235]. In this study, 12% PLA NS had larger particle sizes than 3% and 6% PLA NS. Consequently, larger surface pores could be formed on the surface of 12% PLA NS, which might act as cavities that are capable of trapping a larger amount of air and thus enhance cavitation activity.

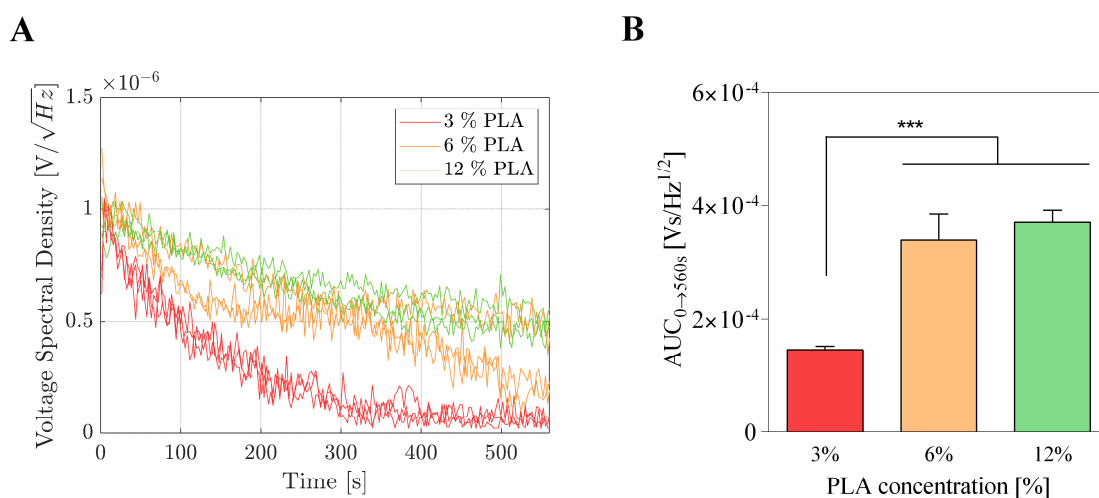


Figure 19 (A) VSD over time and (B) AUC of VSD of NS prepared with different amount of PLA, measured in ultrasound test device (set-up 1) at 750 kHz and 1.02 MPa ($n=3$). Statistically significant difference (one-way ANOVA Tukey's multiple comparisons test) is marked with asterisk: *** ($p \leq 0.001$).

Following the ultrasound exposure, the characterization by DLS revealed NS sizes and PDIs comparable to the NS before freeze-drying (Figure 18A). Particle sizes were 149 nm, 172 nm and 266 nm by ultrasound treatment for 3% PLA NS, 6% PLA NS and 12% PLA NS, respectively. Due to high energy input of ultrasound the aggregates that were formed during freeze-drying, could be disassembled after ultrasound treatment to initial NS sizes. Similar results were found by Papa *et al.*, who demonstrated that microscale (~ 4 mm diameter) polymer aggregates could be disassembled into individual nanoparticles by applying low-energy

ultrasound [213]. A study of Kwan *et al.* characterized polystyrene nanocups before and after ultrasound exposure. The sizes of nanocups were reduced by 10-20% after ultrasound treatment [235]. Collectively, the results demonstrated that polymer concentration had a major influence on particle size, which strongly affected the ultrasound activity.

5.2.2 Effect of Dye-to-Polymer Ratio on the Ultrasound Sensitivity of Nanospheres

For the following experiments, NS were prepared with a standard nanoprecipitation method using poloxamer 188 as stabilizer and a PLA concentration of 3% purified with tangential flow filtration, as it showed the smallest particle sizes, but with a sufficient cavitation activity compared to 6% and 12% PLA. As loaded drug might change the particle characteristics, a water soluble dye RhB loaded in PLA NS at different RhB-to-polymer ratios (blank, 1:100, 1:250, 1:500 or 1:1000) was used as model drug to examine the influence on physicochemical NS characteristics, and their ultrasound sensitivity.

Figure 20A summarizes the average sizes of the NS and their PDI, whilst in Figure 20B the zeta potential is shown. According to Figure 20A, the higher the concentration of RhB, the larger is the average size of the NS. The initial particle size of dye-free NS was about 95 nm, whereas the presence of RhB increased the particle size to 170 nm for the RhB-to-polymer ratio of 1:100. The dependence of the particle size on the concentration of the loaded dye was also observed by K uchler *et al.*, who prepared RhB-loaded nanocarriers using poloxamer 188 as surface stabilizer. They assumed that the localization of hydrophilic dye appears within the poloxamer layer of the nanoparticle close to the W-phase. Higher dye concentrations enable stronger intermolecular interactions (hydrogen bonds) with water [236]. However, the impact of the amount of RhB on particle size was not as pronounced as the effect of the PLA concentration described above. Furthermore, before freeze-drying the PDI values of all formulations were low enough (<0.2) to be considered satisfactory, being even lower than those obtained by other authors for the preparation of similar polymer nanoparticles [237]. The surface charge of the freshly prepared NS was between -18 mV and -22 mV and did not change upon different dye concentrations (Figure 20B). Jonderian *et al.* prepared RhB-loaded PLGA nanoparticles by a single emulsion-solvent evaporation technique, which resulted in similar values of zeta potential (-21.7 mV) [237].

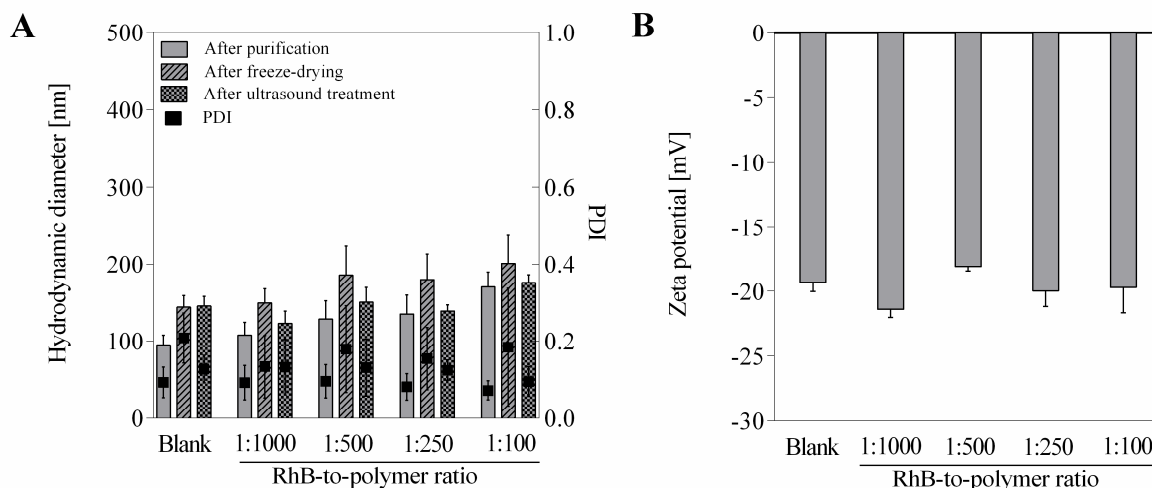


Figure 20 Bar charts comparing the particle size (A), PDI (A) and zeta potential (B) of blank and RhB-loaded NS prepared at different dye-to-polymer ratios, analyzed by DLS in water before (A, B) and after (A) freeze-drying as well as after ultrasound treatment (A). Results are reported as mean \pm SD from at least three independent batches.

After freeze-drying of the samples, the average size as well as PDI increased for all formulations, presented in Figure 20A. Due to potential freeze-drying stress, NS seemed to aggregate and particle size increased up to 200 nm. PDI increased for more than 100% in the formulation with high amounts of RhB (RhB:polymer, 1:100), but it still stayed below 0.3.

Inertial activity of the NS significantly ($p \leq 0.0001$) decreased by loading NS with RhB of different concentrations (Figure 21). Ultrasound activity of blank NS was initially at $1.0 \times 10^{-6} \text{ V}/\sqrt{\text{Hz}}$ and it decreased to $0.5 \times 10^{-6} \text{ V}/\sqrt{\text{Hz}}$ after 10 min of sonication. All loaded NS reached initial cavitation between $1.0 \times 10^{-6} \text{ V}/\sqrt{\text{Hz}}$ and $1.5 \times 10^{-6} \text{ V}/\sqrt{\text{Hz}}$, while the activity dropped during the measurement and after 10 min no sufficient cavitation was observed anymore. The drop in cavitation intensity was detected earlier at higher RhB concentrations, for RhB-to-polymer ratio 1:100 already after 100 s. Additionally, Figure 21B shows that the higher the RhB-to-polymer ratio the higher was the cavitation activity. This could be due to the low hydrophobicity of RhB. When the loaded dye is more hydrophilic than the polymer, the dye is known to deposit preferentially on the surface of the nanoparticles [238]. In this way, RhB could be accumulated on the surface of the PLA NS, which reduced the hydrophobicity of the NS surface with increasing RhB concentration. Already reported in the literature, a more hydrophobic surface is required to prepare nanoparticles that stabilize air bubbles for high acoustic activity [239]. In this way, loaded hydrophilic dye induced higher hydrophilicity of NS surface, this entrapped less air and led to a decrease in acoustic cavitation of NS.

After ultrasound treatment, particle sizes decreased to the initial sizes between 145 nm and 175 nm (Figure 20A), most likely due to aggregates destruction, as reported above. Although the particle size increased with increasing dye concentration, the cavitation activity decreased. Apparently, the concentration of dye and its impact on surface hydrophobicity had a greater impact on ultrasound response of NS, as the impact of particle size, observed in the section above.

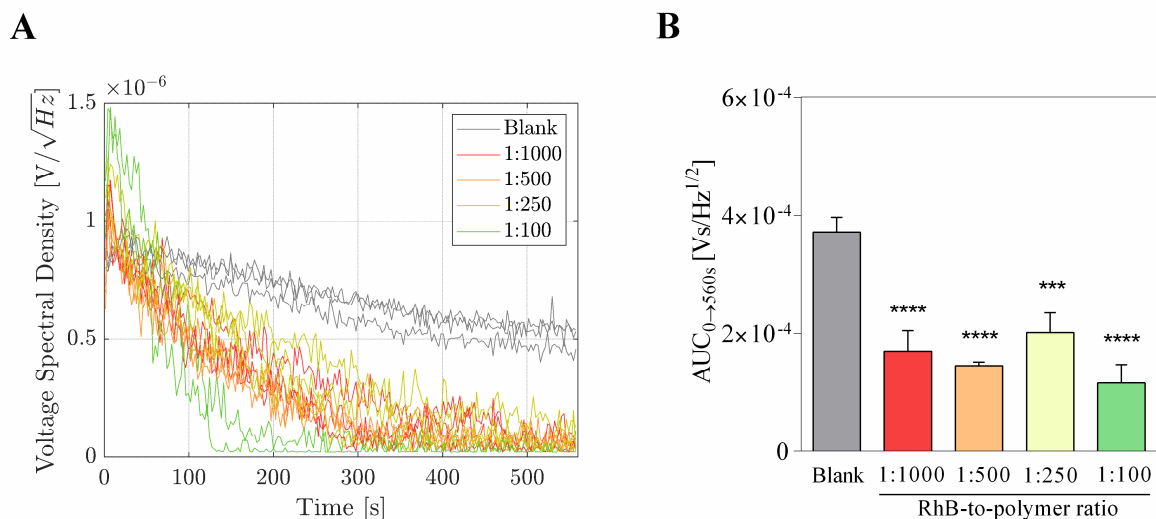


Figure 21 VSD over time (A) and AUC of VSD for the first 560 s of NS prepared as blank or RhB-loaded NS at different dye-to-polymer ratio (n=3). Measurements were performed in set-up 1. Statistically significant difference (one-way ANOVA Tukey's multiple comparisons test) is marked with asterisk: *** (p<0.001), **** (p<0.0001).

5.2.3 Influence of the Purification by Tangential Flow Filtration on Ultrasound Cavitation

After preparation of polymeric nanoparticles a purification process is used to remove additives, surfactants, coating agents, and unloaded drug molecules. The most common method used for nanoparticle purification are ultracentrifugation [240, 241], diafiltrating centrifugal devices [242] and tangential flow filtration [240-242]. Ultracentrifugation and diafiltrating centrifugal devices use centrifugal forces with or without a combination of filters added to centrifuge tubes to separate the nanoparticles from undesired material [240, 242, 243]. While these are simple and easy separation processes, the gravitation forces generated during centrifugation can cause changes in nanoparticle properties such as aggregation [244]. Additionally, centrifuges have a finite limit on the size of the containers, which can be pose difficulties in achieving reproducibility particularly when scaling up to large volumes [240, 242]. Here, tangential flow filtration has been reported to provide a useful alternative. Since 1993, when Allémann *et al.* published a study, where they applied tangential flow filtration for nanoparticle purification [114], numerous studies have used this method in nanoparticle purification processes [245-

247]. The nanoparticle dispersion is pumped tangentially along the filter surface. The pressure forces the filtrate through the membrane while particles travel forward with the tangential flow [248].

To find out if the purification of free dye and excess surfactant remaining in the PLA NS formulation has an impact on the ultrasound cavitation, different diavolumes in tangential flow filtration were applied following freeze-drying and ultrasound testing. RhB-loaded NS at RhB-to-polymer ratio 1:500 with poloxamer 188 as surfactant were prepared. The NS dispersion with an average diameter of about 124 nm (Table 7) underwent diafiltration, which involved the transmembrane pressure of 29 psi and a flow rate of peristaltic pump of 9.1 mL/min. Different diavolumes were used for purification (0, 5, 10, 20, 30, 40, 50 and 60). Diavolume is defined as the volume of diafiltrated medium filled into the tangential flow filtration system compared to the retentate volume [249]. The diavolume should reduce the amount of excess poloxamer 188 and RhB in the dispersion. After each washing step particle size and PDI were measured and compared with the particle size and PDI presented after freeze-drying (Table 7).

Table 7 Hydrodynamic diameter (S) and PDI of NS dispersions after purification by tangential flow filtration and after freeze-drying and their ratio S_f/S_i and PDI_f/PDI_i . Values are mean \pm SD of three measurements for each diavolume from one batch.

Diavolume	Hydrodynamic diameter			PDI		
	S_i [nm]	S_f [nm]	S_f/S_i	PDI_i	PDI_f	PDI_f/PDI_i
0	123 \pm 2	156 \pm 2	1.3	0.20 \pm 0	0.16 \pm 0	0.8
5	114 \pm 0	144 \pm 1	1.3	0.13 \pm 0.02	0.18 \pm 0.02	1.4
10	111 \pm 1	133 \pm 3	1.2	0.13 \pm 0.02	0.18 \pm 0.01	1.4
20	115 \pm 2	123 \pm 2	1.1	0.14 \pm 0.03	0.17 \pm 0.03	1.2
30	112 \pm 2	122 \pm 2	1.1	0.14 \pm 0.02	0.15 \pm 0.01	1.1
40	111 \pm 1	130 \pm 1	1.2	0.12 \pm 0.01	0.14 \pm 0.01	1.3
50	114 \pm 2	132 \pm 2	1.2	0.12 \pm 0.01	0.14 \pm 0.03	1.2
60	120 \pm 1	141 \pm 2	1.2	0.16 \pm 0.01	0.13 \pm 0.01	0.8

Abbreviations: S_i : hydrodynamic diameter after purification, S_f : hydrodynamic diameter after freeze-drying, PDI_i : PDI after purification, PDI_f : PDI after freeze-drying

Samples purified by tangential flow filtration with 5-40 diavolumes appeared to decrease in particle size (up to 111 nm) and PDI (0.12). However, after 50 diavolumes particle size and PDI increased up to 120 nm and 0.16, respectively. The increase in size and PDI of NS by increasing the diavolume is probably due to the increased processing time, during which the NS are pushed toward each other under pressure on the membrane during recirculation. Similar findings were reported by Tavakoli Naeini, who purified polyplexes with tangential flow filtration and demonstrated that increase in diavolume leads to particle aggregation [250]. As observed before, after freeze-drying all washed batches showed an increase in particle size and PDI due to the freezing/drying stress. Among the tested diavolumes, 20 and 30 diavolumes

resulted in lowest S_f/S_i (1.1) and PDI_f/PDI_i ratios of 1.1-1.2 (Table 7), which indicated the lowest aggregation.

As observed in the studies above, the degree of aggregation correlated with the cavitation activity of NS. The smaller the size of NS after freeze-drying was the lower was the cavitation activity. When formulations were filtered with small volumes (diavolume 5) and freeze-dried, the size of NS had increased up to 144 nm making NS stayed acoustically active over the whole treatment period of 560 s (Figure 22A). The inertial cavitation dropped from about 6.0×10^{-4} Vs/Hz^{1/2} at 5 diavolumes to about 4.0×10^{-4} Vs/Hz^{1/2} at 30 diavolumes and even to 2.7×10^{-4} Vs/Hz^{1/2} at 40 diavolumes (Figure 22B). Further increase in diavolumes (>50) increased acoustic activity, most likely due to increase in particle size. The results of this study showed that a tangential flow filtration had an influence on the particle size of NS, which is in direct correlation with cavitation intensity. It was concluded that diavolume of 30 or 50 could be taken into consideration.

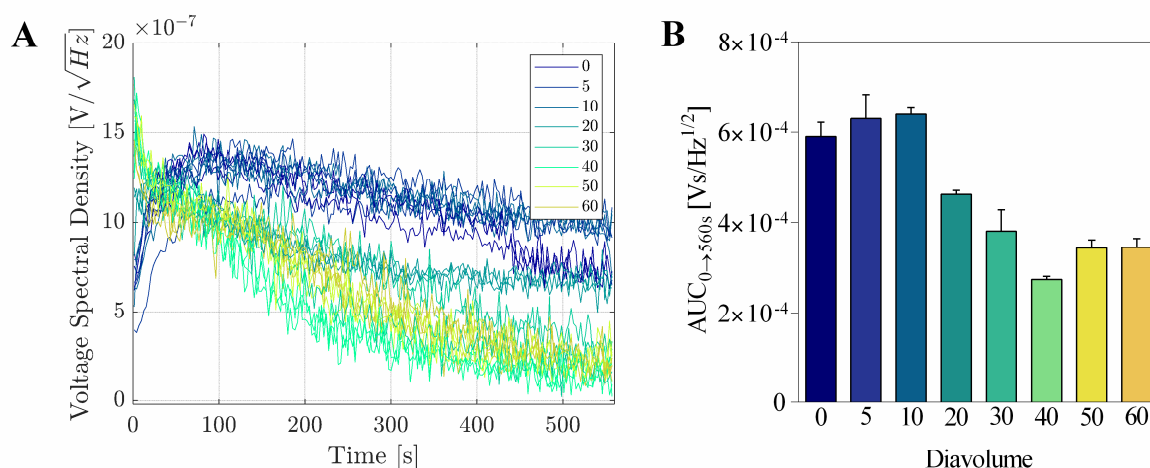


Figure 22 Comparison of VSD over time (A) and AUC of VSD (B) of NS dispersion using different diavolumes (0-60) for purification with tangential flow filtration. Lines represent three individual measurements of cavitation in set-up 1 at 750 kHz and 1.02 MPa (A) and bars represent mean \pm SD (n=3) of AUC (B) at different diavolumes.

5.2.4 Investigating Ultrasound Sensitivity Affected by Dye Hydrophilicity in Nanospheres

Two dyes RhB and C6, both small molecules, were selected as model dyes with varying hydrophilicity to evaluate the influence of the hydrophilicity of the cargo on the physicochemical characteristics of the PLA NS and their ultrasound activity. The RhB is highly hydrophilic with a log P < 2.0, a molar mass of 479.01 g/mol [229] and water solubility of 56.5 mg/mL. C6 is a hydrophobic dye with molar mass of 350.43 g/mol, log P of 4.2 and low solubility in water (<1 mg/mL) [230]. The structures and properties of the two dyes used in the study are shown in Table 6. At physiological pH, C6 is a non-ionic non-polar molecule and has

no ability to form hydrogen bonds with water, which makes it difficult to dissolve in aqueous solvent. However, it is soluble in organic solvents such as, ethanol, methanol, acetone and dimethylformamide. RhB is zwitterionic with a net neutral charge. It simultaneously bears a positive charge at the amine group attached to the xanthene ring and a negative charge at the carboxyl group at the isolated benzene ring [251, 252]. RhB is a fluorescent dye that belongs to the class of xanthene derivatives. It could be easily dissolved in aqueous solution. However, quantum yield of its solution is low and Stokes shift small [253]. C6 belongs to a class of heterocyclic compounds known as benzopyrenes that bear a carbon-carbon double bond which is fixed as *trans* conformation as in *trans*-stilbene through a lactone structure. Stilbene with a *trans* conformation is well known to have a strong fluorescence and high quantum yield [254]. The PLA NS loaded with RhB or C6 were prepared by the standard nanoprecipitation technique. The O-phase consisted of the polyester polymer in dichloromethane and dye in acetone at a dye-to-polymer ratio of 1:500. The W-phase was formed by mixing 0.27% poloxamer 188 with ultrapure water. After nanoprecipitation in the two-syringe system, the organic solvents were removed by evaporation under stirring overnight and washed with the tangential flow filtration system (RhB) or ultracentrifugation (C6).

Figure 23A shows the average hydrodynamic diameter and size distribution of the blank and dye-loaded NS. Compared to the unloaded PLA NS with a particle size of 95 nm, a tendency for particle increase was observed when loaded either with RhB (128 nm) or with C6 (145 nm). Previous reports [255, 256] demonstrated the formation of even larger PLA NS, 211 nm, 224 nm and 200-260 nm for blank NS, RhB NS and C6 NS. Regarding the PDI, the values after purification were low (≤ 0.2) and all NS could be considered as monodispersed. The hydrodynamic diameter of C6-loaded NS was found to be about 20 nm larger than that of the RhB NS. This is in accordance with the report of Gomaa *et al.* [251], who studied RhB and fluorescein isothiocyanate as hydrophilic and hydrophobic model molecules encapsulated in PLGA NS. RhB-loaded NS were 10-160 nm smaller compared to NS with the hydrophobic dye. The reason could be that the hydrophilic dye attempted to exit from the hydrophobic polymer and leaked into the W-phase during the preparation process, resulting in low dye load (Table 8) and smaller particle sizes (Figure 23A). The blank NS formulation showed zeta potential of -19 mV (Figure 23B). Since, both dyes represent nonionic or neutral molecules, they did not have any detectable effect on zeta potential values ranging between -17 mV and -22 mV, compared to blank NS. As seen before the freeze-drying process increased particle size and PDI, which was more pronounced by the RhB NS (Figure 23A) presumably due to the lowest zeta potential.

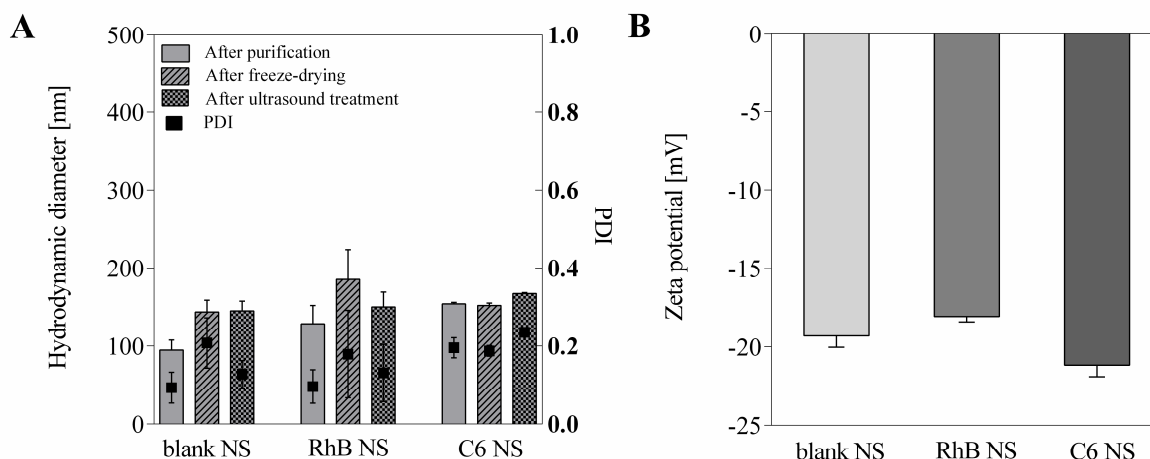


Figure 23 Average hydrodynamic size (A), PDI (A) and zeta potential (B) of blank, RhB- and C6-loaded PLA NS. Results are reported as mean \pm SD of at least three independent samples.

The results of dye encapsulation are shown in Table 8. The entrapment efficiency of the C6 dye with around 30% was considerably higher than for RhB with less than 1%. The encapsulation of RhB by conventional nanoprecipitation is generally less ineffective due to its good water solubility, hydrophilic nature, and low molecular weight. Attempts of the hydrophilic dye to exit from the hydrophobic polymer, resulted in accumulation at the particle surface, and a lower encapsulated amount in the polymer matrix and reduced entrapment efficiency [257, 258]. Zhukova *et al.* calculated the affinity of three dyes with different hydrophilicity to the NS polymer matrix. A more hydrophilic dye could easier leave the NS matrix leaking into W-phase than a hydrophobic dye [230]. In addition to the entrapment efficiency, the dye load was also determined for both dyes. As for entrapment efficiency the same trend was shown for the dye load values, where C6 NS loaded 0.09% and RhB NS less than 0.01% of the dye. The hydrophobic dye could be entrapped more efficiently in PLA NS.

Table 8 Dye load, entrapment efficiency of the different NS and dye release after ultrasound treatment determined by fluorescence spectroscopy (mean \pm SD, n=3).

	RhB PLA NS	C6 PLA NS
Dye loading [%]	0.00073 \pm 0	0.09 \pm 0.05
Entrapment efficiency [%]	0.45 \pm 0.01	30.60 \pm 8.07
Dye release after ultrasound treatment [%]	79.2 \pm 2.6	53.0 \pm 13.5

The ultrasound cavitation diagrams in Figure 24 indicated that C6 NS were more active as RhB NS. The cavitation of C6 NS was comparable with blank NS. Both formulations were ultrasound active the whole 560 s of treatment (Figure 24A). In contrast, the cavitation signal

of RhB NS vanished after 300 s, indicating at no activity afterwards. In the 560 s of treatment time, the AUC of VSD of RhB NS was about $1.8 \times 10^{-4} \text{ Vs/Hz}^{1/2}$, which was 50% less than for C6 NS (Figure 24B). The reason for this difference could be the difference in hydrophobicity of the dyes and their impact on the characteristic of NS surface. As mentioned before the hydrophilic dye attempts to exit from the hydrophobic polymer and accumulates at the particle surface, which induces a more hydrophilic surface characteristic. Hydrophilic surface of particles can poorly stabilize gas-pockets leading to low cavitation activity [239]. Dye release after ultrasound treatment from RhB NS was greater than that from C6 NS (Table 8). This may be due to the higher hydrophobicity of C6 compared to RhB. Similar observations were published by Son *et al.* [259], who loaded chlorin e6 and pheophorbide a with similar structure but different hydrophobicity into polymer nanoparticles and discovered a difference in release patterns, biodistributions, and therapeutic results. The drug with moderate hydrophobicity was released faster from nanoparticles compared with highly hydrophobic drug due to the better solubility in the aqueous environment. They anticipated that rapid release of less hydrophobic drug from nanoparticles could better occur in blood flow before nanoparticles accumulate at tumor sites. However, the release of C6 after ultrasound treatment was with 53% distinctly higher as when no external stimuli was applied (<2%) in a study of Purr *et al.* [260].

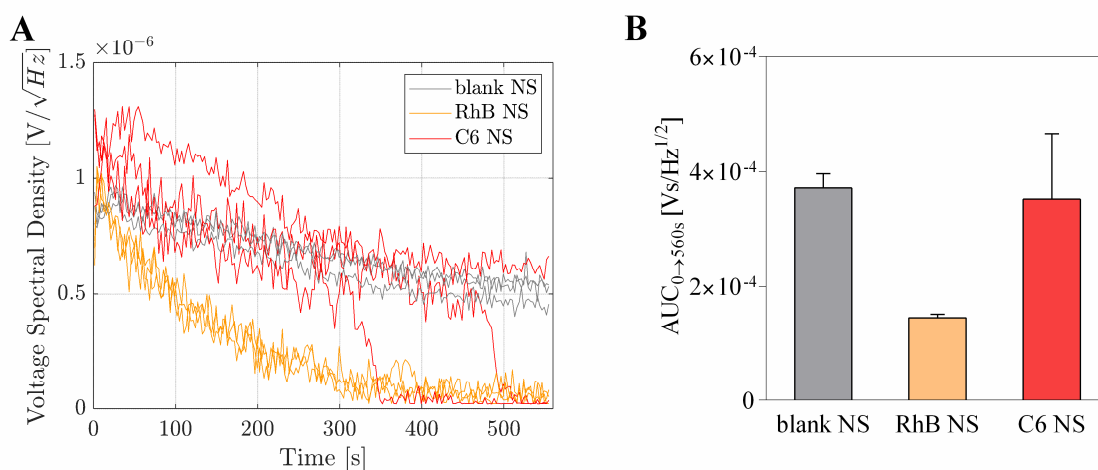


Figure 24 Ultrasound activity of blank, RhB- and C6-loaded PLA NS presented as VSD over time (A) and AUC of VSD. Results are reported as three individual samples (A) and as a mean \pm SD from three independent samples (B). Measurements were performed in set-up 1 at 750 kHz and 1.02 MPa.

5.2.5 Effect of Polymer Type on Dye Encapsulation and Cavitation Activity of Nanospheres

Different types of polymers were evaluated for their suitability to prepare acoustically active NS. Besides PLA also PLGA has been used in several drug formulations which have been approved by the FDA [261-263]. Both polymers are linear, lipophilic, and biodegradable. However, methyl side groups of PLA makes the polymer more hydrophobic than PLGA

resulting in absorbing less water and degrading slower than PLGA [262]. Blank and C6-loaded NS were prepared using 3% PLA (Resomer[®] L206 S) or 3% PLGA (Resomer[®] RG 752 H) in 1:500 dye-to-polymer ratio with the nanoprecipitation method and purified by centrifugation. As stabilizer, 0.27% poloxamer 188 was used.

The hydrodynamic diameter of prepared NS, shown in Figure 25A, varied between 115 nm and 160 nm with PDIs less than 0.2 after purification. Blank PLGA NS were 40 nm bigger than blank PLA NS, while C6-loaded PLGA NS were 30 nm smaller than loaded PLA NS. Loading NS with C6 resulted in lower zeta potentials for both polymer types compared to unloaded NS (Figure 25B). Rafiei *et al.* showed that incorporation of hydrophobic drug reduced zeta potential of nanoparticles [264]. He suggested that a hydrophobic drug and PLGA could interact non-covalently (van der Waals or hydrogen bonds), which resulted in different organization of polymer endings on the surface of nanoparticles leading to reduced surface charge. After freeze-drying particle size increased up to 40% due to the aggregation stress of the freeze-drying process (Figure 25A).

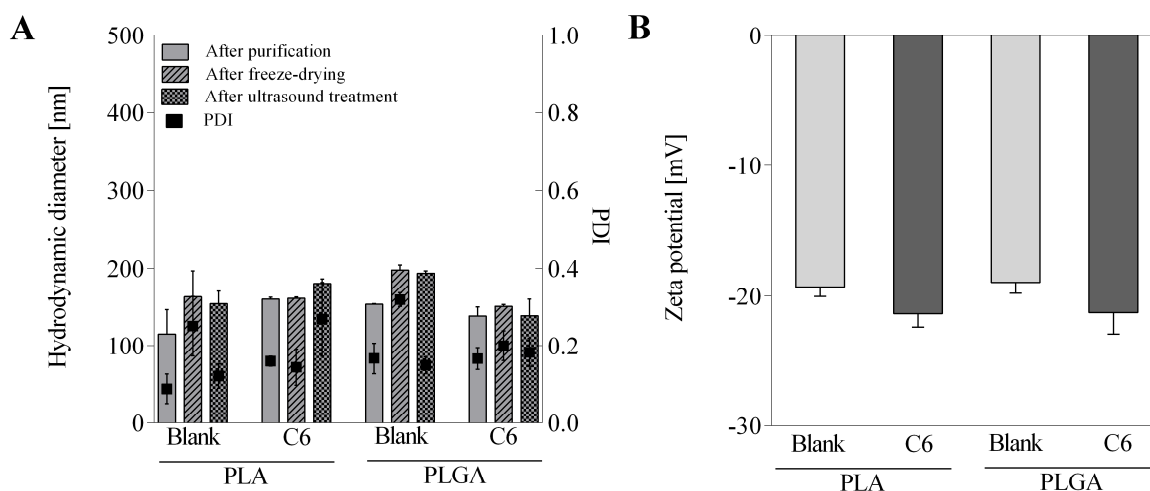


Figure 25 DLS measurements of blank and C6 NS prepared with PLA or PLGA polymer: (A) particle size and PDI, (B) zeta potential (means \pm SD, n = 3).

A similar dye load was obtained for C6 regardless of the polymer type with 0.09% and 0.06% for PLA NS (Table 8) and PLGA NS (Table 9), respectively. Entrapment of the fluorescent dye was for both formulations around 30%, which was comparable to reports by others for C6 [265, 266]. The difference of the polymers did not play any essential role for dye load and encapsulation efficiency. Due to the high hydrophobicity of C6, it could be successfully entrapped in PLA and PLGA NS.

Table 9 Dye loading and entrapment efficiency of C6-loaded PLGA NS and dye release after ultrasound treatment determined by fluorescence spectroscopy (mean \pm SD, n=3).

	C6 PLGA NS
Dye loading [%]	0.06 \pm 0.01
Entrapment efficiency [%]	31.53 \pm 6.06
Dye release after ultrasound treatment [%]	48.6 \pm 3.2

After ultrasound treatment the particle size of PLA and PLGA NS did not change significantly and the sizes stayed below 200 nm (Figure 25A). The use of PLGA polymer led to a decrease in ultrasound activity of NS independent of the presence of dye (Figure 26A). In comparison to PLA NS, which were generally active over the total ultrasound time of 560 s, PLGA NS were only active in the first 200 s. Obviously, the hydrophobic side chain of PLA rendered the NS surface more hydrophobic providing a better stabilization of air pockets on the surface of NS followed by a higher acoustic cavitation [239]. Figure 26B shows that C6 PLA NS accomplished a significantly higher ($p \leq 0.0001$) ultrasound activity with an AUC (VSD) of 3.5×10^{-4} Vs/Hz^{1/2} than C6 PLGA NS with an AUC (VSD) of about 1.0×10^{-4} Vs/Hz^{1/2}. Both, loaded PLA NS and PLGA NS, had an inertial cavitation of 1.0×10^{-6} Vs/ $\sqrt{\text{Hz}}$, which decreased after time. In case of PLGA NS reached the ground platform after 200 s and in case of PLA NS between 350 s and 500 s. In spite of the lower cavitation activity of PLGA NS, 48% of C6 was released after 560 s of ultrasound treatment (Table 9). This is in the same range as released amount of C6 from PLA NS (Table 8). It appears that the initial high inertial cavitation is responsible for the destruction of NS and dye release, while later cavitation activity below 1.0×10^{-6} Vs/ $\sqrt{\text{Hz}}$ did probably not play an important role in dye release.

The cavitation activity profile of NS appears to be independent on the hydrophilicity of the polymer. However, this does not have a significant influence on the amount of dye release. Probably, release of the dye appears only by higher VSD values around 1.0×10^{-6} Vs/ $\sqrt{\text{Hz}}$.

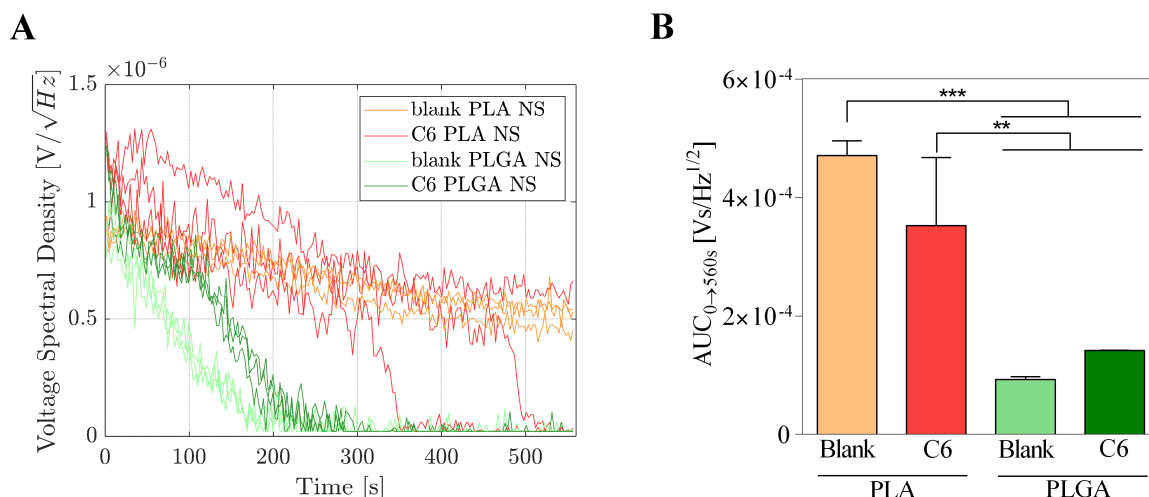


Figure 26 Ultrasound activity of blank and C6-loaded NS prepared with PLA or PLGA polymer: (A) VSD *versus* time for the replicate individual sample and (B) AUC of VSD (n=3). Measurements were performed in set-up 1 at 750 kHz and 1.02 MPa. Statistically significant difference (one-way ANOVA Tukey's multiple comparisons test) is marked with asterisk: ** (p≤0.01); *** (p≤0.001).

5.2.6 Impact of Different Types of PLGA Nanocarriers on Acoustic Cavitation

Since PLGA NS did not have a high acoustic activity, alternatively oily core NC based on PLGA (Resomer[®] RG 752 H) were prepared and characterized. Whereas polymer NC with a matrix structure present a solid colloidal particle in which active molecules are encapsulated within the polymer matrix [84], polymer NC are a soft-vesicular systems including an inner reservoir with drug confined in a liquid and surrounded by a polymer membrane acting as a shell [84, 267]. NC could be advantageous over NS, as their thermo-mechanical properties differ resulting in a lower mechanical rigidity of the capsule which could enable them to uncage and release drugs more easily [267]. In the first step, C6-loaded PLGA NS and NC were prepared at a dye-to-polymer ratio of 1:500 with 0.27% poloxamer 188. Both types of nanoparticles were formed with the same nanoprecipitation technique using two connected syringes. However, NC formation was critical as indicated by large particle size and a multimodal size distribution (data not shown). Therefore, in the first step the emulsification-diffusion evaporation technique according to Quintanar-Guerrero *et al.* [203] was successfully applied. The dye-to-polymer ratio of 1:500 was kept constant. The dye was dissolved in ethyl acetate with 5% Miglyol[®] 812 and homogenized with 2% PVA aqueous solution using the Ultra Turrax[®] at 20.000 rpm for 8 min. The NC were compared with NS and evaluated by DLS and in the ultrasonic field.

The size of C6-loaded NS and NC, presented in the Figure 27A, differed significantly (p≤0.0001). PLGA C6 NS demonstrated a size range of about 130-150 nm, which was not

influenced by purification, freeze-drying or ultrasound examination. In contrast, PLGA C6 NC revealed larger particle sizes about 250 nm that increased after purification and freeze-drying by about 290 nm and 325 nm, respectively. The ultrasound treatment reduced again the size down to size after the purified NC. The difference in particle size between NS and NC has already been reported in recent studies. Varela-Fernández *et al.* encapsulated lactoferrin in PLGA NS and NC, where the NC were two times larger than NS and measured between 180 nm and 280 nm [214]. In another study, Valente *et al.* explained that NC formulation is more complex process compared to NS formulation, because it involves the oily droplet formation and the deposition of the polymer wall. The polymer functions as a stabilizer of the oily droplet, and it is necessary to ensure that the concentration of the polymer in the solution is sufficient to provide complete coverage of all the oily droplets. When the oil to polymer mass ratio is not low enough, larger NC sizes are normally obtained due to insufficient polymer amount available for the formation of smaller oil drops [268]. Increase in size due to centrifugation force in purification process has been shown before [269]. It was demonstrated that the structural integrity of NC with thin shell can be damaged by centrifugation [270], which induces oil leaking and aggregation.

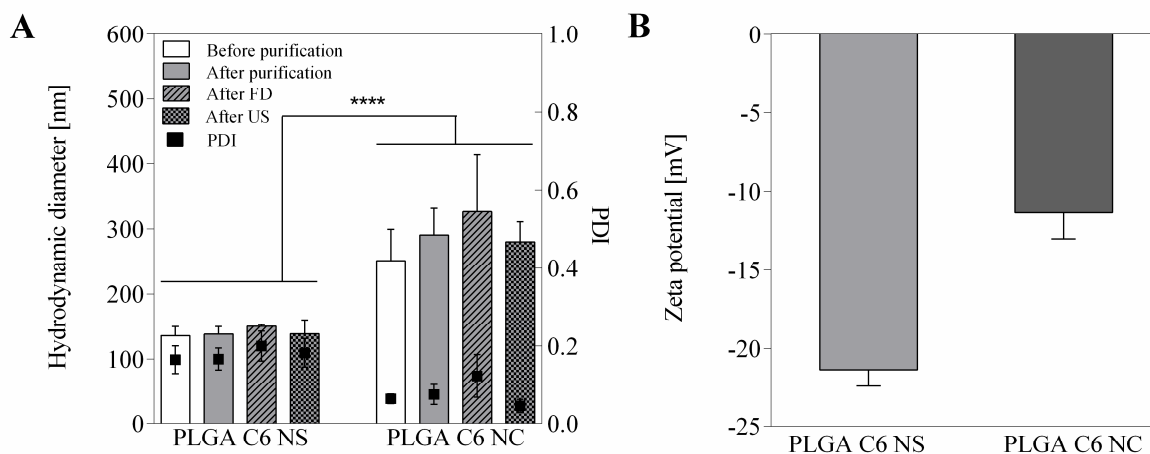


Figure 27 (A) Particle size and PDI before purification, after purification, after freeze-drying (FD) and after ultrasound treatment (US) as well as (B) zeta potential after purification of C6-loaded PLGA NS and PLGA NC (n=3). Statistically significant difference (t-test) is marked with asterisk: **** (p<0.0001).

An additional increase in size appeared after freeze-drying. The PDI was below 0.2 for NS and NC suggesting monodisperse populations. Regarding the surface charge, negatively zeta potential values were obtained due to the acidic character of the polyester polymer (Figure 27B). PLGA NC had a higher zeta potential (-12 mV) as PLGA NS (-22 mV), supporting the idea that C6 in NC is preferentially encapsulated in the inner oil reservoir protected by the

polymeric shell, while C6 could adhere to the surface of NS matrix followed by a changing of the surface properties. Varela-Fernández *et al.* reported a higher surface charge, when drug was incorporated in NC as when the drug was encapsulated in NC [214].

C6 showed a tendency to lower dye load (0.06%) and entrapment efficiency (32%) using NS as nanocarrier in comparison to the NC (dye load of 0.16% and entrapment efficiency of 79%), as presented in Table 10. Similar findings were also reported by Bazylinska *et al.* [271], who obtained a 10% higher encapsulation efficiency for cyanine loaded in NC than in NS. The observed phenomenon could probably be caused by improved incorporation of drug in the oleic core reservoir. In case of NS the retention of C6 closure is provided only by hydrophobic polymeric matrix.

Table 10 Dye loading and entrapment efficiency of C6-loaded PLGA NC and dye release after ultrasound treatment determined by fluorescence spectroscopy (mean \pm SD, n=3).

	PLGA C6 NC
Dye loading [%]	0.16 \pm 0.04
Entrapment efficiency [%]	79.34 \pm 22.26
Dye release after ultrasound treatment [%]	42.2 \pm 25.4

In the ultrasonic measurement set-up, both types of PLGA-based nanoparticles showed similar cavitation profiles (Figure 28A). Kinetic VSD profiles started at 1.2×10^{-6} V/ $\sqrt{\text{Hz}}$ and continually declined in broadband noise over time, when finally no cavitation activity was detected anymore (300 s). The AUC of VSD presented in Figure 28B did not show any significant difference in ultrasound signal between NS and NC. Despite the physicochemical difference between the two nanocarriers, obviously the type of nanocarrier did not affect the cavitation activity or the dye release after the ultrasound treatment (Table 10). The dye release of NS was with 48.6% comparable to NC with 42.2%.

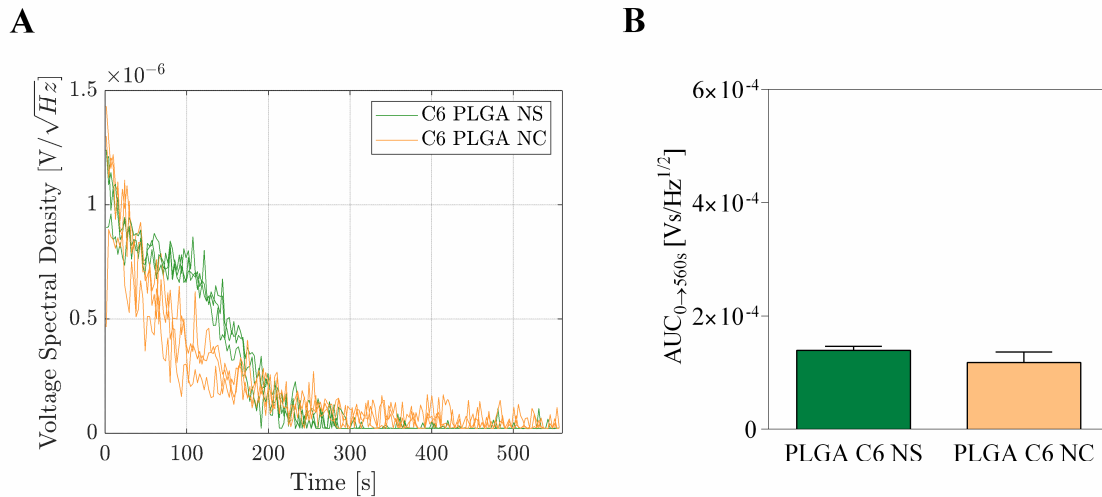


Figure 28 Effect of different types of PLGA nanocarriers on the ultrasound intensity at 750 kHz, 1.02 MPa (set-up 1) for 560 s. (A) Ultrasound response of C6-loaded PLGA NS and NC given as plot of VSD, versus time for three replicate individual sample. (B) AUC of VSD for two different nanocarriers (n=3).

To summarize, loading of hydrophobic dye was two times higher in NC than in NS, however dye release after ultrasound treatment did not change significantly when using different type of nanocarriers. A crucial feature of nanocarriers for a strong and long cavitation activity is the polymer material they are made of. It is important that the nanoparticle surface has hydrophobic characteristics to successfully stabilize nanobubbles on its surface.

5.3 Optimization of the Formulation of Nanocapsules for Ultrasound Model Drug Delivery

5.3.1 Effect of Stabilizer Concentration on Physicochemical Properties and Inertial Cavitation of Nanocapsules

Based on the previous results regarding physicochemical properties and cavitation, for the following experiments NC were selected. NC are normally prepared by an emulsion-diffusion evaporation method where the formulation of NC is governed by a fabrication of an emulsion of oil, polymer and ethyl acetate, dilution with pure water allowing ethyl acetate to diffuse out of the droplets, finally leaving a dispersion of NC [202]. The properties of NC can be varied by changing their composition and the formulation process. In the present study, three different polymer NC loaded with the hydrophobic dye C6 at 1:250 dye-to-polymer ratio were prepared using the Ultra Turrax[®] at a homogenization speed of 20,000 rpm. Different types of commercial PLGA polymers with or without PEG, but all with a 50:50 lactide:glycolide ratio were used. The shell of NC was made of PLGA 502 (Resomer[®] RG 502), PEG_{2k}-PLGA_{11.5k} (PEG average M_n 2,000 g/mol, PLGA average M_n 11,500 g/mol) or PEG_{5k}-PLGA_{7k} (PEG average M_n 5,000 g/mol, PLGA average M_n 7,000 g/mol). The concentration of the steric stabilizer PVA in the formulation was varied (1.5%, 2.0% and 2.5% m/V) in order to investigate its influence on the NC stability and cavitation activity. PVA is the gold standard for the production of PLGA particles due to its amphiphilic properties and high biocompatibility [272]. Lower molecular weight PVA could result in lower stabilization of nanoparticles, while higher molecular weight PVA could result in decreased aqueous solubility and increased viscosity of aqueous PVA solutions [273]. Therefore, PVA with middle molecular weight (31,000 g/mol) and partially hydrolyzed grade (88.7 mol%) was used in this study.

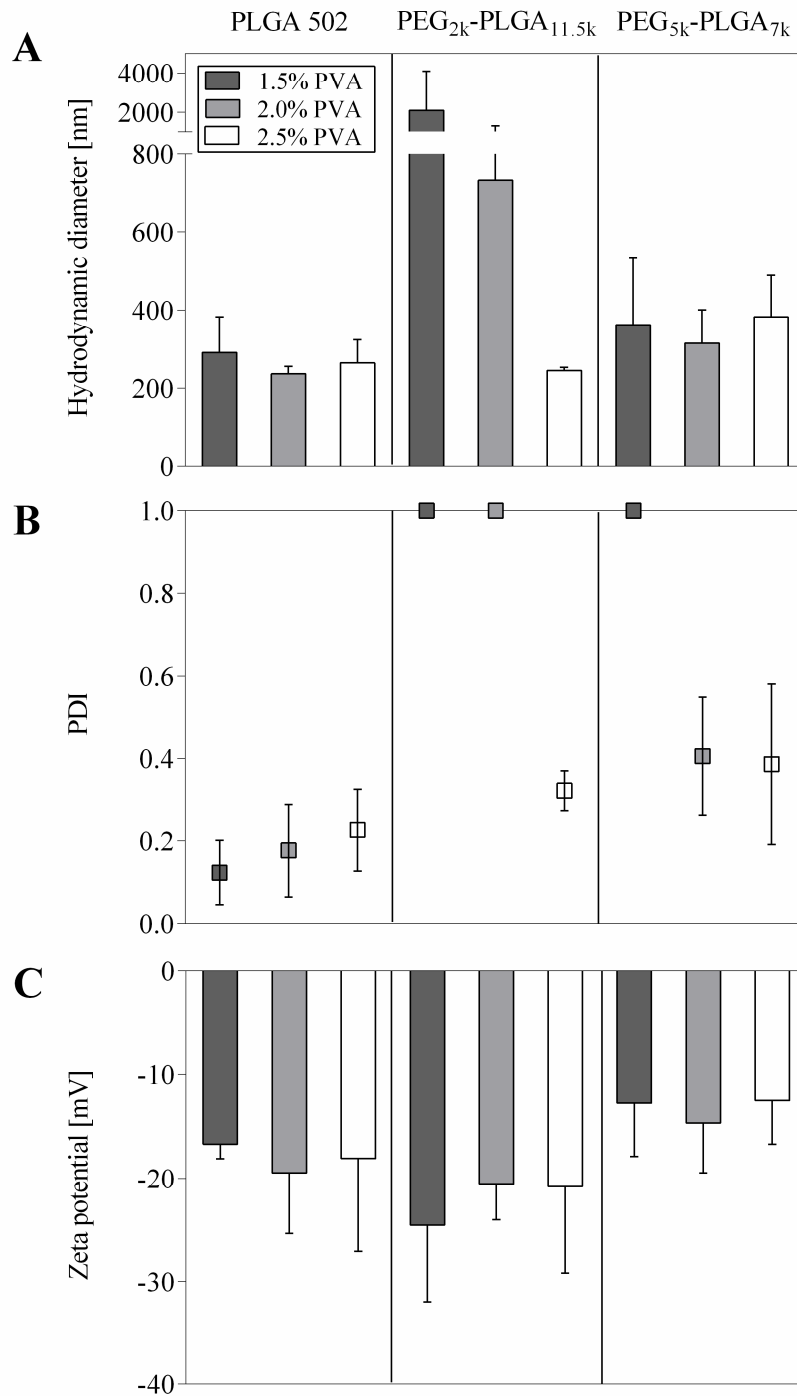


Figure 29 Hydrodynamic diameter (A), PDI (B) and zeta potential (C) of C6-loaded NC prepared with 2.5%, 2.0% or 1.5% PVA. Results are presented as mean \pm SD (n = 3).

The stabilizer forms a layer on the surface, which not only enables particle formation, protecting against coalescence and agglomeration, but also prevents the active or model substance from transferring from the inner to the outer W-phase [274]. The used stabilizer PVA, which is classified as a flexible polymer, is typically used to sterically stabilize PLGA nanoparticles [204, 205]. As shown in Figure 29A, PLGA 502 NC and PEG_{5k}-PLGA_{7k} NC were less

influenced by the PVA concentration than PEG_{2k}-PLGA_{11.5k} NC. PLGA 502 NC resulted in particle sizes of around 250 nm and PDI <0.3. Stability of nanoparticles depends on the affinity of stabilizer to polymer [275]. In comparison to PLGA NC, has surface of PEG-PLGA NC more hydrophilic characteristic, due to PEG group [262]. Görich [276] prepared polymer microparticles and explained the behavior of PVA adsorption on two polymers, which differ in hydrophilicity. The folding of the flexible polymer PVA on the surface of the more hydrophilic polymer is not as pronounced; the substance lies more "flat" on the surface. Thus, the stabilization is poorer, resulting in larger microparticles compared to those from the more lipophilic polymer. In this study, nanoparticles probably undergo similar behavior, since the hydrophobicity of PEG_{5k}-PLGA_{7k} NC was lower comparing to PLGA 502 NC resulting in lower stabilization and increased particle size.

The size was measured 362 nm, 315 nm and 382 nm for formulations with 1.5%, 2.0% and 2.5%, respectively. The hydrodynamic diameter of PEG_{2k}-PLGA_{11.5k} NC was found to increase with lower concentrations of PVA (Figure 29A) suggesting to an insufficient stabilization effect of PVA. The particle size was about 700 nm and 2000 nm for 2.0% and 1.5% PVA, respectively, and the PDI suggested for both formulations multimodal distribution (Figure 29B). By using 2.5% PVA, NC achieved an acceptable particle size around 250 nm with a PDI <0.3. A possible explanation is that a higher stabilizer concentration formed a closer layer, which prevent formulation of larger particles. PVA is a flexible polymer that has multiple attachment possibilities and adheres relatively closely to the surface at low concentrations. At higher concentrations, the PVA folds more strongly, the "trains" become shorter, and the "loops" become larger. Consequently, the stabilization is improved, and the resulting particles are smaller than those at lower PVA concentration [277]. When comparing two variants of PEG-PLGA polymers with distinct molecular weights of PEG, it was observed that PEG_{5k}-PLGA_{7k} NC demonstrated greater stability among the three tested PVA concentrations, whereas PEG_{2k}-PLGA_{11.5k} NC did not exhibit the same level of stability (Figure 29A). PEGylated PLGA has surface active properties similar to that of surfactant and thus can act as an additional stabilizer [278]. PEG_{5k}-PLGA_{7k} with a PEG chain of 5000 Da is probably long enough to preserve a better stabilization effect as PEG_{2k}-PLGA_{11k} with a PEG chain of 2000 Da at lower PVA concentrations. However, the particle size of more than 300 nm and the PDI over 0.4 made a PEG_{5k}-PLGA_{7k} not an appropriate candidate unless the production method is further optimized for future experiments.

Particles prepared from PLGA 502 were negatively charged with a zeta potential around -20 mV (Figure 29C). In the presence of different PVA concentrations, the charges of the nanoparticles did not change and remained negative. Similar results were published by Tham *et al.*, who stabilized PLA nanoparticles with PVA [279]. The zeta potential of PEGylated NC ranged independent of PVA concentration around -25 mV and -15 mV for PEG_{2k}-PLGA_{11.5k} NC and PEG_{5k}-PLGA_{7k} NC, respectively (Figure 29C). The higher the PEG molecular weight was, the less negative was the zeta potential. The increase of PEG molecular weight increases the PEG layer thickness [280], which results in a higher zeta value.

Table 11 Dye load (DL) and entrapment efficiency (EE) of C6 in PLGA 502 NC and PEG-PLGA NC prepared with three different PVA concentrations. Results are presented as mean \pm SD, $n \geq 3$.

	PLGA 502 NC		PEG _{2k} -PLGA _{11.5k} NC		PEG _{5k} -PLGA _{7k} NC	
	DL	EE	DL	EE	DL	EE
2.5% PVA	0.12 \pm 0.03	6.83 \pm 3.05	0.10 \pm 0.04	2.89 \pm 1.03	0.09 \pm 0.02	2.53 \pm 0.94
2.0% PVA	0.10 \pm 0.02	4.31 \pm 0.54	0.10 \pm 0.03	13.39 \pm 16.95	0.07 \pm 0.02	2.55 \pm 1.29
1.5% PVA	0.13 \pm 0.03	13.61 \pm 9.27	0.16 \pm 0.05	48.94 \pm 46.15	0.12 \pm 0.04	3.78 \pm 0.52

In Table 11 it is shown that dye loading and entrapment efficiency decreased with increasing surfactant concentration for all formulations. This effect is highly pronounced due to a constant dye-to-polymer ratio, which makes surfactant concentration the sole factor influencing characterization parameters. The highest dye load and entrapment efficiency values were observed for 1.5% PVA formulations: PLGA 502 NC with dye load of 0.13% and entrapment efficiency of 13.61%, PEG_{2k}-PLGA_{11.5k} NC with dye load of 0.16% and entrapment efficiency 48.94% and PEG_{5k}-PLGA_{7k} NC with dye load of 0.12% and entrapment efficiency of 3.78%. Entrapment efficiency of PEG_{2k}-PLGA_{11.5k} NC prepared with 1.5% PVA was the highest, while it might be related to its largest mean particle size (Figure 29A). During preparation and application of high-speed homogenization the surface area increases, which causes leakage of dye into the surrounding fluid leading to lower dye load and entrapment efficiency [281]. Table 11 indicates decrease in entrapment efficiency and dye load with decreasing PVA concentration.

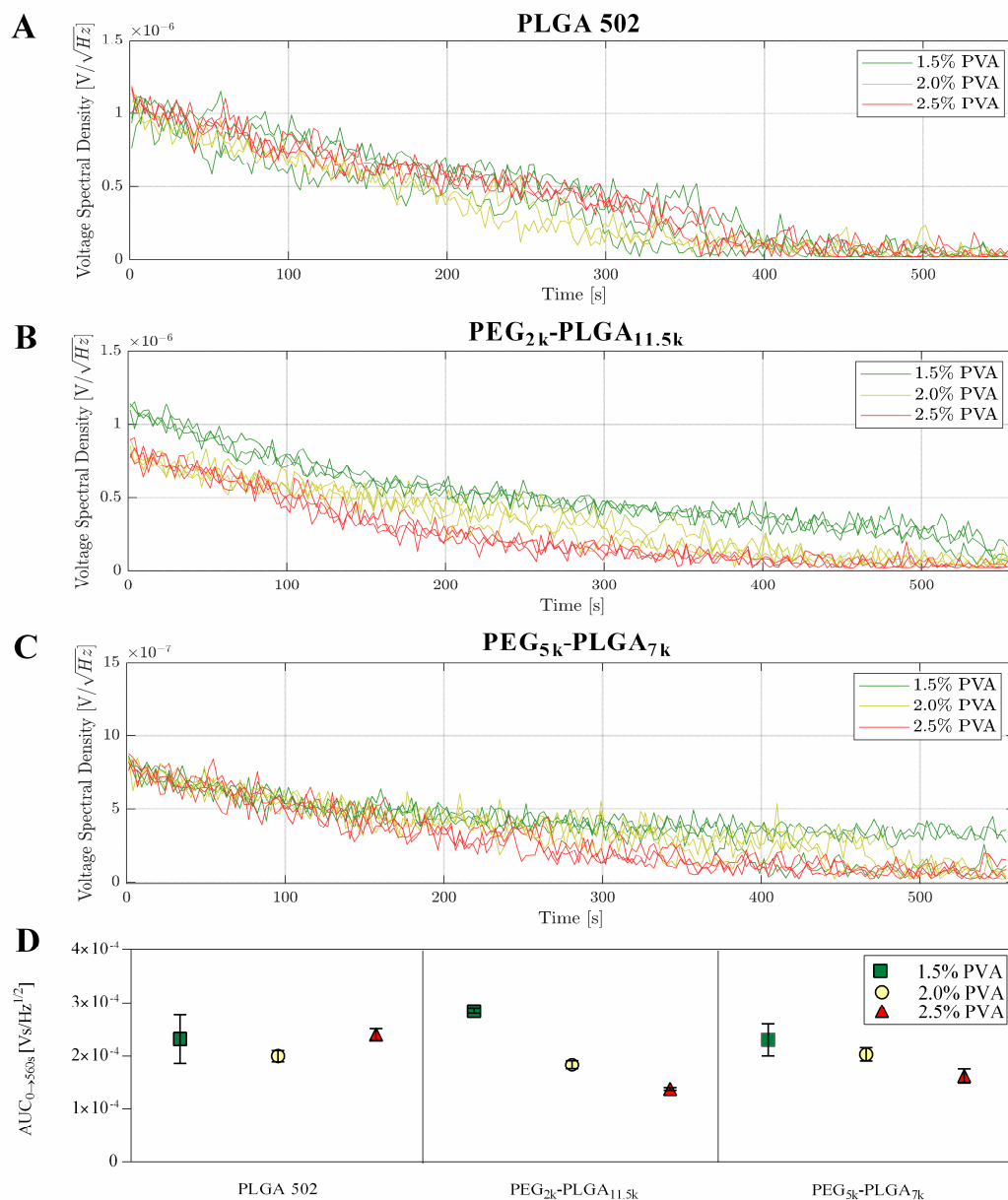


Figure 30 Diagrams comparing the inertial cavitation (VSD) of C6-loaded NC prepared with three different PVA concentrations made of (A) PLGA 502, (B) PEG_{2k}-PLGA_{11.5k} and (C) PEG_{5k}-PLGA_{7k}. (D) AUC of VSD representing the ultrasonic cavitation noise signal at 750 kHz and 1.02 kPa (set-up 1) for different PEGylated NC for the first 560 s. Results are presented as mean ± SD (n = 3).

Furthermore, it was important to find out to what extent the PVA concentration not only stabilizes the NC, but also influence the cavitation behavior of the NC. The results of cavitation activity are presented as the trend of the VSD over time in Figure 30A, B and C and as the AUC of VSD, which was calculated to generate a suitable comparison parameter in Figure 30D. Generally, strong ultrasound enhancement was achieved at lower PVA concentrations (1.5%), and a reduction in the generated intensity was observed with increasing PVA concentrations for PEGylated formulations, while for PLGA formulations the cavitation activity stayed constant.

The AUC of VSD for all formulations with 1.5% PVA was between $2.5 \times 10^{-4} \text{ V/Hz}^{1/2}$ and $3.0 \times 10^{-4} \text{ V/Hz}^{1/2}$. Both PEGylated formulations had a lower cavitation activity at higher PVA concentration (Figure 30B and C). PVA molecules on the surface of NC cause a more hydrophilic character. Higher PVA concentrations and therefore a more hydrophilic surface of NC prevented a formation of air-rich layers around NC and resulted in a low cavitation activity [239]. Another possible explanation for the different cavitation activity is the difference of NC sizes. As described in section 5.2.1 and presented by Kwan *et al.* the probability of inertial cavitation could be directly proportional to the likelihood of a suitable size cavity being presented in the ultrasound field [235]. Using 1.5% of PVA resulted in larger PEG_{2k}-PLGA_{11.5k} NC (Figure 29A), which demonstrated the strongest cavitation activity as smaller particles prepared with 2.0% and 2.5% PVA or other polymer.

All three PLGA NC without PEGylation had comparable cavitation profiles independent of the PVA concentration (Figure 30A). The acoustic cavitation was between $1.8 \times 10^{-4} \text{ V/Hz}^{1/2}$ and $2.5 \times 10^{-4} \text{ V/Hz}^{1/2}$. Due to absence of hydrophilic PEG chains, the overall hydrophobicity of the NC surface was probably higher [282] resulting in a better stabilization of air nanobubbles on the NC surface [239] and higher cavitation activity. The PVA concentration had a stronger effect on PEGylated NC as on non-PEGylated NC.

Based on the DLS and ultrasound results, 2.5% of PVA concentration was found to be optimal to obtain NC with high echogenicity and good dispersibility and, thus, used in the rest of the studies.

5.3.2 Influence of Homogenization and Polymer Type on Nanocapsule Cavitation

For future optimization of the formulation of sonosensitive NC was to adapt the (i) homogenization speed and (ii) the PLGA molar mass and terminal end group in order to improve entrapment efficiency and dye load. Different types of commercial PLGA polymers (Resomer[®] RG 502, Resomer[®] RG 503, Resomer[®] RG 504, Resomer[®] RG 505, Resomer[®] RG 502H) with varying molar masses (7,000-69,000 g/mol) with and without terminal ester groups were used to evaluate the influence of these parameters on particle properties and to select suitable polymers for the ultrasound treatment. In addition, the effect of homogenization speed on particle physicochemical characteristics and ultrasound sensitivity was investigated selecting three different homogenization speeds 11,000 rpm, 12,600 rpm and 15,000 rpm. In the emulsion-diffusion process the 2.5% (m/V) PVA and 1:250 C6-to-polymer ratio were kept constant based on the results reported before.

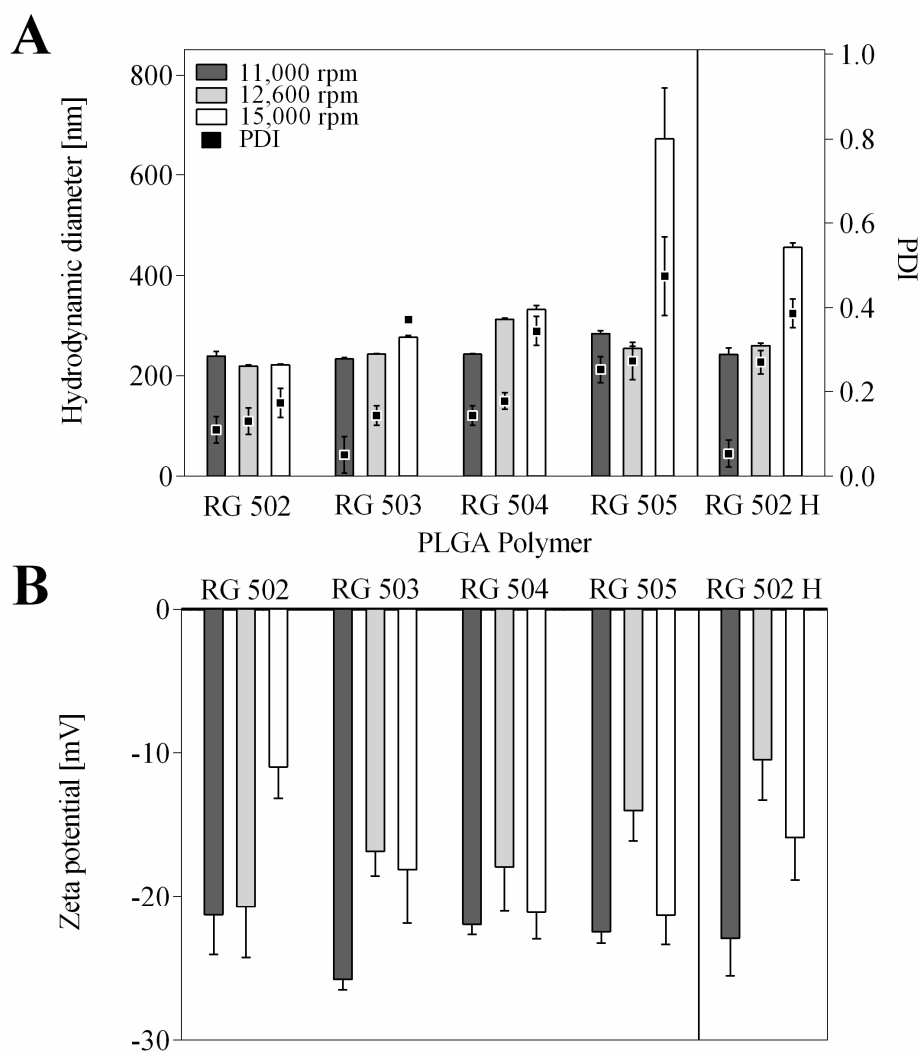


Figure 31 Hydrodynamic diameter (A), PDI (A) and zeta potential (B) of C6-loaded NC prepared with five different PLGA polymers at different homogenization speeds. Results are presented as mean \pm SD, $n = 3$.

When prepared at 11,000 rpm, NC made of PLGA 502 measured 238 nm in contrast to PLGA 505 with particles of 285 nm (Figure 31A). The hydrodynamic diameter was found to be directly correlated with the molar mass of the polymers. The higher the molar mass of the PLGA polymers from PLGA 502 to PLGA 505, the larger were the sizes. Different authors [205, 283] showed a similar effect that was explained by the increased viscosity of the organic solution due to the increased molar mass of the polymer, which prevented emulsification into smaller droplets. PDIs followed a similar pattern as particle sizes and increased from 0.1 to 0.25 by increasing molar mass of PLGA independent on homogenization speed (Figure 31A). TEM pictures (Figure 32) revealed the presence of spherical hollow NC and particle sizes comparable to the DLS values (Figure 31A).

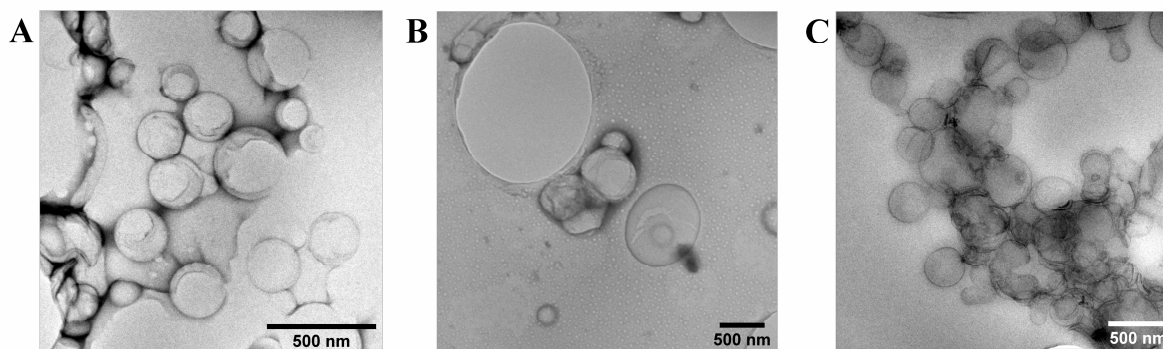


Figure 32 TEM of PLGA NC made of (A) PLGA 502, (B) PLGA 505 and (C) PLGA 502H at 11,000 rpm.

The two major forces responsible for particle size reduction in rotor-stator systems are the mechanical impingement against the wall due to high fluid acceleration, and the shear stress generated in the gap between rotor and stator, due to the rapid rotation of the rotor. The particle size can be altered by controlling the emulsification power [284]. By increasing homogenization speed the hydrodynamic diameter increased for polymers of higher molar mass (Figure 31A). When prepared at 15,000 rpm, NC of PLGA RG 504 formed aggregates with large particle sizes (333 nm) and PDI >0.3 while PLGA RG 505 formed particles larger than 600 nm with PDI >0.4. At high homogenization speeds, the emulsion droplets could increase in size due to supply of more energy resulting in a high rate of re-coalescence of new droplets. This phenomenon is named “over-processing” of the system and has been noted by several authors during high-pressure emulsification [284-286]. They observed that although the increased energy input during emulsification, the emulsions have larger droplet sizes rather than expected smaller sizes. High molar mass PLGA is in this case even more affected due to increased viscosity of the organic solution. With increasing viscosity of the dispersed phase, droplet disruption was more difficult and hence, emulsion droplets increased size [284]. The acid terminated polymer (PLGA 502H) influenced the NC size, but only at the highest homogenization rate. In comparison to PLGA 502 NC, at 11,000 rpm and 12,600 rpm comparable hydrodynamic ratios were observed, only at 15,000 rpm about two times larger NC sizes were reached. This could be due to high energy input in homogenization, which could cause hot spots that aggregate nanoparticles.

The values of zeta potential for NC produced at 11,000 rpm were found to be between -30 mV and -22 mV indicating negative surface charges (Figure 31B). With increasing homogenization speed the zeta potential increased up to -10 mV. Reduced emulsifying efficacy at higher homogenization speeds could be consistent with the marked increase in zeta potential evidenced at 15,000 rpm. Less negative zeta potential may also be related to smaller total surface area

(higher droplet size). A less net negative surface charge would reduce the electrostatic repulsion, thus promoting droplet coalescence [287].

During the formulation process 2.5% PVA (M_n 31,000 g/mol) was used as stabilizer. Although NC preparation included purification steps, a fraction of PVA could remain associated with the nanoparticle. This appeared because PVA is supposed to form an interconnected network with the carbonyl group of PLGA on the particle surface [288]. The residual PVA could influence different physicochemical properties of nanoparticles such as particle size, zeta potential, drug loading and surface hydrophobicity [204]. As a result of higher surface hydrophilicity, a reduction in cellular uptake has to be considered [204].

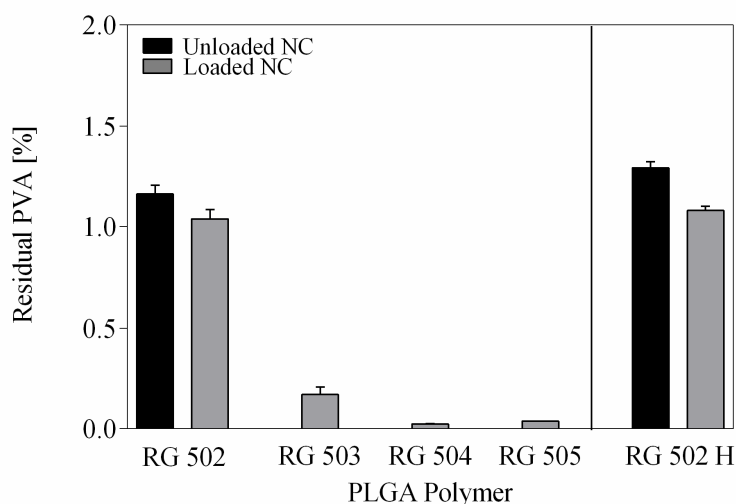


Figure 33 Bar charts comparing the residual amounts of PVA of blank and C6-loaded NC samples prepared at 11,000 rpm. Results are presented as mean \pm SD, $n = 3$.

In the present study, quantitative determination of the residual PVA content *via* UV/VIS spectroscopy was performed by a colorimetric method based on complex formation between residual PVA and I_2/KI solution [204]. As shown in Figure 33, an influence of the molar mass of the polymer could be observed. NC of higher molar mass polymers (PLGA 503, PLGA 504 and PLGA 505) exhibited lower amounts of PVA (<0.2%) than PLGA 502 and PLGA 502H (<2%). This was also reported by Grune *et al.* showing a lower residual PVA content by nanoparticles made of PLGA polymers with higher molar mass [205]. Despite the acid end group and therefore a higher hydrophilicity of the nanoparticle surface, the amount of residual PVA was around 1% comparable to values of PLGA 502. Study from Grune *et al.* [205] also presented comparable values for PLGA 502 and PLGA 502H nanoparticles at about 1.5%. In addition, unloaded NC showed 0.2% higher amount of PVA adsorbed on their surfaces as

loaded NC indicating that dye loading could have an effect on the amount of PVA associated within the NC. Hydrophobic dye could decrease hydrophilicity of the NC surface resulting in lower amount of residual PVA. All PVA values were in a range <4% which was expected by Sahoo *et al.* [204] to have no influence on the biological characteristics. Compared to other studies, the residual content of PVA in this work can be classified as low. Shkodra *et al.* demonstrated for partially hydrolyzed PVA with the molecular weight of 31,000-205,000 g/mol an increased residual amount ranging from 9.3% to 13.3%, which could be reduced by additional washing steps [289]. A similar decrease in residual PVA was also shown by Zambaux *et al.* with a PVA concentration of 5%. While they quantified a residual content of 24% after the first washing step, the PVA amount decreased to 12% after the third washing process [290]. Furthermore, they demonstrated that reducing the PVA concentration to 2% also decreased the PVA residual content to approximately 6% [290].

Table 12 Dye loading (DL) and entrapment efficiency (EE) of C6 in NC prepared with five different PLGA polymers (PLGA 502, PLGA 503, PLGA 504, PLGA 505 and PLGA 502H) at 11,000 rpm, 12,600 rpm and 15,000 rpm. Results are presented as mean \pm SD, n = 3.

Polymer	11,000 rpm		12,600 rpm		15,000 rpm	
	DL	EE	DL	EE	DL	EE
PLGA 502	0.163 \pm 0.023	51.22 \pm 14.63	0.155 \pm 0.033	1.93 \pm 0.39	0.115 \pm 0.007	2.37 \pm 0.14
PLGA 503	0.120 \pm 0.009	20.62 \pm 1.37	0.154 \pm 0.005	33.0 \pm 1.07	0.057 \pm 0.011	3.97 \pm 0.40
PLGA 504	0.086 \pm 0.007	10.48 \pm 0.67	0.089 \pm 0.006	2.89 \pm 0.17	0.032 \pm 0.017	2.75 \pm 1.61
PLGA 505	0.093 \pm 0.009	7.21 \pm 0.72	0.101 \pm 0.045	3.12 \pm 1.54	0.050 \pm 0.004	1.66 \pm 0.11
PLGA 502H	0.142 \pm 0.014	38.72 \pm 7.38	0.148 \pm 0.006	2.86 \pm 0.132	0.116 \pm 0.023	0.81 \pm 0.05

Table 12 indicates changes of the dye load and entrapment efficiency of NC by varying homogenization speed and polymer type. At 11,000 rpm and 12,600 rpm homogenization speed, dye load and entrapment efficiency were comparable while at 15,000 rpm dye load and entrapment efficiency were reduced. A higher homogenization rate increased the surface area which may cause dye diffusion into the surrounding fluid leading to lower entrapment efficiency values [281, 291]. NC prepared with polymers of lower molar mass (PLGA 502 and PLGA 502H) resulted in higher and almost comparable dye load and entrapment efficiency values compared to polymers of higher molar masses. The dye load and entrapment efficiency increased from 0.09% to 0.16% and 7.21% to 51.22%, respectively, as molar mass decreased from 54,000-69,000 g/mol (PLGA 505) to 7,000-17,000 g/mol (PLGA 502). According to Mittal *et al.* [283] the increased viscosity with increasing molecular mass might decrease the diffusion rate of solvent into the external W-phase. Therefore, solvent removal is slowed down

and it takes more time for dye to enter the W-phase, resulting in low entrapment efficiency. Acid-terminated PLGA 502H showed about 10% lower entrapment efficiency than the same molecular weight PLGA with the ester terminus. This observation can likely be attributed to the higher hydrophilicity of PLGA 502H and thus, the lower affinity to hydrophobic dye [292].

The best performing particles in terms of particle size, zeta potential and dye load were formulated with 11,000 rpm. Hence, this setting was used for further investigations.

Table 13 T_m and T_g of PLGA from pure polymer, physical mixture of C6 and polymer, and C6-loaded NC, determined by DSC in two heating-cooling cycles at 10 °C/min; T_m was calculated from the first run and T_g from second run.

	Sample	T_m [°C]	T_g [°C]
Polymer	PLGA 502	45.15	33.43
	PLGA 503	47.74	38.85
	PLGA 504	47.28	39.17
	PLGA 505	49.01	40.22
	PLGA 502H	46.53	31.28
Physical mixture	PLGA 502	46.02	37.41
	PLGA 503	53.30	43.20
	PLGA 504	52.94	44.49
	PLGA 505	53.00	43.61
	PLGA 502H	51.08	38.71
C6-loaded NC	PLGA 502	46.02	36.42
	PLGA 503	49.88	35.01
	PLGA 504	49.88	37.53
	PLGA 505	50.55	37.64
	PLGA 502H	47.01	31.72

A DSC analysis was carried out to investigate the solid state characteristics of the NC. The aim was to characterize the thermal profile of the NC, and the interaction between the C6 and the polymer. Each sample was measured in two heating and cooling cycles (from 5 °C to 220 °C), with the first cycle used to determine T_m and the second cycle to determine T_g . Table 13 summarizes the T_m and T_g values. Figure 34 shows the thermograms of the first and second runs of the active ingredient C6 and the C6-loaded NC prepared from different PLGA polymers. Free C6 showed a sharp endothermic melting peak at 211 °C in the first run, comparable to observations at Trapani *et al.* [293]. This peak was absent in almost all NC formulations probably due to low encapsulation rates of C6, thus an influence of the dye could not be observed. In PLGA 504 formulation, an exothermic peak was observed, indicating a possible

crystallization or oxidation event of the dye [294]. This peak disappeared in the second run. The pure polymers showed a sharp endothermic melting peak between 45.15 °C and 49.01 °C, which could also be observed for the polymer NC (46.02-50.55 °C) indicating that polymer as well as NC are in crystalline state [205] and that encapsulated Miglyol 812 did not change the thermic properties of NC. In the second run T_g was measured. PLGA polymers with a 50:50 lactide to glycolide monomer ratio typically have T_g of >42 °C, which increases with higher molecular weight [295]. In this study, the values were lower. Polymers showed T_g values between 31.28 °C and 40.22 °C, while their physical mixtures with C6 showed a higher values (37.41-44.49 °C). C6-loaded NC showed similar T_g as polymers with an observed molar mass dependency (31.72-37.64 °C). T_g is influenced by the amount of free polymer chain ends in PLGA. The local mobility of low molar mass polymer is hindered due to higher concentration of chain ends leading to lower T_g . With increasing molar masses, the end groups have higher mobility due to their local excess free volume, which results in higher T_g [296]. The encapsulation of C6 demonstrated plasticization of the NC, which reduced the T_g by 1-6 °C compared to the physical mixture. This could be attributed to the formation of hydrogen bonds between amine groups of C6 and the carbonyl groups of PLGA. The reduction in T_g was also correlated with entrapment efficiency of the C6 (Table 12). The higher the entrapment efficiency, the greater was the reduction. The only exception was PLGA 502, where a reduction in T_g was only 1 °C despite high entrapment efficiency. A similar reduction in the T_g by approximately 8 °C was reported for diflupolol [297] and 13 °C for flurbiprofen [298] and thymoquinone [299] after encapsulation in PLGA nanoparticles.

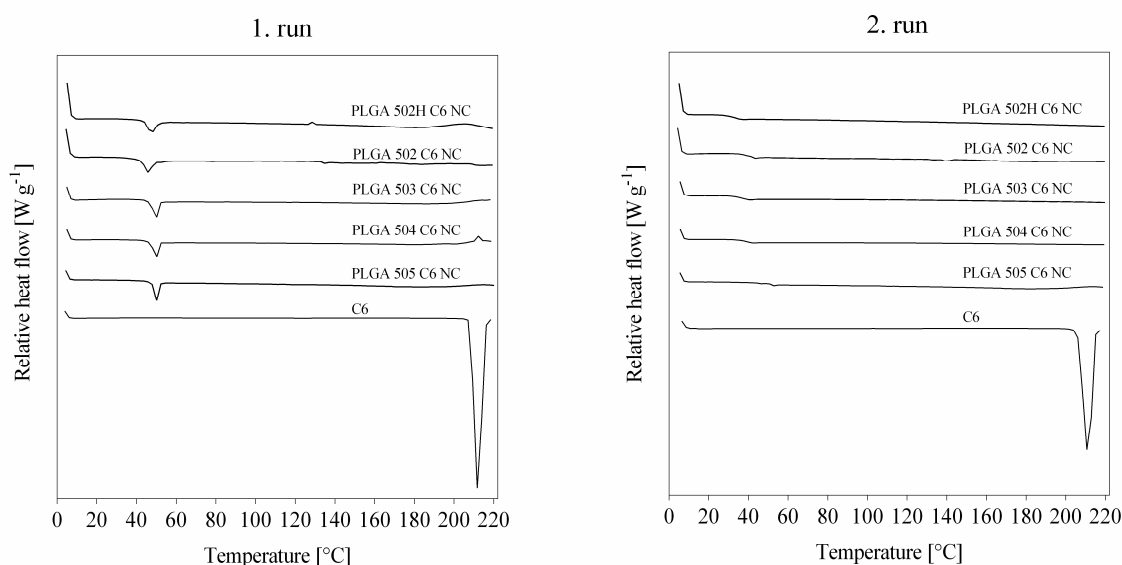


Figure 34 DSC graphs comparing the thermal behavior of C6 and C6-loaded NC. Analysis was performed in two heating-cooling cycles at 10 °C/min.

Upon freeze-drying, rehydration and ultrasound exposure, all loaded polymer NC were capable of seeding cavitation. The profiles of acoustic cavitation are shown in Figure 35A, B, and C.

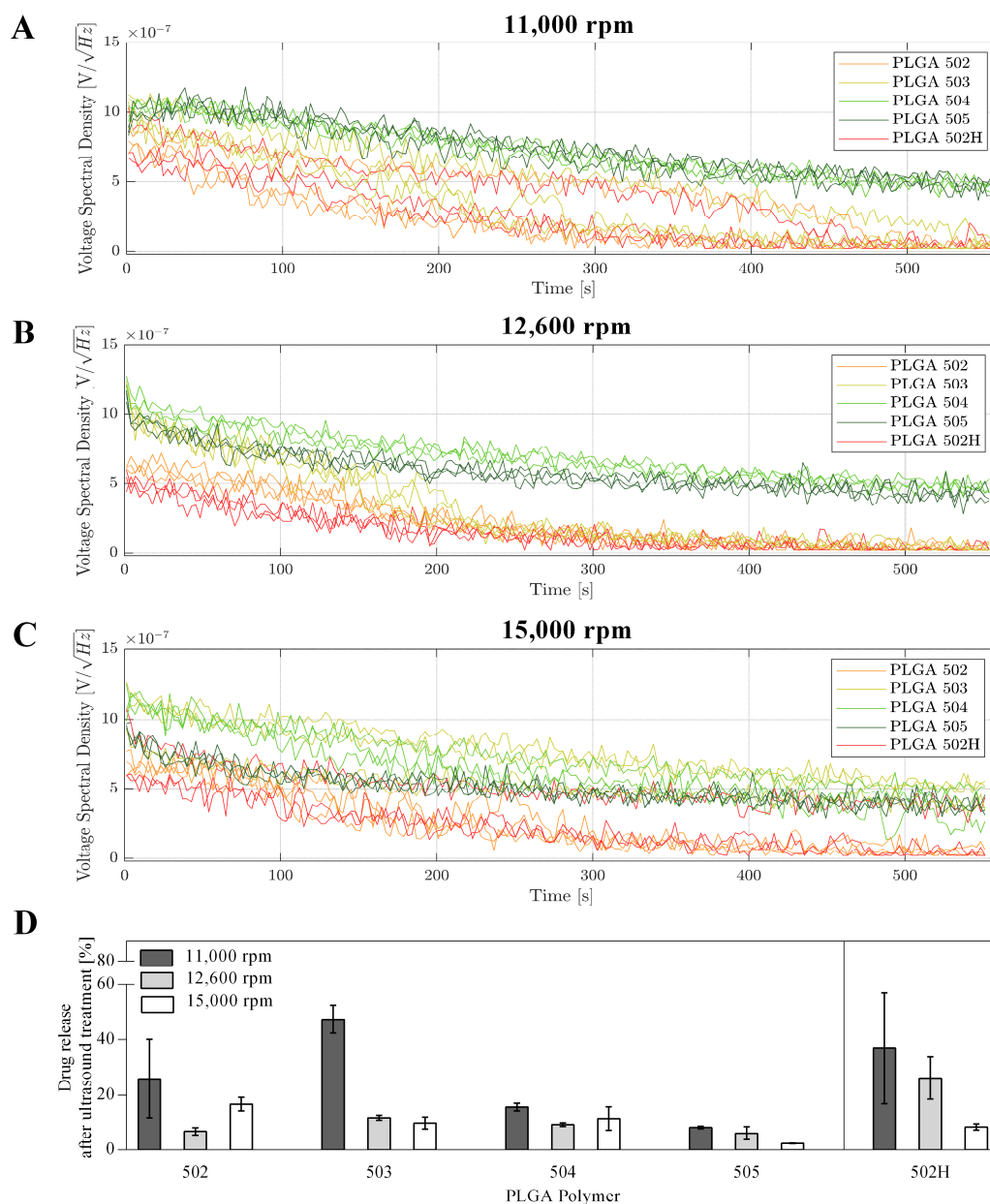


Figure 35 Diagrams comparing the inertial cavitation (VSD) of C6-loaded NC prepared with five different PLGA polymers at (A) 11,000 rpm, (B) 12,600 rpm and (C) 15,000 rpm at 750 kHz and 1.02 kPa (set-up 1) for three individual measurements. (D) Release of C6 after ultrasound treatment is presented as mean \pm SD, n = 3.

The higher the polymer mass, the higher was the cavitation activity, independent of the preparation conditions. NC made of PLGA 504 and PLGA 505 were active for the whole time of treatment with decreased kinetic profiles from $10 \times 10^{-7} V/\sqrt{Hz}$ to $5 \times 10^{-7} V/\sqrt{Hz}$. The cavitation of lower molar mass polymers (PLGA 502 and PLGA 502H) started at $5 \times 10^{-7} V/\sqrt{Hz}$ and reached the minimum after 300 s. A possible explanation might be

a stronger hydrophilic characteristic of PLGA 502 comparing to polymers with higher molecular mass resulting in a weaker cavitation activity. Additionally, hydrophilic PVA on NC surface can induce a reduction in ultrasound activity [204]. The effect of higher PVA concentration on the cavitation activity was already discussed in section 5.3.1. Different homogenization rates did not show relevant differences in cavitation activity of NC. However, the release of C6 from NC induced by ultrasound inertial cavitation was lower in formulations prepared with a polymer of higher molar mass (Figure 35D). PLGA with higher molar mass possesses higher hydrophobicity, resulting in an increased affinity of C6 towards lipophilic polymer compared to the surrounding aqueous medium. Comparing different homogenization rates, NC prepared at 11,000 rpm exhibited in highest dye release up to 47%, while particles prepared at 15,000 rpm with a maximum of 16%. NC prepared at lower homogenization rate were characterized with smaller particle sizes (Figure 33A) and consequently in larger surface area, which give NC a better opportunity to be imploded in smaller parts during ultrasound explosion and accomplish a higher dye release.

5.3.3 Impact of PEGylation on Ultrasound Cavitation of Nanocapsules

The goal of PEGylation is to prevent opsonisation of NC in order to achieve a longer blood circulation [300] after systemic application. In the present study, it was aimed to evaluate the ability of the PEG chains at NC surface to effect the NC cavitation capability. Various blends of PLGA 502 with PEG_{2k}-PLGA_{11.5k} or PEG_{5k}-PLGA_{7k} were prepared leading to final PEGylation degrees between 0% and 38% (w/w) presented in Table 3 (see section 4.1.1.3). An O-phase with 2% (w/w) total polymer content and C6 (1:250 dye-to-polymer ratio) was homogenized with W-phase (2.5% (m/V) PVA) using the standard emulsion-diffusion evaporation method.

According to Figure 36A and B it could be found that increasing the degree of PEG induced an increase of the hydrodynamic diameter of the obtained NC. This effect was stronger presented in NC made of PEG_{5k}-PLGA_{7k} (Figure 36B). NC prepared with 38% PEG led to a mean hydrodynamic diameter of more than 1000 nm compared to the preparation of NC by using only PLGA 502 (non-PEGylated), which led to a particle diameter of 255 nm. Similar findings were reported by Dirauf *et al.*, who could not form separable solid nanoparticles, but rather self-assembled structures, when high PEG to PLGA ratios were used [301]. PEG-PLGAs are copolymers with amphiphilic properties, enabling the formation of diverse drug delivery systems depending on several factors such as the PEG and PLGA chain length and the PEG degree [302]. The findings in the literature indicate a preference for micelle formation when the

PEG fraction is between 25% and 45% [302]. Figure 36B shows a PDI >0.2 for NC with PEG content above 20%, which suggested a polydisperse size distribution of the resulting NC. NC prepared of PEG_{2k}-PLGA_{11.5k} did not show an increase in particle size with an increased degree of PEG, most probably, due to low degree of PEGylation.

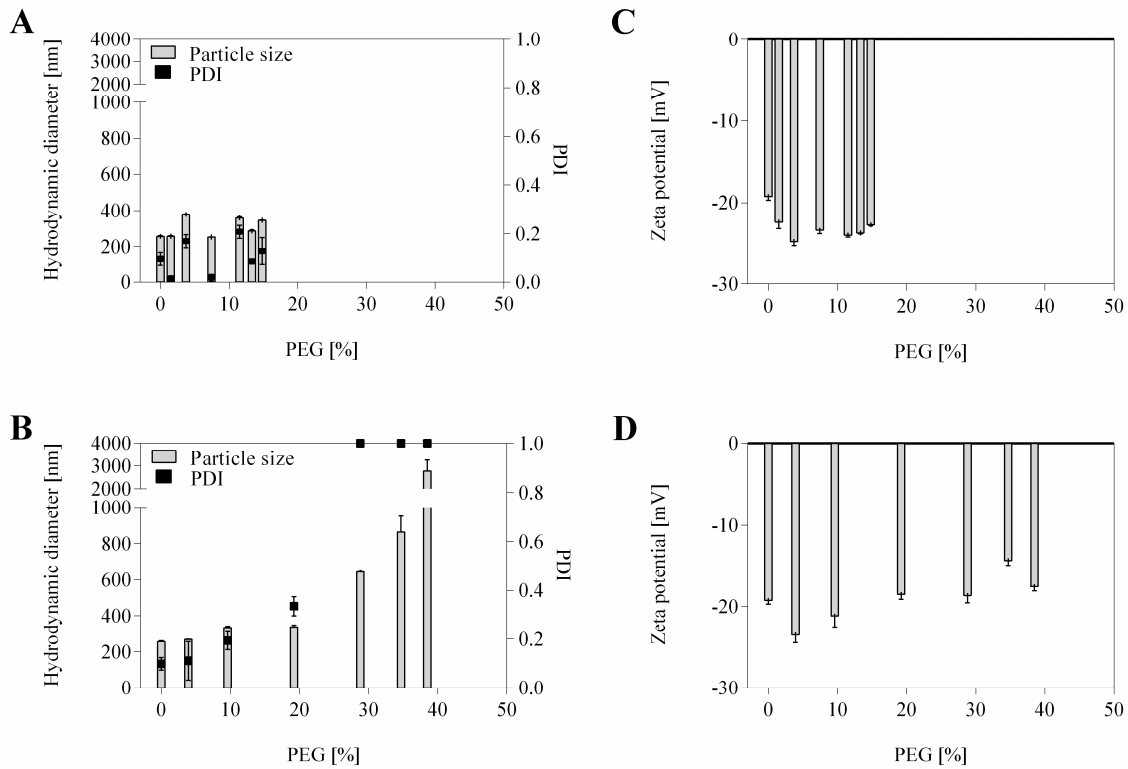


Figure 36 Hydrodynamic diameter (A, B), PDI (A, B) and zeta potential (C, D) of C6-loaded NC prepared with PLGA 502 and PEG_{2k}-PLGA_{11.5k} (A, C) or PEG_{5k}-PLGA_{7k} (B, D) at different percentage of PEG. Results are presented as mean ± SD from two independent batches.

In the present study, percentage of PEG in PEG_{2k}-PLGA_{11.5k} was probably not high enough to have an effect on zeta potential and the zeta potential stayed below -20 mV. With increasing PEG fraction in PEG_{5k}-PLGA_{7k}/PLGA 502 blends, the zeta potential of NC stayed between -22 mV and -15 mV (Figure 36D). A minor increase in zeta potential could be explained by the shielding effect of PEG, which masks the surface charges of uncapped PLGA residues.

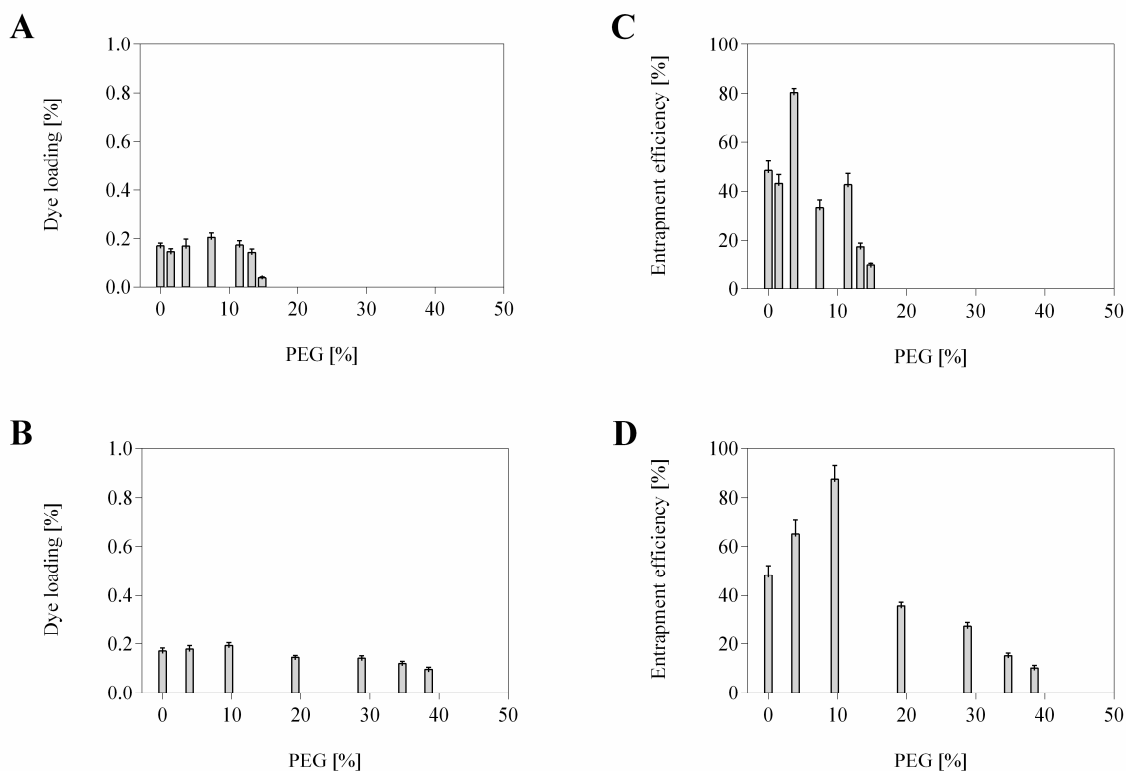


Figure 37 Dye loading (A, B) and entrapment efficiency (C, D) of C6 in PEGylated NC prepared with PLGA 502 and PEG_{2k}-PLGA_{11.5k} (A, C) or PEG_{5k}-PLGA_{7k} (B, D). Results are presented as mean \pm SD from two independent batches.

Figure 37 shows that dye load and entrapment efficiency increased when a certain percentage of PEG was added to the polymeric blend of PEG_{2k}-PLGA_{11.5k}/PLGA 502 and PEG_{5k}-PLGA_{7k}/PLGA 502. In fact, for a fraction between 5% and 10% PEG the maximum of dye load was obtained, corresponding to 0.20% and 0.19% for PEG_{2k}-PLGA_{11.5k}/PLGA 502 and PEG_{5k}-PLGA_{7k}/PLGA 502, respectively. The maximum of entrapment efficiency was observed at 3.7% PEG for PEG_{2k}-PLGA_{11.5k}/PLGA 502 (80%) and at 9.6% PEG for PEG_{5k}-PLGA_{7k}/PLGA 502 (86%). For the formulations with an increased percentage of PEG, independent of the polymer, the dye load and entrapment efficiency considerably decreased probably due to a higher percentage of the hydrophilic PEG polymer and formation of micelles, which could alter the process of encapsulation of lipophilic dye [302]. NC prepared with PEG_{5k}-PLGA_{7k}/PLGA 502 could encapsulate higher amounts of dye compared to PEG_{2k}-PLGA_{11.5k}/PLGA 502 at higher PEG degrees. This is most likely, due to larger particles (Figure 36B), which was already noticed in other publications [303, 304].

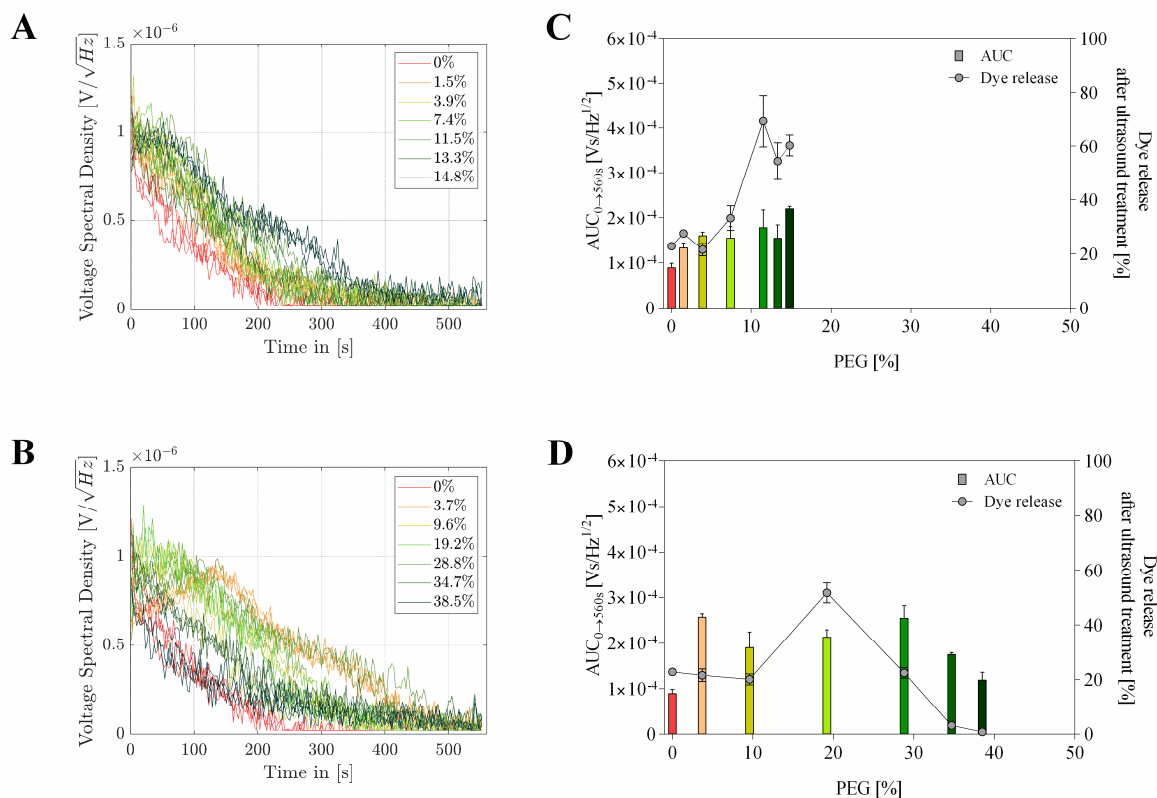


Figure 38 (A, B) Diagrams comparing the inertial cavitation (VSD) of C6-loaded PEG-PLGA NC prepared with different % of PEG_{2k}-PLGA_{11.5k} (A) or PEG_{5k}-PLGA_{7k} (B). Three individual measurements were made at 750 kHz and 1.02 kPa (set-up 1). (C, D) AUC of VSD representing the ultrasonic cavitation noise signal for the first 560 s and release of C6 after ultrasound treatment for NC prepared with PEG_{2k}-PLGA_{11.5k} (C) or PEG_{5k}-PLGA_{7k} (D). Results of dye release are presented as mean ± SD, from two independent batches.

Additionally, all formulations were examined in the ultrasonic field and, subsequent dye release was fluorimetrically quantified (Figure 38). The NC of pure PLGA 502 showed a decreased cavitation kinetic with a starting cavitation at $1.0 \times 10^{-6} \text{ V}/\sqrt{\text{Hz}}$ (Figure 38A and B) and $\text{AUC} = 0.9 \times 10^{-4} \text{ V}/\text{Hz}^{1/2}$ (Figure 38C and D). With increasing PEG the maximum cavitation response was achieved with 14.8% and 28.8% PEG for PEG_{2k}-PLGA_{11.5k}/PLGA 502 ($\text{AUC} = 2.2 \times 10^{-4} \text{ V}/\text{Hz}^{1/2}$, Figure 38 C) and PEG_{5k}-PLGA_{7k}/PLGA 502 ($\text{AUC} = 2.6 \times 10^{-4} \text{ V}/\text{Hz}^{1/2}$, Figure 38 D), respectively. Cavitation activity decreased when higher PEG concentrations were used in PEG_{5k}-PLGA_{7k}/PLGA 502 blends and reach with 40% PEG similar values as pure PLGA 502 ($\text{AUC} = 1.2 \times 10^{-4} \text{ V}/\text{Hz}^{1/2}$). This suggested that higher amount of PEG chains on PLGA NC increased the surface hydrophilicity [305] and provided reduction in cavitation activity of NC. Previous studies found that a more hydrophobic surface of nanoparticles is required to prepare air stabilizing nanoparticles with high acoustic activity [306-308]. In case of PEG_{2k}-PLGA_{11.5k}/PLGA 502, no decrease in acoustic cavitation was shown, most likely due to lower amounts of PEG (<15%).

Dye release after ultrasound exposure followed the cavitation pattern (Figure 38C and D). At lower PEGylation degrees, cavitation activity as well as dye release were lower. When formulation consisted up to 11.3% and 19.2% of PEG, the dye release was the highest for PEG_{2k}-PLGA_{11.5k}/PLGA 502 (69%) and PEG_{5k}-PLGA_{7k}/PLGA 502 (52%), respectively. At higher PEG concentrations, the dye release decreased, reaching no dye release after using PEGylation degree of more than 30%. Although larger nanoparticles enhance cavitation activity, as shown before, the observed decline in acoustic activity and subsequent reduction in dye release can likely be attributed to hydrophobic nature of PEG_{5k}-PLGA_{7k}/PLGA 502 NC, leading to less stable nanobubbles on their surface. However, for PEG_{2k}-PLGA_{11.5k}/PLGA 502 the highest available PEG concentration was 14.8% and further comparison was not possible.

The obtained results clearly showed that there is a necessity to adapt the PEG degree in preparation of PEG-PLGA NC in order to achieve comparable particle size, dye encapsulation and cavitation activity as for NC made of pure PLGA. As for the future development of PEGylated NC, the optimal degree of PEG should be around 10% when using PEG_{2k}-PLGA_{11.5k}/PLGA 502 blends to get NC with monomodal particle size distribution, negative zeta potential, high dye load and high acoustic activity as well as high dye release after ultrasound treatment. In case of PEG_{5k}-PLGA_{7k}/PLGA 502 blends, the most optimal degree of PEG should be below 5%.

5.4 Stability of Nanocapsules

5.4.1 Storage Stability of Lyophilized Nanocapsule Formulations

PLGA 502 (Resomer[®] RG 502) NC and PEG_{2k}-PLGA_{11.5k} NC with (1:250 C6-to-polymer ratio) or without C6-loading were selected for a storage stability test at 2-8 °C (refrigerator), 25 °C (room temperature) and 40 °C (accelerated temperature) for up to 6 months. All formulations were prepared by emulsion-diffusion method with homogenization speed of 11,000 rpm (8 min) including an O-phase of 2% (w/w) selected polymer and 5% (w/w) Miglyol[®] 812, and W-phase of 2.5% (w/V) PVA followed by freeze-drying in 15% (m/V) aqueous trehalose solution before storage under controlled conditions. After reconstitution, samples were analyzed for particle size, zeta potential and cavitation activity. Solid-state characterization of lyophilizates included Karl-Fischer titration, DSC and XRD measurements. Freeze-dried samples were closed in vials with stopper as well as sealed with aluminum peel-off seals and stored at three different temperatures for 6 months. The lyophilizates were dissolved by adding 3 mL ultrapure water. During reconstitution, the vials were gently swirled to ensure wetting of the complete lyophilizate. All lyophilizates instantaneously (<5 s) dissolved upon reconstitution. Trenkenschuh *et al.* shown that higher concentrations of cryoprotectant reduce the reconstitution time of lyophilized nanoparticles [309]. In their case, the presence of 10% of cryoprotectant (<6 s) reduced reconstitution time compared to 2.5% cryoprotectant (>50 s). A comparison of different excipients showed in other studies that trehalose is preferable with respect to other cryoprotectants to obtain a redispersible lyophilized nanoparticle product [310-312]. This was usually related to characteristics of trehalose, which are low hygroscopicity, the absence of internal hydrogen bonds thus allowing a more flexible formation of hydrogen bonds with nanoparticles, a very low chemical reactivity and, a higher T_g [313]. For these reasons, trehalose was chosen as a cryoprotectant in this study.

The initial particle size of loaded and blank PLGA 502 NC was 280 nm and 330 nm, respectively, with a PDI below 0.2 for both formulations (Figure 39A). PLGA NC revealed significant ($p \leq 0.05$) increase in particle size and higher PDI when the C6 was incorporated. The hydrophobic dye could be encapsulated in NC made of hydrophobic polymer and oily core with a high dye load resulting in size increase. After storage under different conditions none of the PLGA NC lyophilizates showed changes of particle size or PDI after 6 months of storage independent of the presence of C6 (Figure 39A), which suggested that stabilization was provided without signs of aggregation over time. PEGylated NC showed initial sizes of 305 nm and 280 nm for loaded and unloaded NC, respectively (Figure 39B). PLGA 502 NC showed

a modern increase in particle size, when C6 was loaded. However, the particle size of loaded PEG-PLGA NC did not show a distinct trend in increased particle size. The PDI of blank PEG-PLGA was initially 0.2 and increased up to 0.3 after 12 months of storage, while PDI of loaded PEG-PLGA NC increased from 0.1 to 0.2. However, particle size values did not revealed an increase.

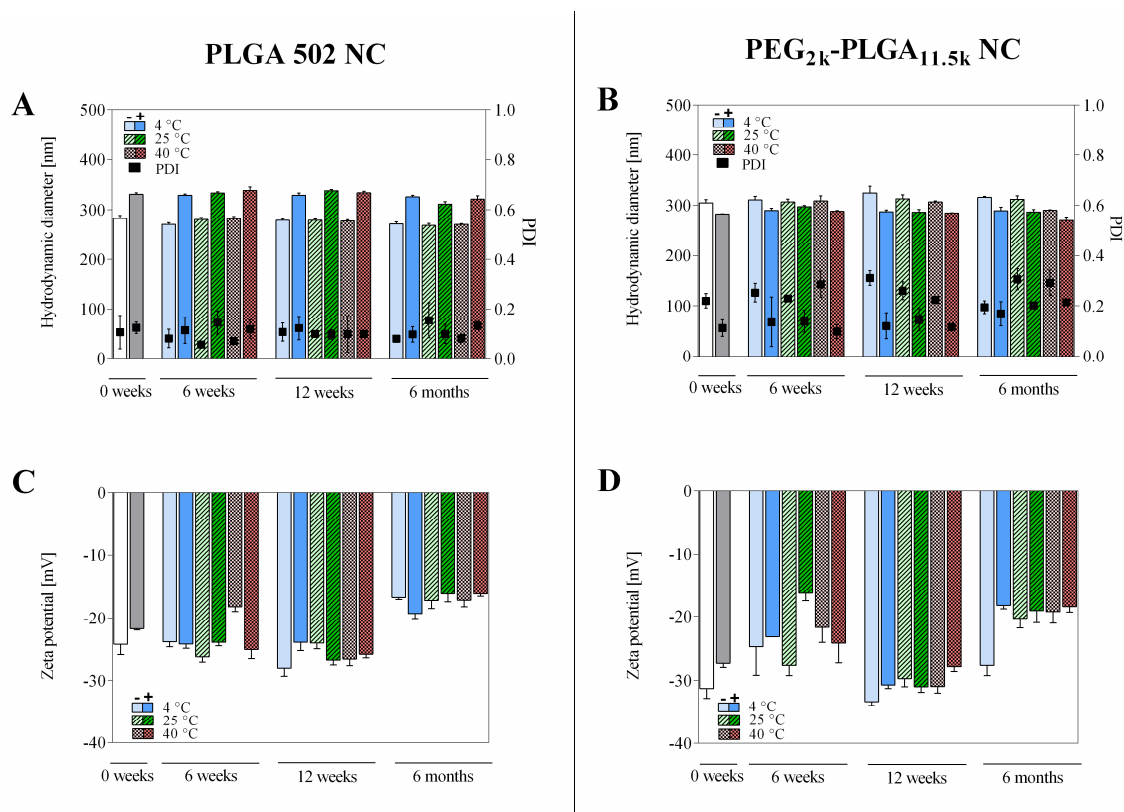


Figure 39 Diagrams comparing particle size and PDI (A, B), zeta potential (C, D) of PLGA 502 NC (A, C) and PEG_{2k}-PLGA_{11.5k} NC (B, D) with (+) and without (-) C6 after 0 weeks, 6 weeks, 12 weeks and 6 months of storage. Results are reported as mean \pm SD (n = 3).

Zeta potentials between -20 mV and -30 mV did not change upon 12 weeks of storage (Figure 39C and D). After 6 months of storage, the negative charges of all formulations decreased, and with the extension of the storage time, the absolute potential values of the zeta potential of the different groups decreased up to -15 mV. Alshememry *et al.* assumed that this phenomenon can be due to the trapping of the cryoprotectant on the surface of the nanoparticles [314]. The increase of the surface charge of the PLGA nanoparticles after long term stability studies was reported also in other studies [315, 316], providing indicator of nanoparticles modification upon storage.

The T_g of NC lyophilizates are summarized in Figure 40A, B, C and D. The T_g is one of the determinants of storage stability [317] and was evaluated with DSC. Thermograms of PLGA 502 NC and PEG_{2k}-PLGA_{11.5k} NC remained unchanged after storage at 4 °C, 25 °C and 40 °C

and were all characterized by one T_g between 80 °C and 110 °C. This endothermic event should be attributable to trehalose. According to Hinrichs *et al.* [318], DSC curves of trehalose showed a T_g around 120 °C. Disaccharides, such as trehalose, possess a much higher T_g than monosaccharides, do not contain reducing groups and are therefore often used as stabilizers for lyophilization [319]. It is recommended that lyophilizates should have a T_g value 20 °C above the ambient storage temperature to minimize mobility [320]. Referring to this recommendation, the T_g of lyophilizates (>80 °C) is in this study at least 40 °C higher as storage temperature assuming that temperature should not have a significant effect on storage stability of lyophilizates. Since the concentration of trehalose was high, thermal properties of NC could not be detected and the comparison between PLGA and PEGylated PLGA as well as dye influence were not possible.

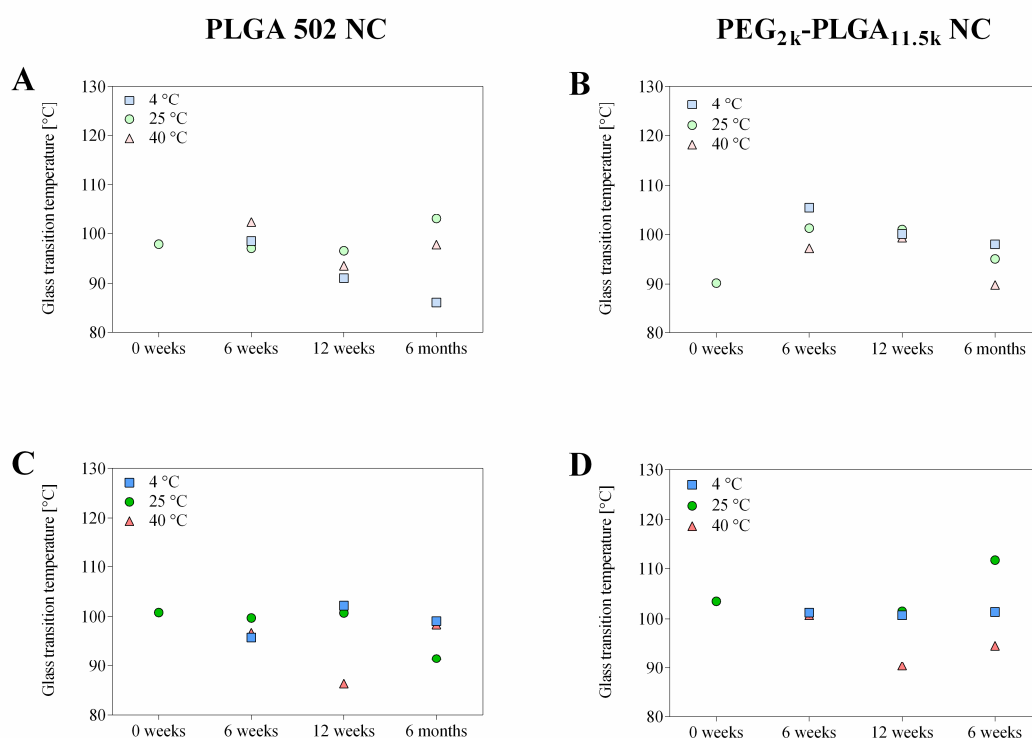


Figure 40 Diagrams comparing T_g of blank (A, B) and C6-loaded (C, D) PLGA 502 NC (A, C) and PEG_{2k}-PLGA_{11.5k} NC (B, D) lyophilizates using 15% trehalose as cryoprotectant after 0 weeks, 6 weeks, 12 weeks and 6 months of storage.

DSC results were in agreement with XRD measurements. For blank NC, the XRD pattern showed no distinct peak at the time point 0 (Figure 41). After storage, samples remained fully amorphous independent of the NC type. Ebied *et al.* characterized a pure C6 powder by XRD, which exhibited a pattern of several diffraction peaks of various intensities, indicating that the C6 is polycrystalline [321]. However, the absence of peaks on the XRD patterns for C6-loaded

PLGA 502 or PEG_{2k}-PLGA_{11.5k} NC in Figure 41 was most probably indicated to high concentration of trehalose and its amorphous state [322].

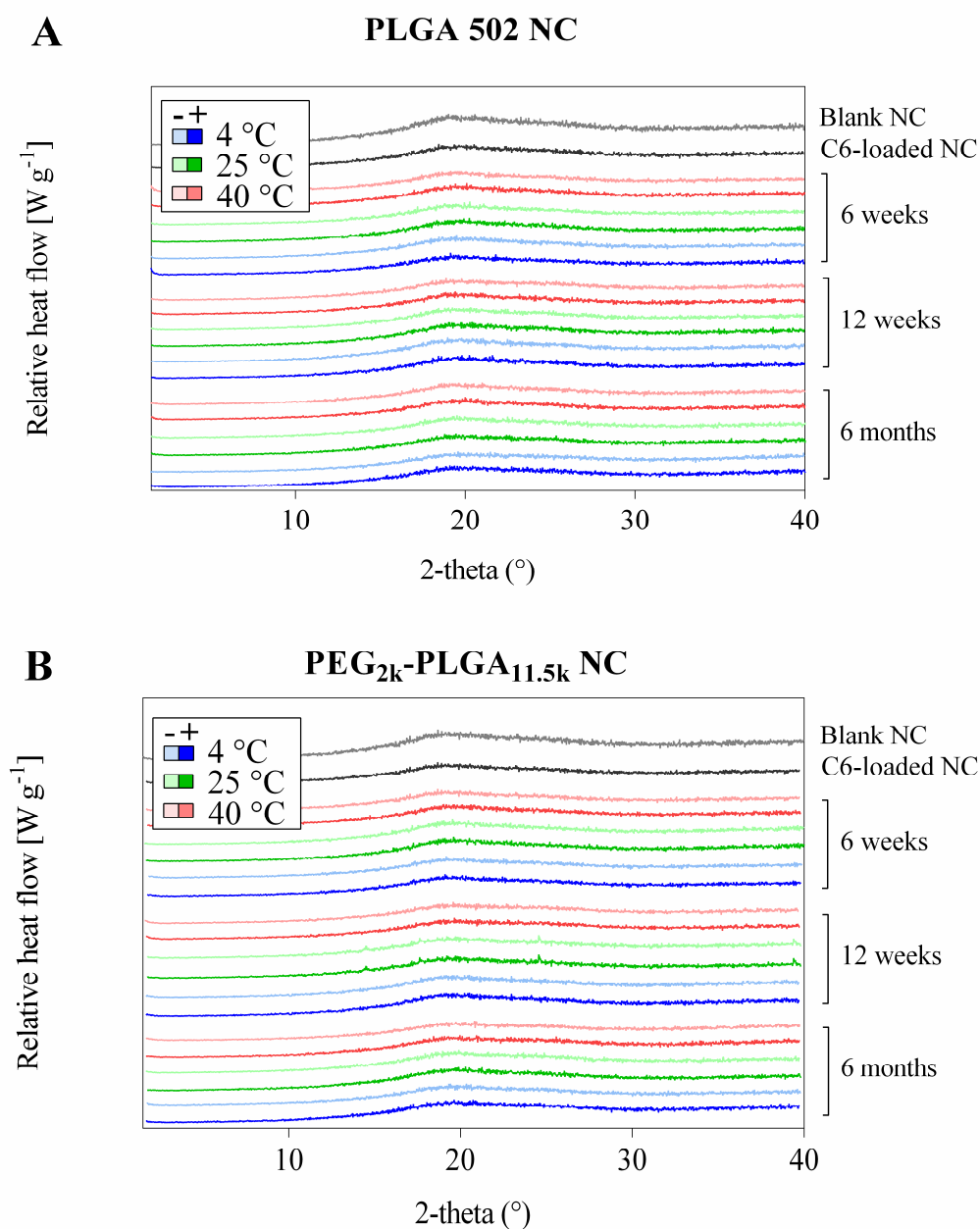


Figure 41 Diagrams comparing XRD measurements of blank (-) and C6-loaded (+) PLGA 502 NC (A) and PEG_{2k}-PLGA_{11.5k} NC (B) lyophilizates using 15% trehalose as cryoprotectant after 6 weeks, 12 weeks and 6 months of storage. Grey and black line represent lyophilizates of blank NC and C6-loaded NC, respectively, at time point 0 weeks.

It is widely believed that the stability of nanoparticle lyophilizates depends on reduced molecular movement, which helps to prevent chemical reactions in the dried state. As a result, it is commonly assumed that lower moisture levels can lead to improved stability [323]. Therefore, the purpose of this study was to investigate how different storage conditions affect the moisture contents and storage stability of NC formulations. Residual moisture levels at time

point 0 were around 1% for blank PLGA NC and PEGylated NC (Figure 42A and B). This indicates that PEGylated polymer despite its more hydrophilic nature as PLGA polymer did not have an effect on the residual moisture content of lyophilizates. However, the dye encapsulation showed an effect on residual moisture with increase of 0.2% in PLGA 502 NC and decrease of 0.3% in PEG_{2k}-PLGA_{11.5k} NC. Upon 6 months of storage, the solid-state properties of the lyophilizates showed an increase in residual moisture content over time up to 2%. This phenomenon could be attributed to three possible factors: i) transfer of moisture from the stopper to the sample [324], ii) diffusion of moisture diffusion through the stopper, and iii) the existence of microleaks in the seal connecting the stopper and the vial [317]. Sasaki *et al.* noted that in the early phase of storage the moisture content within the lyophilized sample increase due to moisture transfer from the stopper to the sample. However, in later stages, this increase was a result of external permeation through the stopper [325]. The low fill volume and thus lyophilizate mass contributes to the pronounced increase of water content upon uptake of only little absolute water amounts. In general, the most pronounced increase in residual moisture was observed upon 40 °C. Increased residual moisture could be an indicator for water taken up during storage. In this case, water could act as a plasticizer, which lowers the T_g . When T_g drops below the storage temperature, it results in a poor stabilization [326]. However, in this case the water content increased up to 2%, which is still in the range of the residual moisture content of commercial lyophilized products between $\leq 1.0\%$ to 3% [327-329] and did not increase that much to effect the stability of NC, shown as constant particle size and zeta potential during storage (Figure 39).

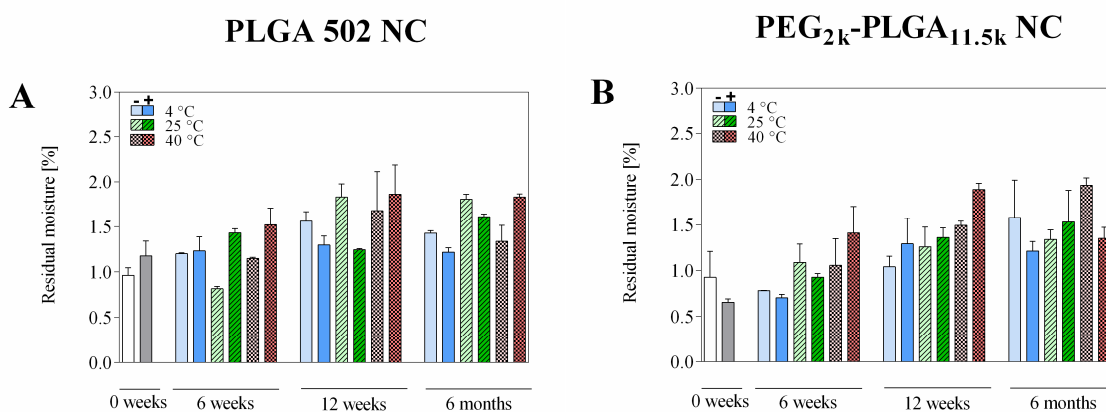


Figure 42 Diagrams comparing residual moisture of blank (-) and C6-loaded (+) PLGA 502 NC (A) and PEG_{2k}-PLGA_{11.5k} NC (B) after 0 weeks, 6 weeks, 12 weeks and 6 months of storage. Results are reported as mean \pm SD (n = 3).

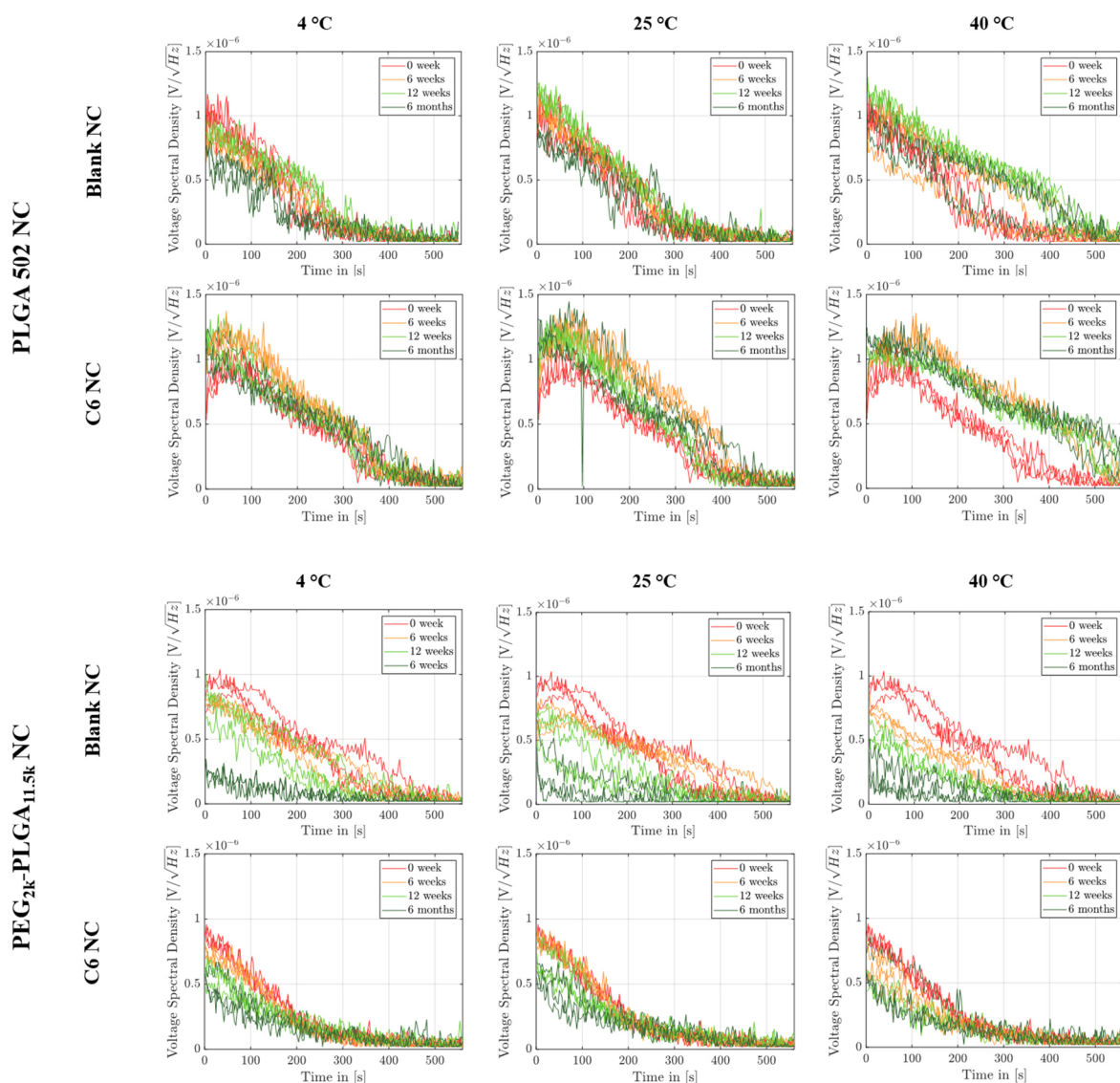


Figure 43 Diagrams comparing the inertial cavitation (VSD) of C6-loaded (+) and unloaded (-) PLGA 502 NC and PEG_{2k}-PLGA_{11.5k} NC after 0 weeks, 6 weeks, 12 weeks and 6 months stored at 4 °C, 25 °C and 40 °C. Ultrasonic cavitation noise signal was measured at 750 kHz and 1.02 kPa (set-up 1) for 560 s. Three individual measurements are shown for every sample.

All cavitation signal curves (VSD *versus* time) are represented in Figure 43. It can be seen that profiles remained comparable over the period of 6 months for loaded or unloaded PLGA 502 NC. Thus, the cavitation activity was not affected by the encapsulation of dye. However, samples stored at 40 °C showed an increase in cavitation intensity and duration already after 6 weeks. The samples tested at 0 weeks were ultrasound active for 300 s and 350 s for blank and C6-loaded PLGA 502 NC, respectively. After 6 month of storage at 40 °C, PLGA 502 NC were ultrasound active at least for 500 s, which is 200 s more than at the beginning. However, a greater effect on cavitation activity during storage was noted for PEGylated NC. Both loaded and unloaded formulations showed lower level of broadband noise during storage. Cavitation activity after 6 months of storage decreased up to 75% and 20% for unloaded and loaded

PEGylated NC, respectively. The reason could be a low T_g of PEG_{2k}-PLGA_{11.5k} NC, which was measured for the loaded NC at 31.95 °C (data not shown). While samples were stored near or above T_g , it could affect polymer thermal properties. Polymer could transit from glassy to rubbery state, resulting in an increased molecular mobility, removal of the pores and vanishing of air pockets from the surface during storage. The decrease of cavitation air nuclei resulted in lower cavitation profiles. The variability in sonic responses between the replicate samples of unloaded PEGylated NC is quite large in comparison to loaded formulations. Loaded PEG_{2k}-PLGA_{11.5k} NC appeared in smaller particle sizes, which could affect the lower cavitation activity already at the time point 0, which was already explained in section 5.2.1.

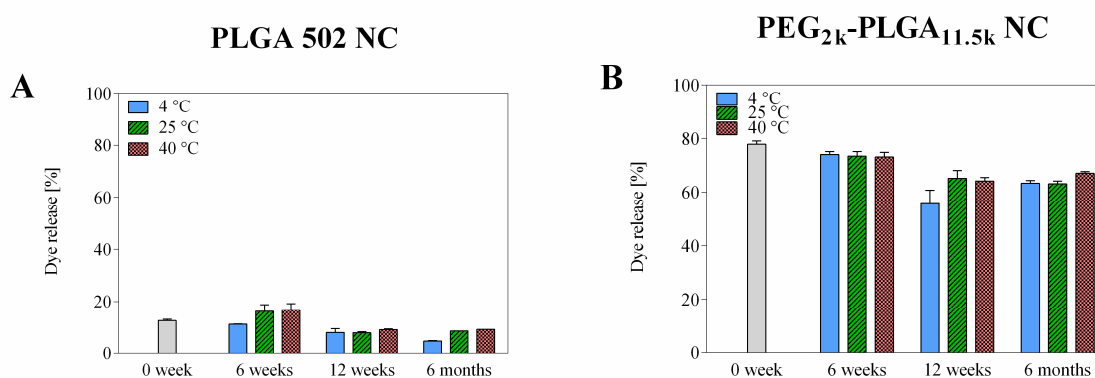


Figure 44 Diagrams comparing C6 release after ultrasound treatment of (A) PLGA 502 NC and (B) PEG_{2k}-PLGA_{11.5k} NC after 0 weeks, 6 weeks, 12 weeks and 6 months of storage. Results are reported as mean \pm SD (n = 3).

To further prove that lyophilized C6-loaded NC are stable under long-term storage conditions, C6 release after cavitation measurements was quantified (Figure 44). PLGA 502 NC released up to 20% of dye, while PEGylated NC up to 80%. The results indicated that both NC formulations exhibited a decrease in dye release after 6 months storage. The decrease was more obvious for PLGA 502 NC with up to 60% reduction of dye release after 6 months. In comparison, PEG_{2k}-PLGA_{11.5k} NC released 20% of dye less after 6 months than at the starting point. A possible explanation could be lower cavitation activity of PEG_{2k}-PLGA_{11.5k} NC after time. Overall, PLGA 502 formulations showed a higher stability in cavitation activity, while PEG_{2k}-PLGA_{11.5k} NC had a better release data upon storage up to 6 months independent of storage conditions.

The storage stability study with PLGA 502 and PEG_{2k}-PLGA_{11.5k} NC showed promising results. This study plays a crucial role in confirming that the formulation characteristics, which significantly affect its performance remained in an acceptable range after storage.

5.4.2 Determination of the Physicochemical Properties and Ultrasound Activity of Nanocapsules after Incubation in Different Biologically Relevant Media

Nanoparticles are usually dispersed in a physiological solution before being used for biological *in vitro* and *in vivo* studies [330]. The main question addressed in the present chapter was, whether different dispersion media used for rehydration of nanoparticles affect their physicochemical stability and cavitation activity. For this purpose, PLGA (Resomer® RG 502) NC were prepared by emulsion-diffusion method and loaded with C6 in 1:250 dye-to-polymer ratio. NC were lyophilized with 15% trehalose aqueous solution and redispersed to a final concentration of 1 mg/mL in six analyzed media: ultrapure water, 5% glucose, 0.9% NaCl, PBS, RPMI and ALF. Properties of the dispersion media are summarized in Table 14. The pH was kept constant between 7.0-7.4, while ALF was used as an acidic media with pH 4.5. The ionic strength and conductivity of ultrapure water and 5% glucose was zero, while no ions were presented in a solution, which could conduct electricity.

Table 14 Characteristics of the media used to disperse PLGA NC at 25 °C.

Dispersion media	pH	Ionic strength [mM]	Osmotic concentration [mOsm/L]	Conductivity** [mS/cm]
Ultrapure water	7.1	0	0	0.001 ± 0.0
5 % glucose	7.0	0	326 ± 1	0.002 ± 0.0
0.9 % NaCl	7.0	154.0	334 ± 3	15.52 ± 0.56
PBS	7.3	166.5	322 ± 12	14.94 ± 0.52
RPMI	7.4	NA	278*	13.90 ± 0.0
ALF	4.5	979.8	40 ± 2	15.83 ± 0.06

Abbreviation: NA (not applicable). *Reported by the manufacturer. **Measured with Zetasizer NanoZS.

In Figure 45A no differences in size of NC between dispersion media was observed. The hydrodynamic diameter of NC was scattered around 290 nm for all samples. Compared to freshly redispersed NC in ultrapure water (PDI <0.1), similar PDIs were found for the other dispersion media. The PDI values were all below 0.2 indicating monodisperse NC. In Figure 45B could be seen that zeta potential values were around -26 mV when measured in ultrapure water and 5% glucose. NaCl, PBS, RPMI and ALF increased the zeta potential from -26 mV in ultrapure water to an average of -1 mV in the other four media due to counter ions presented in these complex media. This indicates that electrolytes in media likely constitute a part of the surface charge increase [331].

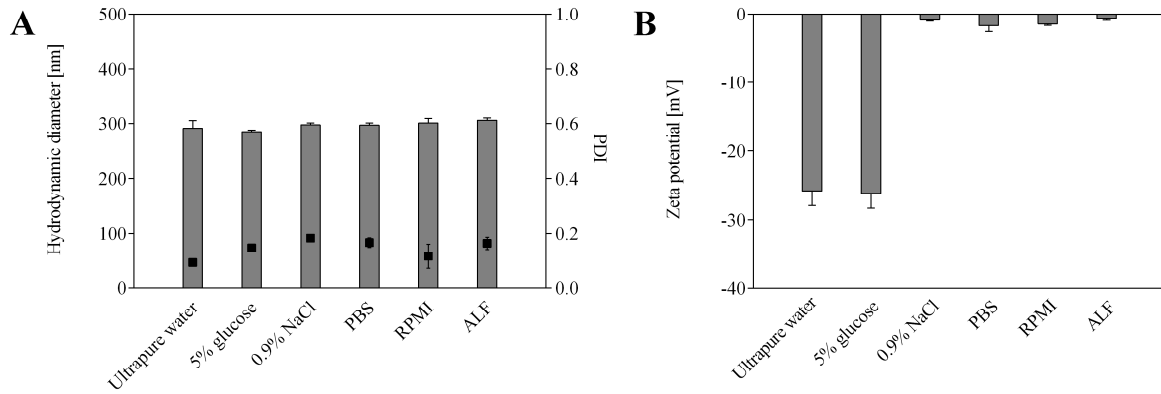


Figure 45 Hydrodynamic diameter (A), PDI (A) and zeta potential (B) of PLGA NC incubated in different biologically relevant media for 1 h. Data are means of three independent experiments.

Upon rehydration in different dispersion media all PLGA NCs showed ultrasound activity (Figure 46A). The cavitation profiles all started at $1.0 \times 10^{-6} \text{ V}/\sqrt{\text{Hz}}$ and declined until they reached a minimum cavitation after 300 s, PLGA NC dispersed in 5% glucose already after 200 s.

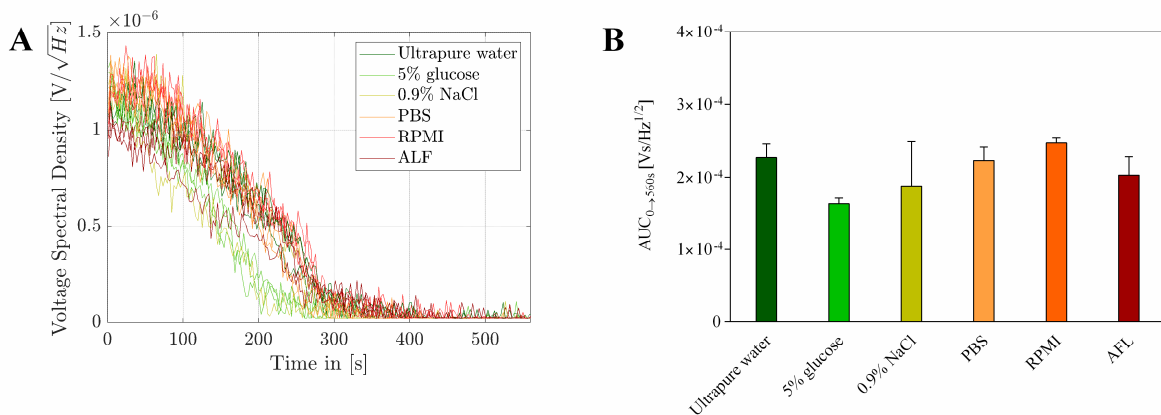


Figure 46 Diagrams comparing the inertial cavitation (VSD) (A) and AUC of VSD (B) for C6-loaded PLGA 502 NC redispersed in six different biologically relevant media. Ultrasonic cavitation noise signal was measured at 750 kHz and 1.02 kPa (set-up 1) for 560 s. Results are presented as three individual measurements for every sample or are presented as mean ± SD, n = 3.

Additionally, the AUC of the first 560 s of VSD curves was calculated and presented in a Figure 46B. The graph indicates a higher activity of NC dispersed in RPMI compared to ultrapure water. All other dispersion media had similar cavitation activity as water ($\text{AUC} = 2.3 \times 10^{-4} \text{ V}/\text{Hz}^{1/2}$) or lower. The lowest activity was observed by PLGA NC redispersed in 5% glucose ($\text{AUC} = 1.6 \times 10^{-4} \text{ V}/\text{Hz}^{1/2}$). The 5% glucose solution had a viscosity of 1.023 mPa.s, which is higher compared to water with 0.895 mPa.s. Nazari-Mahroo *et al.* proposed that the viscosity could affect the air bubble dynamics in the collapse phase of

cavitation process, particularly at high ultrasonic amplitude and high viscosity [332]. By higher viscosities the expansion amplitude of the cavitation bubble is decreased, and the collapse time is shortened with the increase of viscosity [333]. Luo *et al.* proved that the viscosity of the media could suppress the formation of the micro-jet in the collapse phase, as well as delays the velocity of the micro-jet flowing toward the surface [334]. Therefore, it is possible that by 5% glucose solution, a higher viscous media, the cavitation effect was weaker due to reduction in air bubble dynamic.

5.5 Investigation of Parameters Influencing Acoustic Measurements

5.5.1 Cavitation Activity of Nanocapsules at Different Frequencies

The following chapter focuses on the cavitation intensity evaluated as VSD in the frequency and pressure range enabled in ultrasound measurement set-up. The broadband FUS transducer covered a frequency range from 0.5 MHz to 1 MHz and was in this work calibrated for four frequencies: 650 kHz, 750 kHz, 850 kHz and 950 kHz. At each frequency, a range of different peak negative pressure was achieved by variable settings of the input voltage from 1 V to 3.5 V (Figure 47). For each of the frequencies the peak negative pressure of 1.02 MPa was selected for further experiments, which resulted at input voltage of 3.20 V, 2.37 V, 2.28 V and 3.40 V for frequencies of 650 kHz, 750 kHz, 850 kHz and 950 kHz, respectively.

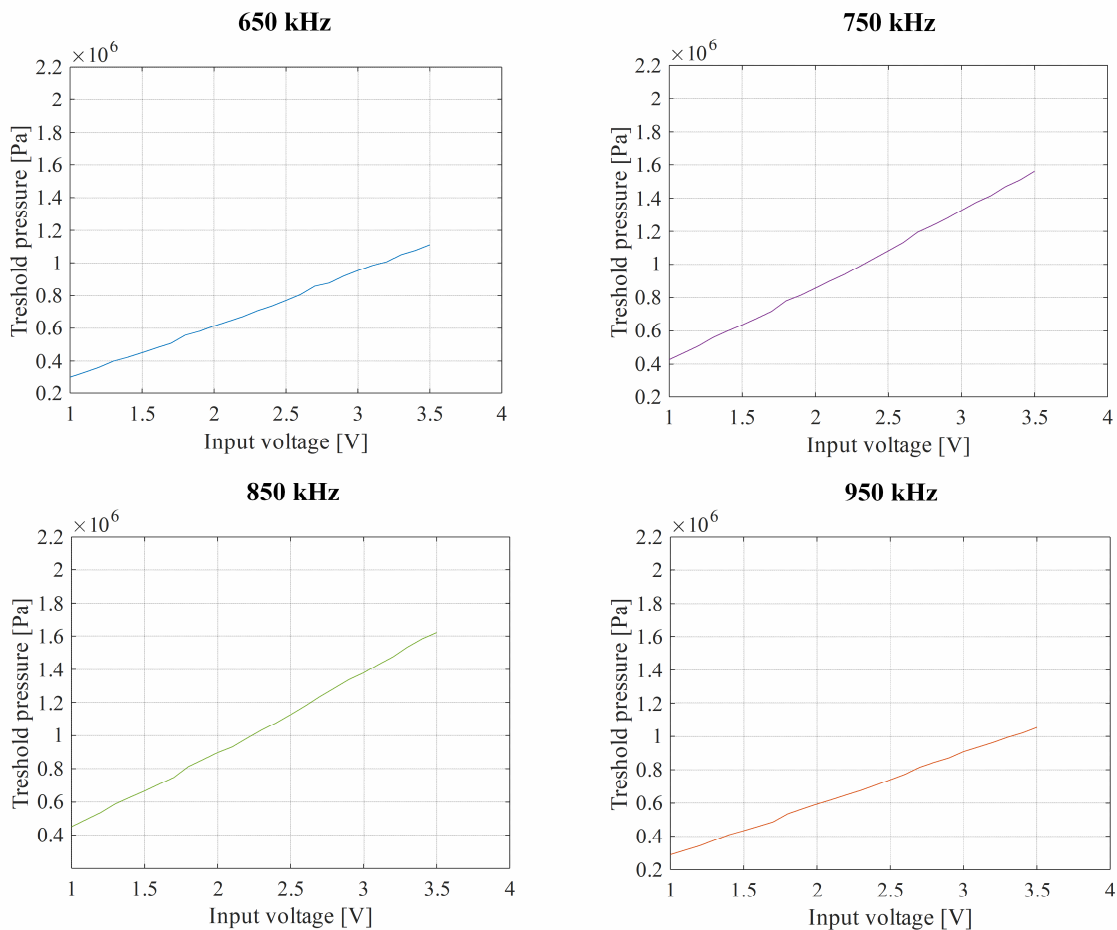


Figure 47 Calibration curves of threshold pressure between 1 V and 3.5 V of input voltage for 650 kHz, 750 kHz, 850 kHz and 950 kHz.

The NC were investigated for the inertial cavitation activity at the already mentioned ultrasound frequencies. Three different dye-to-polymer ratios (1:500, 1:250 and 1:100) were used to prepare C6-loaded PLGA (Resomer[®] RG 752S) NC by emulsion-diffusion preparation technique using 2.5% PVA as stabilizer. Prepared NC dispersions were lyophilized with 15%

trehalose. For each of the selected frequencies, NC redispersed in ultrapure water were placed in a standard polystyrene cuvette, their inertial cavitation was measured, and the VSD profile was calculated.

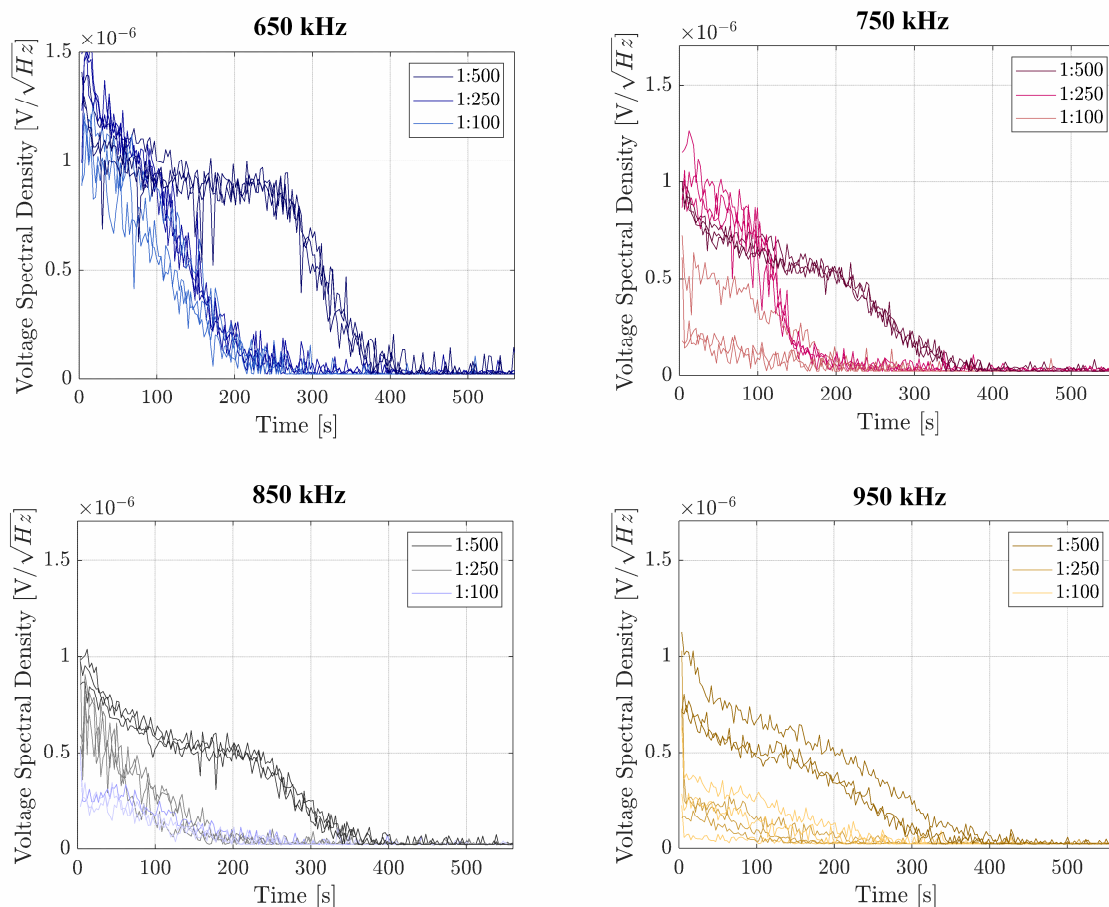


Figure 48 Cavitation profiles of C6-loaded PLGA (RG 752S) NC prepared at different dye-to-polymer concentrations (1:500, 1:250 and 1:100) at 650 kHz, 750 kHz, 850 kHz and 950 kHz and 1.02 MPa in the set-up 1. The results are given as plots of the VSD *versus* time for the replicate individual samples.

Figure 48 shows the resulting inertial cavitation activity of the three different C6-loaded NC over time. In general, the VSD profile of NC prepared with 1:500 dye-to-polymer ratio showed the longest and strongest cavitation activity. The activity started at $1.5 \times 10^{-6} \text{ V}/\sqrt{\text{Hz}}$ or $1.0 \times 10^{-6} \text{ V}/\sqrt{\text{Hz}}$ depending on the frequency and lasted at least 300 s. In comparison to NC of 1:500 dye-to-polymer ratio, the other two NC preparations had lower initial cavitation, steeper decrease in the kinetic profile and shorter duration time independent on frequency. Similar findings were reported in section 5.2.2 for the RhB NS. Comparing different frequencies, a typical cavitation behavior can be recognized, since NC showed a decreased cavitation activity using higher frequencies (Figure 48). From the literature, it is known that the rarefaction pressure phase is longer at lower frequencies where bubbles have relatively long growth periods. Whereas at high frequencies, collapse and fragmentation of bubbles occurs

more quickly due to decrease in the rarefaction period, thus smaller bubbles are produced. Therefore, the cavitation collapse is more energetic and violent at lower frequencies [335, 336]. At all frequencies, the VSD began at a local maximum value and decreased continuously. Surface air bubbles so called cavitation nuclei are destroyed over time resulting in a reduction of the total amount of residual nuclei and the weaker inertial cavitation activity. The highest cavitation activity of all NCs was observed at 650 kHz. The difference in cavitation intensity between 750 kHz, 850 kHz and 950 kHz was not as pronounced as the difference comparing 650 kHz to other three frequencies.

5.5.2 Impact of Water Tank Temperature on Ultrasound Cavitation of Nanocapsules

The human body temperature differ between individuals by nearly 2.2 °C [337] depending on sex [338], age [339], health condition [340] and time of the day [341]. Temperature changes could influence tissue properties, which was demonstrated to have an influence on inertial cavitation threshold of gas bubbles [342]. In the following, a study was designed to evaluate the cavitation of PLGA (Resomer[®] RG 502) NC across water tank temperatures of 25-40 °C in the ultrasound set-up under atmospheric pressure. A digital thermometer was used to record the water temperature. Previous studies described the importance of temperature, since various factors such as viscosity, density, vapor tension, surface tension and gas content depend on it and thus affect bubble cavitation activity [343]. C6-loaded NC were prepared using a standard emulsion-diffusion method followed by lyophilization with 15% trehalose. Lyophilized NC were redispersed in 3 mL ultrapure water and evaluation of ultrasound activity in ultrasound device.

The signal profiles of VSD (Figure 49A) showed a clear temperature-dependent response. Despite the offset degree of broadband noise was the same at all temperatures ($1.2 \times 10^{-6} \text{ V}/\sqrt{\text{Hz}}$), this temperature-dependency was observed already after 50 s when the individual profiles for the highest measured temperature (40 °C) start to diverse. Cavitation activity of NC increased on moving from 40 °C onto 25 °C, which gave the highest response of all investigated temperatures. The values for mean average AUC of VSD in Figure 49B increased linearly with temperature from 40 °C to 25 °C. Phan *et al.* experimentally and numerically investigated the single cavitation bubble dynamics and the thermodynamic effects at ambient temperatures varying between 20 °C and 80 °C [344]. He found that collapsing time increased and collapsing intensity decreased with an increase in the ambient temperature. The bubble collapse is controlled by liquid inertia at lower temperatures, while heat transfer from the bubble to the liquid is the controlling mechanism at higher temperatures. Similar analytical

and experimental data were obtained by Florschuetz *et al.* [345] and Takada *et al.* [346]. Another explanation for temperature-dependent response could be the low T_g of PLGA forming the shell of NC. NC made of Resomer[®] RG 502 have shown a T_g at 39.46 °C (section 5.3.2). At this temperature the polymer transits from glassy to rubbery state resulting in vanishing of surface pores and air pockets along the surface of the NC. The loss of air bubbles could cause lower acoustic activity at higher temperatures. The previous observations by Blum *et al.* [347] also supported this so called “defect hypothesis”. They used phospholipids to stabilize hydrophobic MSNs. The nanoparticles could initiate cavitation when the lipids were kept in gel phase below their melting temperature. As soon as the temperature reached T_m of the lipids, the nanoparticles lost their acoustic activity. The authors verified that the cavitation activity is depended on the thermal properties of the surface of nanoparticles.

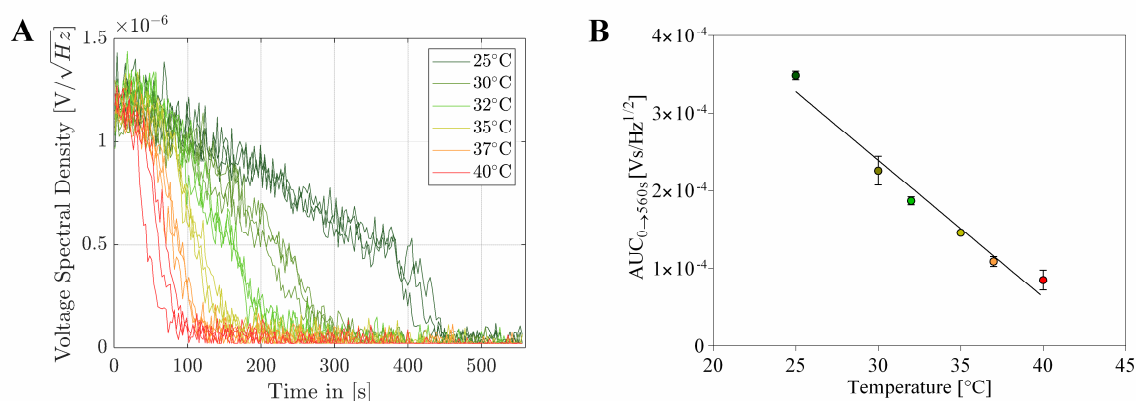


Figure 49 Effect of temperature on the acoustic response of PLGA (RG 502) NC in the ultrasound set-up 1 at 750 kHz and 1.02 MPa and different water bath temperatures. (A) The results are given as plots of the VSD *versus* time for the replicate individual samples. (B) Linearity of AUC of VSD at different water bath temperatures with R^2 of 0.9676 is presented ($n=3$).

5.5.3 Impact of the Presence of Ethanol on Acoustic Cavitation of Nanocapsules

In this study, PLGA (Resomer[®] RG 502) NC loaded with C6 in 1:250 dye-to-polymer ratio were prepared with emulsion-diffusion technique and after purification lyophilized in 15% trehalose aqueous solution. After rehydration of NC, water was unable to wet all the pores due to *Cassie-Baxter* state and Laplace pressure and air could be entrapped on the hydrophobic surface of NC [180, 223]. For this reason, the air nanobubbles remain stable on the hydrophobic surface of NC and continuously grow under ultrasound insonation following with collapse and disruption of neighboring NC.

To further elucidate the role of air pockets on the surface of NC in the acoustic cavitation process, ethanol with a lower surface tension as water [348] was used to potentially wet the air-filled pores and exchange the entrapped air. The ultrasound response of the NC dispersions

was measured in the presence of different amounts of ethanol (Figure 50). The surface tension of the ethanol-water mixture at 30 °C is 46.88 mN/m and 37.38 mN/m for 10% (m/V) and 20% (m/V) ethanol, respectively [348]. The addition of 10% (m/V) ethanol to the NC dispersion (333 mg/mL) quenched the ultrasound signal for about 50%. Doubling the ethanol concentration resulted in a quenching for more than 70%. With increasing ethanol concentration, the surface tension decreased, which provided a better wetting effect of the pores on the NC surface. The ethanol seems to destroyed the bubbles and displace the entrapped gas, which lowered the acoustic cavitation response.

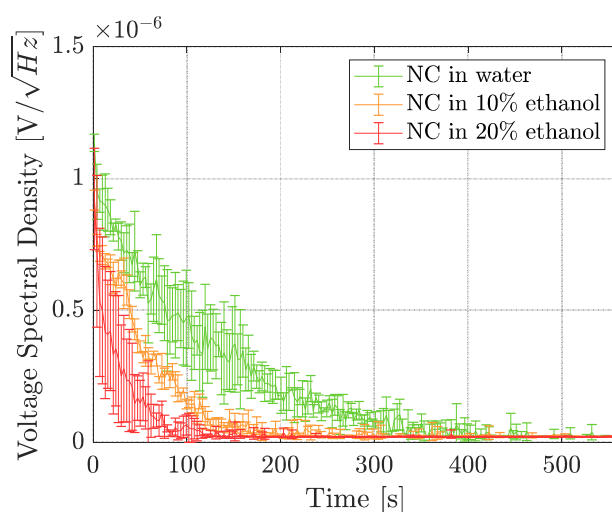


Figure 50 Quenching of the ultrasound response of PLGA (RG 502) NC in the presence of water, 10% (m/V) ethanol or 20% (m/V) ethanol and measured for the acoustic cavitation in the set-up 1 at 750 kHz and 1.02 MPa. The results are given as plots of the VSD *versus* time for mean of three replicate individual samples.

According to the previous studies the broadband cavitation response depends on the air volume set into inertial cavitation [221, 349]. A possible explanation for the cavitation response of nanocarriers could be nano-sized gas pockets trapped on the rough surface of the nanoparticles, which acts as nucleation sites for inertial cavitation.

5.5.4 The Use of Tissue Mimicking Phantoms

To provide a more clinically realistic ultrasonic environment, a tissue-mimicking phantom was used to simulate biological tissue. The most important biological properties of materials for ultrasound experiment are sound speed, mass density, attenuation coefficient, and backscatter coefficient [350]. In this study, a tissue mimicking phantom consisting of 10 % PVA and 90 % ultrapure water was chosen. Braunstein *et al.* produced 10% PVA hydrogel with a sound speed of 1556 m/s [351], which is similar to soft tissue [352]. Additionally, a 3 mm canal was set up through the phantom, which imitated a smaller blood vessel [353]. A peristaltic pump provided perfusion through the canal of the phantom with a constant velocity of 10 cm/s, similar to the

human circulatory system with values between 0.1 cm/s and 40 cm/s depending on the blood vessel type [354]. The phantom was placed in the central zone of the FUS transducer, NC water dispersion was pumped through, and inertial cavitation was measured.

The aim was to show cavitation behavior of PLGA (Resomer[®] RG 502) NC in a through-flow phantom system. NC were prepared with standard emulsion-diffusion method and loaded with C6 in a dye-to-polymer range of 1:250, resulting in 0.22% dye load. The average VSD of NC at three different frequencies (550 kHz, 750 kHz and 950 kHz) and constant peak negative pressure of 1.02 MPa across a ratio of MIs from 0.3 to 1.9 is shown in Figure 51. As material erosion can occur, the frequency and peak negative pressure must be chosen to not put tissue under mechanical destruction. It is necessary to adjust limit values using MI to describe the mechanical bioeffects. The FDA has approved MI value of 1.9 as a maximum in clinical use [182]. At low acoustic power (MI below 0.3) the acoustic response is considered as linear and no special enhanced signal is generated. Therefore, this study focused on intermediate (MI = 0.2-0.5) and high (MI >0.5) acoustic powers, where bubbles undergo rarefaction that is greater than compression. This non-linear oscillation results in bubble destruction [181, 183].

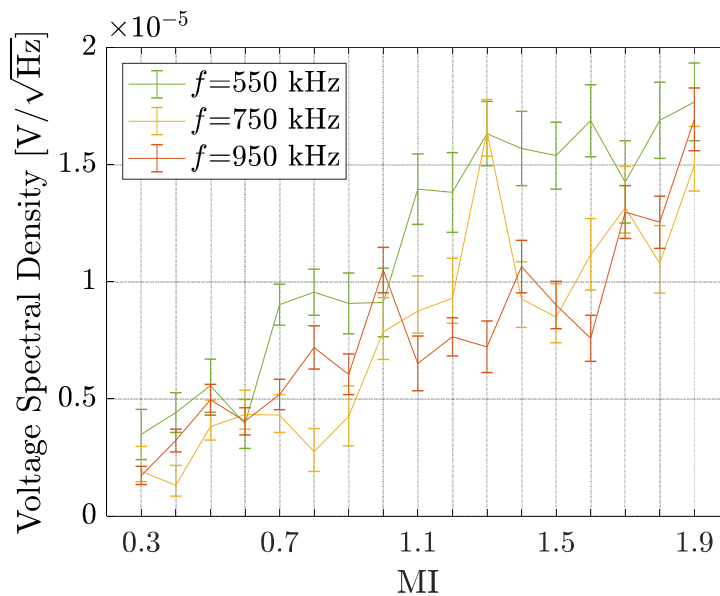


Figure 51 Average VSD of NC at different MIs and different burst excitation frequencies ($f=550$ kHz, $f=750$ kHz and $f=950$ kHz). 80 pulses were applied for each sonication set in set-up 3.

In Figure 51 cavitation of NC was already shown at MI 0.3 for all frequencies, which matches previous literature for different contrast agents [221, 355]. In general, VSD increased linearly with increasing MI. At lowest frequency (550 kHz) a slight deviation from the linear trend at the higher MIs (MI >1.3) was observed, presumably due to different behaviors of the bubbles from pulse to pulse [349]. In general, the strongest inertial cavitation was obtained at 550 kHz,

due to an increase in rarefaction period and production of bigger bubbles, already discussed in the section 5.5.1.

At all three frequencies dye release was measured. At 550 kHz (Figure 52A) dye release increased potentially from 17% to 25% with increasing MI and reached the platform at 0.7 MI. Higher frequencies, 750 kHz (Figure 52B) and 950 kHz (Figure 52C), showed different dye release profiles. At MI below 0.7 dye release was constant at 19% and 20% for 750 kHz and 950 kHz, respectively. Dye release increased up to 29% at MI higher than 0.8 but no further release occurred by going beyond MI of 1.1. PLGA NC showed inertial cavitation below 1.9 and are therefore possible carriers for ultrasound-targeted drug delivery. This study has elucidated that among three different frequencies, dye release at 950 kHz was the highest. This may provide a reliable basis for acoustic parameter optimization in ultrasound-assisted dye delivery.

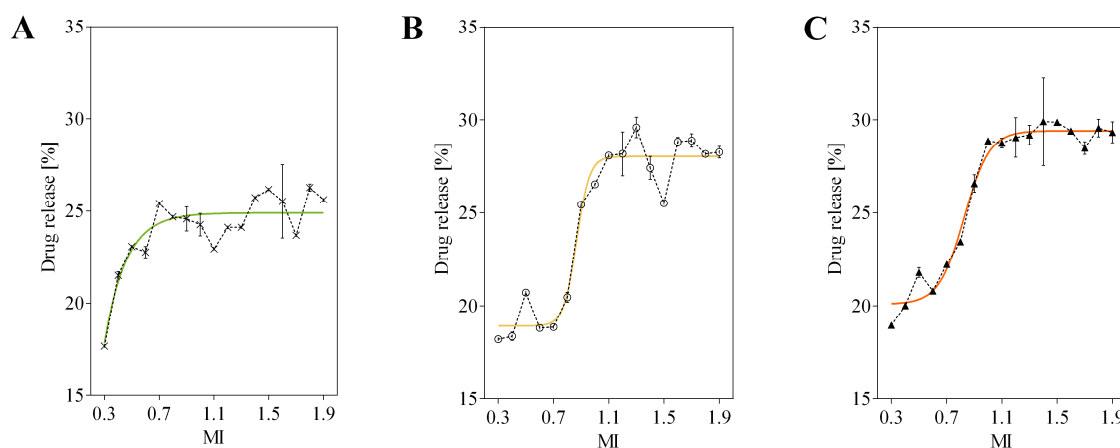


Figure 52 Release of C6 from PLGA NC over a range of MIs from 0.3 to 1.9 and at different frequencies: (A) 550 kHz, (B) 750 kHz and (C) 950 kHz (n=3).

5.6 Analysis of Protein Corona Composition on Nanocapsules

The “biomolecule corona” refers to the layer of biomolecules that can adsorb onto the surface of nanoparticles when they come into the contact with biological fluids [356]. It is formed due to the interaction between nanoparticles and biomolecules such as serum proteins, enzymes, lipids, and carbohydrates, depending on the nanoparticle surface properties and the characteristics of the biological fluid [357]. However, studies have primarily focused on examining the protein component of biomolecule corona, therefore it can also be referred as protein corona [331, 358-361].

The adsorption of proteins onto the nanoparticles surface in biological fluids is known to affect their acoustic activity [239, 308]. To assess, to what extent the ultrasound cavitation response is affected by bounded proteins, a batch of NC was prepared by an emulsion-diffusion evaporation method employing 2% (w/w) Resomer[®] RG 502, Resomer[®] RG 502H, Resomer[®] RG 505 or PEG_{2k}-PLGA_{11.5k} polymer as well as 5% (w/w) Miglyol[®] 812 in O-phase and 2.5% (m/V) PVA in W-phase. The loaded NC were prepared in 1:250 C6-to-polymer ratio. The process parameters stayed the same as in the section 5.4.1. Physicochemical NC characteristics are given in Table 15.

Table 15 Average hydrodynamic diameter, PDI, zeta potential and entrapment efficiency of the C6 for all used formulations. Data are means from three samples with SD values.

Sample	Hydrodynamic diameter [nm]	PDI	Zeta potential [mV]	Entrapment efficiency [%]
PLGA 502 NC (blank)	275.3 ± 2.1	0.06 ± 0.01	-19.4 ± 0.4	-
PLGA 502 NC (C6)	290.7 ± 14.5	0.09 ± 0.01	-25.8 ± 2.1	43.5 ± 2.5
PLGA 502H NC (blank)	286.3 ± 7.1	0.06 ± 0.01	-22.3 ± 5.9	-
PLGA 502H NC (C6)	350.0 ± 1.4	0.16 ± 0.01	-25.8 ± 0.4	95.4 ± 2.7
PLGA 505 NC (blank)	382.3 ± 2.9	0.19 ± 0.02	-24.8 ± 0.8	-
PLGA 505 NC (C6)	367.0 ± 11.1	0.32 ± 0.03	-26.9 ± 0.9	6.9 ± 0.9
PEG _{2k} -PLGA _{11.5k} NC (blank)	203.7 ± 4.0	0.09 ± 0.04	-30.4 ± 1.9	-
PEG _{2k} -PLGA _{11.5k} NC (C6)	229.0 ± 3.0	0.12 ± 0.02	-22.3 ± 0.6	41.9 ± 0.3

The NC batch for these studies shows a higher hydrodynamic diameter of the NC. However, the rest of the results are in accordance with previously reported batches. Average hydrodynamic particle diameters measured by DLS were found to be between 203 nm (PEG_{2k}-PLGA_{11.5k} NC) and 328 nm (PLGA 505 NC) with direct correlation with the molar mass of the polymers, already described in section 5.3.2. The PDI for all formulations was <0.2, suggesting narrow size distributions, except for PLGA 505 NC (C6) with a PDI 0.32. In general, C6-loaded

NC were found to have higher average hydrodynamic diameters and PDIs as unloaded NC. All particles exhibited negative zeta potentials, ranging from -19.4 mV (PLGA 502 NC) to -30.4 mV (PEG_{2k}-PLGA_{11.5k} NC). The entrapment efficiency of C6 was higher for PLGA 502 NC (43.5%) than for PLGA 505 NC (6.9%). C6 was encapsulated considerably more efficiently with 95.4% found for PLGA 502H NC.

5.6.1 Effect of the Inertial Cavitation of Nanocapsules on the Serum Protein Adsorption

An initial hypothesis-generating experiment was conducted to assess the influence of the inertial cavitation of NC on the protein corona. C6-loaded PLGA (Resomer[®] RG 502) and PEG_{2k}-PLGA_{11.5k} NC were redispersed in ultrapure water and (i) incubated in 10% FBS for 60 min and exposed to ultrasound, (ii) incubated in 10% FBS for 60 min without ultrasound exposure or (iii) incubated in 10% FBS for 1 min and directly exposed to ultrasound. The concentration of NC was kept at 0.5 µg/mL for all experiments. The NC were washed by centrifugation, the proteins bound to the NC surface detached and subsequently, analyzed using SDS-PAGE (Figure 53A).

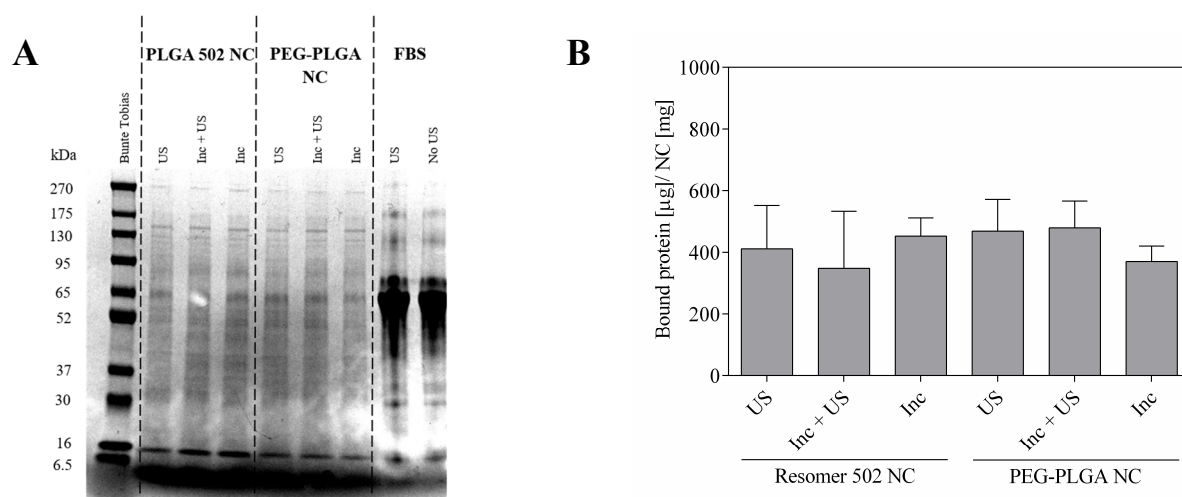


Figure 53 (A) A picture of reducing SDS-PAGE of proteins desorbed from PLGA 502 NC and PEG_{2k}-PLGA_{11.5k} NC following incubation in 10% FBS for 1 min and ultrasound exposure (US), incubation in 10% FBS for 60 min and ultrasound exposure (Inc + US) or incubation in 10% FBS for 60 min without ultrasound exposure (Inc). 5% FBS was used as positive control. (B) BCA assay of proteins desorbed from NC. Data are representative of three samples from one batch.

5% diluted FBS, which was used as reference, did not demonstrate any difference between samples expose to ultrasound or not under the chosen conditions. The most prominent band at approximately 66 kDa was likely to correspond to BSA [362]. The NC samples were characterized by a protein pattern composed of multiple protein bands ranging from 16 kDa to 270 kDa. An accumulation of protein bands occurs between 37 kDa and 95 kDa and a sharply defined band was located at the top of the gel above 130 kDa. Besides, two distinctive bands

appeared around 30 kDa. Figure 53A shows that the composition of the protein corona of PEGylated NC as well as non-PEGylated NC remained stable after ultrasound insonation. As the MI of ultrasound settings remain under 1.9, it was not expected to see any changes in protein properties and their binding affinities. However, if a high dosage of ultrasound is used, it can thermally and sonochemically induce denaturation of proteins [363].

To focus on the behavior of the protein corona formed around NC upon exposure to ultrasound, the BCA assay was applied after purification and separation of the NC from unbound serum proteins. With this quantitative colorimetric assay the total amount of proteins bound to the NC was determined (Figure 53B). Control experiments confirmed that the particles and the C6 did not interfere with photometric measurement of the PierceTM BCA assay (data not shown). After protein corona formation and centrifugation, the redispersed pellets in 1% SDS were heated to detach bound proteins and 10 μ L of each sample were mixed with 200 μ L of the freshly prepared BCA solution. Following 1 h incubation at 37 $^{\circ}$ C, the samples were measured for a protein concentration. The amount of bound proteins was in the same concentration range for PLGA 502 NC and PEG_{2k}-PLGA_{11.5k}, with around 400 μ g/mg. The amount of bound proteins did not change after ultrasound treatment, which correlates with SDS-PAGE data. It was suggested that in this setting the ultrasound had no influence on the protein binding.

5.6.2 Influence of Serum Incubation Temperature on Cavitation Activity

A variation of the water tank temperature of the ultrasound set-up has been shown to exert an impact on the inertial cavitation, as previously shown in section 5.5.2. In order to assess the influence of the incubation temperature of NC with serum proteins on their ultrasound activity, an investigation was conducted to examine the effect of temperature variations. For this purpose, C6-loaded PLGA (Resomer[®] RG 502) NC were incubated in aqueous 10% BSA or 10% HSA with a concentration of 40 mg/mL. Serum albumin represents the most abundant protein component in the blood plasma of all vertebrates and constitutes around 60% of all proteins in serum [364-366]. Due to its high prevalence in serum, it is a suitable option to consider before conducting experiments with serum or blood. In HS, the concentration of serum albumin typically ranges from 35 mg/mL to 50 mg/mL [364]. Although BSA and HSA share only 76% similarity in their structure, chemical composition and biological functions [367, 368], BSA is widely used as a substitute for HSA in many biochemical and pharmacological applications due to its lower production costs and ready availability [367].

Incubation of NC in BSA or HSA was performed at 25 $^{\circ}$ C and 37 $^{\circ}$ C for 60 min before exposed to ultrasound. Additionally, NC were redispersed in ultrapure water, 10% BSA or 10% HSA

without incubation. In Figure 54A (BSA) and B (HSA) VSD of NC ultrasound response is plotted over time of 560 s. NC redispersed in water were ultrasound active for 300 s with the initial VSD level of $1.0 \times 10^{-6} \text{ V}/\sqrt{\text{Hz}}$. A comparable cavitation profile was detected for NC only redispersed in 10% serum albumin with no difference between BSA or HSA. NC that were additionally incubated at 25 °C for 60 min in BSA or HSA demonstrated a similar cavitation trend as non-incubated NC. When the temperature was increased to 37 °C, the decrease in cavitation activity was observed for both types of serum albumins. Qi *et al.* [369] showed theoretically and practically that BSA molecules are adsorbed on the bubble wall, when air bubbles are exposed to aqueous BSA solution, which affect cavitation activity of air bubbles. As the temperature increases (from 25 °C to 37 °C), the cavitation intensity profiles showed a concomitant decrease. The change in the wall properties of nanobubbles on the NC surface due to increased temperature may increase the shell elasticity of bubble wall resulting in lower cavitation intensity at 37 °C. Guo *et al.* [370] showed that the higher the shell elasticity and viscosity, the higher the damping, leading to higher threshold values, which could mean lower cavitation intensity. NC incubated in HSA showed two times higher initial cavitation activity ($0.5 \times 10^{-6} \text{ V}/\sqrt{\text{Hz}}$) (Figure 54A) as NC incubated in BSA ($0.25 \times 10^{-6} \text{ V}/\sqrt{\text{Hz}}$) (Figure 54B). A difference was also observed in the duration of inertial cavitation. NC incubated in HSA were 100 s longer active as NC incubated in BSA. This indicates that not only incubation temperature has an impact on ultrasound activity of NC but also the type of serum albumin.

In order to investigate the different acoustic activity of BSA and HSA, serum albumins without NC were exposed to ultrasound. Results in Figure 54C and D represent the cavitation profiles of both serum albumins incubated at 25 °C and 37 °C for 60 min. Cavitation activity of BSA was low, starting at $0.25 \times 10^{-6} \text{ V}/\sqrt{\text{Hz}}$ when incubated at 25 °C and was active for 150 s. When BSA was incubated at 37 °C, no signal was detected already at the start of the measurement. In contrast, the inertial cavitation profiles of HSA showed higher initial broadband noise of $0.5 \times 10^{-6} \text{ V}/\sqrt{\text{Hz}}$ at 25 °C and $1.0 \times 10^{-6} \text{ V}/\sqrt{\text{Hz}}$ at 37 °C as well as a longer cavitation duration of about 300 s. Evidently, serum albumins alone could have a specific acoustic activity, which could provide additional inertial cavitation to NC in the body. Why albumins are acoustically active, has not been described in the literature yet, but most probably proteins could induce a heterogeneous nucleation on the NC surface in a liquid, resulting in different inertial cavitation. Consequently, differences of albumins from different mammalian species could have an importance on ultrasound cavitation. Some major differences in electrophoretic behavior [371], thermal and chemical stability [372], binding and photochemical properties [373] exist between BSA and HSA. The difference in acoustic cavitation between BSA and

HSA is likely due to their hydrophilic and thermal properties. As mentioned before, the structure of BSA and HSA differ, affecting their hydrophilicity. HSA is more hydrophobic than BSA [368, 374], which could improve the acoustic activity [239]. Regarding the thermal characteristics, Michalik *et al.* showed in a DSC study that HSA has a higher thermal stability than its bovine counterpart [375]. This could also be an explanation why BSA lost ultrasound activity at 37 °C (Figure 54C).

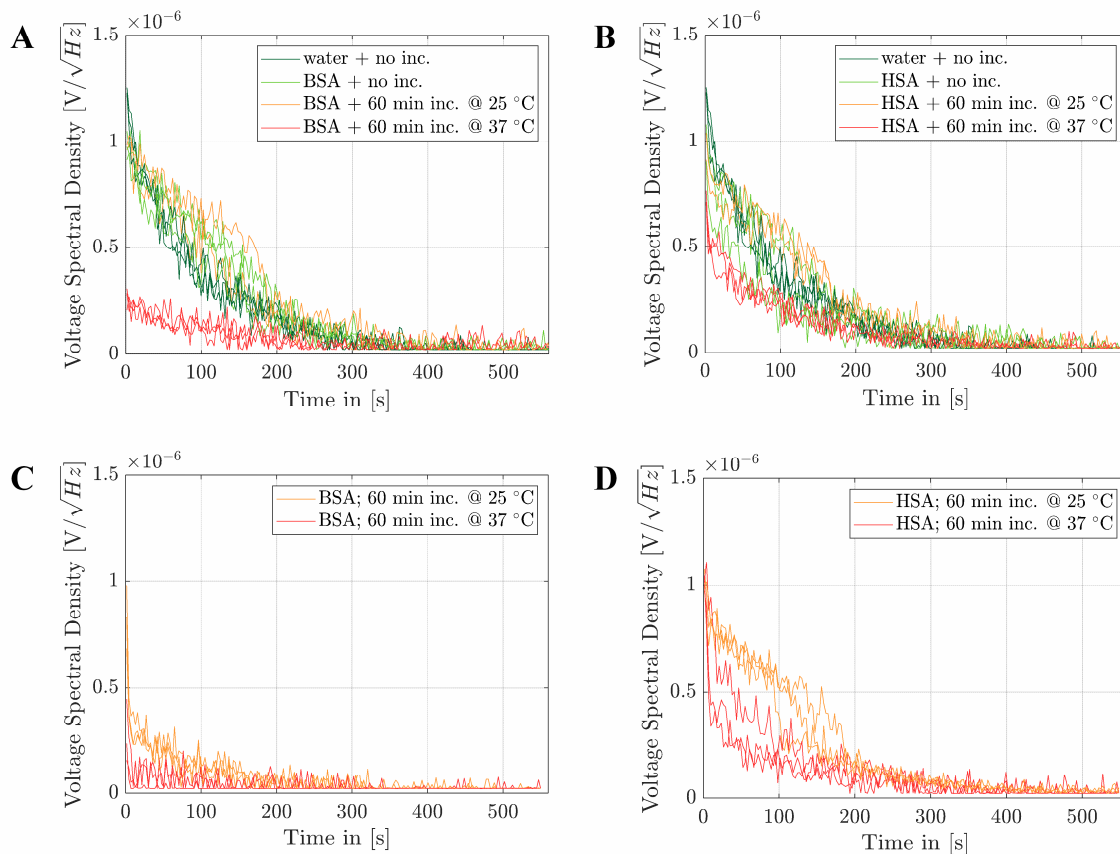


Figure 54 Ultrasound response of (A) C6-loaded PLGA 502 NC redispersed in ultrapure water and 10% BSA, (B) C6-loaded PLGA 502 NC redispersed in ultrapure water and 10% HSA, (C) 10% BSA and (D) 10% HSA at 750 kHz and 1.02 kPa (set-up 1) after incubation at different temperatures for three individual measurements.

To further validate the effect of incubation parameters on inertial cavitation of NC, FBS was used since it represents a complex mixture of various molecules (proteins, lipids, carbohydrates, hormones, enzymes) [376] and gives a more realistic representation of biological environment as just BSA or HSA. The effect of incubation time was investigated on C6-loaded PLGA (Resomer® RG 502) NC incubated in aqueous 10% FBS at 37 °C for different time slots followed by ultrasound exposition. NC measured directly after adding 10% FBS showed high inertial cavitation with an initial value of $1.2 \times 10^{-6} \text{ V}/\sqrt{\text{Hz}}$ and 300 s of signal duration (Figure 55A). With increasing incubation time, ultrasound profiles changed. After 5 min of incubation in 10% FBS, inertial cavitation of NC started at $0.9 \times 10^{-6} \text{ V}/\sqrt{\text{Hz}}$ and lasted for 200 s. After

10 min of incubation the ultrasound response was negligible. Following transformation of the VSD values to AUC, the resulting signal-response curve exhibited distinct decline in inertial cavitation intensity (Figure 55B). According to Figure 55B, the NC-induced ultrasound response reached a plateau with about $0.3 \times 10^{-4} \text{ V/Hz}^{1/2}$ at 10 min of incubation. As mentioned before temperature could affect the shell elasticity of protein wall that occurs on nanobubble surface after incubation [370]. It seem that 10 min of incubation is sufficient for proteins to cover all surface of nanobubbles on NC followed by the decrease in the cavitation activity due to increased shell elasticity of bubble wall as a result of higher temperature.

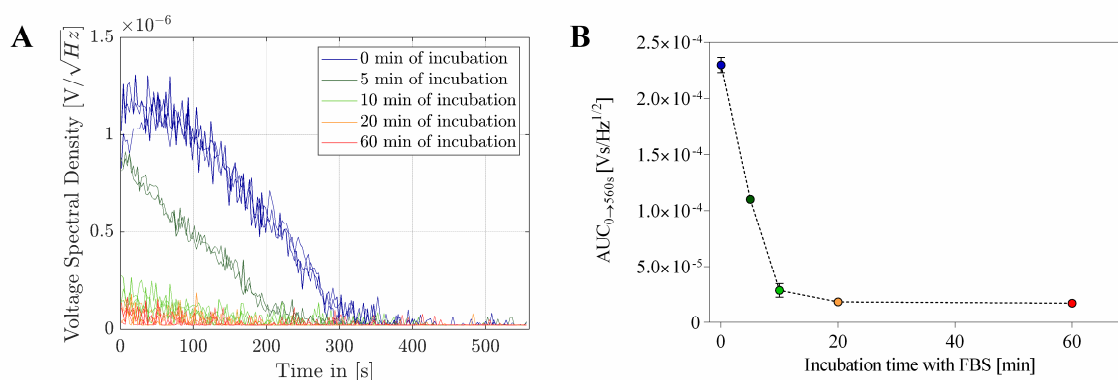


Figure 55 Effect of incubation time of C6-loaded PLGA 502 NC in 10% FBS on acoustic response in the ultrasound at 750 kHz and 1.02 kPa (set-up 1). (A) The results are given as plots of the VSD *versus* treatment time of the three replicate individual samples. (B) AUC of VSD at different incubation times presented in means \pm SD of replicates from three independent experiments.

In summary, temperature and duration of incubation of NC in serum have a strong impact on inertial cavitation. In agreement with previous experiments, lower incubation temperatures lead to higher ultrasound response.

5.6.3 Determination of Physicochemical Properties and Ultrasound Activity of Nanocapsules after Incubation in Different Culture Media

Numerous studies suggested that the protein corona composition plays a crucial role in dictating the interaction of nanoparticles with their surrounding environment. One of the factors that determine the composition of the nanoparticle protein corona could also be the composition of media used for dispersion of nanoparticles for biological experiments [377]. Strojjan *et al.* has determined the effect of different dispersion media, including divalent ions and macromolecules, on the composition of the protein corona of nanoparticles [331]. To investigate, whether different dispersion affect the resulting protein corona, their physicochemical properties and ultrasound activity, dispersions of C6-loaded and unloaded PLGA 502 NC were prepared in six different biologically relevant media: ultrapure water,

5% (m/V) glucose, 0.9% (m/V) NaCl, PBS and RPMI. Properties of the media used were presented in Table 14. The dispersion media in this study are commonly employed in most cell culture laboratories or typically applied in humans and have the potential to serve as dispersion media for NC in *in vitro* experiments [378-381]. The protein corona was formed in 10% FBS since this is typically used the cell culturing [382].

In Figure 56A no difference in size of C6-loaded PLGA 502 NC between dispersion media was seen with a hydrodynamic diameter around 280 nm for all samples. The formation of the protein corona in 10% FBS increased the hydrodynamic diameter up to 370 nm independent of dispersion media. Upon contact with proteins, some of the proteins adhered to NC surface [383, 384] and increased the hydrodynamic diameter [361, 385, 386]. Yu *et al.* [387] and Lee *et al.* [388] reported similar increase in particle size, when PLGA nanoparticles were incubated in 10% PLGA, which is normally attributed to the protein adsorption on the nanoparticle surface.

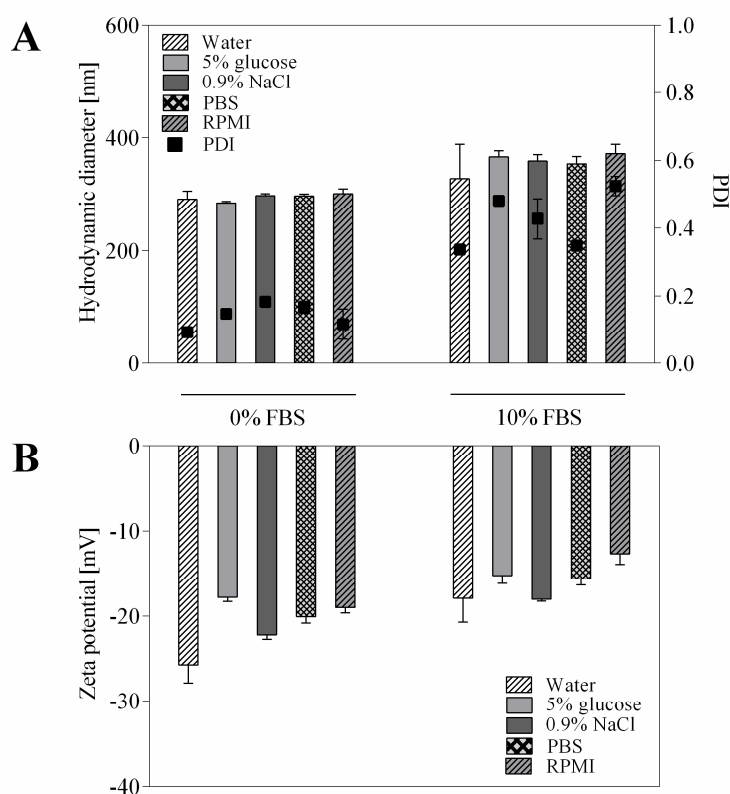


Figure 56 Characterization of C6-loaded PLGA 502 NC in different dispersion media with or without 10% FBS. Hydrodynamic diameter (A), PDI (A) and zeta potential (B) are presented. Data are means \pm SD from three independent experiments.

In comparison to freshly redispersed lyophilizates in ultrapure water, an increase in PDI was observed for almost all other dispersion media (Figure 56A). In generally, higher PDI values (>0.3) were found for NC incubated in 10% FBS. The size distribution profiles (data not shown)

of the NC incubated in 10% serum indicated three different particle size groups attributed to non-attached proteins, NC and NC agglomerates resulting in increased PDI values. Similar profiles were presented by Zhang *et al.* who incubated PLGA nanoparticles in PBS and 10% FBS and reported multimodality of nanoparticle distribution [389].

The zeta potential of polymer NC exhibited different affects upon incubation in various media (Figure 56B). It was observed that the intrinsically negative charged NC dispersed in water became less negative in 0.9% NaCl, PBS and RPMI. When the ionic strength of media increased (Table 14), the absolute values of the zeta potential were reduced [390]. Multivalent ions in the presence of NC seemed to reduce the overall net charge [391]. Regardless of the dispersion media, the presence of FBS led to a change of the zeta potential values of NC due to the formation of the protein layer at the NC surface [391]. In Figure 56B, FBS was found to change the surface charge from an initial value of about -25 mV from redispersed NC in ultrapure water to more than -20 mV in addition of FBS. In addition, NC dispersed in other media revealed an increase of the zeta potential between -18 mV and -12 mV, when FBS was added. Very similar values demonstrated that zeta potential in media with 10% FBS, which was suggested to be dominated by the presence of charged proteins presented in the outer shell due to electrostatic interactions [331], while in media without FBS the ion composition (i.e. ionic strength, type and concentration) determined the zeta potential [392].

In order to gain a deeper understanding on the impact of different dispersion media on NC in the biological system, it is crucial to examine how dispersed NC interact with proteins in the biological environment. To assess the overall protein adsorbed onto the NC, SDS-PAGE protein separation was employed. The pattern of detached proteins from NC that were dispersed in different media and incubated with 10% FBS appeared to be very similar (Figure 57A). In addition, C6-loaded NC did not showed any greater diversity of profiles than unloaded NC. Moreover, four prominent bands of small molecular weight protein (65 kDa, 37 kDa, 30 kDa and 16 kDa) appeared in all NC staining profile, regardless of the dispersion media. These identified proteins are also present in the positive control of 5% FBS. Among all tested samples, the protein with the molecular weight of approximately 65 kDa is the most prevalent, and its molecular weight is consistent with the molecular weight of albumin [362]. The appearance of bands around 30 kDa and 37 kDa could be related to binding of apolipoprotein E (ApoE, 34 kDa) [393] or beta-2-glycoprotein I, also known as apolipoprotein H (ApoH, 38 kDa), which was also detected by Partikel *et al.* [359] in protein corona of PLGA nanoparticles incubated in FBS. The band below 16 kDa is most likely relative to apolipoprotein C (ApoC) [394] or

hemoglobin fetal subunits also reported by Antonio *et al.* [395] and Partikel *et al.* [359]. The results were emphasized by the colorimetric BCA assay to analyze the total amount of accumulated proteins (Figure 57B). The quantified protein amount of samples redispersed in water was about 300 $\mu\text{g}/\text{mg}$. Higher protein amount was detected for the NC dispersed in media containing ions with the highest amount of 500 $\mu\text{g}/\text{mg}$ for the NC dispersed in RPMI. Evidences in the literature suggest that higher ionic strength of surrounding media allows proteins to adsorb in a more dense packed layer due to shielding effect [396]. The ionic strength values of different media were given in Table 14. Ultrapure water have an ionic strength at 0 mM, while media containing ions at around 160 mM. The experimental results shown that amount of bound protein in media with high ionic strength was higher than in water. However, the results of 5% glucose media was also higher than water though the ionic strength of 5% glucose is 0 mM.

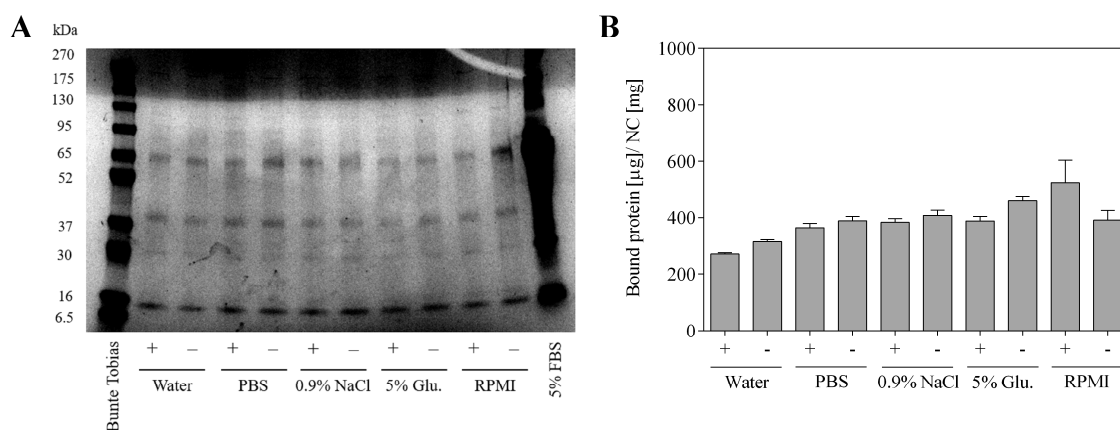


Figure 57 (A) SDS-PAGE and (B) BCA assay of proteins desorbed from C6-loaded (+) and unloaded (-) PLGA 502 NC dispersed in different media and incubated in 10% FBS for 60 min. 5% FBS on the right is reported for reference and positive control derived from pure serum diluted with ultrapure water. “Bunte Tobias” denotes lane loaded with molecular mass standards. BCA assay data are representative of three independent experiments.

After redispersion in different media and 10% FBS all formulations were examined in the ultrasonic field (Figure 58). The VSD profiles showed no differences between the various dispersion media. All dispersion media are water-based and have a surface tension similar or higher to water [397-400], suggested to be unable to wet all the pores on the NC surface enabling the entrapment of air. In contrast, the results presented in Figure 50 showed that ethanol with lower surface tension as water wetted the surface much better, which caused poor inertial cavitation. All samples in Figure 58 had an initial cavitation activity between $1.0 \times 10^{-6} \text{ V}/\sqrt{\text{Hz}}$ and $1.5 \times 10^{-6} \text{ V}/\sqrt{\text{Hz}}$, which decreased during treatment and approached the bottom after 300 s. In the previous section, it was already demonstrated that incubation in FBS for more than 10 min has an adverse effect on cavitation activity, therefore the 10% FBS was added to the dispersion directly before the treatment. Despite several studies showing that

proteins and other biological molecules on the hydrophobic nanoparticle surfaces in biological fluids reduce their acoustic activity [308, 401], there was no difference observed in cavitation profiles, when FBS was added to the NC dispersed samples.

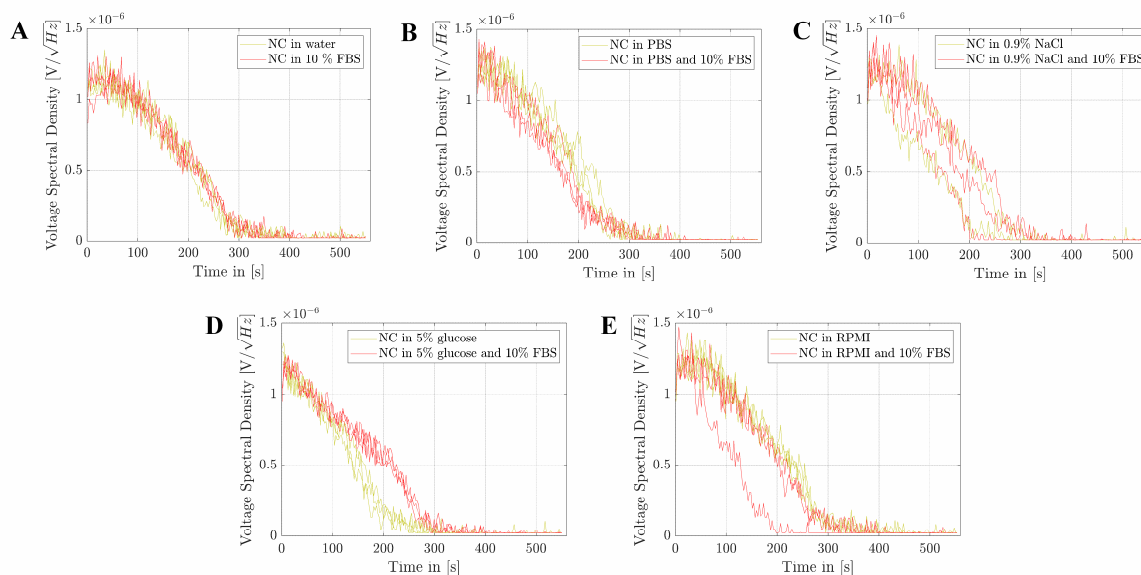


Figure 58 VSD plotted over time of C6-loaded PLGA 502 NC dispersed in five different media with or without 10% FBS for three individual samples. Ultrasound response was measured at 750 kHz and 1.02 kPa (set-up 1).

In general, there were no obvious differences in protein corona profiles and ultrasound activity, when NC were redispersed in different biologically relevant media. The media composition was found to influence the NC surface charge differently but without inducing irreversible aggregation.

5.6.4 Effect of Polymer Molar Mass and PEGylation on the Protein Corona and Depending on the Serum Type

The present study examined the protein corona that forms around various types of PLGA NC using two different serum types, FBS and HS. NC investigated in this study were composed of the biodegradable polymer PLGA, which was stabilized with PVA and synthesized using an emulsification-diffusion method. Various commercial PLGA polymers were utilized differing in their molar mass (7,000-69,000 g/mol), terminal groups (ester or acid) and PEGylation, but all with 50:50 lactide:glycolide ratio to evaluate the influence of these parameters on the protein corona. NC were prepared with or without C6 incorporation in a concentration of 1:250 dye-to-polymer ratio. After NC were dispersed in water at the concentration of 0.5 $\mu\text{g/mL}$, incubated in serum and washed of unbound proteins, the protein corona was characterized by SDS-PAGE and BCA assay.

The results obtained from SDS-PAGE demonstrated a noticeable contrast in corona protein identity between the two different biological incubation fluids (Figure 59). Three separate electrophoresis runs were conducted to ensure accuracy of the results. The protein patterns were reproducible and one representative example of the gel used for the incubation of different NC with FBS is presented in Figure 59A.

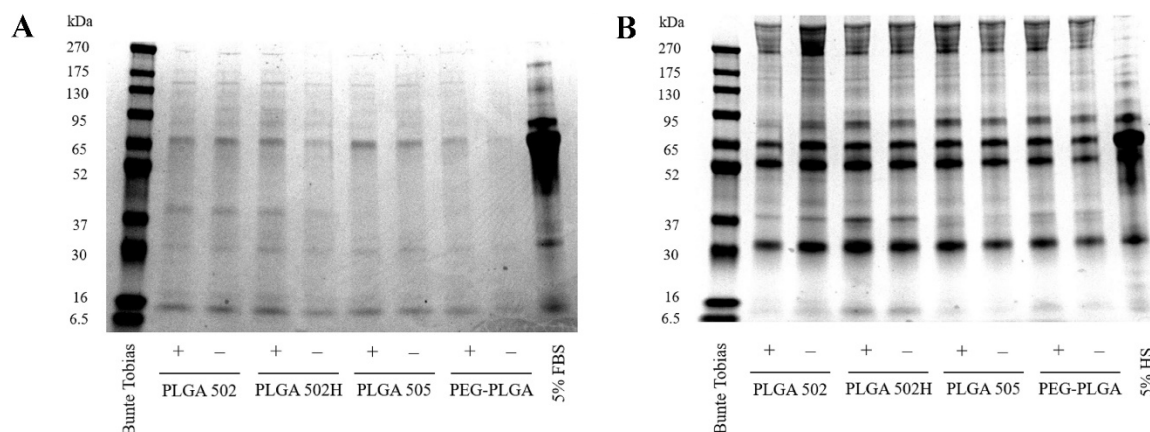


Figure 59 SDS-PAGE of adsorbed serum proteins obtained from the protein corona of PLGA and PEG-PLGA NC following incubation in (A) 10% FBS and (B) 10% HS. NC were loaded with C6 (+) or unloaded (-). 5% FBS or 5% HS on the right lane were reported as reference and positive controls derived from pure serum diluted with ultrapure water. “Bunte Tobias” denotes the lane loaded with molecular mass standards.

The presence of a dominant band at around 65 kDa, corresponding to serum albumin, was prominent in the positive control (5% FBS). The protein pattern of the NC displayed numerous protein bands with molecular weights ranging from 6.5 kDa to 270 kDa. Prominent bands were observed at about 30 kDa, 37 kDa and 65 kDa. Figure 59A shows that the pattern of the protein corona remained comparable over a wide range of different types of NC, while the intensity of the protein bands at around 30 kDa, 37 kDa and 65 kDa for different NC changed. In comparison to the corona of PLGA 502 NC and PLGA 502H NC, the PLGA-PEG NC yielded a protein pattern consisting of less protein bands with considerably lower intensity, which was also reported by Partikel *et al.* [358]. The most prominent change in the band intensity was at around 37 kDa. The bands at 37 kDa showed a higher density for PLGA 502 NC and PLGA 502H NC, independent on the presence of the dye. Based on the size, the appearance of these bands could be related to ApoE (34 kDa) [393] or ApoH (38 kDa) [359]. The PEGylated NC have a higher hydrophilicity than non-PEGylated NC because of the hydrophilic PEG chains [358]. Owing to their lipid-binding domains, apolipoproteins tend to have a preference for adsorbing onto hydrophobic nanoparticles [402-404], such as PLGA 502 NC. This could be the reason, why the band at 37 kDa was not seen at PEGylated NC, but it was seen at PLGA 502 NC. Furthermore, Hartl *et al.* has identified overproportional amount of ApoE presented on nanoparticles with the lowest hydrophilicity [405]. Bertrand *et al.* has shown that nanoparticles

with higher PEG density appeared to have lower abundance of ApoE [360]. It was seen that hydrophilicity according to acidic ending of PLGA 502H polymer did not have such a strong effect on the interaction with ApoE or ApoH. However, the molecular mass of polymer could play an important role by interaction between polymer and protein. With increasing molecular weight (PLGA 502 NC to PLGA 505 NC), however, less protein seemed to bind to the NC surface, underlining the effect of a lower number of presented polymer end groups. Spreen *et al.* [406] explained that higher molecular weight polymer results in lower amount of polymer chains to form a NC of a fixed size. Consequently, this phenomenon results in a reduced number of terminal ester groups on the nanoparticle surface available for further protein interaction. For FBS incubation (Figure 59A), this observation was confirmed with lighter band at 37 kDa for PLGA 505 NC compared to its counterpart of lower molecular mass.

Another interesting observation made by the current study was that the composition of the protein corona changed when HS was used instead of FBS. When using HS, the protein signature was found to be dominated by three intense protein bands on the SDS-PAGE (Figure 59B), with corresponding molecular weights of about 30 kDa, 52 kDa and 65 kDa. It is likely that the 65 kDa band corresponds to HSA, while the bands at 30 kDa and 52 kDa are presumed to correspond to the light and heavy chain subunit of immunoglobulin G (IgG), respectively. Another band slightly below 95 kDa could resemble transferrin with molecular mass of 75 kDa [407]. In comparison to FBS, the use of HS resulted in visibility of bands that represent IgG light and heavy chains, which could be consistent with the reduced antibody content of FBS. Pisani *et al.* described the same phenomenon of the reduced amount of immunoglobulins in the FBS protein corona [408]. Pusch *et al.* also observed that the pattern with nanoparticles incubated in the presence of FBS and HS appeared distinctively different [409]. In general, the intensity of all protein bands was stronger when HS was used instead of FBS at the same concentration.

Additionally, the quantification of corona proteins was preformed by BCA assay and revealed a higher adsorbed amount of proteins after NC incubation in HS as in FBS (Figure 60). The results indicated that the total concentration of proteins was approximately twice as high after incubation in 10% HS compared to 10% FBS. For example, the amount of protein bound to C6-loaded PLGA 502 NC after the addition of 10% serum was 185 $\mu\text{g}/\text{mg}$ for HS and 450 $\mu\text{g}/\text{mg}$ for FBS. This provides additional evidence that the different adsorptive capacities of PLGA NC for two serum types were a result of higher affinity of multiple human proteins to the surface of NC. In general, the quantity of bound proteins was higher in comparison to FBS, which could

be attributed to the higher protein content of HS and stronger affinity of HS to the nanoparticle surface [359]. Thereby, surface properties regarding the end groups (either acidic- or ester-terminated) seemed to impact the binding behavior. For FBS and HS, the protein amount bound to PLGA 502H NC was twofold as high as on PLGA 502 NC. Due to the amphiphilic constitution of proteins and their permanently charged state [410], ionic interactions between amino acids of the proteins and carboxylic residues on the nanoparticle surface outweighed potential hydrophobic attraction to the lipophilic polymer backbone.

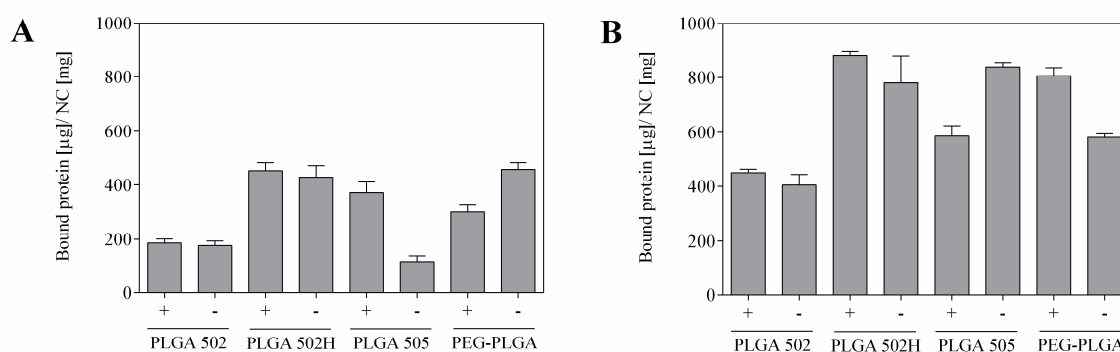


Figure 60 Quantification of the total amount of proteins adsorbed on C6-loaded (+) or unloaded (-) NC after incubation with (A) 10% FBS and (B) 10% HS for 60 min at 37 °C and subsequent purification (n=3, mean ± SD).

The acquired data revealed that the type of serum had a profound effect on corona composition in both quantitative and qualitative terms. Regarding the molecular weight of the polymer and polymer hydrophobicity, adsorption profiles on NC systems with similar physicochemical characteristics differ qualitative, while surface end group identity differ quantitative. The findings suggested that the origin of the protein source is a critical determinant in defining the biological identity of NC. As such, caution must be exercised in extrapolating results obtained from animal models directly to humans [409]. Nevertheless, FBS remains a widely used protein source for examining of the reaction at the interface between nanoparticles and biomolecules [385, 411].

5.6.5 Influence of pH and Ionic Strength on Protein Corona and Inertial Cavitation

Using artificial body fluids for the testing of nanoparticles ensures a constant composition as well as easy accessibility compared to physiological body fluids like plasma or blood but lacks the biomolecule (proteins, lipids) content [209]. During uptake in cells, the protein corona is suggested to be retained and afterward degraded in lysosomes. In this study, we used as dispersion media for NC an ALF (pH 4.5), which mimics the conditions within lysosomes [208, 209] to examine the influence of lower pH values on biomolecule adsorption as well as

cavitation behavior of NC. As before, the same four different PLGA NC were selected for this study either loaded with C6 or not. To investigate changes of the protein corona, NC were redispersed in ALF and incubated in 10% FBS. NC were separated by centrifugation and the remaining proteins were visualized using SDS-PAGE as described above.

A protein binding preference and structure change in response to pH, which can dramatically alter its stability and biological activity [377, 412, 413]. Protein adsorption is preferred at its isoelectric point (pI) because electrostatic repulsion and protein-protein interactions are minimized, allowing compact protein molecules to tightly pack onto the surface of the nanoparticles [414]. The pI value of HSA and BSA is around 4.7 [415], which is close to the pH of ALF media and albumin adsorption to NC could reach its maximum.

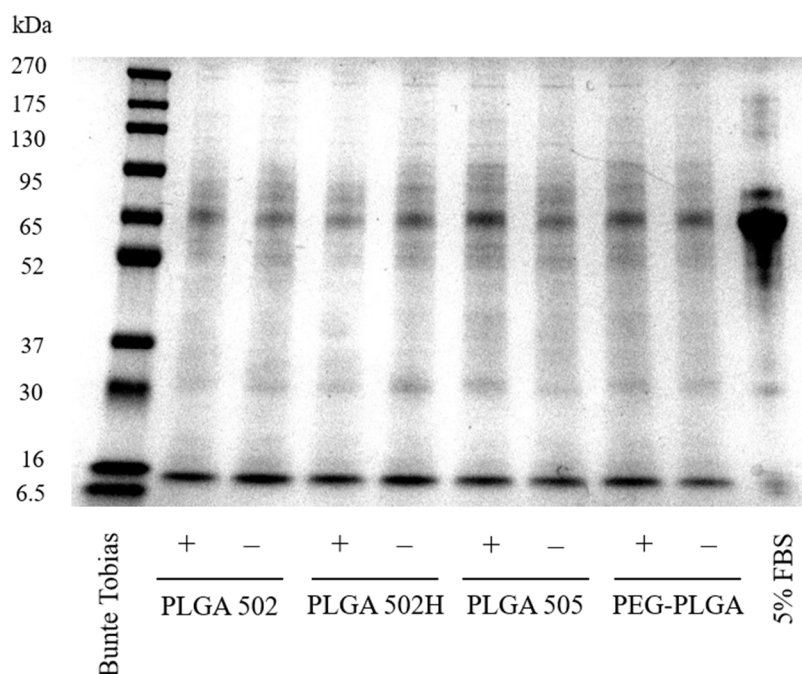


Figure 61 Qualitative determination by SDS-PAGE of the FBS-derived protein corona of four different PLGA NC loaded with (+) or without (-) C6 and dispersed in ALF. 5% FBS on the right is reported for reference and positive control derived from pure serum diluted with ultrapure water. “Bunte Tobias” denotes lane loaded with molecular mass standards.

An overview of the bound proteins on different NC incubated in FBS and ALF is visualized in Figure 61. The most dominant protein was FBA at around 65 kDa. The intensity of its band was much stronger as by other proteins indicating a stronger protein adsorption. Besides the fact that FBA is the most abundant protein in the serum [364-366], also its pI lies in the same range as ALF pH. Some other proteins, such as fibrinogen (pI 5.5-5.8), IgG (pI 5.9-6.1), transferrin (pI ~6), hemoglobin (pI 6.3), ApoE (pI 5.3), apolipoprotein A1 (pI 5.9-5.5), clusterin (pI 4.9-5.4) [414] own higher pI. At pH less than pI, protein molecules are strongly positively charged,

which adsorb onto the negatively charged nanoparticle surface by electrostatic attraction. Due to a high net charge of proteins, electrostatic repulsion exist between protein molecules adsorbed on the nanoparticles and unadsorbed molecules in bulk. The electrostatic repulsion between the adsorbed and unadsorbed molecules hinders the further adsorption and limits the amount of the surface adsorbed protein at pH 4.5 [416].

Along with pH, the surrounding solution ionic strength is an essential parameter that greatly influences the architecture and biological activity of protein corona [377, 413]. Ionic strength of media used for NC redispersion were presented in Table 14. The ionic strength value of pH 4.5 ALF aqueous solution was calculated as 979.8 mM. It was seen that this value was about six times higher as the values of 0.9% NaCl and PBS solutions. Higher ionic strength results in a shielding effect where the adsorption of charged proteins to oppositely charged nanoparticles is hindered, while the adsorption to similarly charged nanoparticles is enhanced [377, 417, 418]. These shielding electrostatic interactions allow proteins to adsorb in a more closely packed layer [396].

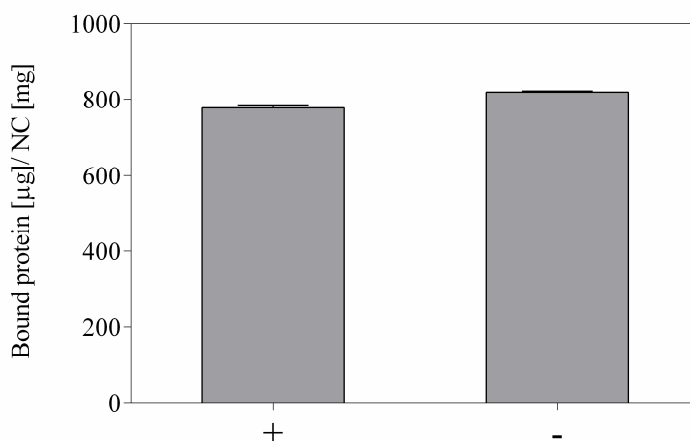


Figure 62 BCA assay quantification of the total amount of proteins adsorbed on C6-loaded (+) or unloaded (-) PLGA 502 NC redispersed in ALF pH 4.5 after incubation with 10% FBS for 60 min at 37 °C and subsequent purification (n=3, mean \pm SD).

The quantification of the total amount of proteins adsorbed on PLGA 502 NC after redispersion in ALF (Figure 62) showed higher values as other redispersion media (Figure 60), when incubated in FBS. Comparing ALF values to ultrapure water with ionic strength at 0 mM, the adsorbed amount of proteins was three times higher, while this value was just two times higher as in the media with ionic strength about 160 mM (0.9% NaCl, PBS). This observation confirmed the fact that ionic strength influence the adsorption of proteins onto nanoparticles. However, excessively high ionic strength can cause charge screening, leading to unwanted

aggregation of protein-nanoparticle complexes [419]. In ALF redispersed PLGA 502 NC showed after incubation in FBS a hydrodynamic diameter of more than 1000 nm and polydispersity (data not shown). In comparison with other dispersion media (Figure 56), the ALF solution induced a greater aggregation of NC. In general, pH and ionic strength conditions that lead to a less stable conformation for the protein in solution will lead to an increased adsorbed mass, assuming that the protein molecule is more stable on the solid surface [377, 420].

However, in the present study, the NC were incubated in ALF medium for 1 h. In contrast, Rabel *et al.* [421] incubated nanoparticles for 72 h, observing rapid reduction in the quantity of adsorbed proteins during the first hours of incubation in ALF. This reduction is likely attributed to the strong electrostatic interactions of negatively charged proteins and the cationic polymer. In the present study, no cationic polymers were used, which could result in slower dissociation and degradation of the proteins from the nanoparticle surface. However, still further studies of long time stability are needed to see if the ALF has a degradation effect on NC protein corona. Rabel *et al.* [421] also found that a small amount of aggregated or denatured proteins remained on the surface of nanoparticles over the entire testing period. Similar findings were reported by Bertoli *et al.* [422] who investigated the lysosomal degradation of corona-bound proteins and demonstrated that the majority of these proteins were degraded in the lysosomes within 8-16 h following cellular uptake.

Additionally, the influence of lower pH value on the cavitation activity of NC was investigated (Figure 63). The aim was to stress NC and to observe their cavitation behavior.

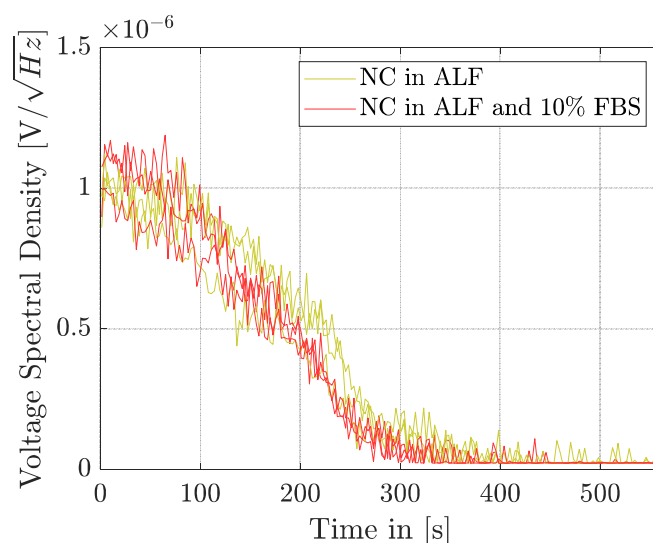


Figure 63 VSD plotted over time of C6-loaded PLGA 502 NC dispersed in ALF pH 4.5 with or without 10% FBS. Ultrasound response was measured at 750 kHz and 1.02 kPa (set-up 1) for three individual measurements.

Comparing cavitation profiles of NC dispersed in ALF with results of other dispersion media from Figure 58, a difference was not observed. Cavitation profile started at $1.0 \times 10^{-6} \text{ V}/\sqrt{\text{Hz}}$ and decreased over time until it reached the baseline after 300 s. Addition of 10% FBS before ultrasound measurement did not change the cavitation profile as already seen before using other dispersion media.

In summary, these results indicate that the protein corona of NC changes after dispersion in an acidic ALF media and incubation in FBS for 1 h. However, the change in the pH did not influence the cavitation activity of NC, and the cavitation profile was comparable with NC in other used dispersion media.

5.7 Biological Studies of NC Suitable for Ultrasound Model Drug Delivery

Administration of nanoparticles may cause irritating effects on cells or tissues and demands for careful evaluation of biocompatibility [423]. Therefore, assessment of nanoparticle toxicity is necessary in biomedical applications. In this study, the *in vitro* cytotoxicity of a variety of polymer NC considered as drug delivery systems was examined using different methods to measure changes in cell viability. The colorimetric MTS assay was selected to determine metabolic activity and it is based on the selective ability of viable cells to reduce MTS tetrazolium salt to colored formazan, which relies on their metabolic activity and is frequently used for screening of cytotoxicity [424]. Since the MTS assay allows for determination of metabolically active cells, the LDH assay can be applied to measure the degree of all membrane damaging effects [425]. Membrane damage was quantified by the release of the cytosolic enzyme LDH since a potential site of interaction of NC is the cell membrane [426]. The LDH test was applied to provide information on the effects of NC after short incubation times. As target cells LNCaP cell line and PBMC were used. LNCaP cell line represents a candidate for prostate cancer and has often been used to study different aspects of prostate cancer progression [427]. When NC enter the body through injection, into the circulatory system, they can come in direct contact with human PBMC before ultimately being distributed to the tumor where they can accumulate [428]. Despite the likely increased exposure to NC, a potential cytotoxicity in PBMC after exposure to NC, was investigated in this study. The physicochemical characteristics of PLGA (Resomer[®] RG 502) NC and PEG_{2k}-PLGA_{11.5k} NC considered for the cytotoxic experiments are given in Table 16.

Table 16 Average hydrodynamic diameter, PDI, zeta potential and entrapment efficiency of the C6 for all formulations used in the biological experiments. Data are means from two charges with SD values.

Sample	Hydrodynamic diameter [nm]	PDI	Zeta potential [mV]	Entrapment efficiency [%]
PLGA 502 NC (blank)	270.3 ± 5.7	0.10 ± 0.01	-15.9 ± 0.7	-
PLGA 502 NC (C6)	275.0 ± 3.0	0.13 ± 0.01	-15.5 ± 0.4	43.5 ± 2.5
PEG _{2k} -PLGA _{11.5k} NC (blank)	246.7 ± 4.0	0.14 ± 0.01	-22.0 ± 1.1	-
PEG _{2k} -PLGA _{11.5k} NC (C6)	289.0 ± 3.0	0.18 ± 0.02	-20.4 ± 0.9	5.8 ± 0.1

Average hydrodynamic particle diameters measured by DLS were found to be between 270 nm and 275 nm for PLGA NC and between 247 nm and 289 nm for PEGylated NC. The PDI for all formulations was <0.2 suggesting narrow size distributions. For PEG_{2k}-PLGA_{11.5k} NC loading of the NC led to higher average hydrodynamic diameter. In contrast, for PLGA 502 NC a loading did not show impact on particle sizes. All particles exhibited negative zeta potentials

ranging from -15.5 mV (PLGA 502 NC) to -22.0 mV (PEG_{2k}-PLGA_{11.5k} NC). The entrapment efficiency of C6 was higher for PLGA 502 NC (43.5%) than for PEG_{2k}-PLGA_{11.5k} NC (5.8%). The underlying effects were discussed already above.

5.7.1 Influence of PLGA NC with and without PEG on Metabolic Cell Activity

The MTS assay was chosen as a test for the influence of C6-loaded and unloaded PLGA (Resomer[®] RG 502) NC and PEG-PLGA (PEG_{2k}-PLGA_{11.5k}) NC on the metabolic activity of LNCaP prostate cancer cell line and PBMC. Cells were incubated with the NC at concentrations of 6 µg/mL, 60 µg/mL, and 600 µg/mL for 72 h. Figure 64 displays the calculated cell viability, with cell viability below 70% being considered cytotoxic according to DIN EN ISO 10993-5 [211]. The NC dilutions were prepared with concentrations ensuring that the highest concentration sample did not surpass 1 mg/mL. This precaution was taken as at higher NC concentrations an interference between the assay and the unspecific absorption of the nanoparticles could not be excluded [429]. Additionally, excessive high concentration of nanoparticles could completely cover the cells hindering their access to nutrients and oxygen in the medium and potentially resulting in unspecific cell death, which could lead to misinterpretations of *in vitro* results [430]. Untreated cells were used as negative control and were set as 100% viable cells. The applied positive control (9% Triton X-100 solution) resulted in a reduction of cell viability to $6.2 \pm 4.0\%$ and $3.4 \pm 0.1\%$ for LNCaP cell line and PBMC, respectively, thus confirming the validity of the method [431, 432]. An interaction of the NC with the cell culture medium was excluded by incubating the particles without cells, where a low absorbance was comparable to the background.

At the concentrations of 6 µg/mL and 60 µg/mL, none of the tested nanoparticles showed a cytotoxic effect on LNCaP cell line (Figure 64A) or PBMC (Figure 64B) after 72 h, independent of C6 incorporation and PEGylation. The viability values were comparable to those of the negative control (100%). This confirmed and supplemented previous research in the literature regarding the high biocompatibility of PLGA and PEG-PLGA nanoparticles [433-435]. In the previous studies, Ernst *et al.* [429] and Arnold *et al.* [436] determined that blank PLGA nanoparticles with or without PEG are non-toxic in concentrations up to 1 mg/mL using the MTT (3-[4,5-dimethylthiazol-2-yl]-2,5-diphenyltetrazolium bromide) assay. Another study presented examples indicating the crucial role of size and zeta potential of PLGA nanoparticles in defining the resulting cytotoxicity. An ideal nanoparticle size can provide an EPR effect, enhancing drug uptake by cancer cells, while proper zeta potential contribute to improved nanoparticle stability [437]. The systematic review indicated that PLGA nanoparticles with

sizes of less than 300 nm and an absolute zeta potential of ~ 20 mV are advantageous, aligning with the characteristics observed in this study for NC.

According to Figure 64A and B, at the highest test concentration (600 $\mu\text{g}/\text{mL}$), cell viability values were below 70% showing a moderate cytotoxicity for all PLGA and PEG-PLGA NC, except for blank PEG-PLGA NC, which appeared as non-toxic on both cell lines, most probably due to the stealth effect of PEG [438, 439]. Gryparis *et al.* reported a decrease in cytotoxicity with increasing PEG degree in the mPEG-PLGA copolymer used to prepare the nanoparticles [440]. The low viability values in Figure 64 could be attributed to technical settings and high water levels in the samples. Stock solutions of NC were prepared in water, while further dilutions were prepared with cell culture medium. Consequently, the highest NC concentration was in a more hypotonic environment as the other two NC concentrations, where the amount of water was negligible. The effect of water was previously shown by Božič *et al.* [441] where the results show that the media with very low osmolarity, such as distilled water, lead to low cell viability. Similar findings were observed with water controls, where the metabolic activity of cells was affected in a concentration-dependent manner when water was added in three different dilutions to the LNCaP cells (Figure 64A) or PBMC (Figure 64B). The cell viability decreased to 48.65-76.59% (D1), probably due to a hypotonic environment that was caused by the addition of water in the cell culture.

Comparing two types of cell lines, the metabolic activity in the presence of different quantities of the four NC formulations tested mostly resulted in similar effects, as seen in Figure 64. However, PBMC showed a slight higher cytotoxicity, which might be attributed to their higher cell sensitivity. Blood cells have the highest turnover value *per day* [442], which could mean they are constantly regenerating, and are, therefore, the most sensitive type of cells. However, different nanoparticles have different toxic effects in human PBMC or LNCaP. Schleifman *et al.* [443] used PLGA nanoparticles and observed no significant cytotoxic effects on PBMC up to nanoparticle concentration 2 mg/mL. Gryparis *et al.* tested blank mPEG-PLGA nanoparticles at various concentration on LNCaP cells and showed that more than 600 $\mu\text{g}/\text{mL}$ nanoparticles were required in order to cause cell growth inhibition after 24 h [440].

The data revealed that the blank and C6-loaded PLGA and PEG-PLGA NC had no relevant cytotoxic effect on both cell lines. This result is consistent with other reports, which showed no cytotoxicity of blank PLGA and PEGylated nanoparticles up to 600 $\mu\text{g}/\text{mL}$ indicating that such delivery systems could be ideal for cancer-targeting purposes.

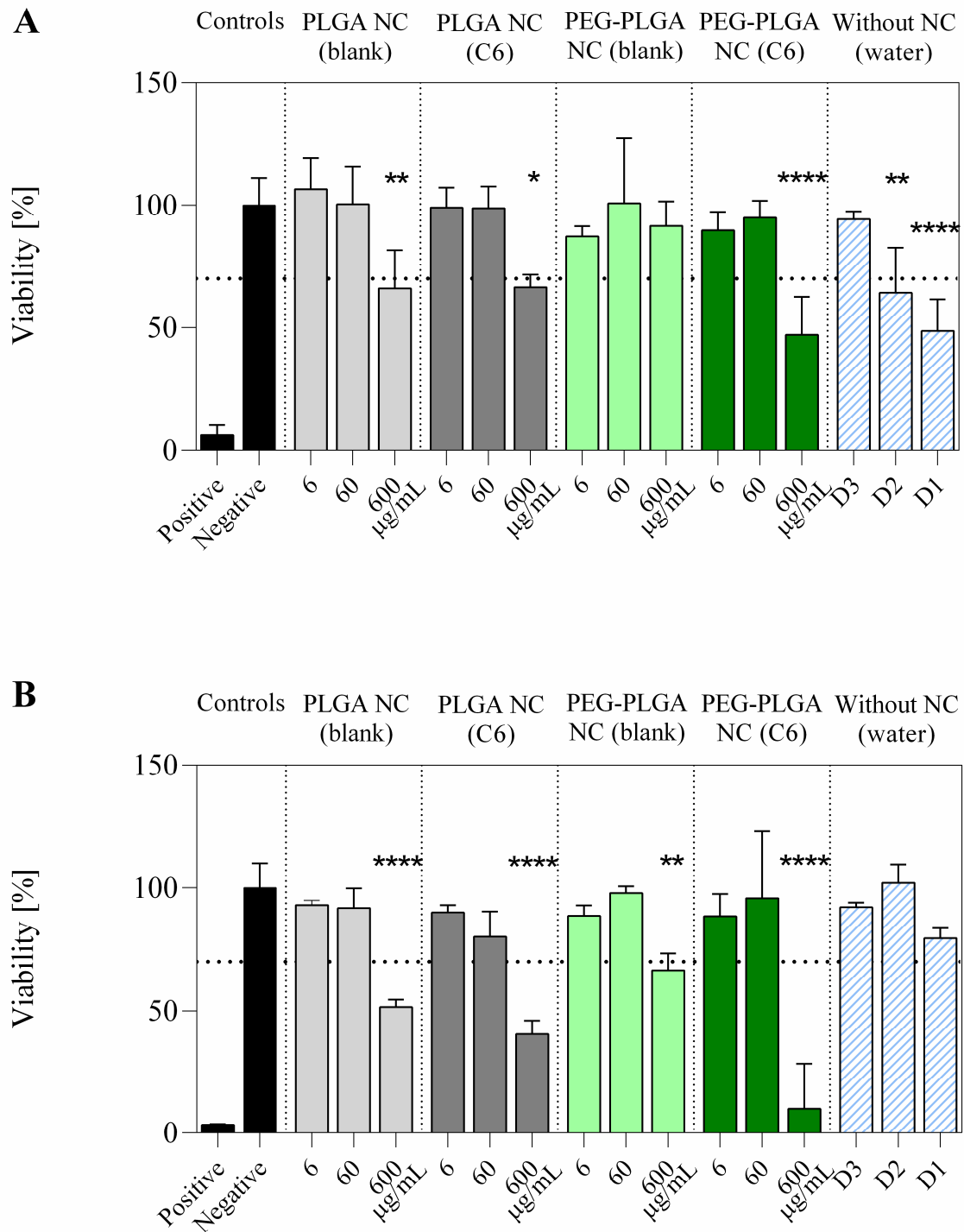


Figure 64 *In vitro* MTS viability assay after 72 h showing the effects of different NC formulations on (A) LNCaP cells and (B) PBMC compared to untreated cells (negative control). Cells treated with 9% Triton X-100 solution were used as positive control. Three different dilutions were prepared from stock solution using cell culture medium resulting in NC concentration of 6 µg/mL (D3), 60 µg/mL (D2) and 600 µg/mL (D1). A cell viability >70% was considered as non-toxic according to DIN EN ISO 10993-5 (dotted line). Statistically significant differences (two-way ANOVA Dunnett's multiple comparisons test) are marked with asterisks: * ($p \leq 0.05$); ** ($p \leq 0.01$); **** ($p \leq 0.0001$).

5.7.2 Determination of Membrane Damage in LNCaP Cells Detected by LDH Assay

To assess the damage of cell membranes of LNCaP cells as the initial point of interaction with NC, the extracellular concentration of LDH was quantified. Three different concentrations (6 $\mu\text{g/mL}$, 60 $\mu\text{g/mL}$ and 600 $\mu\text{g/mL}$) of C6-loaded and unloaded PLGA (Resomer[®] RG 502) NC and PEG-PLGA (PEG_{2k}-PLGA_{11.5k}) NC were tested over 6 h (Figure 65). The incubation of cells with 9% Triton X-100 solution was used as positive control and set as 100% LDH release. In control cells, which were not treated with NC, the release of the enzyme was found to be at 32.5% (negative control).

As shown in Figure 65 cytotoxicity of the NC formulations was not dose dependent and no additional cytotoxicity was observed with LNCaP cell lines as a result of dye-loading in PLGA and PEG_{2k}-PLGA_{11.5k} NC when compared to the negative control. Hwang *et al.* [444] and Ma *et al.* [445] also reported a negligible change in LDH release when different types of cells were incubated with blank PLGA nanoparticles. In contrast, in cells to which water control was added, significant LDH release was detected, which was already discussed above for the MTS assay.

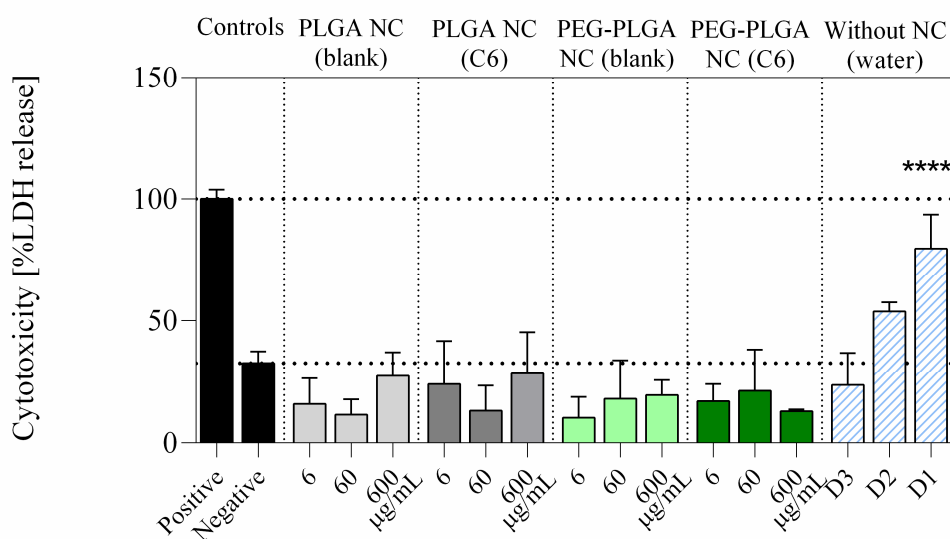


Figure 65 *In vitro* LDH membrane damage assay carried out on LNCaP cells, treated with three different concentrations (6 $\mu\text{g/mL}$ (D3), 60 $\mu\text{g/mL}$ (D2) and 600 $\mu\text{g/mL}$ (D1)) of the different nanoparticle formulations. Dotted lines represent the negative (untreated cells) and positive (cells treated with 9% Triton X-100 solution) controls. Statistically significant difference (two-way ANOVA Dunnett's multiple comparisons test) is marked with asterisk: **** ($p \leq 0.0001$).

Although different assays and cell types were used, the results and the rank order of the polymer NC with regard to their cytotoxicity were in a comparable ranges. MTS and LDH assay gave similar results, since membrane damage after 6 h (LDH) was always followed by a decrease of the metabolic activity (MTS) 72 h after exposure to the NC.

6 Conclusion

The use of therapeutic ultrasound represents an effective and promising method for achieving a controlled drug release to a region of interest without disrupting surrounding tissue. Its increased popularity over the last decade for cancer treatment is mostly due to its ability to transmit energy in a non-invasive, non-ionizing and painless way into the body, while focusing the beam with a high precision on the diseased tissue at overall relatively low-costs. The ultrasound thereby is used to induce inertial cavitation at microbubbles, liposomes, vaporizing nanodroplets or gas nanobubbles resulting into bubble disruption and release of the drug. The disadvantage of the before mentioned drug delivery systems is their relatively large particle size, which prevents targeted transport by passive drug targeting making them less effective for cancer therapy. Alternatively, polymer nanoparticles can be used as drug delivery system as they are able to enter the tumor site and release the drug *via* ultrasound cavitation locally. The aim of this project was to develop and produce different dye-loaded polymer based NS and NC, which were used as inertial cavitation nuclei leading to cavitation under diagnostic ultrasound parameters with sufficient dye release. The polymer nanoparticles showed a capability of trapping and stabilizing air bubbles on the surface after lyophilization with 15% trehalose and reconstitution, resulting in generation of a high broadband noise at frequencies of 750 kHz and peak negative pressure of 1.02 MPa.

For this purpose, biodegradable nanoparticles based on the polyesters PLA and PLGA were prepared by nanoprecipitation and emulsion-diffusion method. By varying concentration and type of polymer, dye-to-polymer ratio, purification procedures and types of dye, NS in the size range of 95-221 nm and with negative zeta potential were formed and characterized. The concentration of the polymer was found to have a pronounced effect on the hydrodynamic diameter, while the more lipophilic dye C6 resulted in considerably higher entrapment efficiency as RhB. No differences were shown between PLA NS and PLGA NS in terms of physicochemical properties. Additionally, the NC were prepared with different homogenization rates, different quantities of the stabilizing agent (PVA) and different types of PLGA polymers varying in the end groups (free acid group, ester-terminated and PEGylated) and molecular weights (7,000 – 69,000 g/mol). In comparison to NS, NC revealed larger particle sizes about 250 nm, but with a higher encapsulation efficiency probably due to the improved incorporation of dye in the oleic core reservoir. The homogenization rate during preparation could be selectively altered to produce particles with defined hydrodynamic diameters and dye encapsulation. Stabilizer concentrations below 2.5% and PLGA polymers with high molecular

weights induced an increase in hydrodynamic diameter. In addition, the copolymer PEG-PLGA was used to investigate the influence of hydrophilic surface modification on NC properties. Increasing the amount of PEG in the copolymer led to an increased hydrodynamic diameter and considerable decrease in C6 entrapment efficiency. The latter observation can be linked to the increased hydrophilicity of the nanoparticle thereby impacting the encapsulation process of the lipophilic dye.

A decisive criterion for effective sonosensitive therapy is a high inertial cavitation of nanoparticles and efficient drug release. Therefore, all formulations were tested in an ultrasound device. The hydrophobic dye and larger particles supported higher inertial cavitation of polymer nanoparticles. The hydrophilic differences of the PLGA polymers were reflected in modified cavitation profiles, independent of the homogenization rate. The higher the molecular weight and the more hydrophobic the polymer (free acid group), the higher was the detectable cavitation activity. In addition, the dye release induced by ultrasound inertial cavitation was dependent on the molecular weight and hydrophobicity of the polymer. The PEGylated PLGA nanoparticles showed higher cavitation profiles compared to PLGA nanoparticles. The decrease in cavitation activity was observed when the PEGylation degree exceeded 40%. The dye release after ultrasound treatment decreased with increasing PEG concentration, reaching the lowest dye release at a PEGylation degree of more than 30%. Since the differences in particle sizes and cavitation profiles between NS and NC were considered negligible, but a higher encapsulation efficiency for NC was observable, the focus for further examination was on C6-loaded NC prepared from PLGA 502 or PEG_{2k}-PLGA_{11.5k}. Both lyophilized formulations showed a high physicochemical stability as well as cavitation activity under different storage conditions.

In the following, the preparation process of NC was optimized with respect to a successful sonosensitive response, and several ultrasound parameters were tested to improve cavitation activity and dye release at the highest possible frequencies as well as the lowest peak negative pressures. Low peak negative pressure is necessary to stay below the maximum values of the MI=1.9, an ultrasound security parameter given by the FDA. The broadband focused ultrasound transducer covered a frequency range from 0.5 MHz to 1 MHz and was in this work calibrated for four frequencies (650 kHz, 750 kHz, 850 kHz and 950 kHz). For each of the frequencies the peak negative pressure of 1.02 MPa was selected for further experiments. Comparing different frequencies, a typical cavitation behavior could be recognized. NC showed a decreased cavitation activity using higher frequencies due to less energetic and violent cavitation collapse.

Another aspect was the testing of NC at different temperatures as well in the presence of ethanol. Although, it was found that inertial cavitation decreased with increasing temperature, NC still exhibited high cavitation activity at normal body temperature (37 °C). Ethanol provided a better wetting effect of the pores on the NC surface, which probably lowered the inertial cavitation response.

Before nanoparticles are further used for biological studies, they are usually dispersed in a physiological solution. For this purpose, the PLGA NC were tested in different biologically relevant media. The media composition was found to influence the NC surface charge but without inducing aggregation. On contact of nanoparticles with biological fluids the direct formation of a protein corona occurs, which changes the physicochemical and biological properties of the particles. The assessment of this change is therefore of high interest for the applicability of the particles *in vivo*. To stimulate the interaction of the particles with biomolecules of the blood, particles were incubated with FBS or HS, and the binding of proteins was studied. The protein corona of the individual NC differed in the amount of bound proteins and in their composition under selected conditions. It was found that the PEGylated PLGA NC and PLGA polymers with higher molecular mass showed a different protein composition as lower molecular mass PLGA polymers potentially due to the hydrophilic interactions. The total amount of bound proteins was distinctly affected by the choice of serum and pH of dispersion media. The protein corona of the NC was also investigated after ultrasound treatment and showed that protein composition did not change after ultrasound treatment, as the MI of ultrasound settings remained below 1.9 all the time. No differences were observable between different biologically relevant media in terms of cavitation profiles. However, in contrast to FBS, HS itself led to a slightly increased broadband noise.

For intravenous applications, the biocompatibility of the nanoparticle containing formulations is essential. To determine the toxicity of the NC, the interactions with isolated prostate cancer cells, and PBMC, were both examined with *in vitro* cytotoxicity assays. The metabolic activity and membrane effects were assessed after 72 h or 6 h incubation, respectively. In both cell lines, NC did not show a cytotoxic effect irrespective of dye loading and PEGylation up to 600 µg/mL.

The present work provides insight into the mechanism of ultrasound sensitive nanoparticles for tumor targeted drug delivery. However, the results were obtained using model substances to understand and improve the function of sonosensitive nanoparticulate systems. For further development the presented results should be verified using a broader range of different drug

types. Particularly those molecule classes considered as potential drug candidates for tumor therapy need to be tested. Besides small molecules biologics like monoclonal antibodies, bispecifics, and antibody-drug conjugates or nucleic acids for gene therapy are used to treat cancer. The combination of sonosensitive nanoparticles and ultrasound could potentially enhance the tissue permeability and increases the efficiency of delivery of macromolecular drugs to target tissue. However, for clinical application, it is necessary to proof the ability for targeted drug delivery and safety profiles *in vivo*. Besides, the effects of ultrasound in biological tissue will be require a more thorough investigation to understand the short- and long-term effects of ultrasound on the body and the complex environments of tumors. Eventually, one challenge is to overcome the upscaling of the laboratory process to production scale for industry production of nanoparticles and the development of a robust and reliable manufacturing process.

7 Zusammenfassung

Der Einsatz von therapeutischem Ultraschall ist eine wirksame und vielversprechende Methode zur gezielten und kontrollierten Freisetzung von Wirkstoffen in einer bestimmten Region des Körpers ohne das umgebende Gewebe zu schädigen. Ultraschallwellen einer bestimmten Wellenlänge führen dabei zur Induktion von Inertialkavitationen beispielsweise an Mikrobläschen, Liposomen, verdampfenden Nanotröpfchen oder Gas-Nanoblasen, was schlussendlich zum Platzen der Bläschen und zur Freisetzung des Wirkstoffes zur Folge hat. Die zunehmende Beliebtheit des Ultraschalls zu diesem Zweck in den letzten zehn Jahren ist vor allem auf seine Fähigkeit zurückzuführen Energie zu geringen Kosten auf nicht-invasiven, nicht-ionisierende und schmerzfreie Weise in den Körper zu übertragen und gleichzeitig den Strahl mit hoher Präzision auf das betroffene Gewebe fokussieren zu können. Der Nachteil dieser Wirkstofffreisetzungssysteme ist jedoch ihre relativ große Partikelgröße, die einen gezielten Transport durch passives Drug-Targeting verhindert und damit die Krebstherapie weniger wirksam macht. Alternativ können Polymer-Nanopartikel als Wirkstofftransportsystem verwendet werden, da sie in der Lage sind in den Tumor einzudringen und den Wirkstoff durch Ultraschallkavitation lokal freizusetzen. Ziel dieses Projekts war die Entwicklung und Herstellung verschiedener farbstoffbeladener Polymer-Nanosphären und -Nanokapseln, die als Inertialkavitationskerne verwendet wurden und unter diagnostischen Ultraschallbedingungen zur Kavitation mit ausreichender Farbstofffreisetzung führen.

Zu diesem Zweck wurden biologisch abbaubare Nanopartikel auf der Basis der Polyester PLA und PLGA durch Nanopräzipitation und Emulsions-Diffusions-Methode hergestellt. Durch Variieren der Polymerkonzentration und des -typs, des Farbstoff-Polymer-Verhältnisses, der Aufreinigungsverfahren und der Farbstofftypen wurden NS im Größenbereich von 95-221 nm und mit negativem Zetapotenzial gebildet und charakterisiert. Es wurde festgestellt, dass die Konzentration des Polymers einen ausgeprägten Einfluss auf den hydrodynamischen Durchmesser hat, während der lipophilere Farbstoff C6 zu einer deutlich höheren Beladungseffizienz als RhB führte. Hinsichtlich der physikochemischen Eigenschaften wurden keine Unterschiede zwischen PLA NS und PLGA NS festgestellt. Darüber hinaus wurden die NC mit unterschiedlichen Homogenisierungsraten, unterschiedlichen Mengen des Stabilisators (PVA) und unterschiedlichen Typen von PLGA-Polymeren hergestellt, die sich in den Endgruppen (freie Carbonsäuren, Ester-terminiert und PEGyliert) und den Molekulargewichten (7.000 - 69.000 g/mol) unterschieden. Im Vergleich zu NS wies NC eine größere Partikelgröße von etwa 250 nm auf, jedoch mit einer höheren Verkapselungseffizienz,

die wahrscheinlich auf den verbesserten Einbau des Farbstoffs in das Ölkernreservoir zurückzuführen ist. Die Homogenisierungsrate während der Herstellung konnte selektiv verändert werden, um Partikel mit definierten hydrodynamischen Durchmessern und Farbstoffeinkapselung zu erzeugen. Stabilisatorkonzentrationen unter 2,5% oder PLGA-Polymere mit hohen Molekulargewichten führten zu einer Zunahme des hydrodynamischen Durchmessers. Darüber hinaus wurde das Copolymer PEG-PLGA verwendet, um den Einfluss der hydrophilen Oberflächenmodifikation auf die Eigenschaften des NC zu untersuchen. Die Erhöhung des PEG-Anteils im Copolymer führte zu einer Vergrößerung des hydrodynamischen Durchmessers und zu einer beträchtlichen Verringerung der Effizienz der C6-Verkapselung. Die letztgenannte Beobachtung kann mit der erhöhten Hydrophilie des Nanopartikels in Verbindung gebracht werden, was sich auf den Verkapselungsprozess des lipophilen Farbstoffs auswirkt.

Ein entscheidendes Kriterium für eine wirksame sonosensitive Therapie ist eine hohe Inertialkavitation von Nanopartikeln und eine effiziente Wirkstofffreisetzung. Daher wurden alle Formulierungen in einem Ultraschallgerät getestet. Der hydrophobe Farbstoff und die größeren Partikel unterstützten eine höhere Inertialkavitation der Polymer-Nanopartikel. Die hydrophilen Unterschiede der PLGA-Polymere spiegelten sich unabhängig von der Homogenisierungsrate in veränderten Kavitationsprofilen wider. Je höher das Molekulargewicht und je hydrophober das Polymer (freie Carbonsäure), desto höher war die nachweisbare Kavitationsaktivität. Darüber hinaus war die durch Ultraschall-Inertialkavitation induzierte Farbstofffreisetzung abhängig vom Molekulargewicht und der Hydrophobie des PLGA-Polymers. Die PEGylierten PLGA-Nanopartikel zeigten im Vergleich zu PLGA-Nanopartikeln höhere Kavitationsprofile. Die Kavitationsaktivität nahm ab, wenn der PEGylierungsgrad 40 % überstieg. Die Farbstofffreisetzung nach der Ultraschallbehandlung nahm mit steigender PEG-Konzentration ab und erreichte die niedrigste Farbstofffreisetzung bei einem PEGylierungsgrad von mehr als 30 %. Da die Unterschiede in den Partikelgrößen und Kavitationsprofilen zwischen NS und NC als vernachlässigbar angesehen wurden aber eine höhere Verkapselungseffizienz für NC zu beobachten war, konzentrierte sich die weitere Untersuchung auf C6-beladene NC, die aus PLGA 502 oder PEG2k-PLGA11.5k hergestellt wurden. Beide lyophilisierten Formulierungen zeigten eine hohe physikochemische Stabilität sowie Kavitationsaktivität unter verschiedenen Lagerungsbedingungen.

Im Folgenden wurde der Herstellungsprozess von NC im Hinblick auf eine erfolgreiche sonosensitive Reaktion optimiert und es wurden verschiedene Ultraschallparameter getestet,

um die Kavitationsaktivität und die Farbstofffreisetzung bei möglichst hohen Frequenzen und niedrigen Spitzenunterdrücken zu verbessern. Ein niedriger Spitzenunterdruck ist notwendig, um unter den Höchstwerten des $MI=1,9$ zu bleiben, einem von der FDA vorgegebenen Ultraschall-Sicherheitsparameter. Der fokussierte Breitband-Ultraschallwandler deckt einen Frequenzbereich von 0,5 MHz bis 1 MHz ab und wurde in dieser Arbeit für vier Frequenzen (650 kHz, 750 kHz, 850 kHz und 950 kHz) kalibriert. Für jede der Frequenzen wurde der Spitzenunterdruck von 1,02 MPa für weitere Experimente ausgewählt. Beim Vergleich der verschiedenen Frequenzen konnte ein typisches Kavitationsverhalten erkannt werden. NC zeigte bei höheren Frequenzen eine verringerte Kavitationsaktivität aufgrund eines weniger energiereichen und heftigen Kavitationskollapses. Ein weiterer Aspekt war die Prüfung von NC bei verschiedenen Temperaturen sowie in Gegenwart von Ethanol. Obwohl festgestellt wurde, dass die Inertialkavitation mit steigender Temperatur abnahm, zeigten NC bei normaler Körpertemperatur (37 °C) immer noch eine hohe Kavitationsaktivität. Ethanol sorgte für eine bessere Benetzung der Poren auf der NC-Oberfläche, was wahrscheinlich eine Verringerung der Inertialkavitation zur Folge hat.

Bevor Nanopartikel für biologische Studien weiterverwendet werden, werden sie normalerweise in einer physiologischen Lösung dispergiert. Zu diesem Zweck wurden die PLGA-NC in verschiedenen biologisch relevanten Medien getestet. Es wurde festgestellt, dass die Zusammensetzung des Mediums die Oberflächenladung der NC beeinflusst ohne dabei eine Aggregation auszulösen. Beim Kontakt von Nanopartikeln mit biologischen Flüssigkeiten kommt es zur direkten Bildung einer Proteinkorona, die die physikochemischen und biologischen Eigenschaften der Partikel verändert. Die Bewertung dieser Veränderung ist daher von großem Interesse für die Anwendbarkeit der Partikel *in vivo*. Um die Wechselwirkung der Partikel mit Biomolekülen des Blutes zu stimulieren, wurden die Partikel mit FBS oder HS inkubiert und die Bindung von Proteinen untersucht. Die Proteinkorona der einzelnen NC unterschieden sich in der Menge der gebundenen Proteine und in ihrer Zusammensetzung unter ausgewählten Bedingungen. Es wurde festgestellt, dass die PEGylierten PLGA NC und PLGA-Polymere mit höherem Molekulargewicht eine andere Proteinzusammensetzung aufwiesen als PLGA-Polymere mit niedrigerem Molekulargewicht, was möglicherweise auf die hydrophilen Wechselwirkungen zurückzuführen ist. Die Gesamtmenge der gebundenen Proteine wurde insgesamt durch die Art des Serums und den pH-Wert des Dispersionsmediums deutlich beeinflusst. Die Proteinkorona der NC zeigte auch nach der Ultraschallbehandlung keine Veränderung der Proteinzusammensetzung, da der MI der Ultraschalleinstellungen stets unter 1,9 blieb. Hinsichtlich der Kavitationsprofile waren zusätzlich keine Unterschiede zwischen

den verschiedenen biologisch relevanten Medien festzustellen. Im Gegensatz zu FBS führte HS selbst jedoch zu einem leicht erhöhten Breitbandrauschen.

Für intravenöse Anwendungen ist die Biokompatibilität der nanopartikelhaltigen Formulierungen von entscheidender Bedeutung. Um die Toxizität der NC zu bestimmen, wurden die Wechselwirkungen mit isolierten Prostatakrebszellen und PBMC mit *In-vitro*-Zytotoxizitätstests untersucht. Die metabolische Aktivität und die Membraneffekte wurden nach 72 Stunden bzw. 6 Stunden Inkubation bewertet. Bei beiden Zelllinien zeigten NC unabhängig von der Farbstoffbeladung und der PEGylierung keine zytotoxische Wirkung, bis zu 600 µg/mL.

Diese Arbeit gibt einen Einblick in den Mechanismus von ultraschallsensitiven Nanopartikeln für die gezielte Wirkstofffreisetzung an und in Tumorgeweben. Die Ergebnisse wurden jedoch ausschließlich unter Verwendung von Modellsubstanzen generiert, um die Funktion des sonosensitiven nanopartikelartigen Systems zu verstehen und zu verbessern. Für die weitere Entwicklung müssen die vorgestellten Ergebnisse mit einer breiteren Palette von Wirkstoffen und Wirkstoffklassen verifiziert werden, insbesondere mit solchen, die als potenzielle Kandidaten für die Tumorthherapie gelten und schon in Anwendung sind. Dazu gehören kleine Moleküle oder Biologika wie monoklonale Antikörper, bispezifische Antikörper und Antikörper-Wirkstoff-Konjugate sowie Nukleinsäuren für die Gentherapie. Die Kombination von auf sonosensitiven Nanopartikeln und Ultraschall könnte die Gewebedurchlässigkeit verbessern und die Effizienz der Abgabe von makromolekularen Arzneimitteln an das Zielgewebe erhöhen. Um eine klinische Anwendung in Betracht zu ziehen, müssen jedoch die Fähigkeit des Systems zur Verabreichung von Arzneimitteln und dessen Sicherheitsprofile *in vivo* untersucht und bewertet werden. Außerdem sind die Auswirkungen von kurz- und langfristigem Ultraschall in biologischem Gewebe und in der komplexen Umgebung von Tumoren noch nicht ausreichend geklärt. Ein weiterer Forschungsaspekt sollte sich mit der Übertragung des Laborverfahrens auf den Produktionsmaßstab für die industrielle Herstellung von Nanopartikeln und der Entwicklung eines robusten und zuverlässigen Herstellungsverfahrens befassen.

8 References

- [1] E. Rubin, D.S. Strayer, Neoplasia, in: E. Rubin (Ed.) *Rubin's Pathology: Clinicopathologic Foundations of Medicine*, LWW, Philadelphia, 2012, pp. 157-212.
- [2] Leitlinienprogramm Onkologie (Deutsche Krebsgesellschaft, Deutsche Krebshilfe, AWMF): S3-Leitlinie Prostatakarzinom, Kurzversion 6.2, 2021, AWMF Registernummer: 043/022OL, <https://www.leitlinienprogramm-onkologie.de/leitlinien/prostatakarzinom/> (accessed on 10.02.2023).
- [3] E. Blanco, H. Shen, M. Ferrari, Principles of nanoparticle design for overcoming biological barriers to drug delivery, *Nat Biotechnol*, 33 (2015) 941-951.
- [4] K. Bosslet, R. Straub, M. Blumrich, J. Czech, M. Gerken, B. Sperker, H.K. Kroemer, J.-P. Gesson, M. Koch, C. Monneret, Elucidation of the mechanism enabling tumor selective prodrug monotherapy, 58 (1998) 1195-1201.
- [5] C.M. Hartshorn, M.S. Bradbury, G.M. Lanza, A.E. Nel, J. Rao, A.Z. Wang, U.B. Wiesner, L. Yang, P. Grodzinski, Nanotechnology strategies to advance outcomes in clinical cancer care, *ACS Nano*, 12 (2018) 24-43.
- [6] J.W. Wragg, R. Bicknell, Vascular targeting approaches to treat cancer, *Cancer Targeted Drug Delivery* 2013, pp. 59-95.
- [7] B. Bahrami, M. Hojjat-Farsangi, H. Mohammadi, E. Anvari, G. Ghalamfarsa, M. Yousefi, F. Jadidi-Niaragh, Nanoparticles and targeted drug delivery in cancer therapy, *Immunol Lett*, 190 (2017) 64-83.
- [8] T. Dyba, G. Randi, F. Bray, C. Martos, F. Giusti, N. Nicholson, A. Gavin, M. Flego, L. Neamtiu, N. Dimitrova, R. Negrao Carvalho, J. Ferlay, M. Bettio, The European cancer burden in 2020: Incidence and mortality estimates for 40 countries and 25 major cancers, *Eur J Cancer*, 157 (2021) 308-347.
- [9] S.R. Kennedy, L.A. Loeb, A.J. Herr, Somatic mutations in aging, cancer and neurodegeneration, *Mech Ageing Dev*, 133 (2012) 118-126.
- [10] D. Li, N.A. de Glas, A. Hurria, Cancer and aging: General principles, biology, and geriatric assessment, *Clin Geriatr Med*, 32 (2016) 1-15.
- [11] P. Armitage, R. Doll, The age distribution of cancer and a multi-stage theory of carcinogenesis, *Br J Cancer*, 8 (1954) 1-12.
- [12] H. Sung, J. Ferlay, R.L. Siegel, M. Laversanne, I. Soerjomataram, A. Jemal, F. Bray, Global cancer statistics 2020: GLOBOCAN estimates of incidence and mortality worldwide for 36 cancers in 185 countries, *CA Cancer J Clin*, 71 (2021) 209-249.
- [13] A. Hemminki, K. Hemminki, The genetic basis of cancer, in: D.T. Duriel, J.T. Douglas (Eds.) *Cancer Gene Therapy. Contemporary Cancer Research*, Humana Press 2005.
- [14] I. Muylers-Chen, R. Paro, Epigenetics: unforeseen regulators in cancer, *Biochimica et Biophysica Acta (BBA) - Reviews on Cancer*, 1552 (2001) 15-26.
- [15] B.B. Cerqueira, A. Lasham, A.N. Shelling, R. Al-Kassas, Nanoparticle therapeutics: Technologies and methods for overcoming cancer, *Eur J Pharm Biopharm*, 97 (2015) 140-151.
- [16] D. Hanahan, R.A. Weinberg, Hallmarks of cancer: the next generation, *Cell*, 144 (2011) 646-674.
- [17] K.D. Miller, L. Nogueira, A.B. Mariotto, J.H. Rowland, K.R. Yabroff, C.M. Alfano, A. Jemal, J.L. Kramer, R.L. Siegel, Cancer treatment and survivorship statistics, 2019, *CA Cancer J Clin*, 69 (2019) 363-385.
- [18] J.M. Huitink, W.H. Teoh, Current cancer therapies - a guide for perioperative physicians, *Best Pract Res Clin Anaesthesiol*, 27 (2013) 481-492.
- [19] B.W. Lash, P.B. Gilman, Principles of cytotoxic chemotherapy, *Cancer Immunotherapy* 2013, pp. 167-185.
- [20] B.A. Chabner, D.L. Longo, *Cancer chemotherapy, immunotherapy, and biotherapy: principles and practice*, sixth ed., Wolters Kluwer, Philadelphia, 2019.

- [21] E. Chatelut, J.-P. Delord, P. Canal, Toxicity patterns of cytotoxic drugs, *Investigational New Drugs*, 21 (2003) 141-148.
- [22] K. Nurgali, R.T. Jagoe, R. Abalo, Editorial: Adverse effects of cancer chemotherapy: Anything new to improve tolerance and reduce sequelae?, *Front Pharmacol*, 9 (2018) 245.
- [23] J.J. Monsuez, J.C. Charniot, N. Vignat, J.Y. Artigou, Cardiac side-effects of cancer chemotherapy, *Int J Cardiol*, 144 (2010) 3-15.
- [24] A. Urruticoechea, R. Alemany, J. Balart, A. Villanueva, F. Vinals, G. Capella, Recent advances in cancer therapy: An overview, *Current Pharmaceutical Design*, 16 (2010) 3-10.
- [25] C.E. Jansen, M.J. Dodd, C.A. Miaskowski, G.A. Dowling, J. Kramer, Preliminary results of a longitudinal study of changes in cognitive function in breast cancer patients undergoing chemotherapy with doxorubicin and cyclophosphamide, *Psychooncology*, 17 (2008) 1189-1195.
- [26] M. Monje, J. Dietrich, Cognitive side effects of cancer therapy demonstrate a functional role for adult neurogenesis, *Behav Brain Res*, 227 (2012) 376-379.
- [27] N. Pabla, Z. Dong, Curtailing side effects in chemotherapy: a tale of PKC δ in cisplatin treatment, 3 (2012).
- [28] Z. Dede, K. Tumer, T. Kan, B. Yucel, Current advances and future prospects in cancer immunotherapeutics, *Medeni Med J*, 38 (2023) 88-94.
- [29] A.D. Waldman, J.M. Fritz, M.J. Lenardo, A guide to cancer immunotherapy: From T cell basic science to clinical practice, *Nat Rev Immunol*, 20 (2020) 651-668.
- [30] F.S. Hodi, S.J. O'Day, D.F. McDermott, R.W. Weber, J.A. Sosman, J.B. Haanen, R. Gonzalez, C. Robert, D. Schadendorf, J.C. Hassel, W. Akerley, A.J.M. van den Eertwegh, J. Lutzky, P. Lorigan, J.M. Vaubel, G.P. Linette, D. Hogg, C.H. Ottensmeier, C. Lebbé, C. Peschel, I. Quirt, J.I. Clark, J.D. Wolchok, J.S. Weber, J. Tian, M.J. Yellin, G.M. Nichol, A. Hoos, W.J. Urban, Improved survival with ipilimumab in patients with metastatic melanoma, *New England Journal of Medicine*, 363 (2010) 711-723.
- [31] L.A. Kottschade, The future of immunotherapy in the treatment of cancer, *Seminars in Oncology Nursing*, 35 (2019).
- [32] L.B. Kennedy, A.K.S. Salama, A review of cancer immunotherapy toxicity, *CA Cancer J Clin*, 70 (2020) 86-104.
- [33] K. Mortezaee, M. Najafi, Immune system in cancer radiotherapy: Resistance mechanisms and therapy perspectives, *Crit Rev Oncol Hematol*, 157 (2021) 103180.
- [34] L.J. Murray, J. Lilley, Radiotherapy: technical aspects, *Medicine*, 48 (2020) 79-83.
- [35] H.H.W. Chen, M.T. Kuo, Improving radiotherapy in cancer treatment: Promises and challenges, *Oncotarget*, 8 (2017) 62742-62758.
- [36] C. Miaskowski, B. Cooper, S.M. Paul, C. West, D. Langford, J.D. Levine, G. Abrams, D. Hamolsky, L. Dunn, M. Dodd, J. Neuhaus, C. Baggott, A. Dhruva, B. Schmidt, J. Cataldo, J. Merriman, B.E. Aouizerat, Identification of patient subgroups and risk factors for persistent breast pain following breast cancer surgery, *J Pain*, 13 (2012) 1172-1187.
- [37] L.L. Bu, J. Yan, Z. Wang, H. Ruan, Q. Chen, V. Gunadhi, R.B. Bell, Z. Gu, Advances in drug delivery for post-surgical cancer treatment, *Biomaterials*, 219 (2019) 119182.
- [38] A.N. Tavaré, N.J. Perry, L.L. Benzonana, M. Takata, D. Ma, Cancer recurrence after surgery: direct and indirect effects of anesthetic agents, *Int J Cancer*, 130 (2012) 1237-1250.
- [39] R. Feynman, There's plenty of room at the bottom, *Eng. Sci.*, 23 (1960) 22-36.
- [40] Considering whether an FDA-regulated product involves the application of nanotechnology, <https://www.fda.gov/regulatory-information/search-fda-guidance-documents/considering-whether-fda-regulated-product-involves-application-nanotechnology#comment>, (accessed on 14.02.2023).
- [41] Recommendation on the definition of a nanomaterial (2022/C 229/01), [https://eur-lex.europa.eu/legal-content/EN/TXT/?uri=CELEX:32022H0614\(01\)](https://eur-lex.europa.eu/legal-content/EN/TXT/?uri=CELEX:32022H0614(01)), (accessed on 14.02.2023).

- [42] W.H. De Jong, P.J. Borm, Drug delivery and nanoparticles: applications and hazards, *Int J Nanomedicine*, 3 (2008) 133-149.
- [43] J.Y.C. Edgar, H. Wang, Introduction for design of nanoparticle based drug delivery systems, *Curr Pharm Des*, 23 (2017) 2108-2112.
- [44] S.C. Baetke, T. Lammers, F. Kiessling, Applications of nanoparticles for diagnosis and therapy of cancer, *Br J Radiol*, 88 (2015) 20150207.
- [45] S.D. Steichen, M. Caldorera-Moore, N.A. Peppas, A review of current nanoparticle and targeting moieties for the delivery of cancer therapeutics, *Eur J Pharm Sci*, 48 (2013) 416-427.
- [46] J.D. Byrne, T. Betancourt, L. Brannon-Peppas, Active targeting schemes for nanoparticle systems in cancer therapeutics, *Adv Drug Deliv Rev*, 60 (2008) 1615-1626.
- [47] F. Alexis, E.M. Pridgen, R. Langer, O.C. Farokhzad, Nanoparticle technologies for cancer therapy, *Handb Exp Pharmacol*, (2010) 55-86.
- [48] F. Rodriguez, P. Caruana, N. De la Fuente, P. Espanol, M. Gamez, J. Balart, E. Llurba, R. Rovira, R. Ruiz, C. Martin-Lorente, J.L. Corchero, M.V. Cespedes, Nano-based approved pharmaceuticals for cancer treatment: Present and future challenges, *Biomolecules*, 12 (2022).
- [49] J.K. Patra, G. Das, L.F. Fraceto, E.V.R. Campos, M.D.P. Rodriguez-Torres, L.S. Acosta-Torres, L.A. Diaz-Torres, R. Grillo, M.K. Swamy, S. Sharma, S. Habtemariam, H.-S. Shin, Nano based drug delivery systems: recent developments and future prospects, *J Nanobiotechnology*, 16 (2018) 71-71.
- [50] S. Sharifi, S. Behzadi, S. Laurent, M.L. Forrest, P. Stroeve, M. Mahmoudi, Toxicity of nanomaterials, *Chem Soc Rev*, 41 (2012) 2323-2343.
- [51] A. Bakhshian Nik, H. Zare, S. Razavi, H. Mohammadi, P. Torab Ahmadi, N. Yazdani, M. Bayandori, N. Rabiee, J. Izadi Mobarakeh, Smart drug delivery: Capping strategies for mesoporous silica nanoparticles, *Microporous and Mesoporous Materials*, 299 (2020).
- [52] I.I. Slowing, J.L. Vivero-Escoto, C.W. Wu, V.S. Lin, Mesoporous silica nanoparticles as controlled release drug delivery and gene transfection carriers, *Adv Drug Deliv Rev*, 60 (2008) 1278-1288.
- [53] T. Sun, Y.S. Zhang, B. Pang, D.C. Hyun, M. Yang, Y. Xia, Engineered nanoparticles for drug delivery in cancer therapy, *Angew Chem Int Ed Engl*, 53 (2014) 12320-12364.
- [54] Z. Liu, S. Tabakman, K. Welsher, H. Dai, Carbon nanotubes in biology and medicine: In vitro and in vivo detection, imaging and drug delivery, *Nano Res*, 2 (2009) 85-120.
- [55] A. Albanese, W.C.W. Chan, Effect of gold nanoparticle aggregation on cell uptake and toxicity, *ACS Nano*, 5 (2011) 5478-5489.
- [56] D. Pissuwan, T. Niidome, M.B. Cortie, The forthcoming applications of gold nanoparticles in drug and gene delivery systems, *J Control Release*, 149 (2011) 65-71.
- [57] H. Chen, Z. Zhen, T. Todd, P.K. Chu, J. Xie, Nanoparticles for improving cancer diagnosis, *Mater Sci Eng R Rep*, 74 (2013) 35-69.
- [58] F. Soetaert, P. Korangath, D. Serantes, S. Fiering, R. Ivkov, Cancer therapy with iron oxide nanoparticles: Agents of thermal and immune therapies, *Adv Drug Deliv Rev*, 163-164 (2020) 65-83.
- [59] W.E. Bawarski, E. Chidlow, D.J. Bharali, S.A. Mousa, Emerging nanopharmaceuticals, *Nanomedicine*, 4 (2008) 273-282.
- [60] Y. Malam, M. Loizidou, A.M. Seifalian, Liposomes and nanoparticles: nanosized vehicles for drug delivery in cancer, *Trends Pharmacol Sci*, 30 (2009) 592-599.
- [61] D. Lombardo, M.A. Kiselev, Methods of liposomes preparation: Formation and control factors of versatile nanocarriers for biomedical and nanomedicine application, *Pharmaceutics*, 14 (2022).
- [62] L. Sercombe, T. Veerati, F. Moheimani, S.Y. Wu, A.K. Sood, S. Hua, Advances and challenges of liposome assisted drug delivery, *Front Pharmacol*, 6 (2015) 286.
- [63] Y. Lee, D.H. Thompson, Stimuli-responsive liposomes for drug delivery, *Wiley Interdiscip Rev Nanomed Nanobiotechnol*, 9 (2017).

- [64] M. Abri Aghdam, R. Bagheri, J. Mosafer, B. Baradaran, M. Hashemzaei, A. Baghbanzadeh, M. de la Guardia, A. Mokhtarzadeh, Recent advances on thermosensitive and pH-sensitive liposomes employed in controlled release, *J Control Release*, 315 (2019) 1-22.
- [65] D.D. Lasic, Novel applications of liposomes, *Trends in Biotechnology*, 16 (1998) 307-321.
- [66] M.C. Woodle, Sterically stabilized liposome therapeutics, *Advanced Drug Delivery Reviews*, 16 (1995) 249-265.
- [67] U. Bulbake, S. Doppalapudi, N. Kommineni, W. Khan, Liposomal formulations in clinical use: An updated review, *Pharmaceutics*, 9 (2017).
- [68] J. Gong, M. Chen, Y. Zheng, S. Wang, Y. Wang, Polymeric micelles drug delivery system in oncology, *J Control Release*, 159 (2012) 312-323.
- [69] A. Gothwal, I. Khan, U. Gupta, Polymeric micelles: Recent advancements in the delivery of anticancer drugs, *Pharm Res*, 33 (2016) 18-39.
- [70] N. Majumder, N. G Das, S.K. Das, Polymeric micelles for anticancer drug delivery, *Therapeutic Delivery*, 11 (2020) 613-635.
- [71] G.S. Kwon, K. Kataoka, Block copolymer micelles as long-circulating drug vehicles, *Advanced Drug Delivery Reviews*, 16 (1995) 295-309.
- [72] V.A. Feitosa, V.C. Almeida, B. Malheiros, R.D. Castro, L.R.S. Barbosa, N.N.P. Cerize, C.O. Rangel-Yagui, Polymeric micelles of pluronic F127 reduce hemolytic potential of amphiphilic drugs, *Colloids Surf B Biointerfaces*, 180 (2019) 177-185.
- [73] J. Li, L. Zhu, H.F. Kwok, Nanotechnology-based approaches overcome lung cancer drug resistance through diagnosis and treatment, *Drug Resist Updat*, 66 (2023) 100904.
- [74] G.A. Hughes, Nanostructure-mediated drug delivery, *Nanomedicine*, 1 (2005) 22-30.
- [75] B. Haley, E. Frenkel, Nanoparticles for drug delivery in cancer treatment, *Urol Oncol*, 26 (2008) 57-64.
- [76] V.K. Yellepeddi, A. Kumar, S. Palakurthi, Biotinylated poly(amido)amine (PAMAM) dendrimers as carriers for drug delivery to ovarian cancer cells in vitro, *Anticancer Research*, 29 (2009) 2933-2943.
- [77] I.J. Majoros, A. Myc, T. Thomas, C.B. Mehta, J.R. Baker, PAMAM dendrimer-based multifunctional conjugate for cancer therapy: Synthesis, characterization, and functionality, *Biomacromolecules*, 7 (2006) 572-579.
- [78] A.K. Patri, A. Myc, J. Beals, T.P. Thomas, N.H. Bander, J.R. Baker, Synthesis and in vitro testing of J591 antibody-dendrimer conjugates for targeted prostate cancer therapy, *Bioconjugate Chemistry*, 15 (2004) 1174-1181.
- [79] Y. Liu, Y. Ng, M.R. Toh, G.N.C. Chiu, Lipid-dendrimer hybrid nanosystem as a novel delivery system for paclitaxel to treat ovarian cancer, *J Control Release*, 220 (2015) 438-446.
- [80] P. Mittal, A. Saharan, R. Verma, F.M.A. Altalbawy, M.A. Alfaidi, G.E. Batiha, W. Akter, R.K. Gautam, M.S. Uddin, M.S. Rahman, Dendrimers: A new race of pharmaceutical nanocarriers, *Biomed Res Int*, 2021 (2021) 8844030.
- [81] J. Bugno, H.J. Hsu, S. Hong, Tweaking dendrimers and dendritic nanoparticles for controlled nano-bio interactions: potential nanocarriers for improved cancer targeting, *J Drug Target*, 23 (2015) 642-650.
- [82] S. Nigam, D. Bahadur, Dendrimer-conjugated iron oxide nanoparticles as stimuli-responsive drug carriers for thermally-activated chemotherapy of cancer, *Colloids Surf B Biointerfaces*, 155 (2017) 182-192.
- [83] N. Amreddy, A. Babu, J. Panneerselvam, A. Srivastava, R. Muralidharan, A. Chen, Y.D. Zhao, A. Munshi, R. Ramesh, Chemo-biologic combinatorial drug delivery using folate receptor-targeted dendrimer nanoparticles for lung cancer treatment, *Nanomedicine*, 14 (2018) 373-384.
- [84] J.P. Rao, K.E. Geckeler, Polymer nanoparticles: Preparation techniques and size-control parameters, *Progress in Polymer Science*, 36 (2011) 887-913.

- [85] I. Brigger, C. Dubernet, P. Couvreur, Nanoparticles in cancer therapy and diagnosis, *Advanced Drug Delivery Reviews*, 64 (2012) 24-36.
- [86] B.D. Ratner, A.S. Hoffman, F.J. Achen, J.E. Lemons, *Biomaterials Science: An Introduction to Materials in Medicine*, third ed., Elsevier Academic Press 2013.
- [87] P. Couvreur, B. Kante, V. Lenaerts, V. Scailteur, M. Roland, P. Speiser, Tissue distribution of antitumor drugs associated with polyalkylcyanoacrylate nanoparticles, *Journal of Pharmaceutical Sciences*, 69 (1980) 199-202.
- [88] M.S. Hamid Akash, K. Rehman, S. Chen, Natural and synthetic polymers as drug carriers for delivery of therapeutic proteins, *Polymer Reviews*, 55 (2015) 371-406.
- [89] A. Zielinska, F. Carreiro, A.M. Oliveira, A. Neves, B. Pires, D.N. Venkatesh, A. Durazzo, M. Lucarini, P. Eder, A.M. Silva, A. Santini, E.B. Souto, Polymeric nanoparticles: Production, characterization, toxicology and ecotoxicology, *Molecules*, 25 (2020).
- [90] D.M. Valcourt, M.N. Dang, M.A. Scully, E.S. Day, Nanoparticle-mediated co-delivery of notch-1 antibodies and ABT-737 as a potent treatment strategy for triple-negative breast cancer, *ACS Nano*, 14 (2020) 3378-3388.
- [91] M.J. Mitchell, M.M. Billingsley, R.M. Haley, M.E. Wechsler, N.A. Peppas, R. Langer, Engineering precision nanoparticles for drug delivery, *Nat Rev Drug Discov*, 20 (2021) 101-124.
- [92] X. Shan, X. Gong, J. Li, J. Wen, Y. Li, Z. Zhang, Current approaches of nanomedicines in the market and various stage of clinical translation, *Acta Pharm Sin B*, 12 (2022) 3028-3048.
- [93] H. Fessi, F. Puisieux, J.P. Devissaguet, N. Ammoury, S. Benita, Nanocapsule formation by interfacial polymer deposition following solvent displacement, *International Journal of Pharmaceutics*, 55 (1989) R1-R4.
- [94] B. Mishra, B.B. Patel, S. Tiwari, Colloidal nanocarriers: a review on formulation technology, types and applications toward targeted drug delivery, *Nanomedicine*, 6 (2010) 9-24.
- [95] C.V. Sternling, L.E. Scriven, Interfacial turbulence: Hydrodynamic instability and the marangoni effect, *Aiche Journal*, 5 (1959) 514-523.
- [96] S.A. Vitale, J.L. Katz, Liquid droplet dispersions formed by homogeneous liquid-liquid nucleation: "The Ouzo effect", *Langmuir*, 19 (2003) 4105-4110.
- [97] T. Quérette, E. Fleury, N. Sintès-Zydowicz, Non-isocyanate polyurethane nanoparticles prepared by nanoprecipitation, *European Polymer Journal*, 114 (2019) 434-445.
- [98] J.M. Barichello, M. Morishita, K. Takayama, T. Nagai, Encapsulation of hydrophilic and lipophilic drugs in PLGA nanoparticles by the nanoprecipitation method, *Drug Dev Ind Pharm*, 25 (1999) 471-476.
- [99] Y. Tan, P. Wang, K. Xu, W. Li, H. An, L. Li, C. Liu, L. Dong, Designing starch-based nanospheres to make hydrogels with high mechanical strength, *Macromolecular Materials and Engineering*, (2009) NA-NA.
- [100] S. Hornig, H. Bunjes, T. Heinze, Preparation and characterization of nanoparticles based on dextran-drug conjugates, *J Colloid Interface Sci*, 338 (2009) 56-62.
- [101] P. Legrand, S. Lesieur, A. Bochet, R. Gref, W. Raatjes, G. Barratt, C. Vauthier, Influence of polymer behaviour in organic solution on the production of polylactide nanoparticles by nanoprecipitation, *Int J Pharm*, 344 (2007) 33-43.
- [102] M.M. Yallapu, B.K. Gupta, M. Jaggi, S.C. Chauhan, Fabrication of curcumin encapsulated PLGA nanoparticles for improved therapeutic effects in metastatic cancer cells, *J Colloid Interface Sci*, 351 (2010) 19-29.
- [103] I. Limayem Blouza, C. Charcosset, S. Sfar, H. Fessi, Preparation and characterization of spirinolactone-loaded nanocapsules for paediatric use, *Int J Pharm*, 325 (2006) 124-131.
- [104] Z. Zili, S. Sfar, H. Fessi, Preparation and characterization of poly-epsilon-caprolactone nanoparticles containing griseofulvin, *Int J Pharm*, 294 (2005) 261-267.

- [105] D. Fischer, Sustainability in drug and nanoparticle processing, *Handb Exp Pharmacol*, (2023).
- [106] N. Ahmed, C.E. Mora-Huertas, C. Jaafar-Maalej, H. Fessi, A. Elaissari, *Polymeric drug delivery systems for encapsulating hydrophobic drugs*, 2013.
- [107] J.C. Leroux, E. Allémann, E. Doelker, R. Gurny, New approach for the preparation of nanoparticles by an emulsification-diffusion method, *Eur. J. Pharm. Biopharm.*, 41 (1995) 14-18.
- [108] D. Quintanar-Guerrero, E. Allémann, E. Doelker, H. Fessi, Preparation and characterization of nanocapsules from preformed polymers by a new process based on emulsification-diffusion technique, *Pharm Res*, 15 (1998) 1056-1062.
- [109] C.E. Astete, C.M. Sabliov, Synthesis and characterization of PLGA nanoparticles, *Journal of Biomaterials Science, Polymer Edition*, 17 (2006) 247-289.
- [110] R. Dinarvand, N. Sepehri, S. Manoochehri, H. Rouhani, F. Atyabi, Polylactide-co-glycolide nanoparticles for controlled delivery of anticancer agents, *Int J Nanomedicine*, 6 (2011) 877-895.
- [111] C. Bindschaedler, R. Gurny, E. Doelker, Process for preparing a powder of water-insoluble polymer which can be readispersed in a liquid phase, the resulting powder and utilization thereof, US Patent, 1990.
- [112] E. Allémann, R. Gurny, E. Doelker, Preparation of aqueous polymeric nanodispersions by a reversible salting-out process: influence of process parameters on particle size, *Int J Pharm*, 87 (1992) 247-253.
- [113] Y.N. Konan, R. Gurny, E. Allémann, Preparation and characterization of sterile and freeze-dried sub-200 nm nanoparticles, *Int J Pharm*, 233 (2002) 239-252.
- [114] E. Allémann, J.-C. Leroux, R. Gurny, E. Doelker, In vitro extended-release properties of drug-loaded poly(DL-lactic acid) nanoparticles produced by a salting-out procedure, *Pharmaceutical Research*, 10 (1993) 1732-1737.
- [115] D. Quintanar-Guerrero, E. Allémann, H. Fessi, E. Doelker, Preparation techniques and mechanisms of formation of biodegradable nanoparticles from preformed polymers, *Drug Dev Ind Pharm*, 24 (1998) 1113-1128.
- [116] C.P. Reis, R.J. Neufeld, A.J. Ribeiro, F. Veiga, Nanoencapsulation I. Methods for preparation of drug-loaded polymeric nanoparticles, *Nanomedicine*, 2 (2006) 8-21.
- [117] P. Caliceti, S. Salmaso, N. Elvassore, A. Bertucco, Effective protein release from PEG/PLA nano-particles produced by compressed gas anti-solvent precipitation techniques, *J Control Release*, 94 (2004) 195-205.
- [118] J. Jung, M. Perrut, Particle design using supercritical fluids: Literature and patent survey, *J. Supercrit. Fluids*, 20 (2001) 179-219.
- [119] M. Türk, C. Erkey, Synthesis of supported nanoparticles in supercritical fluids by supercritical fluid reactive deposition: Current state, further perspectives and needs, *The Journal of Supercritical Fluids*, 134 (2018) 176-183.
- [120] M. Weber, M. Thies, Understanding the RESS process, in: M. Dekker (Ed.) *Supercritical fluid technology in materials science and engineering: synthesis, properties, and applications*, New York, 2002, pp. 387-437.
- [121] H. Valo, L. Peltonen, S. Vehvilainen, M. Karjalainen, R. Kostianen, T. Laaksonen, J. Hirvonen, Electrospray encapsulation of hydrophilic and hydrophobic drugs in poly(L-lactic acid) nanoparticles, *Small*, 5 (2009) 1791-1798.
- [122] S. Zhao, C. Huang, X. Yue, X. Li, P. Zhou, A. Wu, C. Chen, Y. Qu, C. Zhang, Application advance of electrosprayed micro/nanoparticles based on natural or synthetic polymers for drug delivery system, *Mater. Des.*, 220 (2022).
- [123] R. Sridhar, S. Ramakrishna, Electrosprayed nanoparticles for drug delivery and pharmaceutical applications, *Biomater*, 3 (2013).

- [124] A. Jaworek, Micro- and nanoparticle production by electrospraying, *Powder Technol.*, 176 (2007) 18-35.
- [125] J. Wang, J.A. Jansen, F. Yang, Electrospraying: Possibilities and challenges of engineering carriers for biomedical applications-A mini review, *Front Chem*, 7 (2019) 258.
- [126] A.G. Niculescu, D.E. Mihaiescu, A.M. Grumezescu, A Review of microfluidic experimental designs for nanoparticle synthesis, *Int J Mol Sci*, 23 (2022).
- [127] X. Chen, H. Lv, Intelligent control of nanoparticle synthesis on microfluidic chips with machine learning, *NPG Asia Materials*, 14 (2022).
- [128] M.B. Kulkarni, S. Goel, Microfluidic devices for synthesizing nanomaterials—a review, *Nano Express*, 1 (2020).
- [129] J. Ma, S.M. Lee, C. Yi, C.W. Li, Controllable synthesis of functional nanoparticles by microfluidic platforms for biomedical applications - a review, *Lab Chip*, 17 (2017) 209-226.
- [130] H.K. Patra, A.P. Turner, The potential legacy of cancer nanotechnology: cellular selection, *Trends Biotechnol*, 32 (2014) 21-31.
- [131] M.E. Davis, Z.G. Chen, D.M. Shin, Nanoparticle therapeutics: an emerging treatment modality for cancer, *Nat Rev Drug Discov*, 7 (2008) 771-782.
- [132] Y.D. Livney, Y.G. Assaraf, Rationally designed nanovehicles to overcome cancer chemoresistance, *Adv Drug Deliv Rev*, 65 (2013) 1716-1730.
- [133] N. Bertrand, J. Wu, X. Xu, N. Kamaly, O.C. Farokhzad, Cancer nanotechnology: The impact of passive and active targeting in the era of modern cancer biology, *Adv Drug Deliv Rev*, 66 (2014) 2-25.
- [134] M. Talekar, J. Kendall, W. Denny, S. Garg, Targeting of nanoparticles in cancer: drug delivery and diagnostics, *Anticancer Drugs*, 22 (2011) 949-962.
- [135] S. Wilhelm, A.J. Tavares, Q. Dai, S. Ohta, J. Audet, H.F. Dvorak, W.C.W. Chan, Analysis of nanoparticle delivery to tumours, *Nat Rev Mater*, 1 (2016) 16014.
- [136] D.F. Baban, L.W. Seymour, Control of tumour vascular permeability, *Adv Drug Deliv Rev*, 34 (1998) 109-119.
- [137] S.K. Hobbs, W.L. Monsky, F. Yuan, W.G. Roberts, L. Griffith, V.P. Torchilin, R.K. Jain, Regulation of transport pathways in tumor vessels: role of tumor type and microenvironment, *Proc Natl Acad Sci U S A*, 95 (1998) 4607-4612.
- [138] P. Shubik, Vascularization of tumors: A review, *J Cancer Res Clin Oncol*, 103 (1982) 211-226.
- [139] H. Maeda, The enhanced permeability and retention (EPR) effect in tumor vasculature: the key role of tumor-selective macromolecular drug targeting, *Advan Enzyme Regul*, 41 (2001) 189-207.
- [140] F. Danhier, O. Feron, V. Preat, To exploit the tumor microenvironment: Passive and active tumor targeting of nanocarriers for anti-cancer drug delivery, *J Control Release*, 148 (2010) 135-146.
- [141] C.H. Heldin, K. Rubin, K. Pietras, A. Ostman, High interstitial fluid pressure - an obstacle in cancer therapy, *Nat Rev Cancer*, 4 (2004) 806-813.
- [142] J.F. Liu, B. Jang, D. Issadore, A. Tsourkas, Use of magnetic fields and nanoparticles to trigger drug release and improve tumor targeting, *Wiley Interdiscip Rev Nanomed Nanobiotechnol*, 11 (2019) e1571.
- [143] J.L. Paris, C. Mannaris, M.V. Cabañas, R. Carlisle, M. Manzano, M. Vallet-Regí, C.C. Coussios, Ultrasound-mediated cavitation-enhanced extravasation of mesoporous silica nanoparticles for controlled-release drug delivery, *J Chem Eng*, 340 (2018) 2-8.
- [144] W. Zhao, Y. Zhao, Q. Wang, T. Liu, J. Sun, R. Zhang, Remote light-responsive nanocarriers for controlled drug delivery: Advances and perspectives, *Small*, 15 (2019) e1903060.

- [145] M. Amin, W. Huang, A.L.B. Seynhaeve, T.L.M. Ten Hagen, Hyperthermia and temperature-sensitive nanomaterials for spatiotemporal drug delivery to solid tumors, *Pharmaceutics*, 12 (2020).
- [146] N. Deirram, C. Zhang, S.S. Kermaniyan, A.P.R. Johnston, G.K. Such, pH-responsive polymer nanoparticles for drug delivery, *Macromol Rapid Commun*, 40 (2019) e1800917.
- [147] A.K. Wood, C.M. Sehgal, A review of low-intensity ultrasound for cancer therapy, *Ultrasound Med Biol*, 41 (2015) 905-928.
- [148] S. Son, H.S. Min, D.G. You, B.S. Kim, I.C. Kwon, Echogenic nanoparticles for ultrasound technologies: Evolution from diagnostic imaging modality to multimodal theranostic agent, *Nano Today*, 9 (2014) 525-540.
- [149] P.A. Dijkmans, L.J. Juffermans, R.J. Musters, A. van Wamel, F.J. ten Cate, W. van Gilst, C.A. Visser, N. de Jong, O. Kamp, Microbubbles and ultrasound: from diagnosis to therapy, *Eur J Echocardiogr*, 5 (2004) 245-256.
- [150] J.L. Paris, M.V. Cabanas, M. Manzano, M. Vallet-Regi, Polymer-grafted mesoporous silica nanoparticles as ultrasound-responsive drug carriers, *ACS Nano*, 9 (2015) 11023-11033.
- [151] T. Sun, A. Dasgupta, Z. Zhao, M. Nurunnabi, S. Mitragotri, Physical triggering strategies for drug delivery, *Adv Drug Deliv Rev*, (2020).
- [152] A. Zhang, K. Jung, A. Li, J. Liu, C. Boyer, Recent advances in stimuli-responsive polymer systems for remotely controlled drug release, *Prog Polym Sci*, 99 (2019).
- [153] T. Boissenot, A. Bordat, E. Fattal, N. Tsapis, Ultrasound-triggered drug delivery for cancer treatment using drug delivery systems: From theoretical considerations to practical applications, *J Control Release*, 241 (2016) 144-163.
- [154] M.C. Ziskin, Fundamental physics of ultrasound and its propagation in tissue, *Radiographics*, 13 (1993) 705-709.
- [155] R.S.C. Cobbold, *Foundations of biomedical ultrasound*, 2006.
- [156] F. Ahmadi, I.V. McLoughlin, S. Chauhan, G. ter-Haar, Bio-effects and safety of low-intensity, low-frequency ultrasonic exposure, *Prog Biophys Mol Biol*, 108 (2012) 119-138.
- [157] X. Cheng, M. Zhang, B. Xu, B. Adhikari, J. Sun, The principles of ultrasound and its application in freezing related processes of food materials: A review, *Ultrason Sonochem*, 27 (2015) 576-585.
- [158] W.G. Pitt, G.A. Hussein, B.J. Staples, Ultrasonic drug delivery -a general review, *Expert Opin Drug Deliv*, 1 (2004) 37-56.
- [159] S.J. Patey, J.P. Corcoran, Physics of ultrasound, *Anaesth Intensive Care Med*, 22 (2021) 58-63.
- [160] A. Goldstein, R.L. Powis, Medical ultrasonic diagnostics, in: R.N. Thurston, A.D. Pierce, E.P. Papadakis (Eds.) *Physical Acoustics*, Academic Press 1999, pp. 43-195.
- [161] V. Nahirnyak, T.D. Mast, C.K. Holland, Ultrasound-induced thermal elevation in clotted blood and cranial bone, *Ultrasound Med Biol*, 33 (2007) 1285-1295.
- [162] T. Kenner, The measurement of blood density and its meaning, *Basic Res Cardiol*, 84 (1989) 111-124.
- [163] P.H. Bigg, Density of water in SI units over the range 0-40°C, *Br J Appl Phys*, 18 (1967) 521.
- [164] M.M. Burlew, E.L. Madsen, J.A. Zagzebski, R.A. Banjavic, S.W. Sum, A new ultrasound tissue-equivalent material, *Radiology*, 134 (1980) 517-520.
- [165] O. Dössel, *Bildgebende Verfahren in der Medizin*, 2016.
- [166] D.L. Miller, N.B. Smith, M.R. Bailey, G.J. Czarnota, K. Hynynen, I.R. Makin, Overview of therapeutic ultrasound applications and safety considerations, *J Ultrasound Med*, 31 (2012) 623-634.
- [167] S. Paliwal, S. Mitragotri, Ultrasound-induced cavitation: applications in drug and gene delivery, *Expert Opin Drug Deliv*, 3 (2006) 713-726.
- [168] J. Shriki, Ultrasound physics, *Crit Care Clin*, 30 (2014) 1-24.

- [169] M. Wan, Y.-M. Feng, G.t. Haar, *Cavitation in biomedicine*, Springer Netherlands, 2015.
- [170] E.A. Neppiras, *Acoustic cavitation*, *Physics Reports*, 61 (1980) 159-251.
- [171] S.W. Ohl, E. Klaseboer, B.C. Khoo, *Bubbles with shock waves and ultrasound: a review*, *Interface Focus*, 5 (2015) 20150019.
- [172] A. Tezel, S. Mitragotri, *Interactions of inertial cavitation bubbles with stratum corneum lipid bilayers during low-frequency sonophoresis*, *Nat Nanotechnol*, 85 (2003) 3502-3512.
- [173] G. Tamboia, M. Campanini, V. Vighetto, L. Racca, L. Spigarelli, G. Canavese, V. Cauda, *A comparative analysis of low intensity ultrasound effects on living cells: from simulation to experiments*, *Biomed Microdevices*, 24 (2022) 35.
- [174] K.W. Jang, D. Seol, L. Ding, D.N. Heo, S.J. Lee, J.A. Martin, I.K. Kwon, *Ultrasound-triggered PLGA microparticle destruction and degradation for controlled delivery of local cytotoxicity and drug release*, *Int J Biol Macromol*, 106 (2018) 1211-1217.
- [175] M.D. Luque de Castro, F. Priego-Capote, *Ultrasound-assisted crystallization (sonocrystallization)*, *Ultrason Sonochem*, 14 (2007) 717-724.
- [176] R.E. Apfel, C.K. Holland, *Gauging the likelihood of cavitation from short-pulse, low-duty cycle diagnostic ultrasound*, *Ultrasound Med Biol*, 17 (1991) 179-185.
- [177] C.E. Brennen, *Cavitation and bubble dynamics*, 2013.
- [178] 1 - INTRODUCTION, in: G. Wypych (Ed.) *Handbook of Nucleating Agents*, ChemTec Publishing 2016, pp. 1-3.
- [179] M. Ghasemlou, F. Daver, E.P. Ivanova, B. Adhikari, *Bio-inspired sustainable and durable superhydrophobic materials: from nature to market*, *J Mater Chem A*, 7 (2019) 16643-16670.
- [180] Y. Xue, P. Lv, Y. Liu, Y. Shi, H. Lin, H. Duan, *Morphology of gas cavities on patterned hydrophobic surfaces under reduced pressure*, *Phys Fluids*, 27 (2015).
- [181] T. Şen, O. Tüfekçioğlu, Y. Koza, *Mechanical index*, *Anatolian journal of cardiology*, 15 (2015) 334-336.
- [182] FDA, *Marketing clearance of diagnostic ultrasound systems and transducers*, <https://www.fda.gov/regulatory-information/search-fda-guidance-documents/marketing-clearance-diagnostic-ultrasound-systems-and-transducers>, (accessed on 19.11.2023).
- [183] K. Sinha, Z. Garami, A.B. Lumsden, *Contrast-enhanced ultrasound*, in: A.F. AbuRahma, B.A. Perler (Eds.) *Noninvasive Vascular Diagnosis: A Practical Textbook for Clinicians*, Springer International Publishing, Cham, 2020, pp. 1-30.
- [184] S. Mitragotri, *Healing sound: the use of ultrasound in drug delivery and other therapeutic applications*, *Nat Rev Drug Discov*, 4 (2005) 255-260.
- [185] P. Frinking, T. Segers, Y. Luan, F. Tranquart, *Three decades of ultrasound contrast agents: A review of the past, present and future improvements*, *Ultrasound Med Biol*, 46 (2020) 892-908.
- [186] P. Koczera, L. Appold, Y. Shi, M. Liu, A. Dasgupta, V. Pathak, T. Ojha, S. Fokong, Z. Wu, M. van Zandvoort, O. Iranzo, A.J.C. Kuehne, A. Pich, F. Kiessling, T. Lammers, *PBCA-based polymeric microbubbles for molecular imaging and drug delivery*, *J Control Release*, 259 (2017) 128-135.
- [187] B.H. Lammertink, C. Bos, R. Deckers, G. Storm, C.T. Moonen, J.M. Escoffre, *Sonochemotherapy: from bench to bedside*, *Front Pharmacol*, 6 (2015) 138.
- [188] A. Dasgupta, M. Liu, T. Ojha, G. Storm, F. Kiessling, T. Lammers, *Ultrasound-mediated drug delivery to the brain: principles, progress and prospects*, *Drug Discov Today Technol*, 20 (2016) 41-48.
- [189] P. Nittayacharn, H.-X. Yuan, C. Hernandez, P. Bielecki, H. Zhou, A.A. Exner, *Enhancing tumor drug distribution with ultrasound-triggered nanobubbles*, *J Pharm Sci*, 108 (2019) 3091-3098.
- [190] S. Zhong, Z. Ling, Z. Zhou, J. He, H. Ran, Z. Wang, Q. Zhang, W. Song, Y. Zhang, J. Luo, *Herceptin-decorated paclitaxel-loaded poly(lactide-co-glycolide) nanobubbles:*

- ultrasound-facilitated release and targeted accumulation in breast cancers, *Pharm Dev Technol*, 25 (2020) 454-463.
- [191] R. Guo, N. Xu, Y. Liu, G. Ling, J. Yu, P. Zhang, Functional ultrasound-triggered phase-shift perfluorocarbon nanodroplets for cancer therapy, *Ultrasound Med Biol*, 47 (2021) 2064-2079.
- [192] J.J. Kwan, R. Myers, C.M. Coviello, S.M. Graham, A.R. Shah, E. Stride, R.C. Carlisle, C.C. Coussios, Ultrasound-propelled nanocups for drug delivery, *Small*, 11 (2015) 5305-5314.
- [193] A. Tewabe, A. Abate, M. Tamrie, A. Seyfu, E. Abdela Siraj, Targeted drug delivery - from magic bullet to nanomedicine: Principles, challenges, and future perspectives, *J Multidiscip Healthc*, 14 (2021) 1711-1724.
- [194] S.-E. Stiriba, H. Frey, R. Haag, Dendritic polymers in biomedical applications: From potential to clinical use in diagnostics and therapy, *Angew Chem Int*, 41 (2002) 1329-1334.
- [195] S. Bamrungsap, Z. Zhao, T. Chen, L. Wang, C. Li, T. Fu, W. Tan, Nanotechnology in therapeutics: a focus on nanoparticles as a drug delivery system, *Nanomedicine (Lond)*, 7 (2012) 1253-1271.
- [196] F.U. Din, W. Aman, I. Ullah, O.S. Qureshi, O. Mustapha, S. Shafique, A. Zeb, Effective use of nanocarriers as drug delivery systems for the treatment of selected tumors, *Int J Nanomedicine*, 12 (2017) 7291-7309.
- [197] H. Maeda, K. Tsukigawa, J. Fang, A retrospective 30 years after discovery of the enhanced permeability and retention effect of solid tumors: Next-generation chemotherapeutics and photodynamic therapy -Problems, solutions, and prospects, *Microcirculation*, 23 (2016) 173-182.
- [198] M. Li, G. Zhao, W.K. Su, Q. Shuai, Enzyme-responsive nanoparticles for anti-tumor drug delivery, *Front Chem*, 8 (2020) 647.
- [199] A.A. Atchley, L.A. Frizzell, R.E. Apfel, C.K. Holland, S. Madanshetty, R.A. Roy, Thresholds for cavitation produced in water by pulsed ultrasound, *Ultrasonics*, 26 (1988) 280-285.
- [200] P. Hiltl, A. Grebner, M. Fink, S. Rupitsch, H. Ermert, G. Lee, Inertial cavitation of lyophilized and rehydrated nanoparticles of poly(L-lactic acid) at 835 kHz and 1.8 MPa ultrasound, *Sci Rep*, 9 (2019) 12148.
- [201] K.S. Suslick, D.J. Flannigan, Inside a collapsing bubble: sonoluminescence and the conditions during cavitation, *Annu Rev Phys Chem*, 59 (2008) 659-683.
- [202] D. Moinard-Checot, Y. Chevalier, S. Briancon, L. Beney, H. Fessi, Mechanism of nanocapsules formation by the emulsion-diffusion process, *J Colloid Interface Sci*, 317 (2008) 458-468.
- [203] D. Quintanar-Guerrero, E. Allémann, E. Doelker, H. Fessi, A mechanistic study of the formation of polymer nanoparticles by the emulsification-diffusion technique, *Colloid Polym Sci*, 275 (1997) 640-647.
- [204] S.K. Sahoo, J. Panyam, S. Prabha, V. Labhasetwar, Residual polyvinyl alcohol associated with poly (d,l-lactide-co-glycolide) nanoparticles affects their physical properties and cellular uptake, *J Control Release*, 82 (2002) 105-114.
- [205] C. Grune, C. Zens, A. Czapka, K. Scheuer, J. Thamm, S. Hoepfner, K.D. Jandt, O. Werz, U. Neugebauer, D. Fischer, Sustainable preparation of anti-inflammatory atorvastatin PLGA nanoparticles, *Int J Pharm*, 599 (2021) 120404.
- [206] J. Schindelin, I. Arganda-Carreras, E. Frise, V. Kaynig, M. Longair, T. Pietzsch, S. Preibisch, C. Rueden, S. Saalfeld, B. Schmid, J.Y. Tinevez, D.J. White, V. Hartenstein, K. Eliceiri, P. Tomancak, A. Cardona, Fiji: an open-source platform for biological-image analysis, *Nat Methods*, 9 (2012) 676-682.
- [207] EMA, ICH: Q 1 A (R2): Stability Testing of new Drug Substances and Products, <https://www.ema.europa.eu/en/ich-q1a-r2-stability-testing-new-drug-substances-drug-products-scientific-guideline>, (accessed on 15.11.2022).

- [208] M.R.C. Marques, R. Loebenberg, M. Almukainzi, Simulated biological fluids with possible application in dissolution testing, *Dissolution Technol*, 18 (2011) 15-28.
- [209] M. Rabel, P. Warncke, C. Grüttner, C. Bergemann, H.D. Kurland, R. Müller, V. Dugandžić, J. Thamm, F.A. Müller, J. Popp, D. Cialla-May, D. Fischer, Simulation of the long-term fate of superparamagnetic iron oxide-based nanoparticles using simulated biological fluids, *Nanomedicine (Lond)*, 14 (2019) 1681-1706.
- [210] T.M. Buttke, J.A. McCubrey, T.C. Owen, Use of an aqueous soluble tetrazolium/formazan assay to measure viability and proliferation of lymphokine-dependent cell lines, *J Immunol Methods*, 157 (1993) 233-240.
- [211] ISO, 10993-5: 2009 Biological evaluation of medical devices—part 5: tests for in vitro cytotoxicity, International Organization for Standardization Geneva, 2009, pp. 34.
- [212] S.R. Sirsi, M.A. Borden, State-of-the-art materials for ultrasound-triggered drug delivery, *Adv Drug Deliv Rev*, 72 (2014) 3-14.
- [213] A.L. Papa, N. Korin, M. Kanapathipillai, A. Mammoto, T. Mammoto, A. Jiang, R. Mannix, O. Uzun, C. Johnson, D. Bhatta, G. Cuneo, D.E. Ingber, Ultrasound-sensitive nanoparticle aggregates for targeted drug delivery, *Biomaterials*, 139 (2017) 187-194.
- [214] R. Varela-Fernandez, X. Garcia-Otero, V. Diaz-Tome, U. Regueiro, M. Lopez-Lopez, M. Gonzalez-Barcia, M. Isabel Lema, F.J. Otero-Espinar, Mucoadhesive PLGA nanospheres and nanocapsules for lactoferrin controlled ocular delivery, *Pharmaceutics*, 14 (2022).
- [215] S.B. Alam, G. Soligno, J. Yang, K.C. Bustillo, P. Ercius, H. Zheng, S. Whitlam, E.M. Chan, Dynamics of polymer nanocapsule buckling and collapse revealed by in situ liquid-phase TEM, *Langmuir*, 38 (2022) 7168-7178.
- [216] B. George, M. Fink, M. Plock, P. Hiltl, H. Ermert, G. Lee, Measurement of the cavitation activity of sonosensitive nanoparticles used for local chemotherapy, *Proceedings of the 6. Tagung Innovation Messtechnik*, (2019).
- [217] S. Bhatnagar, H. Schiffter, C.C. Coussios, Exploitation of acoustic cavitation-induced microstreaming to enhance molecular transport, *J Pharm Sci*, 103 (2014) 1903-1912.
- [218] P.-T. Hiltl, M. Fink, S.J. Rupitsch, G. Lee, H. Ermert, Development of sonosensitive poly-(L)-lactic acid nanoparticles, *Curr Dir Biomed Eng*, 3 (2017).
- [219] Y. Araujo Martins, T. Zeferino Pavan, R. Fonseca Vianna Lopez, Sonodynamic therapy: Ultrasound parameters and in vitro experimental configurations, *Int J Pharm*, 610 (2021) 121243.
- [220] Z. Izadifar, P. Babyn, D. Chapman, Ultrasound cavitation/microbubble detection and medical applications, *J Med Biol Eng*, 39 (2018) 259-276.
- [221] W.S. Chen, T.J. Matula, A.A. Brayman, L.A. Crum, A comparison of the fragmentation thresholds and inertial cavitation doses of different ultrasound contrast agents, *J Acoust Soc Am*, 113 (2003) 643-651.
- [222] C.K. Holland, R.E. Apfel, Thresholds for transient cavitation produced by pulsed ultrasound in a controlled nuclei environment, *J Acoust Soc Am*, 88 (1990) 2059-2069.
- [223] A.B.D. Cassie, S. Baxter, Wettability of porous surfaces, *Trans Faraday Soc*, 40 (1944) 546-551.
- [224] A. Yildirim, R. Chattaraj, N.T. Blum, G.M. Goldscheitter, A.P. Goodwin, Stable encapsulation of air in mesoporous silica nanoparticles: Fluorocarbon-free nanoscale ultrasound contrast agents, *Adv Healthc Mater*, 5 (2016) 1290-1298.
- [225] D.Q. Le, V. Papadopoulou, P.A. Dayton, Effect of acoustic parameters and microbubble concentration on the likelihood of encapsulated microbubble coalescence, *Ultrasound Med Biol*, 47 (2021) 2980-2989.
- [226] Y. Zhou, J. Cui, C.X. Deng, Dynamics of sonoporation correlated with acoustic cavitation activities, *Biophys J*, 94 (2008) L51-53.

- [227] J. Montoya Mira, L. Wu, S. Sabuncu, A. Sapre, F. Civitci, S. Ibsen, S. Esener, A. Yildirim, Gas-stabilizing sub-100 nm mesoporous silica nanoparticles for ultrasound theranostics, *ACS Omega*, 5 (2020) 24762-24772.
- [228] K. Tamarov, A. Sviridov, W. Xu, M. Malo, V. Andreev, V. Timoshenko, V.P. Lehto, Nano air seeds trapped in mesoporous Janus nanoparticles facilitate cavitation and enhance ultrasound imaging, *ACS Appl Mater Interfaces*, 9 (2017) 35234-35243.
- [229] Sigma-Aldrich, Safety data sheet - Rhodamine B, 79754, 2022, pp. 1-10.
- [230] V. Zhukova, N. Osipova, A. Semyonkin, J. Malinovskaya, P. Melnikov, M. Valikhov, Y. Porozov, Y. Solovev, P. Kuliaev, E. Zhang, B.A. Sabel, V. Chekhonin, M. Abakumov, A. Majouga, J. Kreuter, P. Henrich-Noack, S. Gelperina, O. Maksimenko, Fluorescently labeled PLGA nanoparticles for visualization in vitro and in vivo: The importance of dye properties, *Pharmaceutics*, 13 (2021).
- [231] N. Sharma, P. Madan, S. Lin, Effect of process and formulation variables on the preparation of parenteral paclitaxel-loaded biodegradable polymeric nanoparticles: A co-surfactant study, *Asian J Pharm Sci*, 11 (2016) 404-416.
- [232] M.L.T. Zweers, D.W. Grijpma, G.H.M. Engbers, J. Feijen, The preparation of monodisperse biodegradable polyester nanoparticles with a controlled size, *Inc J Biomed Mater Res Part B: Appl Biomater*, 66B (2003) 559-566.
- [233] P. Couvreur, G. Barratt, E. Fattal, P. Legrand, C. Vauthier, Nanocapsule technology: a review, *Critical reviews in therapeutic drug carrier systems*, 19 (2002) 99-134.
- [234] E. Trenkenschuh, W. Friess, Freeze-drying of nanoparticles: How to overcome colloidal instability by formulation and process optimization, *Eur J Pharm Biopharm*, 165 (2021) 345-360.
- [235] J.J. Kwan, S. Graham, R. Myers, R. Carlisle, E. Stride, C.C. Coussios, Ultrasound-induced inertial cavitation from gas-stabilizing nanoparticles, *Phys Rev E Stat Nonlin Soft Matter Phys*, 92 (2015) 023019.
- [236] S. Kuchler, M. Abdel-Mottaleb, A. Lamprecht, M.R. Radowski, R. Haag, M. Schafer-Korting, Influence of nanocarrier type and size on skin delivery of hydrophilic agents, *Int J Pharm*, 377 (2009) 169-172.
- [237] A. Jonderian, R. Maalouf, Formulation and in vitro interaction of rhodamine-B loaded PLGA nanoparticles with cardiac myocytes, *Front Pharmacol*, 7 (2016) 458.
- [238] N. Varga, V. Hornok, L. Janovak, I. Dekany, E. Csapo, The effect of synthesis conditions and tunable hydrophilicity on the drug encapsulation capability of PLA and PLGA nanoparticles, *Colloids Surf B Biointerfaces*, 176 (2019) 212-218.
- [239] S. Sabuncu, A. Yildirim, Gas-stabilizing nanoparticles for ultrasound imaging and therapy of cancer, *Nano Converg*, 8 (2021) 39.
- [240] N.K. Shah, R. Ivone, J. Shen, S.A. Meenach, A comparison of centrifugation and tangential flow filtration for nanoparticle purification: A case study on acetalated dextran nanoparticles, *Particuology*, 50 (2020) 189-196.
- [241] M.C. Operti, A. Bernhardt, S. Grimm, A. Engel, C.G. Figdor, O. Tagit, PLGA-based nanomedicines manufacturing: Technologies overview and challenges in industrial scale-up, *Int J Pharm*, 605 (2021) 120807.
- [242] G. Dalwadi, H.A. Benson, Y. Chen, Comparison of diafiltration and tangential flow filtration for purification of nanoparticle suspensions, *Pharm Res*, 22 (2005) 2152-2162.
- [243] R. Mihaila, S. Chang, A.T. Wei, Z.Y. Hu, D. Ruhela, T.R. Shadel, S. Duenwald, E. Payson, J.J. Cunningham, N. Kuklin, D.J. Mathre, Lipid nanoparticle purification by spin centrifugation-dialysis (SCD): a facile and high-throughput approach for small scale preparation of siRNA-lipid complexes, *Int J Pharm*, 420 (2011) 118-121.
- [244] C. Vauthier, B. Cabane, D. Labarre, How to concentrate nanoparticles and avoid aggregation?, *Eur J Pharm Biopharm*, 69 (2008) 466-475.

- [245] C. Webb, N. Forbes, C.B. Roces, G. Anderluzzi, G. Lou, S. Abraham, L. Ingalls, K. Marshall, T.J. Leaver, J.A. Watts, J.W. Aylott, Y. Perrie, Using microfluidics for scalable manufacturing of nanomedicines from bench to GMP: A case study using protein-loaded liposomes, *Int J Pharm*, 582 (2020) 119266.
- [246] N. Dimov, E. Kastner, M. Hussain, Y. Perrie, N. Szita, Formation and purification of tailored liposomes for drug delivery using a module-based micro continuous-flow system, *Sci Rep*, 7 (2017) 12045.
- [247] K.M. Dorney, J.D. Baker, M.L. Edwards, S.R. Kanel, M. O'Malley, I.E. Pavel Sizemore, Tangential flow filtration of colloidal silver nanoparticles: A "green" laboratory experiment for chemistry and engineering students, *J Chem Educ*, 91 (2014) 1044-1049.
- [248] A. Luken, M. Bruckhaus, U. Kosfeld, M. Emondts, M. Wessling, Automated tangential-flow diafiltration device, *HardwareX*, 10 (2021) e00200.
- [249] Millipore, Protein concentration and diafiltration by tangential flow filtration, *Tech Br*, (2003) 1-23.
- [250] A. Tavakoli Naeini, M.-G. Alameh, O.Y. Soliman, M. Lavertu, Purification and surface modification of chitosan-based polyplexes using tangential flow filtration and coating by hyaluronic acid, *J Pharm Sci*, 111 (2022) 2857-2866.
- [251] Y.A. Gomaa, M.J. Garland, F.J. McInnes, R.F. Donnelly, L.K. El-Khordagui, C.G. Wilson, Flux of ionic dyes across microneedle-treated skin: effect of molecular characteristics, *Int J Pharm*, 438 (2012) 140-149.
- [252] V. Jeannot, J.-M. Salmon, M. Deumié, P. Viallet, Intracellular accumulation of rhodamine 110 in single living cells, *J Histochem Cytochem*, 45 (1997) 403-412.
- [253] D. Yang, H. Wang, C. Sun, H. Zhao, K. Hu, W. Qin, R. Ma, F. Yin, X. Qin, Q. Zhang, Y. Liang, Z. Li, Development of a high quantum yield dye for tumour imaging, *Chem Sci*, 8 (2017) 6322-6326.
- [254] H.D. Duong, Y. Shin, J.I. Rhee, Development of novel optical pH sensors based on coumarin 6 and nile blue A encapsulated in resin particles and specific support materials, *Mater Sci Eng C Mater Biol Appl*, 107 (2020) 110323.
- [255] S. Essa, J.M. Rabanel, P. Hildgen, Characterization of rhodamine loaded PEG-g-PLA nanoparticles (NPs): effect of poly(ethylene glycol) grafting density, *Int J Pharm*, 411 (2011) 178-187.
- [256] C. Primard, N. Rochereau, E. Luciani, C. Genin, T. Delair, S. Paul, B. Verrier, Traffic of poly(lactic acid) nanoparticulate vaccine vehicle from intestinal mucus to sub-epithelial immune competent cells, *Biomaterials*, 31 (2010) 6060-6068.
- [257] B. Fernandes, R. Silva, A. Ribeiro, T. Matama, A.C. Gomes, A.M. Cavaco-Paulo, Improved Poly (D,L-lactide) nanoparticles-based formulation for hair follicle targeting, *Int J Cosmet Sci*, 37 (2015) 282-290.
- [258] P.B. O'Donnell, J.W. McGinity, Preparation of microspheres by the solvent evaporation technique, *Adv Drug Deliv Rev*, 28 (1997) 25-42.
- [259] J. Son, D. Lee, J. Yoo, C. Park, H. Koo, A comparative study of the effect of drug hydrophobicity on nanoparticle drug delivery in vivo using two photosensitizers, *Nanomedicine*, 24 (2020) 102151.
- [260] E. Purr, J. Marshall, J. Smith, Preparation of PLGA Nanoparticles Encapsulated with Fluorescent Probe Coumarin-6, *bioRxiv*, (2019) 614875.
- [261] E.M. Elmowafy, M. Tiboni, M.E. Soliman, Biocompatibility, biodegradation and biomedical applications of poly(lactic acid)/poly(lactic-co-glycolic acid) micro and nanoparticles, *J Pharm Investig*, 49 (2019) 347-380.
- [262] H.K. Makadia, S.J. Siegel, Poly lactic-co-glycolic acid (PLGA) as biodegradable controlled drug delivery carrier, *Polymers*, 3 (2011) 1377-1397.
- [263] A. Kumari, S.K. Yadav, S.C. Yadav, Biodegradable polymeric nanoparticles based drug delivery systems, *Colloids Surf B Biointerfaces*, 75 (2010) 1-18.

- [264] P. Rafiei, A. Haddadi, A robust systematic design: Optimization and preparation of polymeric nanoparticles of PLGA for docetaxel intravenous delivery, *Mater Sci Eng C Mater Biol Appl*, 104 (2019) 109950.
- [265] H. Cai, X. Wen, L. Wen, N. Tirelli, X. Zhang, Y. Zhang, H. Su, F. Yang, G. Chen, Enhanced local bioavailability of single or compound drugs delivery to the inner ear through application of PLGA nanoparticles via round window administration, *Int J Nanomedicine*, 9 (2014) 5591-5601.
- [266] S. Wang, Y. Chen, F. Gao, X. Li, Y. Huang, Q.P. Yeng, Q. Zheng, Construction of brain-targeted nanoreactor system and intracerebral drug delivery, *J Pharm Biomed Sci*, 07 (2017) 405-410.
- [267] E.R. Osorio-Blanco, J. Bergueiro, B.E. Abali, S. Ehrmann, C. Böttcher, A.J. Müller, J.L. Cuéllar-Camacho, M. Calderón, Effect of core nanostructure on the thermomechanical properties of soft nanoparticles, *Chem Mater*, 32 (2019) 518-528.
- [268] I. Valente, E. Celasco, D.L. Marchisio, A.A. Barresi, Nanoprecipitation in confined impinging jets mixers: Production, characterization and scale-up of pegylated nanospheres and nanocapsules for pharmaceutical use, *Chem Eng Sci*, 77 (2012) 217-227.
- [269] F. Chouinard, F.W.K. Kan, J.-C. Leroux, C. Foucher, V. Lenaerts, Preparation and purification of polyisohexylcyanoacrylate nanocapsules, *Int J Pharm*, 72 (1991) 211-217.
- [270] J. Fickert, M. Makowski, M. Kappl, K. Landfester, D. Crespy, Efficient encapsulation of self-healing agents in polymer nanocontainers functionalized by orthogonal reactions, *Macromolecules*, 45 (2012) 6324-6332.
- [271] U. Bazylińska, A. Lewińska, Ł. Lamch, K.A. Wilk, Polymeric nanocapsules and nanospheres for encapsulation and long sustained release of hydrophobic cyanine-type photosensitizer, *Colloids Surf A Physicochem Eng Asp*, 442 (2014) 42-49.
- [272] W. Abdelwahed, G. Degobert, H. Fessi, A pilot study of freeze drying of poly(epsilon-caprolactone) nanocapsules stabilized by poly(vinyl alcohol): formulation and process optimization, *Int J Pharm*, 309 (2006) 178-188.
- [273] F.L. Marten, Vinyl alcohol polymers, *Encyclopedia of Polymer Science and Technology*, John Wiley & Sons, Inc.2002.
- [274] N. Gaiti, A. Aserin, Y. Cohen, Mechanistic considerations on the release of electrolytes from multiple emulsions stabilized by BSA and nonionic surfactants, *J Control Release*, 29 (1994) 41-51.
- [275] H. Cortes, H. Hernandez-Parra, S.A. Bernal-Chavez, M.L.D. Prado-Audelo, I.H. Caballero-Floran, F.V. Borbolla-Jimenez, M. Gonzalez-Torres, J.J. Magana, G. Leyva-Gomez, Non-Ionic surfactants for stabilization of polymeric nanoparticles for biomedical uses, *Materials (Basel)*, 14 (2021).
- [276] S.M. Görich, Untersuchung zu verfahrenstechnischen Parametern des W/OW-Triplemulsionsverfahrens für die Mikroverkapselung hydrophiler Makromoleküle, Fachbereich Pharmazie und Lebensmittelchemie, Philipps-Universität Marburg, Marburg/Lahn, 1994.
- [277] S.S. Davis, L. Illum, J. McVie, E. Tomlinson, *Microspheres and drug therapy: pharmaceutical, immunological, and medical aspects*, Elsevier Science Ltd1984.
- [278] Y. Morikawa, T. Tagami, A. Hoshikawa, T. Ozeki, The use of an efficient microfluidic mixing system for generating stabilized polymeric nanoparticles for controlled drug release, *Biol Pharm Bull*, 41 (2018) 899-907.
- [279] C.Y. Tham, Z.A. Abdul Hamid, H. Ismail, Z. Ahmad, Poly (vinyl alcohol) in fabrication of PLA micro- and nanoparticles using emulsion and solvent evaporation technique, *Adv Mat Res*, 1024 (2014) 296-299.
- [280] L. Shi, J. Zhang, M. Zhao, S. Tang, X. Cheng, W. Zhang, W. Li, X. Liu, H. Peng, Q. Wang, Effects of polyethylene glycol on the surface of nanoparticles for targeted drug delivery, *Nanoscale*, 13 (2021) 10748-10764.

- [281] S. Lahkar, M.K. Das, Surface-modified polycaprolactone nanoparticles for the brain-targeted delivery of nevirapine, *J Nanoparticle Res*, 22 (2020).
- [282] L. Marinelli, M. Ciulla, J.A.S. Ritsema, C.F. van Nostrum, I. Cacciatore, M.P. Dimmito, F. Palmerio, G. Orlando, I. Robuffo, R. Grande, V. Puca, A. Di Stefano, Preparation, characterization, and biological evaluation of a hydrophilic peptide loaded on PEG-PLGA nanoparticles, *Pharmaceutics*, 14 (2022).
- [283] G. Mittal, D.K. Sahana, V. Bhardwaj, M.N. Ravi Kumar, Estradiol loaded PLGA nanoparticles for oral administration: effect of polymer molecular weight and copolymer composition on release behavior in vitro and in vivo, *J Control Release*, 119 (2007) 77-85.
- [284] S.M. Jafari, E. Assadpoor, Y. He, B. Bhandari, Re-coalescence of emulsion droplets during high-energy emulsification, *Food Hydrocolloids*, 22 (2008) 1191-1202.
- [285] S. Zafar, S. Akhter, I. Ahmad, Z. Hafeez, M.M. Alam Rizvi, G.K. Jain, F.J. Ahmad, Improved chemotherapeutic efficacy against resistant human breast cancer cells with co-delivery of Docetaxel and Thymoquinone by Chitosan grafted lipid nanocapsules: Formulation optimization, in vitro and in vivo studies, *Colloids Surf B Biointerfaces*, 186 (2020) 110603.
- [286] P. Marie, J.M. Perrier-Cornet, P. Gervais, Influence of major parameters in emulsification mechanisms using a high-pressure jet, *J Food Eng*, 53 (2002) 43-51.
- [287] B.S.B. Bamba, J. Shi, C.C. Tranchant, S.J. Xue, C.F. Forney, L.T. Lim, W. Xu, G. Xu, Coencapsulation of polyphenols and anthocyanins from blueberry pomace by double emulsion stabilized by whey proteins: Effect of homogenization parameters, *Molecules*, 23 (2018).
- [288] A. Carrio, G. Schwach, J. Coudane, M. Vert, Preparation and degradation of surfactant-free PLGA microspheres, *J Control Release*, 37 (1995) 113-121.
- [289] B. Shkodra-Pula, C. Grune, A. Traeger, A. Vollrath, S. Schubert, D. Fischer, U.S. Schubert, Effect of surfactant on the size and stability of PLGA nanoparticles encapsulating a protein kinase C inhibitor, *Int J Pharm*, 566 (2019) 756-764.
- [290] M.F. Zambaux, F. Bonneaux, R. Gref, P. Maincent, E. Dellacherie, M.J. Alonso, P. Labrude, C. Vigneron, Influence of experimental parameters on the characteristics of poly(lactic acid) nanoparticles prepared by a double emulsion method, *J Control Release*, 50 (1998) 31-40.
- [291] A.K. Kushwaha, P.R. Vuddanda, P. Karunanidhi, S.K. Singh, S. Singh, Development and evaluation of solid lipid nanoparticles of raloxifene hydrochloride for enhanced bioavailability, *Biomed Res Int*, 2013 (2013) 584549.
- [292] X. Wang, X. Li, P. Duffy, S. McMahon, X. Wang, J. Lyu, Q. Xu, S. A, N.N. Chen, V. Bi, T. Dürig, W. Wang, Resveratrol-loaded poly(d,l-lactide-co-glycolide) microspheres integrated in a hyaluronic acid injectable hydrogel for cartilage regeneration, *Adv Nanobiomed Res*, 2 (2021).
- [293] A. Trapani, D. Mandracchia, C. Di Franco, H. Cordero, P. Morcillo, R. Comparelli, A. Cuesta, M.A. Esteban, In vitro characterization of 6-Coumarin loaded solid lipid nanoparticles and their uptake by immunocompetent fish cells, *Colloids Surf B Biointerfaces*, 127 (2015) 79-88.
- [294] H.G. Brittain, R.D. Bruce, Chapter 4 - Thermal analysis, in: S. Ahuja, N. Jespersen (Eds.) *Comprehensive Analytical Chemistry*, Elsevier 2006, pp. 63-109.
- [295] K. Park, A. Otte, F. Sharifi, J. Garner, S. Skidmore, H. Park, Y.K. Jhon, B. Qin, Y. Wang, Potential roles of the glass transition temperature of PLGA microparticles in drug release kinetics, *Mol Pharm*, 18 (2021) 18-32.
- [296] M.K. Singh, M. Hu, Y. Cang, H.P. Hsu, H. Therien-Aubin, K. Koynov, G. Fytas, K. Landfester, K. Kremer, Glass transition of disentangled and entangled polymer melts: Single-chain-nanoparticles approach, *Macromolecules*, 53 (2020) 7312-7321.
- [297] C. Grune, C. Kretzer, S. Zergiebel, S. Kattner, J. Thamm, S. Hoepfener, O. Werz, D. Fischer, Encapsulation of the anti-inflammatory dual FLAP/sEH inhibitor diflupolol improves the efficiency in human whole blood, *J Pharm Sci*, 111 (2022) 1843-1850.

- [298] S. Lappe, D. Mulac, K. Langer, Polymeric nanoparticles - Influence of the glass transition temperature on drug release, *Int J Pharm*, 517 (2017) 338-347.
- [299] W.N. Ibrahim, L. Muizzuddin Bin Mohd Rosli, A.A. Doolaanea, Formulation, cellular uptake and cytotoxicity of thymoquinone-loaded PLGA nanoparticles in malignant melanoma cancer cells, *Int J Nanomedicine*, 15 (2020) 8059-8074.
- [300] K. Knop, R. Hoogenboom, D. Fischer, U.S. Schubert, Poly(ethylene glycol) in drug delivery: pros and cons as well as potential alternatives, *Angew Chem Int Ed Engl*, 49 (2010) 6288-6308.
- [301] M. Dirauf, C. Grune, C. Weber, U.S. Schubert, D. Fischer, Poly(ethylene glycol) or poly(2-ethyl-2-oxazoline) – A systematic comparison of PLGA nanoparticles from the bottom up, *Eur Polym J*, 134 (2020).
- [302] K. Zhang, X. Tang, J. Zhang, W. Lu, X. Lin, Y. Zhang, B. Tian, H. Yang, H. He, PEG-PLGA copolymers: their structure and structure-influenced drug delivery applications, *J Control Release*, 183 (2014) 77-86.
- [303] X. Lin, H. Yang, L. Su, Z. Yang, X. Tang, Effect of size on the in vitro / in vivo drug release and degradation of exenatide-loaded PLGA microspheres, *J Drug Deliv Sci Technol*, 45 (2018) 346-356.
- [304] R. Liu, S.S. Huang, Y.H. Wan, G.H. Ma, Z.G. Su, Preparation of insulin-loaded PLA/PLGA microcapsules by a novel membrane emulsification method and its release in vitro, *Colloids Surf B Biointerfaces*, 51 (2006) 30-38.
- [305] M.M. El-Hammadi, J.L. Arias, Recent advances in the surface functionalization of PLGA-based nanomedicines, *Nanomaterials (Basel)*, 12 (2022).
- [306] Q. Jin, S.T. Kang, Y.C. Chang, H. Zheng, C.K. Yeh, Inertial cavitation initiated by polytetrafluoroethylene nanoparticles under pulsed ultrasound stimulation, *Ultrason Sonochem*, 32 (2016) 1-7.
- [307] Q. Wu, F. Zhang, X. Pan, Z. Huang, Z. Zeng, H. Wang, J. Jiao, X. Xiong, L. Bai, D. Zhou, H. Liu, Surface wettability of nanoparticle modulated sonothrombolysis, *Adv Mater*, 33 (2021) e2007073.
- [308] A. Yildirim, R. Chattaraj, N.T. Blum, A.P. Goodwin, Understanding acoustic cavitation initiation by porous nanoparticles: Toward nanoscale agents for ultrasound imaging and therapy, *Chem Mater*, 28 (2016) 5962-5972.
- [309] E. Trenkenschuh, U. Savsek, W. Friess, Formulation, process, and storage strategies for lyophilizates of lipophilic nanoparticulate systems established based on the two models paliperidone palmitate and solid lipid nanoparticles, *Int J Pharm*, 606 (2021) 120929.
- [310] A. Rampino, M. Borgogna, P. Blasi, B. Bellich, A. Cesaro, Chitosan nanoparticles: preparation, size evolution and stability, *Int J Pharm*, 455 (2013) 219-228.
- [311] M. Holzer, V. Vogel, W. Mantele, D. Schwartz, W. Haase, K. Langer, Physico-chemical characterisation of PLGA nanoparticles after freeze-drying and storage, *Eur J Pharm Biopharm*, 72 (2009) 428-437.
- [312] H. Heiati, R. Tawashi, N.C. Phillips, Drug retention and stability of solid lipid nanoparticles containing azidothymidine palmitate after autoclaving, storage and lyophilization, *J Microencapsul*, 15 (1998) 173-184.
- [313] L.M. Crowe, D.S. Reid, J.H. Crowe, Is trehalose special for preserving dry biomaterials?, *Biophys J*, 71 (1996) 2087-2093.
- [314] A. Alshememry, M.A. Kalam, A. Almoghrabi, A. Alzahrani, M. Shahid, A.A. Khan, A. Haque, R. Ali, M. Alkholief, Z. Binkhathlan, A. Alshamsan, Chitosan-coated poly (lactic-co-glycolide) nanoparticles for dual delivery of doxorubicin and naringin against MCF-7 cells, *J Drug Deliv Sci Technol*, 68 (2022).
- [315] M.A. Kalam, A. Alshamsan, Poly (d, l-lactide-co-glycolide) nanoparticles for sustained release of tacrolimus in rabbit eyes, *Biomed Pharmacother*, 94 (2017) 402-411.

- [316] P. Fonte, S. Soares, F. Sousa, A. Costa, V. Seabra, S. Reis, B. Sarmento, Stability study perspective of the effect of freeze-drying using cryoprotectants on the structure of insulin loaded into PLGA nanoparticles, *Biomacromolecules*, 15 (2014) 3753-3765.
- [317] W. Wang, Lyophilization and development of solid protein pharmaceuticals, *Int J Pharm*, 203 (2000) 1-60.
- [318] W.L. Hinrichs, N.N. Sanders, S.C. De Smedt, J. Demeester, H.W. Frijlink, Inulin is a promising cryo- and lyoprotectant for PEGylated lipoplexes, *J Control Release*, 103 (2005) 465-479.
- [319] N.K. Jain, I. Roy, Effect of trehalose on protein structure, *Protein Sci*, 18 (2009) 24-36.
- [320] F. Franks, Long-term stabilization of biologicals, *Bio/Technology*, 12 (1994) 253-256.
- [321] M.S. Ebied, M. Dongol, M. Ibrahim, M. Nassary, S. Elnobi, A.A. Abuelwafa, Structural and optical properties of nanocrystalline 3-(2-benzothiazolyl)-7-(diethylamino) coumarin (C6) thin films for optoelectronic application, *J Electron Mater*, 51 (2022) 5770-5782.
- [322] P. Sundaramurthi, R. Suryanarayanan, Trehalose crystallization during freeze-drying: Implications on lyoprotection, *Phys Chem Lett*, 1 (2009) 510-514.
- [323] J. Yu, T.J. Anchordoquy, Effects of moisture content on the storage stability of dried lipoplex formulations, *J Pharm Sci*, 98 (2009) 3278-3289.
- [324] M.J. Pikal, S. Shah, Moisture transfer from stopper to product and resulting stability implications, *Developments in biological standardization*, 74 (1992) 165-177; discussion 177-169.
- [325] H. Sasaki, J. Kikuchi, T. Maeda, H. Kuboniwa, Impact of different elastomer formulations on moisture permeation through stoppers used for lyophilized products stored under humid conditions, *PDA J Pharm Sci Technol*, 64 (2010) 63-70.
- [326] W.F. Tonnis, M.A. Mensink, A. de Jager, K. van der Voort Maarschalk, H.W. Frijlink, W.L. Hinrichs, Size and molecular flexibility of sugars determine the storage stability of freeze-dried proteins, *Mol Pharm*, 12 (2015) 684-694.
- [327] K. Lo Presti, W. Friess, Adjustment of specific residual moisture levels in completely freeze-dried protein formulations by controlled spiking of small water volumes, *Eur J Pharm Biopharm*, 169 (2021) 292-296.
- [328] A. Duralliu, P. Matejtschuk, P. Stickings, L. Hassall, R. Tierney, D.R. Williams, The influence of moisture content and temperature on the long-term storage stability of freeze-dried high concentration immunoglobulin G (IgG), *Pharmaceutics*, 12 (2020).
- [329] J.C. May, Regulatory control of freeze-dried products: Importance and evaluation of residual moisture, *Freeze-Drying/Lyophilization of Pharmaceutical and Biological Products*, Dekker, New York, 2004, pp. 349-384.
- [330] P. Bihari, M. Vippola, S. Schultes, M. Praetner, A.G. Khandoga, C.A. Reichel, C. Coester, T. Tuomi, M. Rehberg, F. Krombach, Optimized dispersion of nanoparticles for biological in vitro and in vivo studies, *Part Fibre Toxicol*, 5 (2008) 14.
- [331] K. Strojjan, A. Leonardi, V.B. Bregar, I. Krizaj, J. Svete, M. Pavlin, Dispersion of nanoparticles in different media importantly determines the composition of their protein corona, *PLoS One*, 12 (2017) e0169552.
- [332] H. Nazari-Mahroo, K. Pasandideh, H.A. Navid, R. Sadighi-Bonabi, How important is the liquid bulk viscosity effect on the dynamics of a single cavitation bubble?, *Ultrason Sonochem*, 49 (2018) 47-52.
- [333] C. Guo, J. Liu, X. Li, S. Yang, Effect of cavitation bubble on the dispersion of magnetorheological polishing fluid under ultrasonic preparation, *Ultrason Sonochem*, 79 (2021) 105782.
- [334] J. Luo, W. Xu, Y. Zhai, Q. Zhang, Experimental study on the mesoscale causes of the influence of viscosity on material erosion in a cavitation field, *Ultrason Sonochem*, 59 (2019) 104699.

- [335] M.J. Bussemaker, D. Zhang, A phenomenological investigation into the opposing effects of fluid flow on sonochemical activity at different frequency and power settings. 1. Overhead stirring, *Ultrason Sonochem*, 21 (2014) 436-445.
- [336] R.J. Wood, J. Lee, M.J. Bussemaker, A parametric review of sonochemistry: Control and augmentation of sonochemical activity in aqueous solutions, *Ultrason Sonochem*, 38 (2017) 351-370.
- [337] A. Diamond, C.T. Lye, D. Prasad, D. Abbott, One size does not fit all: Assuming the same normal body temperature for everyone is not justified, *PLoS One*, 16 (2021) e0245257.
- [338] E.B. Neves, A.C.C. Salamunes, R.M. de Oliveira, A.M.W. Stadnik, Effect of body fat and gender on body temperature distribution, *J Therm Biol*, 70 (2017) 1-8.
- [339] I.H. Gomolin, M.M. Aung, G. Wolf-Klein, C. Auerbach, Older is colder: Temperature range and variation in older people, *J Am Geriatr Soc*, 53 (2005) 2170-2172.
- [340] C. Wunderlich, J. Reeve, The course of the temperature in diseases: a guide to clinical thermometry, *J Med Sci*, 57 (1869) 47.
- [341] V.E. Del Bene, Temperature, in: H.K. Walker, W.D. Hall, J.W. Hurst (Eds.) *Clinical Methods: The History, Physical, and Laboratory Examinations*, Butterworths, Boston, 1990.
- [342] X. Yang, C.C. Church, A model for the dynamics of gas bubbles in soft tissue, *J Acoust Soc Am*, 118 (2005) 3595-3606.
- [343] J.G. Auret, O.F.R.A. Damm, G.J. Wright, F.P.A. Robinson, Cavitation erosion of copper and aluminium in water at elevated temperature, *Tribol Int*, 26 (1993) 421-429.
- [344] T.-H. Phan, E. Kadivar, V.-T. Nguyen, O. el Moctar, W.-G. Park, Thermodynamic effects on single cavitation bubble dynamics under various ambient temperature conditions, *Phys Fluids*, 34 (2022).
- [345] L.W. Florschuetz, B.T. Chao, On the mechanics of vapor bubble collapse -- A theoretical and experimental investigation. Final Report 2, United States, 1963, pp. 129.
- [346] N. Takada, T. Nakano, K. Sasaki, Formation of cavitation-induced pits on target surface in liquid-phase laser ablation, *Appl Phys A*, 101 (2010) 255-258.
- [347] N.T. Blum, C.M. Gyorkos, S.J. Narowitz, E.N. Mueller, A.P. Goodwin, Phospholipid-coated hydrophobic mesoporous silica nanoparticles enhance thrombectomy by high-intensity focused ultrasound with low production of embolism-inducing clot debris, *ACS Appl Mater Interfaces*, 11 (2019) 36324-36332.
- [348] G. Vazquez, E. Alvarez, J.M. Navaza, Surface tension of alcohol water + water from 20 to 50 .degree.C, *J Chem Eng Data*, 40 (1995) 611-614.
- [349] P. Martinez, N. Bottenus, M. Borden, Cavitation characterization of size-isolated microbubbles in a vessel phantom using focused ultrasound, *Pharmaceutics*, 14 (2022).
- [350] T.J. Hall, M. Bilgen, M.F. Insana, T.A. Krouskop, Phantom materials for elastography, *IEEE Trans Ultrason Ferroelectr Freq Control*, 44 (1997) 1355-1365.
- [351] L. Braunstein, S.C. Bruning, I. Rivens, J. Civale, G.T. Haar, Characterization of acoustic, cavitation, and thermal properties of poly(vinyl alcohol) hydrogels for use as therapeutic ultrasound tissue mimics, *Ultrasound Med Biol*, 48 (2022) 1095-1109.
- [352] E.L. Madsen, J.A. Zagzebski, R.A. Banjavie, R.E. Jutila, Tissue mimicking materials for ultrasound phantoms, *Med Phys*, 5 (1978) 391-394.
- [353] C. Gopalan, E. Kirk, Chapter 2 - The blood vessels, in: C. Gopalan, E. Kirk (Eds.) *Biology of Cardiovascular and Metabolic Diseases*, Academic Press 2022, pp. 35-51.
- [354] G.J. Tortora, B.H. Derrickson, *Anatomie und physiologie*, WILEY-VCH Verlag GmbH & Co. KGaA, Weinheim, 2006.
- [355] Y.S. Tung, J.J. Choi, B. Baseri, E.E. Konofagou, Identifying the inertial cavitation threshold and skull effects in a vessel phantom using focused ultrasound and microbubbles, *Ultrasound Med Biol*, 36 (2010) 840-852.
- [356] M.P. Monopoli, C. Åberg, A. Salvati, K.A. Dawson, Biomolecular coronas provide the biological identity of nanosized materials, *Nat Nanotechnol*, 7 (2012) 779-786.

- [357] R.M. Pearson, V.V. Juettner, S. Hong, Biomolecular corona on nanoparticles: a survey of recent literature and its implications in targeted drug delivery, *Front Chem*, 2 (2014) 108.
- [358] K. Partikel, R. Korte, N.C. Stein, D. Mulac, F.C. Herrmann, H.U. Humpf, K. Langer, Effect of nanoparticle size and PEGylation on the protein corona of PLGA nanoparticles, *Eur J Pharm Biopharm*, 141 (2019) 70-80.
- [359] K. Partikel, R. Korte, D. Mulac, H.U. Humpf, K. Langer, Serum type and concentration both affect the protein-corona composition of PLGA nanoparticles, *Beilstein J Nanotechnol*, 10 (2019) 1002-1015.
- [360] N. Bertrand, P. Grenier, M. Mahmoudi, E.M. Lima, E.A. Appel, F. Dormont, J.M. Lim, R. Karnik, R. Langer, O.C. Farokhzad, Mechanistic understanding of in vivo protein corona formation on polymeric nanoparticles and impact on pharmacokinetics, *Nat Commun*, 8 (2017) 777.
- [361] P. Breznica, R. Koliqi, A. Daka, A review of the current understanding of nanoparticles protein corona composition, *Med Pharm Rep*, 93 (2020) 342-350.
- [362] X. Hong, Y. Meng, S.N. Kalkanis, Serum proteins are extracted along with monolayer cells in plasticware and interfere with protein analysis, *J Biol Methods*, 3 (2016).
- [363] P. Tharkar, R. Varanasi, W.S.F. Wong, C.T. Jin, W. Chrzanowski, Nano-enhanced drug delivery and therapeutic ultrasound for cancer treatment and beyond, *Front Bioeng Biotechnol*, 7 (2019) 324.
- [364] T. Peters, All about albumin: Biochemistry, genetics, and medical applications, Elsevier Science 1995.
- [365] D.C. Carter, J.X. Ho, Structure of serum albumin, *Adv Protein Chem*, 45 (1994) 153-203.
- [366] L.R. Barbosa, M.G. Ortore, F. Spinozzi, P. Mariani, S. Bernstorff, R. Itri, The importance of protein-protein interactions on the pH-induced conformational changes of bovine serum albumin: a small-angle X-ray scattering study, *Biophys J*, 98 (2010) 147-157.
- [367] C. Liu, W. Yang, Q. Gao, J. Du, H. Luo, Y. Liu, C. Yang, Differential recognition and quantification of HSA and BSA based on two red-NIR fluorescent probes, *J Lumin*, 197 (2018) 193-199.
- [368] R. Maier, M.R. Fries, C. Buchholz, F. Zhang, F. Schreiber, Human versus bovine serum albumin: A subtle difference in hydrophobicity leads to large differences in bulk and interface behavior, *Cryst Growth Des*, 21 (2021) 5451-5459.
- [369] S. Qi, B. Assouar, W. Chen, Effects of bovine serum albumin on a single cavitation bubble, *Ultrason Sonochem*, 38 (2017) 473-477.
- [370] X. Guo, Q. Li, Z. Zhang, D. Zhang, J. Tu, Investigation on the inertial cavitation threshold and shell properties of commercialized ultrasound contrast agent microbubbles, *J Acoust Soc Am*, 134 (2013) 1622-1631.
- [371] I. Miller, M. Gemeiner, Peculiarities in electrophoretic behavior of different serum albumins, *Electrophoresis*, 14 (1993) 1312-1317.
- [372] T. Kosa, T. Maruyama, M. Otagiri, Species differences of serum albumins: II. Chemical and thermal stability, *Pharm Res*, 15 (1998) 449-454.
- [373] T. Kosa, T. Maruyama, M. Otagiri, Species differences of serum albumins: I. Drug binding sites, *Pharm Res*, 14 (1997) 1607-1612.
- [374] Y. Akdogan, J. Reichenwallner, D. Hinderberger, Evidence for water-tuned structural differences in proteins: an approach emphasizing variations in local hydrophilicity, *PLoS One*, 7 (2012) e45681.
- [375] A. Michnik, K. Michalik, A. Kluczevska, Z. Drzazga, Comparative DSC study of human and bovine serum albumin, *J Therm Anal Calorim*, 84 (2006) 113-117.
- [376] P.J. Price, E.A. Gregory, Relationship between in vitro growth promotion and biophysical and biochemical properties of the serum supplement, *In Vitro*, 18 (1982) 576-584.
- [377] T. Suzawa, H. Shirahama, Adsorption of plasma proteins onto polymer latices, *Adv Colloid Interface Sci*, 35 (1991) 139-172.

- [378] T. Yao, Y. Asayama, Animal-cell culture media: History, characteristics, and current issues, *Reprod Med Biol*, 16 (2017) 99-117.
- [379] A. Chen, M. Leith, R. Tu, G. Tahim, A. Sudra, S. Bhargava, Effects of diluents on cell culture viability measured by automated cell counter, *PLoS One*, 12 (2017) e0173375.
- [380] S. Lagies, M. Schlimpert, S. Neumann, A. Waldin, B. Kammerer, C. Borner, L. Peintner, Cells grown in three-dimensional spheroids mirror in vivo metabolic response of epithelial cells, *Commun Biol*, 3 (2020) 246.
- [381] L. Pusch, R. Brox, K. Scheuer, T. Yokosawa, M. Wu, B.A. Zubiri, E. Spiecker, K.D. Jandt, D. Fischer, H. Hackstein, Distinct endocytosis and immune activation of poly(lactic-co-glycolic) acid nanoparticles prepared by single- and double-emulsion evaporation, *Nanomedicine (Lond)*, 16 (2021) 2075-2094.
- [382] J.D. Sato, M. Kan, Media for culture of mammalian cells, *Curr Protoc Cell Biol*, 00 (1998) 1.2.1-1.2.15.
- [383] S. Tenzer, D. Docter, J. Kuharev, A. Musyanovych, V. Fetz, R. Hecht, F. Schlenk, D. Fischer, K. Kiouptsi, C. Reinhardt, K. Landfester, H. Schild, M. Maskos, S.K. Knauer, R.H. Stauber, Rapid formation of plasma protein corona critically affects nanoparticle pathophysiology, *Nature Nanotechnology*, 8 (2013) 772-781.
- [384] T. Cedervall, I. Lynch, S. Lindman, T. Berggård, E. Thulin, H. Nilsson, K.A. Dawson, S. Linse, Understanding the nanoparticle–protein corona using methods to quantify exchange rates and affinities of proteins for nanoparticles, *Proc Natl Acad Sci U.S.A.*, 104 (2007) 2050-2055.
- [385] E. Casals, T. Pfaller, A. Duschl, G.J. Oostingh, V. Puentes, Time evolution of the nanoparticle protein corona, *ACS Nano*, 4 (2010) 3623-3632.
- [386] T. Lima, K. Bernfur, M. Vilanova, T. Cedervall, Understanding the lipid and protein corona formation on different sized polymeric nanoparticles, *Sci Rep*, 10 (2020) 1129.
- [387] K. Yu, J. Zhao, Z. Zhang, Y. Gao, Y. Zhou, L. Teng, Y. Li, Enhanced delivery of Paclitaxel using electrostatically-conjugated Herceptin-bearing PEI/PLGA nanoparticles against HER-positive breast cancer cells, *Int J Pharm*, 497 (2016) 78-87.
- [388] S.Y. Lee, H.J. Cho, Amine-functionalized poly(lactic-co-glycolic acid) nanoparticles for improved cellular uptake and tumor penetration, *Colloids Surf B Biointerfaces*, 148 (2016) 85-94.
- [389] E. Zhang, V. Zhukova, A. Semyonkin, N. Osipova, Y. Malinovskaya, O. Maksimenko, V. Chernikov, M. Sokolov, L. Grigartzik, B.A. Sabel, S. Gelperina, P. Henrich-Noack, Release kinetics of fluorescent dyes from PLGA nanoparticles in retinal blood vessels: In vivo monitoring and ex vivo localization, *Eur J Pharm Biopharm*, 150 (2020) 131-142.
- [390] G. Ramírez-García, L. Trapiella-Alfonso, F. d'Orlyé, A. Varenne, Chapter 17 - Electrophoretic methods for characterizing nanoparticles and evaluating their bio-interactions for their further use as diagnostic, imaging, or therapeutic tools, in: C.F. Poole (Ed.) *Capillary Electromigration Separation Methods*, Elsevier 2018, pp. 397-421.
- [391] F. Schlenk, S. Werner, M. Rabel, F. Jacobs, C. Bergemann, J.H. Clement, D. Fischer, Comprehensive analysis of the in vitro and ex ovo hemocompatibility of surface engineered iron oxide nanoparticles for biomedical applications, *Arch Toxicol*, 91 (2017) 3271-3286.
- [392] M. Pavlin, V.B. Bregar, Stability of nanoparticle suspensions in different biologically relevant media, *Dig J Nanomater Biostructures*, Vol. 7 (2012) 1389-1400.
- [393] R.W. Mahley, J. Stanley C. Rall, Apolipoprotein E: Far more than a lipid transport protein, *Annu Rev Genomics Hum Genet* 1(2000) 507-537.
- [394] J.W. Gaubatz, R.C. Hoogeveen, A.S. Hoffman, K.G. Ghazzaly, H.J. Pownall, J. Guevara, M.L. Koschinsky, J.D. Morrisett, Isolation, quantitation, and characterization of a stable complex formed by Lp[a] binding to triglyceride-rich lipoproteins, *J Lipid Res*, 42 (2001) 2058-2068.

- [395] L.C. Antonio, L. Ribovski, P.M. Pincela Lins, V. Zucolotto, The amount of dextran in PLGA nanocarriers modulates protein corona and promotes cell membrane damage, *J Mater Chem B*, 10 (2022) 8282-8294.
- [396] M. Rabe, D. Verdes, J. Zimmermann, S. Seeger, Surface organization and cooperativity during nonspecific protein adsorption events, *J Phys Chem B*, 112 (2008) 13971-13980.
- [397] X. Wang, C. Chen, K. Binder, U. Kuhn, U. Pöschl, H. Su, Y. Cheng, Molecular dynamics simulation of the surface tension of aqueous sodium chloride: from dilute to highly supersaturated solutions and molten salt, *Atmospheric Chem Phys*, 18 (2018) 17077-17086.
- [398] A.T. Palasz, J. Thundathil, R.E. Verrall, R.J. Mapletoft, The effect of macromolecular supplementation on the surface tension of TCM-199 and the utilization of growth factors by bovine oocytes and embryos in culture, *Anim Reprod Sci*, 58 (2000) 229-240.
- [399] F. Li, J. Song, H. Qi, F. Sui, G. Li, Q. Wang, Effects of static magnetic fields on the physical and chemical properties of cell culture medium RPM1 1640, *Electromagn Biol Med*, 26 (2007) 25-32.
- [400] J.Y. Lee, L.M. Hildemann, Surface tension of solutions containing dicarboxylic acids with ammonium sulfate, d-glucose, or humic acid, *J Aerosol Sci*, 64 (2013) 94-102.
- [401] Q. Jin, C.Y. Lin, Y.C. Chang, C.M. Yang, C.K. Yeh, Roles of textural and surface properties of nanoparticles in ultrasound-responsive systems, *Langmuir*, 34 (2018) 1256-1265.
- [402] S. Schottler, G. Becker, S. Winzen, T. Steinbach, K. Mohr, K. Landfester, V. Mailander, F.R. Wurm, Protein adsorption is required for stealth effect of poly(ethylene glycol)- and poly(phosphoester)-coated nanocarriers, *Nat Nanotechnol*, 11 (2016) 372-377.
- [403] T. Cedervall, I. Lynch, M. Foy, T. Berggard, S.C. Donnelly, G. Cagney, S. Linse, K.A. Dawson, Detailed identification of plasma proteins adsorbed on copolymer nanoparticles, *Angew Chem Int Ed Engl*, 46 (2007) 5754-5756.
- [404] A. Gessner, R. Waicz, A. Lieske, B.R. Paulke, K. Mäder, R.H. Müller, Nanoparticles with decreasing surface hydrophobicities: influence on plasma protein adsorption, *Int J Pharm*, 196 (2000) 245-249.
- [405] N. Hartl, F. Adams, O.M. Merkel, From adsorption to covalent bonding: Apolipoprotein E functionalization of polymeric nanoparticles for drug delivery across the blood-brain barrier, *Adv Ther (Weinh)*, 4 (2021).
- [406] H. Spreen, M. Behrens, D. Mulac, H.U. Humpf, K. Langer, Identification of main influencing factors on the protein corona composition of PLGA and PLA nanoparticles, *Eur J Pharm Biopharm*, 163 (2021) 212-222.
- [407] S. Winzen, S. Schoettler, G. Baier, C. Rosenauer, V. Mailaender, K. Landfester, K. Mohr, Complementary analysis of the hard and soft protein corona: sample preparation critically effects corona composition, *Nanoscale*, 7 (2015) 2992-3001.
- [408] C. Pisani, E. Rascol, C. Dorandeu, J.C. Gaillard, C. Charnay, Y. Guari, J. Chopineau, J. Armengaud, J.M. Devoisselle, O. Prat, The species origin of the serum in the culture medium influences the in vitro toxicity of silica nanoparticles to HepG2 cells, *PLoS One*, 12 (2017) e0182906.
- [409] L. Pusch, R. Brox, S. Cunningham, D. Fischer, H. Hackstein, Medium supplementation with human, but not fetal calf serum facilitates endocytosis of PLGA nanoparticles by human primary B-lymphocytes via complement opsonization, *Biochem Biophys Res Commun*, 656 (2023) 10-15.
- [410] I. Gitlin, J.D. Carbeck, G.M. Whitesides, Why are proteins charged? Networks of charge-charge interactions in proteins measured by charge ladders and capillary electrophoresis, *Angew Chem Int Ed Engl*, 45 (2006) 3022-3060.
- [411] R. Gossmann, E. Fahrlander, M. Hummel, D. Mulac, J. Brockmeyer, K. Langer, Comparative examination of adsorption of serum proteins on HSA- and PLGA-based nanoparticles using SDS-PAGE and LC-MS, *Eur J Pharm Biopharm*, 93 (2015) 80-87.

- [412] K. Murayama, Y. Wu, B. Czarnik-Matusewicz, Y. Ozaki, Two-dimensional/attenuated total reflection infrared correlation spectroscopy studies on secondary structural changes in human serum albumin in aqueous solutions: pH-dependent structural changes in the secondary structures and in the hydrogen bondings of side chains, *J Phys Chem B*, 105 (2001) 4763-4769.
- [413] M. Mahmoudi, M.P. Landry, A. Moore, R. Coreas, The protein corona from nanomedicine to environmental science, *Nat Rev Mater*, (2023) 1-17.
- [414] G. Bashiri, M.S. Padilla, K.L. Swingle, S.J. Shepherd, M.J. Mitchell, K. Wang, Nanoparticle protein corona: from structure and function to therapeutic targeting, *Lab Chip*, 23 (2023) 1432-1466.
- [415] V. Vetri, F. Librizzi, M. Leone, V. Militello, Thermal aggregation of bovine serum albumin at different pH: comparison with human serum albumin, *Eur Biophys J*, 36 (2007) 717-725.
- [416] J.G. Lee, K. Lannigan, W.A. Shelton, J. Meissner, B. Bharti, Adsorption of myoglobin and corona formation on silica nanoparticles, *Langmuir*, 36 (2020) 14157-14165.
- [417] K.A. Dill, Dominant forces in protein folding, *Biochemistry*, 29 (1990) 7133-7155.
- [418] K.L. Jones, C.R. O'Melia, Protein and humic acid adsorption onto hydrophilic membrane surfaces: effects of pH and ionic strength, *J Membr Sci*, 165 (2000) 31-46.
- [419] R.L. Pinals, L. Chio, F. Ledesma, M.P. Landry, Engineering at the nano-bio interface: harnessing the protein corona towards nanoparticle design and function, *Analyst*, 145 (2020) 5090-5112.
- [420] M. van der Veen, W. Norde, M.C. Stuart, Electrostatic interactions in protein adsorption probed by comparing lysozyme and succinylated lysozyme, *Colloids Surf B Biointerfaces*, 35 (2004) 33-40.
- [421] M. Rabel, P. Warncke, M. Thurmer, C. Gruttner, C. Bergemann, H.D. Kurland, F.A. Muller, A. Koeberle, D. Fischer, The differences of the impact of a lipid and protein corona on the colloidal stability, toxicity, and degradation behavior of iron oxide nanoparticles, *Nanoscale*, 13 (2021) 9415-9435.
- [422] F. Bertoli, D. Garry, M.P. Monopoli, A. Salvati, K.A. Dawson, The intracellular destiny of the protein corona: A study on its cellular internalization and evolution, *ACS Nano*, 10 (2016) 10471-10479.
- [423] G. Oberdorster, A. Maynard, K. Donaldson, V. Castranova, J. Fitzpatrick, K. Ausman, J. Carter, B. Karn, W. Kreyling, D. Lai, S. Olin, N. Monteiro-Riviere, D. Warheit, H. Yang, I.R.F.R.S.I.N.T.S.W. Group, Principles for characterizing the potential human health effects from exposure to nanomaterials: elements of a screening strategy, *Part Fibre Toxicol*, 2 (2005) 8.
- [424] T.L. Riss, R.A. Moravec, A.L. Niles, S. Duellman, H.A. Benink, T.J. Worzella, L. Minor, Cell viability assays, in: S. Markossian, A. Grossman, K. Brimacombe, M. Arkin, D. Auld, C. Austin, J. Baell, T.D.Y. Chung, N.P. Coussens, J.L. Dahlin, V. Devanarayan, T.L. Foley, M. Glicksman, K. Gorshkov, J.V. Haas, M.D. Hall, S. Hoare, J. Inglese, P.W. Iversen, S.C. Kales, M. Lal-Nag, Z. Li, J. McGee, O. McManus, T. Riss, P. Saradjian, G.S. Sittampalam, M. Tarselli, O.J. Trask, Jr., Y. Wang, J.R. Weidner, M.J. Wildey, K. Wilson, M. Xia, X. Xu (Eds.) *Assay Guidance Manual*, Eli Lilly & Company and the National Center for Advancing Translational Sciences, Bethesda (MD), 2004.
- [425] F.K. Chan, K. Moriwaki, M.J. De Rosa, Detection of necrosis by release of lactate dehydrogenase activity, *Methods Mol Biol*, 979 (2013) 65-70.
- [426] V. Francia, D. Montizaan, A. Salvati, Interactions at the cell membrane and pathways of internalization of nano-sized materials for nanomedicine, *Beilstein J Nanotechnol*, 11 (2020) 338-353.
- [427] M.A. Castanares, B.T. Copeland, W.H. Chowdhury, M.M. Liu, R. Rodriguez, M.G. Pomper, S.E. Lupold, C.A. Foss, Characterization of a novel metastatic prostate cancer cell line of LNCaP origin, *Prostate*, 76 (2016) 215-225.

- [428] S. Pourhoseini, R.T. Enos, A.E. Murphy, B. Cai, J.R. Lead, Characterization, bio-uptake and toxicity of polymer-coated silver nanoparticles and their interaction with human peripheral blood mononuclear cells, *Beilstein J Nanotechnol*, 12 (2021) 282-294.
- [429] J. Ernst, Ex vivo - Untersuchung des therapeutischen Potentials von Nanopartikel-basierten inhalativen Antibiotika-Formulierungen zur Behandlung von Biofilm-assoziierten Infektionen bei Cystischer Fibrose, Friedrich-Schiller-Universität, Jena, 2021, pp. 169.
- [430] K. Wittmaack, Excessive delivery of nanostructured matter to submersed cells caused by rapid gravitational settling, *ACS Nano*, 5 (2011) 3766-3778.
- [431] M.M. Borner, E. Schneider, F. Pirnia, O. Sartor, J.B. Trepel, C.E. Myers, The detergent Triton X-100 induces a death pattern in human carcinoma cell lines that resembles cytotoxic lymphocyte-induced apoptosis, *FEBS Letters*, 353 (1994) 129-132.
- [432] R. Angelo, K. Rousseau, M. Grant, A. Leone-Bay, P. Richardson, Technosphere insulin: defining the role of Technosphere particles at the cellular level, *J Diabetes Sci Technol*, 3 (2009) 545-554.
- [433] D.K. Man, L. Casettari, M. Cespi, G. Bonacucina, G.F. Palmieri, S.C. Sze, G.P. Leung, J.K. Lam, P.C. Kwok, Oleanolic acid loaded PEGylated PLA and PLGA nanoparticles with enhanced cytotoxic activity against cancer cells, *Mol Pharm*, 12 (2015) 2112-2125.
- [434] N. Gunday Tureli, A. Torge, J. Juntke, B.C. Schwarz, N. Schneider-Daum, A.E. Tureli, C.M. Lehr, M. Schneider, Ciprofloxacin-loaded PLGA nanoparticles against cystic fibrosis *P. aeruginosa* lung infections, *Eur J Pharm Biopharm*, 117 (2017) 363-371.
- [435] N. Lababidi, C.V. Montefusco-Pereira, C. de Souza Carvalho-Wodarz, C.M. Lehr, M. Schneider, Spray-dried multidrug particles for pulmonary co-delivery of antibiotics with N-acetylcysteine and curcumin-loaded PLGA-nanoparticles, *Eur J Pharm Biopharm*, 157 (2020) 200-210.
- [436] K. Arnold, Entwicklung von in-vitro Modellen der Lunge zur biopharmazeutischen Testung von Nanopartikeln, Lehrstuhl für Pharmazeutische Technologie, Friedrich-Schiller-Universität Jena, Jena, 2016, pp. 96.
- [437] H.I. Chiu, N.A. Samad, L. Fang, V. Lim, Cytotoxicity of targeted PLGA nanoparticles: a systematic review, *RSC Adv*, 11 (2021) 9433-9449.
- [438] M. Bauer, C. Lautenschlaeger, K. Kempe, L. Tauhardt, U.S. Schubert, D. Fischer, Poly(2-ethyl-2-oxazoline) as alternative for the stealth polymer poly(ethylene glycol): comparison of in vitro cytotoxicity and hemocompatibility, *Macromol Biosci*, 12 (2012) 986-998.
- [439] D. Segat, R. Tavano, M. Donini, F. Selvestrel, I. Rio-Echevarria, M. Rojnik, P. Kocbek, J. Kos, S. Iratni, D. Sheglmann, F. Mancin, S. Dusi, E. Papini, Proinflammatory effects of bare and PEGylated ORMOSIL-, PLGA- and SUV-NPs on monocytes and PMNs and their modulation by f-MLP, *Nanomedicine*, 6 (2011) 1027-1046.
- [440] E.C. Gryparis, M. Hatziapostolou, E. Papadimitriou, K. Avgoustakis, Anticancer activity of cisplatin-loaded PLGA-mPEG nanoparticles on LNCaP prostate cancer cells, *Eur J Pharm Biopharm*, 67 (2007) 1-8.
- [441] B. Bozic, S. Zemljic Jokhadar, L. Kristanc, G. Gomiscek, Cell volume changes and membrane ruptures induced by hypotonic electrolyte and sugar solutions, *Front Physiol*, 11 (2020) 582781.
- [442] R. Sender, R. Milo, The distribution of cellular turnover in the human body, *Nat Med*, 27 (2021) 45-48.
- [443] E.B. Schleifman, N.A. McNeer, A. Jackson, J. Yamtich, M.A. Brehm, L.D. Shultz, D.L. Greiner, P. Kumar, W.M. Saltzman, P.M. Glazer, Site-specific genome editing in PBMCs with PLGA nanoparticle-delivered PNAs confers HIV-1 resistance in humanized mice, *Mol Ther Nucleic Acids*, 2 (2013) e135.
- [444] T.L. Hwang, I.A. Aljuffali, C.F. Lin, Y.T. Chang, J.Y. Fang, Cationic additives in nanosystems activate cytotoxicity and inflammatory response of human neutrophils: lipid nanoparticles versus polymeric nanoparticles, *Int J Nanomedicine*, 10 (2015) 371-385.

[445] L.J. Ma, R. Niu, X. Wu, J. Wu, E. Zhou, X.P. Xiao, J. Chen, Quantitative evaluation of cellular internalization of polymeric nanoparticles within laryngeal cancer cells and immune cells for enhanced drug delivery, *Nanoscale Res Lett*, 16 (2021) 40.

9 Appendix

9.1 Publications and Conference Contributions

9.1.1 Publications

B. George, M. Lehner, M. Fink, S. J. Rupitsch, H. Ermert, P.T. Hiltl, U. Savšek, G. Lee, Determination of the cavitation pressure threshold in focused ultrasound wave fields applied to sonosensitive, biocompatible nanoparticles for drug delivery applications, *Current Directions in Biomedical Engineering*, 6 (2020) 539-542.

B. George, U. Savšek, D. Fischer, H. Ermert, S. Rupitsch, Investigation of inertial cavitation of sonosensitive and biocompatible nanoparticles in flow-through tissue mimicking phantoms employing focused ultrasound, *Biomedical Engineering / Biomedizinische Technik*, 66 (2021) 349-353.

B. George, U. Savšek, D. Fischer, H. Ermert, S.J. Rupitsch, Investigation of inertial cavitation induced by modulated focused ultrasound stimuli, *Current Directions in Biomedical Engineering*, 8 (2022) 459-462.

B. George, M. Wittenbrink, U. Savšek, C. Kroh, D. Fischer, H. Ermert, S.J. Rupitsch, Prototype of a coupling device to investigate focused ultrasound-induced inertial cavitation for drug delivery applications, *Current Directions in Biomedical Engineering*, 9 (2023) 162-165.

9.1.2 Conference Contributions

Poster presentation: U. Savšek, B. George, P. T. Hiltl, M. Fink, S. J. Rupitsch, H. Ermert, G. Lee. Ultrasound-induced release of coumarin-6 from polymer nanoparticles. 24th Annual Meeting Controlled Release Society Local Chapter Germany, February 20-21 2020, Munich, Germany

Poster presentation: U. Savšek, B. George, S. J. Rupitsch, H. Ermert, D. Fischer, G. Lee. *In vitro* release of coumarin-6 from sonosensitive polymer nanoparticles. 25th Annual Meeting Controlled Release Society Local Chapter Germany, March 03-05 2021, Aachen (Virtual Meeting), Germany

Poster presentation: U. Savšek, B. George, S. J. Rupitsch, H. Ermert, D. Fischer, G. Lee. Ultrasound-induced release of rhodamin B from polylactic acid nanoparticles. 12th World Meeting on Pharmaceutics, Biopharmaceutics and Pharmaceutical Technology (PBP), May 11-14 2021, Virtual Meeting

Oral presentation: U. Savšek, B. George, S. J. Rupitsch, H. Ermert, G. Lee, D. Fischer. Investigation of sonosensitive PEG-PLGA and PLGA nanocapsules for drug delivery with use of focused ultrasound. 20th Annual International Symposium for Therapeutic Ultrasound, June 06 – 09 2021, Gyeong ju (Hybrid Meeting), Korea

Poster presentation: U. Savšek, B. George, S. J. Rupitsch, H. Ermert, D. Fischer, G. Lee. Sonosensitive nanocapsules: An emerging non-invasive method for a local drug release. Jahrestagung der Deutschen Pharmazeutischen Gesellschaft, September 28 – October 01 2021, Virtual Meeting

Poster presentation: U. Savšek, B. George, S. J. Rupitsch, H. Ermert, G. Lee, D. Fischer. Sonosensitive nanocapsules: an emerging non-invasive method for local drug release. 13th World Meeting on Pharmaceutics, Biopharmaceutics and Pharmaceutical Technology (PBP), March 18-31 2022, Rotterdam, The Netherlands

Abstract: U. Savšek, B. George, S. J. Rupitsch, H. Ermert, G. Lee, D. Fischer. Ultrasound sensitive polymer nanocapsules as an emerging non-invasive method for drug delivery. 16th Thementage Grenz- und Oberflächentechnik (ThGOT) und 13. Thüringer Biomaterialien Kolloquium, June 14-15 2022, Zeulenroda, Germany

Oral presentation: U. Savšek, B. George, S. J. Rupitsch, H. Ermert, G. Lee, D. Fischer. Investigation of inertial cavitation of sonosensitive nanocapsules dispersed in different media relevant for therapeutic application. 44th Annual International Conference of the IEEE Engineering in Medicine and Biology Society, July 11-15 2022, Glasgow, Scotland, UK

Poster presentation: U. Savšek, B. George, S. J. Rupitsch, H. Ermert, G. Lee, D. Fischer. Polymer based nanocapsules for ultrasound mediated drug delivery. Jahrestagung der Deutschen Pharmazeutischen Gesellschaft, September 13-16 2022, Marburg, Germany

9.2 Erklärung der Eigenleistung

Teile der vorliegenden Arbeit sind durch Kooperationen mit anderen Wissenschaftlern zustande gekommen. Diese sind an den entsprechenden Stellen namentlich genannt und im Folgenden mit ihren Beiträgen aufgelistet:

1. Aufbau des Ultraschall-Setups und Untersuchung der Kavitationseigenschaften der Nanopartikel (Methodenentwicklung, Interpretation der Ergebnisse):
Benedikt George, Prof. Dr. Stefan J. Rupitsch (Albert-Ludwigs-Universität Freiburg, Deutschland). und Prof. Dr. Helmut Ermert (Univeristätsklinik Erlangen, Deutschland)
2. Untersuchung der zytotoxischen Effekte der Nanopartikel (Methodenentwicklung, Probenvorbereitung, Messung, Auswertung, Interpretation der Ergebnisse):
Anže Zidar, Prof. Dr. Matjaž Jeras und Prof. Dr. Julijana Kristl (University of Ljubljana, Slowenien)

Basel, den 11.12.2023

Ula Savšek